2015

Dose verification for ophthalmic plaque brachytherapy quality assurance

Michael R. Weaver
University of Wollongong

DOSE VERIFICATION FOR OPHTHALMIC PLAQUE BRACHYTHERAPY QUALITY ASSURANCE

MICHAEL R. WEAVER

Bachelor of Engineering (Honours Class I)

A dissertation submitted in fulfilment of the degree of
Doctor of Philosophy

UNIVERSITY OF
WOLLONGONG

School of Physics

2015

CERTIFICATION

I, Michael R. Weaver, declare that this thesis, submitted in fulfilment of the requirements for the award of Doctor of Philosophy, in the School of Physics, Faculty of Engineering and Information Sciences, University of Wollongong, is wholly my own work unless otherwise referenced or acknowledged. The document has not been submitted for qualifications at any other academic institution.

Michael R. Weaver
May 2015

Dedicated to my patient and loving wife, Phillipa

Table of Contents

List of Tables

List of Figures

List of Listings

List of Abbreviations

3D Three-Dimensional

PANOPTES Pixelated, Automated Nuclear Ophthalmic Plaque Treatment Evaluation System

AAPM The American Association of Physicists in Medicine

ABS American Brachytherapy Society

ANSTO Australian Nuclear Science and Technology Organisation

API Application Programming Interface

C-V Capacitance-Voltage

CI Confidence Internal

COMS Collaborative Ocular Melanoma Study

CS Chip Select

DAC Digital-to-Analogue Converter

EMI Electromagnetic Interference

FDA U.S. Food and Drug Administration

FPGA Field Programmable Gate Array

FWHM Full Width at Half Maximum

HDL Hardware Descriptor Language

HDPE High density polyethylene

I-V Current-Voltage

IBICC Ion Beam-Induced Charge Collection

ICCC Illawarra Cancer Care Centre

MCA Multichannel Analyser

PCB Printed Circuit Board

PLL Phase-Locked Loop

PMMA Polymethylmetacrylate

RF Radio Frequency

ROPES Radiation Oncology Physics and Engineering Services Pty. Ltd., Australia

SCA Single Channel Analyser

SDD Source-Detector Distance

SDI Serial Data In

SDO Serial Data Out

SPI Serial Peripheral Interface

TLD Thermoluminescent Dosimeter

TOT Time-Over-Threshold

TPS Treatment Planning System

USB Universal Serial Bus

Dose Verification for Ophthalmic Plaque Brachytherapy Quality Assurance

Michael R. Weaver

Abstract

Intraocular melanoma is a rare form of cancer with a high mortality rate and limited effective treatment options. It causes death in 45% of patients within 15 years, typically within 6 – 9 months of the first signs of metastatic spread. Plaque brachytherapy is one of the most common treatments, and has proven to be quite successful at local tumour control. It involves temporarily stitching a small, radionuclide-bearing device, called an eye plaque, on the surface of the eye above the tumour.

The accuracy of treatment planning and dose verification procedures remains sub-optimal, due to the very high gradient of the radiation field immediately adjacent to the sources. Ideally, the dose distribution should be directly measured using the actual plaque and brachytherapy sources via a high-resolution spatial dosimetry sensor. The reverse-biased silicon diode has proven to be particularly well suited to real-time, accurate dosimetry due to the high tissue-equivalence of silicon.

The current recommended treatment planning process is based on TG-43U1 formalism, which assumes infinite water surroundings and does not account for material heterogeneities. Plaque brachytherapy treatment, however, includes regions of high Z_{eff} materials, including bone and the plaque, which have been shown to significantly affect dose. An accurate dose verification system for plaque brachytherapy would have great potential for improved treatment efficacy and reduced damage to healthy tissue through dose optimisation and encouraging patient-specific plaque customisation.

The project aimed to develop a high-precision, volumetric dosimetry system, the Panoptes, based on silicon detector technology. Two variants of the concept were developed and validated experimentally; the first with a single-diode detector, and the second with a pixelated detector array.

When tested with a brachytherapy plaque fitted with ten ^{125}I seeds, the dose measured with the single-diode detector was within 4% of the TG-43U1 formalism at distances greater than 3.0 mm from the plaque.

Medipix detectors demonstrated the potential of using pixelated detectors and spectroscopic dosimetry in ^{125}I plaque brachytherapy by showing a correlation within 1% between event counting and charge modes. This illustrated that event counting would be a feasible dosimetry technique in the subsequent design of the Panoptes.

Depth-dose measurements using the Panoptes showed agreement within $\sim 4\%$ with Monte Carlo simulations, Plaque Simulator software and the TG-43U1 formalism along the central plaque axis. A volumetric dosimetry tool, such as the Panoptes, could offer much to improve current dose verification and treatment planning practises in eye plaque brachytherapy.

KEYWORDS: ophthalmic, eye, plaque, brachytherapy, I-125, dosimetry, Medipix, pixelated

Acknowledgements

I would like to express my appreciation and gratitude to my supervisors, Professor Anatoly Rozenfeld, Associate Professor Michael Lerch and Dr. Daniel Franklin, without your great support and encouragement, this thesis would never have been realised. You have taught me many invaluable skills during my development in becoming a research scientist and helped prepare me for my career ahead.

I would also like to sincerely thank the supportive staff and students at the Centre for Medical Radiation Physics who have helped me along the way. Thanks to Dr. Marco Petasecca, you have always had time for my questions and provided endless help around the lab. Thanks to Dr. Dean Cutajar, you provided me with guidance for all manner of things more times than I care to remember.

I would like to thank my collaborators from the Brookhaven National Laboratory, Instrumentation Division; the Medipix Collaboration; SPA BIT foundry; the Australian Nuclear Science and Technology Organisation; the Geant4 collaboration; and the Prince of Wales Hospital, Radiation Oncology. Especially, Dr. Jan Jakůbek, Dr. Gianluigi De Geronimo and Dr. Don Pinelli for your support, patience and understanding.

I would like to express special thanks to my friends and family who were always there to provide me with encouragement and support and who helped me stay resilient and robust of character against the icy fingers of insanity which constantly clawed at my soul during this study. Thanks to my parents, Robert and Margie, who did everything in their power to ease the burden of my work. A big heartfelt thanks to Sheridan Gho, for the camaraderie and help in deciphering my excuse for a consciousness into what has become this document. Most of all, I would like to thank the person this thesis has probably affected the most beyond me, my wife, Phillipa. For being there, no matter what, to share my successes and frustrations and for all those hours of proofing and brightening my life - thank you*!*

Chapter 1

Introduction

> *There are three classes of people: those who see, those who see when they are shown, those who do not see.*
>
> — Leonardo Di Vinci

Uveal melanoma is the most common of the intraocular cancers, and yet is a disease that few are likely to be aware of. It affects a relatively low number of people worldwide, with age-standardised incidence rates in Australia being amongst the highest, at around seven people per million[1]. However, despite its low incidence, the prognosis for the disease can be very serious, with metastasis, or the development of distant secondary malignant growth, commonly occurring in the liver and affecting approximately 50% of uveal melanoma patients[2]. Metastatic disease is rarely responsive to treatment with death usually occurring within six to nine months of the first signs of metastatic symptoms[3]. Patients whose cancer is successfully treated still often suffer degradation in vision or pain in the affected eye.

There are several treatments aimed at controlling intraocular cancers, the most common of which include enucleation and radiotherapy. Enucleation involves complete removal of the globe of the eye and is often used in treating large tumours, in cases where maintaining useful vision is unlikely. The two most common forms of

radiotherapy are external beam therapy and plaque brachytherapy. External beam therapies, particularly proton and heavy ion beam therapies, have been shown to have good efficacy[4–7], but are limited in availability. Plaque brachytherapy is much more widespread and has been shown to have similar clinical outcomes to enucleation, with the advantage of preservation of the eye and vision[8,9].

In plaque brachytherapy, a small, metallic partially-spherical cap, called a *plaque* with small embedded radionuclide sources is sutured onto the eye, above the tumour. Here, it delivers a therapeutic dose of radiation to the tumour whilst shielding the surrounding healthy tissue. The plaque remains in place long enough to deliver the prescribed dose, usually 85 Gy to the tumour apex, at a rate of around $0.6\,\mathrm{Gy\,h^{-1}}$ to $1.05\,\mathrm{Gy\,h^{-1}}$[10]. The sources used are usually either iodine-125 (^{125}I), palladium-103 (^{103}Pd) or ruthenium-106 (^{106}Ru).

Plaque brachytherapy has been shown to have excellent local tumour control, or eradication of clonogenic tumor cells, in around 90% of cases, with an overall mean survival of approximately 84 % after five years[8,9,11–17]. The treatment is associated with a number of radiation-induced side effects such as retinopathy, optic neuropathy, choroidopathy, cataract, and scleral necrosis as well as loss of visual acuity[18] and chronic pain or discomfort in the treated eye[19]. Furthermore, large tumours have also proved difficult to treat, with the recommended treatment being enucleation[10].

Currently in plaque brachytherapy, treatments are planned using the Task Group 43U1 formalism[20], as recommended by The American Association of Physicists in Medicine (AAPM) and the American Brachytherapy Society (ABS). The TG-43U1 protocol is a set of dose calculation formalisms that are used by clinicians to predict dose distributions of the radiation sources used in brachytherapy, known as *seeds*. These calculations form the basis for the treatment plans for patients and ultimately determine the success of the treatment. While this dosimetry formalism has been

supplemented as recently as 2007[21] to accommodate concerns such as calculating down to distances of 1.0 mm with low-energy brachytherapy sources, some major caveats remain.

The TG-43U1 and its supplement, TG-43U1S1, are limited in their practical accuracy as they assume an environment of infinite homogeneous water medium and do not account for the material heterogeneities inherently present in and around the treatment area. These heterogeneities occur due to surrounding structures such as the metal backing of the plaque and the bony structures around the eye, and cause variable attenuation of the delivered dose due to differences in their atomic properties.

Of the few treatment planning systems that can provide heterogeneity-corrected dose calculations, such as Plaque Simulator[22], none has yet received certification by either the Conformité Européenne (CE) or the U.S. Food and Drug Administration (FDA). Until such certification is granted, the AAPM will not recommend the treatment planning software as a primary dose calculation tool.

Without a reliable and certified treatment planning system (TPS) that accounts for material heterogeneities, there is a need for the development of methods for preoperative treatment verification, such as a reliable tool capable of high resolution, real-time dosimetry for physical simulation of treatment plans.

Intraocular tumours are intrinsically difficult to treat due to their small size and the presence of nearby structures that must be avoided or protected in order to preserve vision. Ideally, when treating with radiotherapy, dose delivery to tumour cells should be maximised and dose to healthy tissue should be avoided or minimised. Of course, this degree of selectivity is rarely feasible; however since normal cells have better repair mechanisms, they are able to survive higher doses than cancer cells[23]. This illustrates the delicate balance between success and failure in radiotherapy and the importance of accurate dosimetry.

Various techniques have been used in the literature for plaque dosimetry including thermoluminscent dosimeters (TLDs), polymer gels, radiochromic films, liquid scintillators, plastic scintillators and semiconductor diodes. No existing ocular plaque dosimetry technique provides fast, high-quality sampling of the 3D dose distribution, particularly close to the plaque surface.

Several limitations and uncertainties in plaque radiotherapy currently remain. These include an absence of preoperative treatment verification, imprecision in the surgical placement of the plaque, the lack of any certified treatment planning that can account for heterogeneous materials, source-related uncertainties, and, to some extent, measurement of tumour geometry. The current lack of research and development into plaque brachytherapy treatment verification can be, in part, attributed to the relatively low financial incentive resulting from low rates of incidence of the disease in addition to the inherent technological challenges. Despite this, the high individual patient cost provides a compelling reason to focus research attention on developing better treatment tools, in this under-investigated field. Development of a practical plaque treatment verification system is now technologically feasible and will offer many benefits for plaque brachytherapy.

1.1 Objectives and Scope

The overall aim of this thesis is to address the current lack of preoperative treatment verification in plaque brachytherapy. This aim is further subdivided into the following strategic elements:

- Identify the shortcomings of the quality assurance systems in plaque brachytherapy;
- Experimentally assess the validity of using a single silicon diode detector for

plaque brachytherapy dosimetry;

- Experimentally assess the validity of using a pixelated silicon detector for plaque brachytherapy dosimetry with an existing device;
- Optimise detector design for two plaque brachytherapy dosimetry concepts: translational and rotational;
- Integrate the detector into an electronic readout system for real-time measurements; and
- Evaluate the developed dosimetry system in plaque brachytherapy treatments.

1.2 Thesis Structure

To address these objectives, this thesis is divided into three parts:

Part I, which focuses the study, providing relevant context and a semiconductor dosimetry background;

Part II, which provides validation of the various concepts used in the research problem; and

Part III, which details the development and evaluation of a novel dosimetry system for plaque brachytherapy called the PANOPTES (Pixelated Automated Nuclear Ophthalmic Plaque Treatment Evaluation System).

These parts are further divided into seven chapters making up a total of nine chapters in the thesis.

Part I is comprised of Chapter 2 and Chapter 3, and provides context, background information and project motivation. Chapter 2 provides a review of the current literature relating to intraocular melanoma, treatments and dosimetry techniques associated

with plaque brachytherapy. Chapter 3 provides a brief background on semiconductor radiation detector systems and their application in dosimetry.

Part II is comprised of Chapter 4 and Chapter 5 and details validation studies of single and multiple detector concepts, respectively. Chapter 4 evaluates the concept of using a single silicon detector to measure surface dose of an eye plaque. Building on this, Chapter 5 proposes and evaluates two concepts of using pixelated silicon semiconductors to generate dose volumes using translation and rotation, respectively. These chapters have resulted in the following publications:

- M. Weaver, J. Green, M. Petasecca, M. .L .F. Lerch, D. Cutajar, D. R. Franklin, J. Jakůbek, M. Carolan, M. Conway, S. Pospíšil, T. Kron, P. Metcalfe, M. Zaider, and A. Rosenfeld, "Three-dimensional dosimetry imaging of I-125 plaque for eye cancer treatment," *Nuclear Instruments and Methods in Physics Research Section A: Accelerators, Spectrometers, Detectors and Associated Equipment*, vol. 633, pp. S276–S278, May 2011.

- M. Weaver, M. Petasecca, M. .L .F. Lerch, D. Cutajar, J. Jakůbek, S. Pospíšil, and A. Rosenfeld, "Dosimetry verification in eye brachytherapy using silicon pixelated detectors," *Radiation Measurements*, vol. 46, no. 12, pp. 2010–2013, Dec. 2011.

The final part, Part III, details the design through to testing of the PANOPTES and consists of Chapters 6 to 8. The design and development details of the PANOPTES and its constituent parts are presented in Chapter 6. Chapter 7 characterises the PANOPTES detector using several methods to establish expected outcomes and dosimetric accuracy and reliability. The work from Chapter 7 resulted in the following publication:

- M. Weaver, M. Petasecca, D. L. Cutajar, M. L. F. Lerch, G. De Geronimo, D. Pinelli, A. Cullen, D. Prokopovich, V. Perevertaylo, and A. Rosenfeld, "Panoptes:

Calibration of a dosimetry system for eye brachytherapy," *Radiation Measurements*, vol. 71, pp. 310–314, Dec. 2014.

The performance of the PANOPTES is evaluated in Chapter 8 through comparison of dose volume measurements against both calculated and simulated results.

The final chapter in the thesis provides a summary of the outcomes of each chapter, and provides some recommendations for further improvements to plaque brachytherapy.

This document structure is depicted in Figure 1.1, showing the relationship of the parts and chapters and detailing the primary outcomes for each chapter.

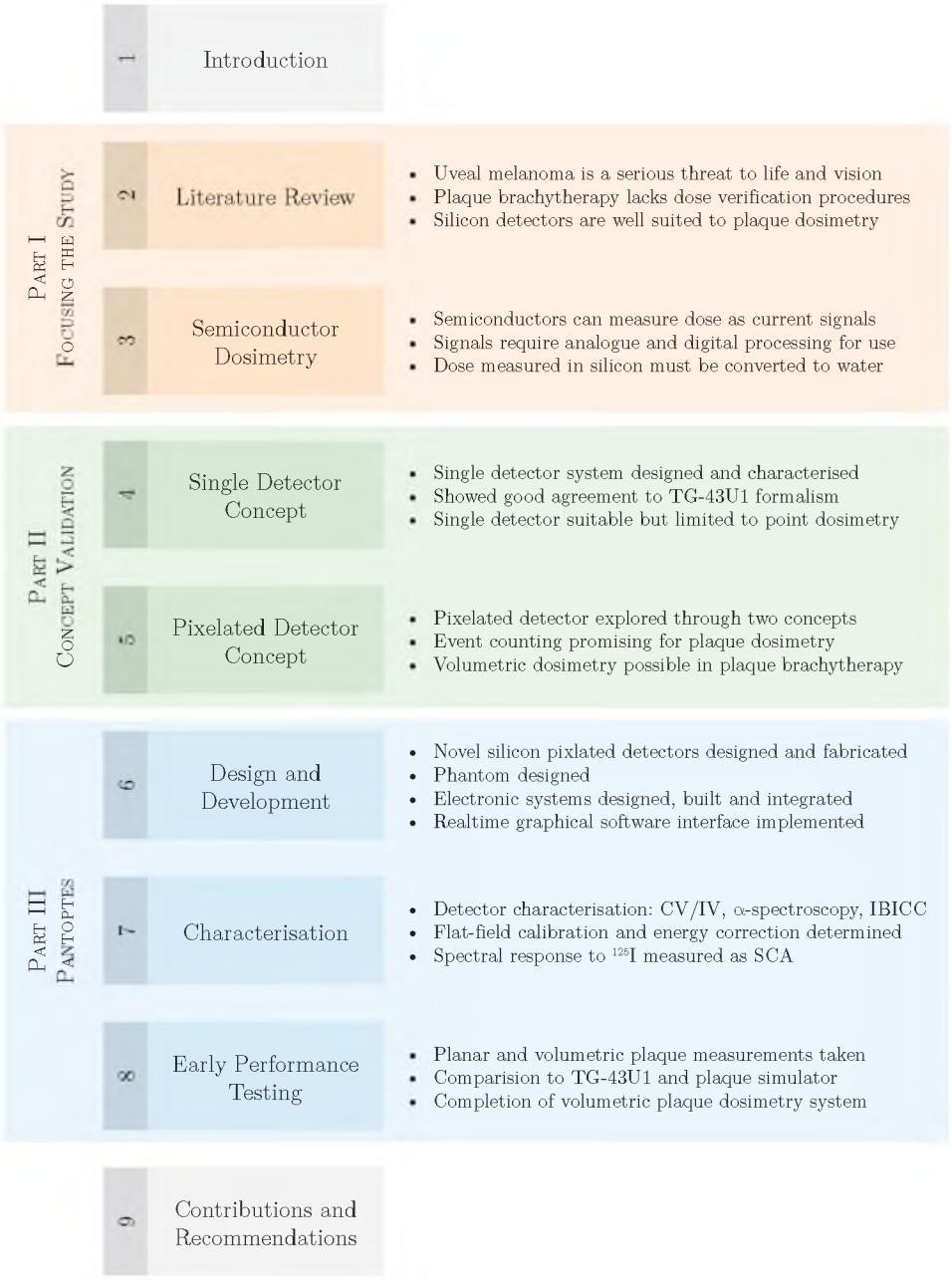

Figure 1.1: Summary of each chapter within the thesis.

Part I

Focusing the Study

Chapter 2

Literature Review

This chapter provides a background on the anatomy of the eye, intraocular cancer incidence and outcomes and several common treatments including plaque brachytherapy. It also reviews current dosimetry practises and the limitations of plaque brachytherapy, including a review of previously used dosimetry techniques.

2.1 Ocular Cancer

This section introduces some fundamental concepts in ocular oncology, including the anatomy of the human eye, and the prevalence, pathology and mortality rates of intraocular cancer. Australia, like many other places in the world, does not have access to the full range of available treatments for uveal melanoma. Plaque brachytherapy is the most common radiotherapy treatment for the disease and has proven to have very good clinical outcomes. Despite this, rates of side effects are still high and there are several limiting factors in the treatment process that could be improved, including: accurate definition of the tumour geometry; surgical placement of the plaque; treatment planning; and uncertainties in source placement.

2.1.1 Ocular Anatomy

The human eye is a complex sensory organ which focuses incident light onto a photosensitive layer of specialised cells, so that the resulting image can be converted into electrical signals for interpretation by the brain as vision. Anatomically, it comprises three concentric tunicae, or layers, as shown schematically in Figure 2.1. From outermost to innermost, these are:

- the fibrous layer consisting of the cornea and sclera;
- the vascular layer, called the uvea, consisting of the iris, the ciliary body and the choroid; and
- the retina.

Within the retinal layer is the vitreous body, a transparent, gelatinous substance that does not contain any vital cells.

The cornea covers the most anterior part of the eye, including the anterior chamber, the iris and the lens. It functions as a barrier against foreign materials and also as a powerful refractive surface, providing approximately 65 % – 75 % of the eye's total focusing power.

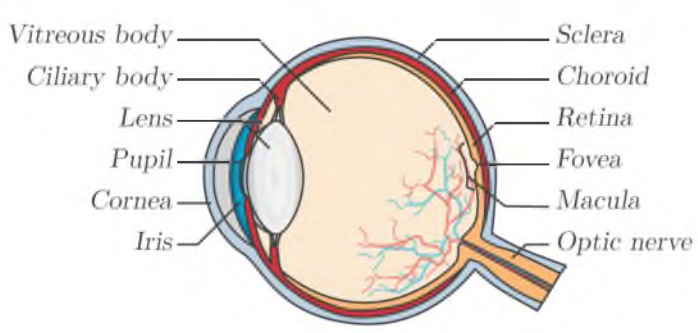

Figure 2.1: Schematic of human eye including the *a*) outer layer (sclera and cornea) *b*) vascular uveal layer (iris, ciliary body and choroid) *c*) retinal layer *d*) central vitreous body.

The sclera is contiguous to the cornea and is observed as the white of the eye. It is approximately 1 mm thick and is made up of strong, dense connective tissue that gives firmness and structure to the globe. The sclera also provides insertion points for the extraocular muscles, assists in controlling the intraocular pressure and acts as a form of mechanical protection for the intraocular features. The sclera is capable of tolerating extremely high radiation doses[24].

The uvea, or uveal tract, is made up of the iris, the ciliary body and the choroid. The iris is the coloured layer located anteriorly on the globe. It serves as the aperture for the ocular optics by controlling the size of the hole in its centre called the pupil. Contiguous to this is the ciliary body which contains the ciliary muscle fibres and ciliary processes, used for focusing the lens and generation of the aqueous humour. The other side of the ciliary body is met by the choroid. The choroid makes up the majority of the uvea and is highly vascular, providing blood for the ocular structures.

The retina comprises a number of layers of densely packed cells which convert light into neural signals. One of the most critical parts of the retina is the macula. It is located temporal to the optical nerve at a distance of approximately 3 mm and is responsible for the sharpest central region of vision. The optic nerves are responsible for conveying all vision signals to the brain.

Although intraocular tumours can develop throughout the eye, *uveal melanomata* are the most common due to their vascular prominence and include tumours which have developed in the iris, ciliary body or the choroid[3].

2.1.2 Intraocular Cancer

The symptoms of intraocular cancer tend to include pain within the eye and loss in vision or visual acuity. The disease seriously threatens the life of the patient if local tumour spread cannot be controlled or metastatic disease occurs, for which there is

no cure[25]. There are several types of intraocular cancer that can occur, each with differing incidence frequencies.

Metastatic melanoma of the uvea is the most common primary intraocular cancer in adults and the second most common primary malignant melanoma which occurs in the body[26,27]. Of the melanomata occurring in the uveal tract, 80 % – 90 % are located within the choroid[3,28,29], while occurrence of metastases within the iris, ciliary body, retina, optic disc and vitreous humour are rare[30].

The highest incidence rates of uveal melanoma have been observed in Northern Europe and Australia while the lowest rates have been observed among Asian, Hispanic and dark skinned populations[31,32]. The age-standardised incidence rates in Australia for men are 0.80 per 100,000 (95% CI 0.71 – 0.89) and for women are 0.61 per 100,000 (95% CI 0.53 – 0.69)[1]. By comparison, the mean, aged-adjusted incidence of uveal melanoma in the United States is 0.51 per 100,000 and has remained unchanged from 1973 – 2008[29]. Overall, the incidence rate of uveal melanoma has remained relatively stable across Europe, North and Central America, Asia and Oceania over the period 1983 – 1997[31].

Metastasis occurs vascularly, spreading to the liver and other parts of the body[3]. Even in cases where local tumour control of primary uveal melanoma is successful, the dangerous cells can remain dormant for many years[33]. Of these cases, metastatic disease will still occur in about 40 % – 50 % of uveal melanoma patients[2,34]. The prognosis of metastatic spread is extremely poor, with fatalities usually occurring within around six to nine months of the first signs of symptoms[3].

Uveal melanoma related mortality is 31 % by 5 years and is 45 % by 15 years[35]. Earlier diagnosis and management is associated with better outcomes and a better chance of salvaging the eye and vision[3,36]. The size, shape and location of the tumour also affect the treatment outcome[37–40].

The prognoses of uveal melanomata typically worsen with increasing tumour thickness. Estimates of 5-year mortality rates following enucleation (removal of the eye) were 16 % for small, 32 % for medium, and 53 % for large tumours[37] (Table 2.1).

2.2 Current Treatments

Modern treatment of choroidal melanoma offers good preservation of vision in most cases[3,6,41]. Despite this, there has been no improvement in survival rate over the last 25 years[42]. This is thought to be due to latent acting dormant circulating malignant cells which can be established in the system prior to tumour control[2].

There are a number of treatments for intraocular cancer which may be selected based on factors such as the size, shape and location of the tumour and treatment availability. These include transpupillary thermotherapy, photodynamic therapy, orbital exenteration, and, in further-progressed tumours, chemotherapy, and immunotherapy. However, the most common treatments for intraocular cancer are enucleation, endoresection and radiotherapy. There are two main types of radiotherapy that are used for the treatment of ocular cancers: external beam radiotherapy, and plaque brachytherapy, the latter of which is the focus of this thesis.

Table 2.1: Choroidal melanoma estimates of 5-year mortality following treatment with enucleation (removal of the eye) based on tumour size[37]. The 95% confidence intervals are displayed in brackets.

Tumour Size	Basal Diameter	Height	5-y Mortality, %
Small	$< 10\,\text{mm} - 11\,\text{mm}$	$< 2\,\text{mm} - 3\,\text{mm}$	16 (14 – 18)
Medium	$< 15\,\text{mm} - 16\,\text{mm}$	$3\,\text{mm} - 8\,\text{mm}$	32 (29 – 34)
Large	$> 15\,\text{mm} - 16\,\text{mm}$	$> 8\,\text{mm}$	53 (50 – 56)

2.2.1 Enucleation

Enucleation is a process that involves the removal of the entire globe of the eye. Today, this treatment is used for advanced tumours, when there is little hope for salvaging useful vision. It is also occasionally used where tumour development has led to a blind, painful eye or when more conservative methods of treatment have not been successful. The empty socket is filled with an implant and rehabilitated for six weeks, after which a prosthetic eye is inserted[43,44]. Despite the irrevocable and severe nature of the procedure, the 5-year mortality is up to 53% for large tumours (see Table 2.1 for further details)[37].

2.2.2 Endoresection

Endoresection, or local resection, refers to the surgical removal of the tumour from within the eye and can be achieved either through the scleral surface or the retina. Trans-scleral resection describes access to the tumour mass through a lamellar flap incised in the sclera above the tumour, while transretinal resection enters through the retina. Trans-scleral resection of an ocular tumour is surgically difficult, but in some cases is still regarded as the best option. Depending on the location of the tumour, this technique offers conservation of the central vision or temporal field, where radiotherapy, as an alternative, has a higher risk of optic neuropathy[45]. Recurrence rates at 4 years for trans-scleral local resection range from 6% to 58% depending on the risk factors present[46,47].

2.2.3 External Beam Radiotherapy

External beam therapy treats intraocular cancers by delivering a beam of charged particles, such as protons or helium-ions, through air, usually into the anterior side of the eye. As depicted in Figure 2.2, these heavy charged particles deliver dose with a

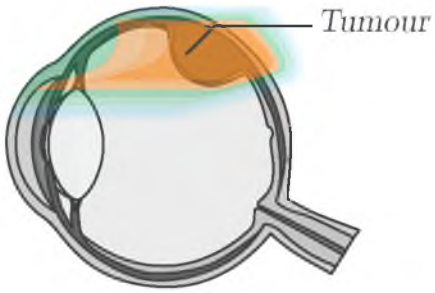

Figure 2.2: A depiction of external hadron beam radiotherapy, showing the effect of the spread out Bragg peak on dose distribution (*colour*).

distribution that follows the spread out Bragg peak, depositing maximum dose close to the end of the particle's path through the tumour.

Due to the incident direction of the treatment, the anterior features of the eye and the ocular adnexa receive, on average, 70% of the dose delivered to the tumour. This undesirable dose can lead to adverse affects such as eyelash loss, dry eye, keratitis, corneal ulceration, iris neovascularization, iridocyclitis, cataract, and glaucoma[18,48–50].

In comparison to proton therapy, plaque brachytherapy is less expensive, less time consuming and less likely to cause discomfort and cosmetic deficit from conjunctival and eyelid irradiation[3]. In addition to this, proton and heavy ion therapies are unavailable in many places, including Australia, unlikely plaque brachytherapy. However, plaque brachytherapy results in higher rates of recurrence compared to external beam radiotherapy (1.5 % – 15 %[51–53] versus 3 % – 4 %[6,54,55]).

2.2.4 Plaque Brachytherapy

Radiotherapies are the most common treatments for uveal melanoma, and of these, plaque brachytherapy is the most prevalent treatment. This treatment option is selected based on the size, shape and location of the tumour, tending to be preferred in the case of medium-sized choroidal melanomata. In plaque brachytherapy, a device called a *plaque*, which contains a radioactive source, is sutured to the eye adjacent to the

tumour, where it is kept in place for a predetermined treatment duration (Figure 2.3).

The shape of the plaque is based on a shelled spherical cap to fit the surface of the eye. It delivers dose through either:

- '*seeds*' of a radionuclide within an insert in metal backing (Figure 2.4); or
- a radionuclide layer deposited onto a backing metal (Figure 2.5).

Typical radionuclides used for the seeds include iodine-125 (^{125}I), palladium-103 (^{103}Pd) or cesium-131 (^{131}Cs), whilst ruthenium-106 (^{106}Ru) is used for the uniformly coated plaques. Table 2.2 provides a summary of radionuclides detailing their emission type, energies and half-lives. In both plaque styles, material with a high atomic number such as gold, silver or stainless steel is used as a shield on the outer side. This shield protects posterior features such as the brain and improves safety for surgeons and handlers. Figure 2.3 shows an example of the dose distribution of a seeded plaque. These plaques also incorporate various design features including flanges, eyelets and notches to fit around the optic nerve.

Several designs of eye plaques are currently in use throughout the world. The Radiation Oncology Physics and Engineering Services Pty. Ltd., Australia (ROPES)[57–59] series plaques are commonly used in Australia; whilst the Eckert & Ziegler BEBIG GmbH, Germany[56] plaque series are popular in Europe; and the Collaborative Ocu-

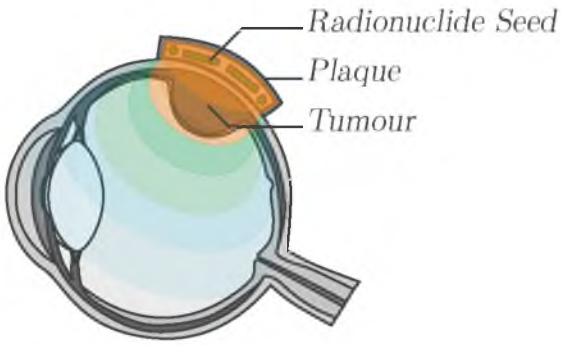

Figure 2.3: A depiction of plaque brachytherapy showing an example of contoured dose gradients within the eye (*colour*).

Figure 2.4: ROPES 15 mm seed-bearing plaque, showing the metal backing (*left*), acrylic insert (*right*) and assembled device (*centre*).

Figure 2.5: A sample of BEBIG ^{106}Ru eye plaques that illustrate different designs, targeting specific locations on the eye.[56]

Table 2.2: A list of common radionuclides used in plaque brachytherapy, including their radiation type and energies.

Radionuclide	Primary emission	Energy	Half-life (days)
^{125}I	γ	28.51 keV[a]	54.9
^{103}Pd	γ	20.74 keV[a]	17.0
^{131}Cs	γ	30.3 keV[a]	9.7
^{106}Ru	β	3.5 MeV[b]	373.6

[a] Weighted mean energy
[b] Maximum energy
Note: These values are nominal assuming typical encapsulation of sources.

lar Melanoma Study (COMS) plaque series is commonly used throughout the world. Despite the large variations in plaque design, the treatment has proven to have good clinical outcomes.

The COMS Group demonstrated that there were no survival differences between patients treated with ^{125}I plaque brachytherapy and those treated with enucleation[8]. There has since been a strong trend towards radiotherapy as the main treatment for uveal melanoma (1.8 % for 1973 – 1975 vs. 62.5 % 2006 – 2008), with no change in the 5-year relative survival rate in the United States from 1973 – 2008[29]. The COMS Group reports recommend ^{125}I for use in ophthalmic brachytherapy plaques[60] and it gained subsequent widespread usage in practice. Four years later, the radionuclide ^{103}Pd became available and subsequent studies have demonstrated good patient outcomes in areas including local control and visual acuity results compared to charged particle, ^{125}I or ^{106}Ru plaques[16,61]. Due to the ^{103}Pd source having a lower weighted mean energy (20.74 keV) than ^{125}I (28.37 keV) palladium photons have a shorter range in tissue, allowing adequate dose delivery to targeted regions whilst better avoiding normal tissue for medium sized plaques.

2.2.4.1 Plaque Brachytherapy Treatment Planning

Treatment planning for plaque brachytherapy is conducted by determining geometric details of the tumour, selecting an appropriate plaque, calculating the dose and, in some institutions, verification in software.

The geometry of a tumour can be determined through the use of fundus photography, A-scan (one-dimensional) and B-scan (two-dimensional) ultrasonography[62], fluorescein angiography[63], X-ray computed tomography (CT) or magnetic resonance imaging (MRI)[3,64].

Plaque selection is made after the tumour position, size and shape have been determined. During this process, the prescription point is determined and the model,

activity and number of seeds are chosen. The selected dose rate usually falls within the range recommended by the ABS in 2003, $0.6\,\mathrm{Gy\,h^{-1}} - 1.05\,\mathrm{Gy\,h^{-1}}$ [10]. Using this rate, the implant duration, usually $3\,\mathrm{d} - 7\,\mathrm{d}$, can be calculated in order to deliver the prescription dose. The original COMS trials recommended a prescription dose of 100 Gy to the apex of the tumour, but this has since been revised to 85 Gy [10,65].

Treatment parameter recommendations were re-evaluated in 2012, considering the biological effective dose as a function of position, dose, radionuclide and implant duration [66]. The study found that shorter implant durations may correlate to better outcomes compared to seven day implants when treating small or medium tumours. For additional verification, some institutions support their dosimetry calculations with the use of a treatment planning system.

The most common TPS in plaque brachytherapy is Plaque Simulator, available from BEBIG GmbH [22]. Plaque Simulator allows for the planning of plaque brachytherapy treatments using the standard TG-43U1 formalism [20] or using updated dosimetry calculations, where the user can include some heterogeneity effects of the seed holder insert, metal backing and air-eye interface. The accuracy of Plaque Simulator has been evaluated and shown to be in good agreement with radiochromic film [67,68], diode dosimeters [69] and thermoluminescent dosimeters [70]. Despite this, the Plaque Simulator documentation states that it is

> *intended for treatment simulation only [and] is neither [Conformité Européenne (CE)] certified nor [U.S. Food and Drug Administration (FDA)] approved as a treatment planning software. Dose data extracted for planning have to be verified by the physicist.* [22]

As such, the Plaque Simulator is not recommended by the AAPM or the ABS as a primary dosimetry calculation approach.

2.2.4.2 Treatment Limitations of Plaque Brachytherapy

Currently in Australia, planning for plaque brachytherapy is typically performed using the recommended TG-43U1 formalism dose calculations with the optional support of a TPS. There is only limited potential for physicists to confidently customise the plaque layout or design for a particular patient and further refining dose distributions based on factors such as tumour shape, location and proximity to vital structures. While plaque brachytherapy is a good treatment candidate for ocular cancer management, some significant challenges remain, in particular:

1. *Loss of vision and other side effects*

   Plaque brachytherapy requires not only tumour control but management of iatrogenic side-effects and complications which affect normal tissue. In fact, the success of local tumour control in the treatment means there is a shift in focus towards reduction and management of these side effects[71].

   Such complications tend to increase in likelihood with tumour size due to the greater overall treatment dose and control of dose distributions. They can include radiation-induced retinopathy, optic neuropathy, choroidopathy, cataract, and scleral necrosis[14,18,40,72–78].

   Despite preservation of the eye, a relatively large portion of patients lose useful vision after treatment[18,79] and only around 17 % of patients with large melanomas will avoid blindness for at least two years[80]. According the COMS Group[8,9,11–13], at three years 57 % of patients treated with ^{125}I retained at least 20/200[1] vision which worsens over time[15,81]. By comparison, studies showed about 76 % of patients treated with ^{103}Pd retained acuity of at least 20/200[16,82]. Vision must often be sacrificed for survival where tumours are large[40,76,80] or surround the

[1] If a person has a visual acuity of X/Y, that person can resolve the same level of detail at a distance of X that a normal person could at a distance of Y.

optic nerve[72,83]. Here, enucleation is more commonly used in place of plaque therapy.

2. *Inability to treat large tumours*

   Large ocular melanomata are a significant threat to patients (see Table 2.1). For tumours with a basal diameter greater than 16 mm and/or thickness greater than 8 mm, the recommended treatment is enucleation[10]. A ten year follow-up study by Shields et al.[40] showed that amongst 354 patients with large tumours (greater than 8 mm thick), enucleation was necessary in 34 % of patients and metastasis developed in 55 % of cases. For patients with large uveal melanomata who were treated using ^{125}I plaque brachytherapy, only 26 % (95 % CI, 16 % – 37 %) had avoided blindness at 2 years[80].

   Dose gradients can vary dramatically between tumours of different sizes. For example, for a tumour with a thickness of 10 mm treated with ^{125}I and receiving 85 Gy at the apex, the inner sclera receives 644 Gy (10 mm away from apex). By contrast, treatment of a tumour with a thickness of 3 mm with the same apex dose would deliver a dose of 166 Gy to the inner sclera. Similarly for ^{103}Pd, 85 Gy to tumour apexes of 10 mm and 3 mm delivers inner scleral doses of 766 Gy and 164 Gy, respectively[71,84]. This is a base-apex dose ratio of about 8 : 1 and 9 : 1 for 10 mm tumours treated with ^{125}I and ^{103}Pd, respectively; and about 2 : 1 for 3 mm tumours for both radioisotopes. These steep dose gradients are even more exaggerated for the beta-emitting ^{106}Ru source[18]. The phenomenon makes treating large tumours a difficult task when attempting to spare normal, healthy structures.

3. *Failure to eliminate the tumour threat*

   Local treatment failure for plaque brachytherapy, defined as tumour growth, recurrence or extrascleral extension, was reported in the COMS study to be

as low as 10.3 % (95 % CI, 8.0 % – 13.2 %) by five years[12]. A summary of plaque brachytherapy clinical studies is presented in Table 2.3, showing local control, distant failure and overall survival outcomes. This data demonstrates that although the treatment outcomes are very good, the disease is a significant threat to the patient with local control and overall survival averaging about 90 % and 84 % at five years, respectively[2]. In some cases enucleation is performed after plaque brachytherapy treatment either due to failure to control the tumour or as the result of radiation-induced pain or other side-effects like neovascular glaucoma.

In general, early failures may have been due to geometric misalignment of the plaque over the tumour while late failures could be related to a radiation-resistant tumour or lack of sterilisation[18]. Tumours with greater thickness or in close proximity to the foveal avascular zone, in the macula, have a greater failure risk[12].

[2]Calculated as the mean of local control and overall survival data at five years from all categories reported in the literature presented in Table 2.3.

Table 2.3: Summary of plaque brachytherapy clinical study outcomes

Nuclide	Study	No. of patients	Mean dose (Gy)	Mean follow up (mo)	Mean initial lesion dimensions	Local control (%)	Distant failure (%)	Overall survival (%)
^{106}Ru	Heindl et al.[89]	100	—	—	—	93 (5 yr)	10 (5 yr)	—
	Damato et al.[6]	458	115	46.8[a]	10.6/3.2 (D/T)[a]	99 (2 yr), 98 (5 yr), 97 (7 yr)	—	—
	Gündüz et al.[14]	630	—	62.4	(D)<10, 4 (T)[a]	91 (5yr)	12 (5 yr), 22 (10 yr)	—
	Wilson and Hungerford[53]	140	100	45.3	9.7/4.2 (D/T)	88.6	5	81 (6.7 yr)
	Seregard et al.[90]	266	100	43	10/4.4 (D/T)	90	11 (4 yr), 14 (5 yr)	83.1
	Lommatzsch[91]	309	100	80	COMS-S (100%)	84 (5 yr), 69.9 (6.7 yr)	12.9 (7 yr)	87.1
	Literature average	317	104	55.5	10.1/3.9 (D/T)	89.3, 91.5 (5 yr)	12 (5 yr)	85.1
^{125}I	COMS[8,9,11–13]	657	85	60	11.4/4.8 (D/T)	90	10 (5 yr), 18 (10 yr)	82 (5 yr)
	Leonard et al.[17]	37	85	100	12.3/6.3 (D/T), T2 (81%)	76	13.5	59.5
	Correa et al.[92]	120	83	50.4[a]	12.2/5.9 (D/T), COMS-M (73%)	95.3 (2 yr), 88.4 (5 yr)	9.5 (2 yr), 20.3 (5 yr)	86.7, 94.4 (2 yr), 84.1 (5 yr)
	Jensen et al.[19]	156	—	74.4[a]	—	92 (5 yr)	10 (5 yr), 27 (10 yr)	80, 83 (5 yr)
	Lumbroso-Le Rouic et al.[52]	136	112	62[a]	10.3/4.7 (D/T)	98.5	5.9, 1.7 (2 yr), 4 (5 yr)	89, 93.8 (2 yr), 88 (5 yr)
	Nag et al.[93]	78	85–100	49[a]	COMS-M (100%)	93 (5 yr)	—	86 (5 yr)
	Jones et al.[94]	63	85–100	36	4.5(T)	84	4.8 (3 yr)	—
	Char et al.[5]	449	70	—	4.6 (T)	87	—	—
	Wilson and Hungerford[53]	190	100	47.3	10.2/5.9 (D/T)	95.8	3.7	94 (8.3 yr)
	Quivey et al.[95]	150	95	68	9.7/3.7 (D/T)	81 (5 yr), 78 (5.6 yr)	17.3 (5 yr)	78
	Fontanesi et al.[81]	144	79	46	975 (V)	97.7	5.5 (4 yr)	—
	Quivey et al.[96]	239	70	36	10.9/5.5 (D/T)	91.7 (3 yr), 82 (5 yr)	7.5 (3 yr), 12 (5 yr)	—
	Char et al.[4]	98	70	41	10.7/5.5 (D/T)	86.7	8.2 (4.2 yr)	80.6 (4.2 yr)
	Packer et al.[15]	64	91	64	—	92.2 (5 yr), 87.5 (5.3 yr)	15.6 (5 yr), 17.2 (6 yr)	82.8
	Petrovich et al.[97]	85	102.6	37	6.1 (T), T2/T3 (96%) COMS-M (100%)	—	11, 10.6 (8 yr)	88, 88 (5 yr), 84 (8 yr)

Summary of plaque brachytherapy clinical study outcomes (cont.)

Nuclide	Study	No. of patients	Mean dose (Gy)	Mean follow up (mo)	Mean initial lesion dimensions	Local control (%)	Distance failure (%)	Overall survival (%)
	Literature average	170	92	52, 59[a]	11.55/5.5 (D/T), 10.5/4.35 (D/T)	93.5, 88.1 (5 yr)	8.4, 3.7 (2 yr), 6.2 (3 yr), 12.7 (5 yr) 22.5 (10 yr)	84, 94.1 (2 yr), 83.8 (5 yr)
^{103}Pd	Leonard et al.[17]	5	85	22.5	10.6/2.7 (D/T), T2 (80%)	100	0	100
	Finger et al.[98]	24	84.1	35.5, 30[a]	2.6 (T)	95.9	4.1 (6 yr)	91.7
	Finger et al.[16]	400	73	51	T1/T2 (85.5%), COMS-M (92%)	96.7	6, 3.3 (2 yr), 7.4 (5 yr), 13.4 (10yr)	87
	Literature average	400	73	43.3	N/A	96.3	N/A	87
^{131}Cs	Leonard et al.[17]	11	85	20	12.6/5.4 (D/T), T2/T3 (82%)	91	0	100
Other	Shields et al.[40][b]	354	—	—	(T)>8	91 (5 yr), 87 (10 yr)	30 (5 yr), 55 (10 yr)	—
	De Potter et al.[72][c]	93	90–110	78	3<(T)[a]<6	84 (5 yr), 73 (10 yr)	12 (4 yr), 13 (5 yr), 16 (10 yr)	81
	Lean et al.[99][d]	56	94.5	39	13.2/6.8 (D/T), T3 (68%)	91	9 (4 yr)	—
	Literature average	168	N/A	59	N/A	91, 87.5 (5 yr), 80 (10 yr)	10.5 (4 yr), 21.5 (5 yr), 35.5 (10 yr)	N/A

[a] Median value
[b] ^{125}I and ^{106}Ru
[c] ^{125}I ($n = 63$), ^{192}Ir ($n = 15$), ^{60}Co ($n = 12$) and ^{106}Ru ($n = 3$)
[d] ^{125}I and ^{192}Ir

Note: Literature averages were calculated as the means of the reported values from the available data and, where appropriate, over specified duration.
diameter ≡ D (mm); thickness ≡ T (mm); volume ≡ V (cm^3); N/A = not applicable
COMS-S: 1.5 mm ≤ T < 2.5 mm and 5 mm ≤ D < 16 mm;
COMS-M: 2.5 mm ≤ T ≤ 10 mm and D ≤ 16 mm;
COMS-L: T > 10 mm and D > 16 mm[85–87].
T1: T < 2.5 mm and D < 10 mm;
T2: 2.5 mm ≤ T ≤ 10 mm and D < 16 mm;
T3 and T4: T > 10 mm or D > 16 mm[10,88].

Source: Adapted from Leonard et al.[17].

2.2.4.3 Uncertainties in Plaque Brachytherapy

Dose verification for plaque brachytherapy systems has attracted relatively little research attention due to the low rates of incidence of ocular melanoma compared to other cancers and the intrinsic technical difficulty of accurate estimation of dose in this environment.

The literature shows that, for plaque brachytherapy, local control and overall survival are very good, as shown in Table 2.3. Despite this, there is much potential for improvement, as patients still frequently need to undergo enucleation and/or suffer from significant radiation-induced side effects such as cataract, radiation induced maculopathy and retinopathy. This has directed current research efforts towards reducing such radiation induced side effects to normal tissue[71] by addressing the remaining uncertainties in plaque brachytherapy. These uncertainties include:

1. *Tumour geometry*

   The dimensions of shape, size and location of the ocular tumour have some margin of error imparted by the imaging modality used. The most common methods for tumour dimensioning are ophthalmoscopy (62 % used as primary method), B-scan ultrasonography (18 %) and nomography (12 %)[100]. The COMS ultrasound protocol is a standard method of tumour measurement which has been highly reliable in treatment planning[100,101]. New generation, high-resolution B-Scan probes have operating frequencies that range from 20 MHz – 100 MHz and provide resolution in the range of 23 µm – 75 µm[102,103]. Three-dimensional ultrasonography has been reported to have a resolution of 150 µm axially and 270 µm laterally[104].

   Despite these good resolutions, in a study of 644 patients with unilateral medium sized choroidal melanoma, clinical and echograph measurements agreed to within ±2 mm of histopathological in only 90 % and 57 % of cases for tumour height and

longest basal diameter, respectively[100]. It has also been shown that ophthalmoscopy can misrepresent some choroidal tumours as mild, normally pigmented elevations of the retina[71]. However, in these cases, ultrasonography can be used to provide the additional dimensional information required. In cases of photography based fluorescein or indocyanine green angiography, the tumour basal dimension can be overrepresented[105,106]. Currently, CT and MRI images are limited in both spatial resolution and accuracy for delineation of ocular tumours[71].

The development of image fusion tools for plaque brachytherapy and more reliable imaging technologies will allow for three dimensional modelling of patient data with clearer representation of the tumour. Such a system would prove useful for providing information to potential preoperative dose verification tools.

2. *Plaque placement*

Surgical placement of the plaque on to the eye is the origin of the largest uncertainty between planned and actual source location in relation to patient anatomy. Plaque misalignment is more profound in certain difficult regions such as adjacent to the optic nerve. Currently, there are a number of slotted plaques available which attempt to accommodate this issue.

Placement of the plaque can be verified through a number of methods; namely, ultrasonography, scleral depression and transillumination[105,106]. When placement verification is performed using ultrasound imaging, it should be done in 2D or 3D along the longitudinal and transverse meridian lines[107].

A 2003 ABS report[10] recommends that an additional 2 mm – 3 mm be added to the tumour basal margin for placement can help mitigate the potential of tumour volume underdosing. It has been shown that better tumour coverage is

achieved through a gross-tumour-volume to planning-tumour-volume total basal expansion of 3 mm or greater and/or prescribing beyond the tumour apex[61]. Whilst this will improve tumour control, it will also increase unwanted dose to normal tissue. Preoperative dose verification is needed to optimise outcome and reduce the extent of side effects.

3. *Treatment planning*

Currently, the AAPM and ABS[10] both recommend that treatment planning be undertaken using the dosimetry formalisms from the reports, TG-43U1 (2004) and TG-43U1S1 (2007)[20,21]. These reports are limited to the use of homogeneous water as a surrounding medium and do not account for the effects of heterogeneous materials, including high Z_{eff} materials such as the plaque insert or backing, or surrounding bony structures. The minimum dose calculation distance for these formalisms is 1.0 mm (updated from the 5.0 mm minimum of the 1995 TG-43 Report[65]).

The treatment planning software, Plaque Simulator[22], is widely used to aid in treatment planning though it has not received FDA or Conformité Européenne (CE) certification. As such, it is not recommended by the AAPM and ABS for use as a primary dose calculation tool. There have been many studies showing significant discrepancies between homogeneous and heterogeneous dose calculations and measurements, especially when plaque presence is considered[70,108–114]. The AAPM and ABS recommend calculating homogeneous and heterogeneous dose separately.

A preoperative volumetric dosimetry approach to plaque brachytherapy would be of great benefit as it would inherently account for heterogeneous materials and complement existing TPS tools.

4. *Source uncertainties*

   Prior to a plaque brachytherapy treatment, the radionuclide sources should be verified using a well-type ion chamber which has been appropriately calibrated as per recommendations from the AAPM Low Energy Brachytherapy Source Calibration Working Group[115]. The AAPM Task Group No. 138 have calculated that for the dose at 1.0 cm on the seed's transverse plane, the k = 2 expanded uncertainty for low-energy sources is 8.7 %[116]. This is calculated considering the uncertainty from S_K (air-kerma strength) measurements, measured dose, Monte Carlo dose estimate, TPS interpolation uncertainties, and total dose calculation uncertainty.

Development of accurate and reliable methods for preoperative dose verification and enhancing the accuracy and capabilities of treatment planning would be a significant contribution to addressing some of the above problems. Greater confidence in treatments allow for an increased degree of patient specific plaque customisation, aimed at improved conformity of dose to tumour geometry and a reduction in dose delivered to non-cancerous tissues. Plaque customisation could be implemented through changing seed numbers and configurations along with combining seeds of different radionuclides and activities in existing plaques, or complete plaque redesign if the facilities are available.

2.3 Dosimetry

Radiation is frequently used for imaging and therapy and it is essential to measure and understand the relationship between dose and effect. Though treatments are undertaken for their therapeutic qualities, they come hand-in-hand with an associated risk of detrimental side-effects.

These iatrogenic, or treatment-induced side effects can be deterministic or stochastic. The severity of deterministic radiation-induced tissue damage, such as radiation burns to the skin, increases with increased dose. The probability of the occurrence of stochastic effects, such as radiation-induced mutations, is dependent on dose but the severity of the effect is not. Consequently, even for small doses of radiation there is some possibility of serious detrimental side effects, of which the most concerning is secondary cancer induction[117].

The aim of radiotherapy is to kill cancerous cells through damage inflicted by ionising radiation. Both cancerous cells and normal tissue are affected by radiotherapy but the success of the treatment lies in the fact that the normal tissue cells have more effective repair mechanisms and can thus withstand a significantly higher dose. Good radiotherapy treatment outcomes depend upon careful management of the dose such that the cancer cells are destroyed without causing irreparable harm to healthy tissue. These conflicting requirements put tight restrictions on the temporal and spatial distribution of the applied dose.

When irradiating tumours that are close to critical structures, steep dose gradients are needed, resulting in very little margin for error. Through measurement and calculation of the absorbed dose in these regions, radiotherapy treatments may be verified and, if necessary, modified to optimise treatment efficacy and minimise collateral damage[118].

In plaque brachytherapy, steep dose gradients are necessary if the tumour is to receive the full prescribed dose while avoiding overdosing structures such as the optic nerve, lens, iris or cornea. When healthy tissues are affected, function of critical organs can be diminished or the patient may experience pain or discomfort.

For irradiation of tumours close to the optic nerve, special plaques with an accommodating notch are typically used[70,119–121]. It has been recognised that notched

^{106}Ru plaques can overdose the optic nerve with doses of 50 Gy or greater; in some cases this leads to radiation damage to the optic nerve causing a loss of vision (optic neuropathy)[39]. Custom, collimated plaques have also been designed to offer a more homogeneous dose gradient and limit dose to the sclera and adjacent structures[70].

To preserve the useful function of the eye, accurate delivery and dosimetry in this region is critical. Simulation of dose distributions from complex plaque designs is both difficult and time-consuming. The ability to perform accurate experimental dosimetry in three dimensions using a physical simulation of the proposed treatment will therefore provide the opportunity for rapid and precise confirmation of planned dose delivery profiles for quality assurance purposes.

A number of methods currently exist for plaque dosimetry, although most have shortcomings which preclude their use in real-time dosimetry. These methods are reviewed in the following section.

2.3.1 Plaque Dosimetry

The dose gradients in the eye resulting from ocular brachytherapy plaques are necessarily very steep. Therefore, it is desirable to be able to accurately characterise the spatial dose profiles for treatment verification and optimisation. The dose profiles are significantly affected by the choice of plaque and tumour geometries, which cause significant differences in maximum and mean dose rates[12,18,40,80,84].

In order to develop a clinically valid system for pretreatment verification of plaques, the adopted dosimetry technique should be reliable, accurate, fast and straightforward. A recent review of dosimetry of plaques for intraocular tumours was included in the Task Group 129 report[71]. Table 2.4 presents a summary of studies demonstrating various dosimetry techniques used in plaque brachytherapy, including thermoluminescent dosimeters (TLDs), polymer gel, radiochromic film, liquid and plastic scintillators,

diodes and some other less commonly used techniques.

TLDs [70,108–112,122–127] have been used for dosimetric measurements in ophthalmic plaques and other types of brachytherapy. Although TLDs are sufficiently compact for this application, they are impractical for real-time clinical use.

Polymer gels [128] provide good spatial resolution in three dimensions, however they are not practical for this application due to their cost, long imaging time, sensitivity to light, temperature and oxygen and requirement of a magnetic resonance scanner for readout.

Radiochromic film [67,68,70,124,129–131] is a well-known two-dimensional dosimetry technique, which provides good accuracy and spatial resolution. However, it requires an impractically long processing time to be used for everyday preoperative plaque dosimetry.

Liquid scintillators [130] have been used in few studies for plaque dosimetry. They have the benefit of accommodating plaques of any shape, but are reported to have large regions of low accuracy in dose measurement, especially at the plaque edges and at distances greater than 10 mm from the plaque.

Plastic scintillators have been used for the surface dose mapping of ^{106}Ru plaques. They were shown to have excellent resolution (0.15° in azimuthal, and 0.01° tilt angles) and quite low uncertainty in water ($< 7\,\%$). The process requires complex positioning mechanisms whose plaque loading requirements limit the practicality of this method for real-time applications[132–134].

Diodes have yielded good dosimetric results[135–137], although when implemented as single devices, they are not convenient for volumetric dosimetry. The technology interfaces well with digital systems for fast and effective readout[69,113,114,124,130]. The planar fabrication process[138,139] is well developed and has enabled the

production of two dimensional devices, extending beyond the capabilities of single diodes.

These dosimeter technologies each have advantages and disadvantages, and offer varying degrees of usefulness to plaque dosimetry. To address the dosimetric and clinical needs of plaque brachytherapy, a technology with high resolution, high accuracy, large dynamic range and real-time readout is required.

Silicon diodes were selected as the preferred dosimeter for this project as they met the above requirements and due to their relative achievable resolution, design flexibility and strong institutional expertise over the other dosimeter technologies. Plastic scintillators, whilst offering many of the features of silicon diodes, were relatively less suited to measuring well defined sensitive volumes.

Table 2.4: Review of ophthalmic plaque dosimetry techniques

Method	Source	Details
TLD	Weaver[108], Luxton et al.[109]	LiF (powder and blocks) determine plaque scattering and effect of backing with ^{125}I seeds; plaque presence and absence of backing decreased dose.
	Wu et al.[110]	LiF TLD-100, $1 \times 1 \times 1\,\mathrm{mm}^3$; ^{125}I source; backing causes dose enhancement at close range.
	Harnett and Thomson[122]	^{125}I source; compared to calculated dose with close correlation; gold backing had no influence.
	Alberti et al.[123]	$1\,\mathrm{mm}^3$ 68 TLDs used in 24 mm eye phantom for 3D dosimetry; 85 % of measured data within 10 % of calculated data.
	Chiu-Tsao et al.[111]	LiF, $1 \times 1 \times 1\,\mathrm{mm}^3$; ^{125}I source; silastic and/or gold in a plaque used in a head phantom caused dose reduction; silastic alone showed similar results to silastic and gold.
	de la Zerda et al.[112]	LiF in two sizes, $1\,\mathrm{mm}^3$ cubes and $1.0 \times 1.0 \times 0.5\,\mathrm{mm}^3$; ^{125}I seed in COMS 20 mm plaque; dose reduction along central axis, relative to homogenous case, dose enhancement due to backscattering material placed opposite plaque.
	Astrahan et al.[70]	LiF (1 mm × 1 mm ⌀ rods) and radiochromic film; create slotted plaques for extended collimation effect; produces more homogeneous dose distribution to tumour and reduces dose to uninvolved adjacent structures and dose to sclera by up to 50% compared to conventional plaque design.

Review of ophthalmic plaque dosimetry techniques (cont.)

Method	Source	Details
	Soares et al.[124]	LiF:Mg, Ti of the type MTS-N (1 mm/3 mm thick × 5 mm ⌀); 15 s prereadout, 12 s readout, 3 h annealing; overall uncertainty 8 % – 10 % depending on phantom.
	Bilski et al.[125]	LiF:Mg,Ti and LiF:Mg,Cu,P. ⌀ 2 mm × 500 µm thick; radiosensitive layer 65 µm – 80 µm thick; almost tissue equivalent, dose threshold 100 µGy. Dose mapping on eye plaque axis from 0.1 mm – 10 mm depth
	Olko et al.[126,127]	300 µm thick 2D TLD films, Spatial resolution of 500 µm, limited by TL light propagation along the surface of the film
Polymer gel	Chan et al.[128]	Polymer gel forms phantom and detector; 3D dose distribution with good spatial resolution (pixel size 300 µm) Requires MRI to readout - unable to determine dose near edges.
Radiochromic film	Wu and Krasin[129]	Good spatial resolution but requires processing and analysis; used with ^{125}I plaque to determine dose to critical structures.
	Astrahan et al.[70]	Radiochromic and TLD used to evaluate collimated plaque design; see[70] above.
	Soares et al.[124]	Two types of film used; variations in inter-sheet thickness led to measurement uncertainties of 7.5 % (1σ) for absorbed dose; see[124] above for further detail.

Review of ophthalmic plaque dosimetry techniques (cont.)

Method	Source	Details
	Krintz et al.[67]	Film type MD-55 (Nuclear Associates); scanned with laser densiometer; 100 µm pixel size; ^{125}I seed; film saturates at 200 Gy; suitable for ^{125}I brachytherapy dosimetry; compared to Plaque Simulator[22] which disagreed with dose distributions along sclera due to inadequate silastic insert transmission factor.
	Kirov et al.[130]	HD-810 film; requires 5 h – 65 h irradiation and 48 h development time; reproducibility of 10 % – 15 % for film in region of interest; see[130] above.
	Acar[131]	GAFCHROMIC ® EBT film; ^{125}I seeds loaded in COMS plaques (14 mm, 16 mm, 18 mm and 20 mm); film gave 13 % dose decrease compared to Plaque Simulator[22].
	Poder and Corde[68]	GAFCHROMIC ® EBT film; ^{125}I seeds loaded in ROPES plaques; Stainless steel plaque backing uniformly reduced dose by 4 %; No backing film measurements matched Plaque Simulator and RADCALC® within 2 % and 4 %, respectively.
Liquid scintillator	Kirov et al.[130]	Liquid scintillator acts as a detector material and a phantom; Accommodate plaque of any shape; 3D dose distribution by tomographic reconstruction; inaccurate very close to and > 10 mm from plaque; within 25 % of film and diode dose measurements; see[130] above.
Plastic scintillator	Flühs et al.[132]	A 1 mm^3 detector used in mixed ^{106}Ru and ^{125}I radiation field gave an uncertainty of 15 %.

Review of ophthalmic plaque dosimetry techniques (cont.)

Method	Source	Details
	Fluhs et al.[133], Eichmann et al.[134]	BC-400 Scintillator (Saint-Gobain Crystals) with R647-01 PMT (Hamamatsu Photonics); BEBIG GmbH CCB ^{106}Ru Plaque[56]; plaque surface dose measurement aimed at quality assurance; mechanical positioning; uncertainty in dose rates to water $< 7\,\%$; complex and time consuming process.
Diodes	Cygler et al.[113]	⌀ 2.5 mm × 60 µm thick; plaque backing caused increase in dose when close to backing and decrease when further away; diode response relates to photon energy and highly sensitive to geometric changes.
	Meli and Motakabbir[114]	p-type Si diode (Scanditronix, GR-p); ^{125}I source; compared to water, gold backing causes dose reduction and silver backing causes dose enhancement.
	Knutsen et al.[69]	Stereotactic diode (size $2.5 \times 2.5 \times 0.3\,\mathrm{mm}^3$) showed agreement with the Bebig TPS within $4\,\% - 11\,\%$.
	Soares et al.[124]	p-type Si diode, $0.2\,\mathrm{mm}^3$ sensitive volume; sources of ^{90}Sr-^{90}Y and ^{106}Ru-^{106}Rh; with $10\,\% - 151\,\%$ of dosimeters tested.
	Kirov et al.[130]	500 µm stereotactic diode, current integrated over 30 s; BEBIG GmbH CCX ^{106}Ru plaque[56]; good agreement with film measurements from approximately 5.4 mm – 10 mm from inner plaque surface; matched film and 3D scintillator within 25 % for most points.

Review of ophthalmic plaque dosimetry techniques (cont.)

Method	Source	Details
	Weaver et al.[140,141]	Medipix2 detector family[142,143]; high resolution; 256×256 pixels of $55\,\mu m \times 55\,\mu m$ pitch; good agreement between charge collection mode, count mode and TG43U1; fast readout.
Other	Soares et al.[124]	Series of aforementioned dosimeters tested in addition to alanine, small ion chamber and diamond detectors; intercomparison indicated a measurement uncertainty of $10\,\% - 15\,\%$ at 1 mm for ophthalmic plaque dosimetry.

In addition to the experimental techniques for determining dose mentioned in Table 2.4, other methods for dosimetric planning are also frequently used, such as calculation and superposition using the aforementioned TG-43U1 formalism[20,21,65,84,144–147], Monte Carlo modelling[84,111,120,148–155] and discrete ordinate calculations[156,157].

Experimental dosimetry in ocular radiotherapy, where tumours are small and can be close to critical structures such as the optical nerve, demands high spatial resolution dosimetry and high detector dynamic range due to the steep dose gradients involved. Whilst some error exists in defining precise tumour geometries and surgical plaque placement, recent advances in semiconductor dosimetry now offer the potential for improvements to treatment planning and verification, including:

- decreasing dose to normal ocular structures;
- reducing dose to the apex of the tumour;
- increasing the dose gradient outside the tumour; and
- reducing the target volume[71].

Such a system would allow for continued research and development of the treatment through an increased capability to reproducibly measure quantitative dose volumes for outcome comparison. It would also encourage the increased development of customised plaques, especially with current 3D printing technologies. This will become increasingly useful as future developments with slotted and otherwise customised plaques may allow for reduced dose to normal tissue, improve local control and preserve eye function[83,93,121,132].

The focus of this study is to provide pretreatment quality assurance for plaque brachytherapy through practical, high spatial resolution real-time dosimetry. Figure 2.6 depicts the various aspects of the research problem and their relationships for this study.

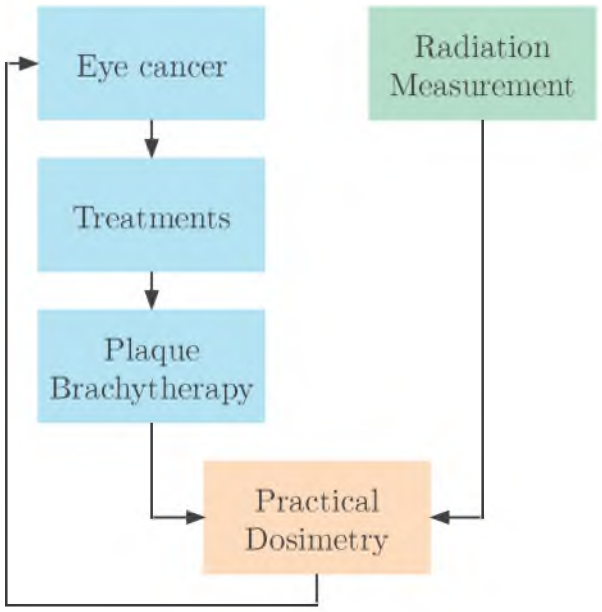

Figure 2.6: The aim of this study is based upon the need for preoperative dose verification for use in a clinical environment. For this to be realised, the project requires the design, development and evaluation of a suitable radiation measurement system.

2.4 Conclusion

Ocular cancer is a relatively rare disease which seriously threatens the lives of those afflicted. One of the most common and widespread treatments for the disease is plaque brachytherapy. This treatment involves placing a radionuclide source over the tumour and keeping it in place for several days until the prescription dose is delivered to the tumour, after which the source is removed.

Whilst there are several major challenges in using plaque brachytherapy, one of the most significant is accurate and precise dose delivery. The dose gradients from the plaque must be very steep to deliver maximum dose to the tumour, whilst minimising dose to the normal surrounding structures.

These steep dose gradients make dosimetry a challenging task. A number of technologies have been used for measuring plaque dose distributions. Currently there is no method used for real-time preoperative dose verification of assembled plaques that is capable of measuring such steep gradients.

Due to favourable characteristics in speed, reliability, design and interfacing flexibility and institutional expertise, this study will focus on using silicon diodes detectors for the development of a volumetric dosimetry tool for plaque brachytherapy.

Chapter 3

Semiconductor Dosimetry

In the previous chapter, it was concluded that plaque brachytherapy currently lacks any practical form of rapid preoperative dose verification, and that silicon semiconductor detectors would be a suitable candidate technology for such a system. This chapter provides a background on the fundamentals of semiconductors and their use in radiation detection for dosimetry.

Semiconductor detectors have been successfully used for dosimetry in low dose rate brachytherapy[135,158,159] and provide a good platform for dose verification in plaque brachytherapy.

Radiation detection systems are made up of a series of subsystems, each performing specific tasks in the process of measuring radiation. As depicted in Figure 3.1, most modern semiconductor detector systems use the following basic processes for a radiation measurement:

1. **Signal formation:** Incident ionising radiation creates a number of charge carriers within the detector, proportional to the deposited energy.

2. **Charge collection:** Charge carriers are collected and measured as a small current pulse.

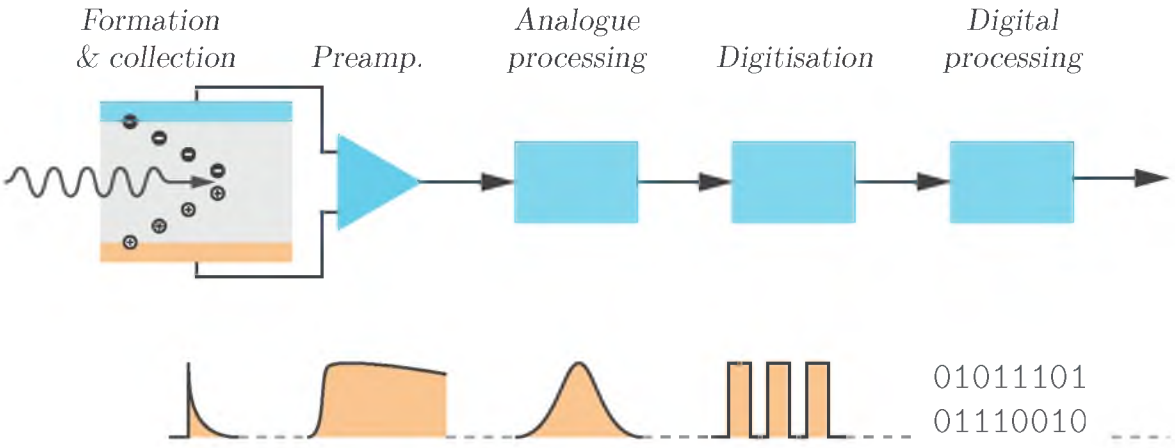

Figure 3.1: Basic detector functions: Radiation is absorbed in the sensor and converted into an electrical signal. This low-level signal is integrated in a preamplifier, fed to a pulse shaper, and then digitised for subsequent storage and analysis[160].

3. **Preamplification:** The current pulse is converted to a voltage signal and amplified.

4. **Analogue processing:** The voltage signal is shaped into a standardised Gaussian pulse to simplify data acquisition; pulse height is now approximately proportional to deposited energy.

5. **Digitisation:** The pulses are characterised as desired - typically by digitally measuring the pulse amplitude and/or time of arrival.

6. **Digital handling:** Recorded pulses are logged or binned in a histogram for further processing.

The early stages of the process chain (1 - 4) are considered to be the *analogue front end* and are one of the most critical aspects of the system. Each stage in the process causes some change in the signal to make it usable by subsequent stages and to eventually create some form of interpretable information. The stages, along with the relevant theory, will be detailed over the next sections of this chapter.

3.1 Signal Formation and Charge Collection

When an ionising particle interacts with a semiconductor, such as silicon, it deposits energy into the material through the generation of charge carrier pairs along the particle's path. The process involves the incident particle causing a negatively charged electron to move from the valence band to the conduction band and leave an effectively positively charged hole in the crystal lattice. Together these charge carriers are referred to as an *electron-hole pair*. The energy required to create an electron-hole pair is independent of the energy and type of the incident particle and is a function of the material and its temperature. For silicon this value is $\in_{Si}= 3.62\,\text{eV}/\textit{electron-hole pair}$[161].

With the stimulation of an applied electric field, the electron-hole pairs are separated and swept to opposite ends of the device where they are read out by ohmic contact terminals, before they can recombine. This process is depicted in Figure 3.2, with applied electric field V_{Bias} and signal current, i.

If an ionising particle deposits all of its energy in the active area of a detector, the number of electron-hole pairs created is proportional to the incident energy of the particle, and thus signal charge measured. Further details of the physical processes are discussed in Section 3.1.1.

In plaque brachytherapy, typical dose rates are in the range of $0.6\,\text{Gy}\,\text{h}^{-1} - 1.05\,\text{Gy}\,\text{h}^{-1}$ [10] and source activities can be in the order of hundreds of megabecquerels. When coupled with low latency readout, high acquisition rates allow these high event rates to be read out as single events, which is an attractive feature in dosimetry devices.

In order to optimise the design and function of a semiconductor dosimeter, it is essential to have an understanding of the fundamental electrical and physical characteristics. The following sections provide some theory on band energy, semiconductors, p-n junctions and diode detectors.

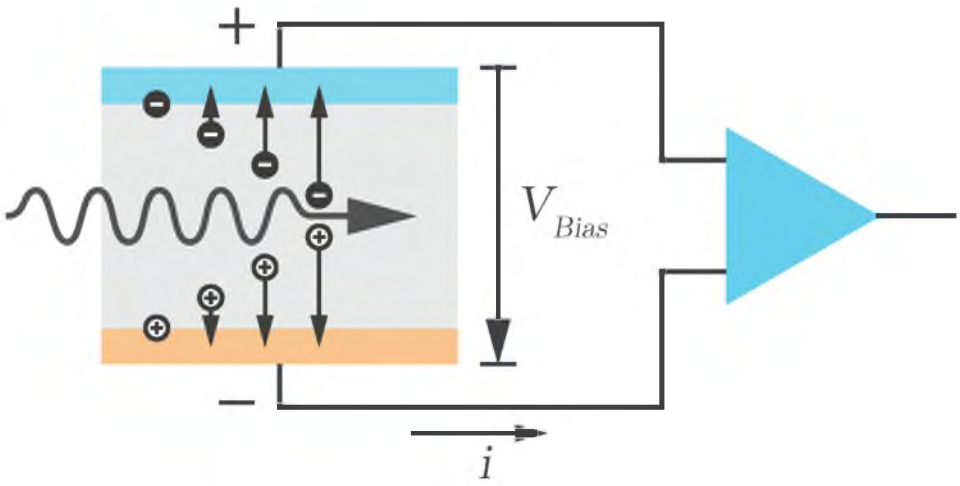

Figure 3.2: This figure shows the basic function of a single detector, where incident radiation causes ionisation of the detector's sensitive volume and leads to the generation of charge. It is subsequently read out through an amplification system.

3.1.1 Semiconductor Sensor Physics

The theory of energy bands in solids can be used to explain the electrical conduction properties of semiconductor materials. By changing the type and concentration of impurities in semiconductors, these properties can be manipulated. This phenomenon is used in semiconductor junctions and can be utilised for the field of medical radiation physics, as it provides a means for the measurement of energy deposited in matter by ionising radiation. More complex arrangements of these modified semiconductors are used to create other devices and are covered at the end of this section.

3.1.1.1 Band Structure in Solids

The electrons of an isolated atom have atomic orbitals and take on discrete values called energy levels. When such atoms are brought together to form a molecule, these atomic orbitals split and become molecular orbitals, each with a discrete energy level as a result of the Pauli exclusion principle. The number of molecular orbitals is proportional to the number of energy levels that occur within the molecule. In solids, the number of atoms and hence the number of molecular orbitals is often extremely large (usually

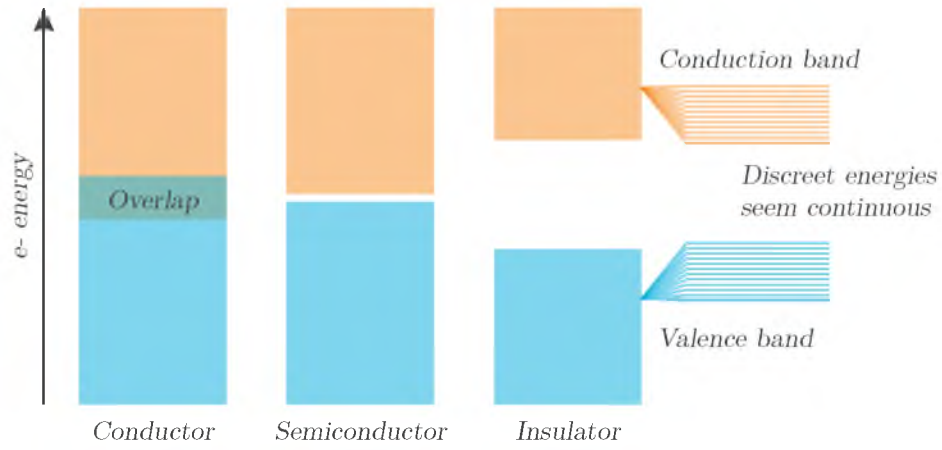

Figure 3.3: Energy bands for metals, semiconductors and insulators have different *band gaps* sizes affecting their respective properties of conduction. Each band is actually made up of a large number of closely spaced energy levels.

in the order of 10^{23}). This means that the number of discrete energy levels is also very large and, as a result, the differences between these levels is very small. This causes the energies to appear as a continuous *band* rather than a set of individual energy levels.

Generally in solid-state physics, materials are classified as conductors, semiconductors or insulators of electrical current, depending on the allowable energies in their bands. The highest band that is totally filled with electrons at a temperature of absolute zero is called the *valence band*. The lowest energy band that contains no electrons or is partially filled with electrons at absolute zero is called the *conduction band*. The space between these bands is called a band gap.

If the bands overlap, electrons can easily be excited to move from the valence band into the conduction band. This contributes to the conduction of electrical current in the presence of an electric field. Materials with these properties are good conductors and often metals. If the valence band is completely full and there is a large gap to the next energy band, typical electric fields will not excite electrons enough to move up into the conduction band. This type of material is known as an insulator. When

the band gap is very small, electrons can be excited to move from the valence band to the conduction band, thermally or otherwise, allowing conduction. Materials which exhibit this band structure are known as *intrinsic semiconductors*. Figure 3.3 shows a simplified depiction of the energy bands for conductors, semiconductors and insulators.

3.1.1.2 Semiconductors

The properties of a semiconductor material provide a useful mechanism for controlling the resistivity of that material using an applied voltage or current. For intrinsic semiconductors, such as silicon crystal, each of the four valence electrons is bound to a neighbouring silicon atom, causing the conduction band to be scarcely populated. Through a process known as *doping*, which involves the controlled addition of impurities to intrinsic semiconductors, *extrinsic* semiconductors can be created. Doping involves the addition of atoms with either more or less valence electrons.

By replacing one of the silicon atoms in the lattice with a *donor* atom that has five valence electrons, such as arsenic, four of the donor electrons bind to the surrounding silicon atoms whilst the fifth remains free. This type of semiconductor is known as an *n-type semiconductor* because the major charge carriers are *negative* electrons[162]. The diagram labelled '*n*-type' in Figure 3.4 depicts a silicon crystal lattice with an extra electron contributed by a donor atom. The energy level of this additional of this electron lies slightly below those in the conduction band and, when stimulated into the conduction band, provides an appreciable level of conductivity (see *n-type* in Figure 3.5). The level of doping used in typical semiconductors is low enough that the effects from radiation interactions from the dopants are insignificant.

If the impurity atom is an *acceptor* and has a valency of three, such as gallium, its three electrons will bind to only three of the neighbouring silicon atoms, leaving a vacant site or a '*hole*' in the lattice (see *p-type* in Figure 3.4). This causes energy levels to exist just above the valence band which accept electrons from the valence

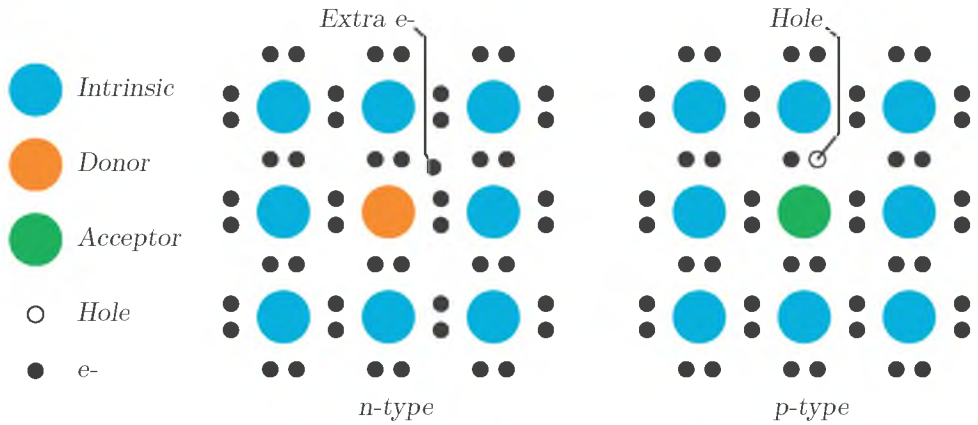

Figure 3.4: Doped semiconductor crystal lattice structures showing the extra electron in n-type doping and the missing electron in p-type doping.

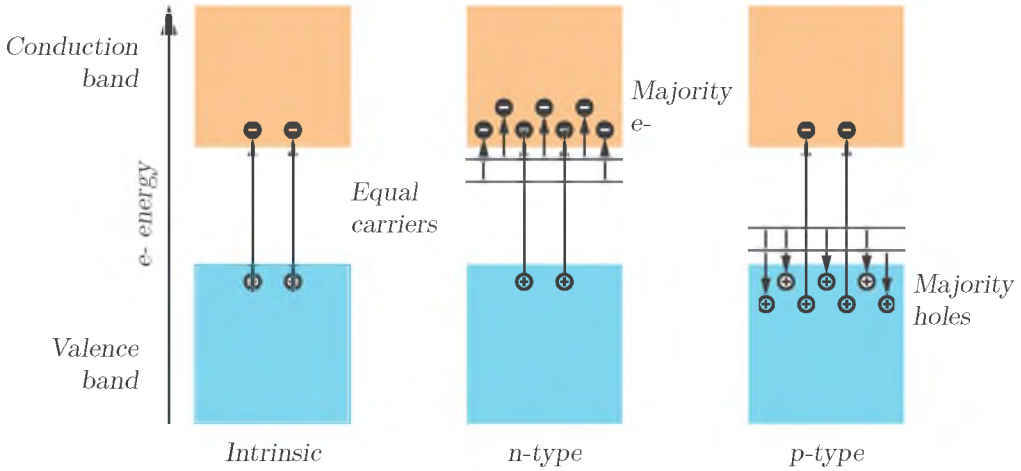

Figure 3.5: Doped semiconductors showing electrons in the conduction band and holes in the valence band. For temperatures above 0 K, intrinsic semiconductors have equal numbers of electrons and holes as charge carriers. In *n-type* semiconductors, electrons are the majority carrier, while in *p-type* semiconductors holes are the majority carrier.

band (see *p-type* in Figure 3.5). When the hole from this impurity atom is filled with an electron, the hole can effectively move about the lattice contributing to electrical conduction. This type of semiconductor is called a *p-type semiconductor* as its major charge carriers are '*positive*' holes. The higher concentration of electrons in *n*-type semiconductors and holes in *p*-type semiconductors means that their majority carriers are electrons and holes, respectively.

3.1.1.3 Semiconductor Junctions

A *p-n junction* is defined as the boundary between *p*-type and *n*-type semiconductors in a single crystal. It is a two-terminal device featuring an anode at the *p*-type contact, and a cathode at the *n*-type, and forms the basis of most semiconductor devices.

. Charge carriers are able to diffuse across the interface of the *p*-type and *n*-type semiconductors in a process called *diffusion*. This occurs as the charge carriers move along the concentration gradient to regions of lower concentration in an attempt to establish equilibrium. Electrons will diffuse from the *n*-type material towards the *p*-type region, leaving positively charged ions at their donor atoms. Similarly, holes will diffuse from the *p*-type material to the *n*-type material, instead leaving their acceptor atoms negatively charged.

As the mobile carriers cross the junction, the fixed ions that remain establish a built-in electric field at the junction. This electric field causes some of the charge carriers to move in the opposite direction of the movement caused by diffusion. Here the net current flow becomes zero when equilibrium is reached. This area in which no net current flows is depleted of mobile charge carriers, and so aptly named the *depletion region*, as shown in Figure 3.6.

The *depletion region* offers useful properties for radiation detection. Any electron-hole pairs that are generated in this region will be forced towards opposite sides of the junction by the in-built electric field that exists across the region. Electrons are

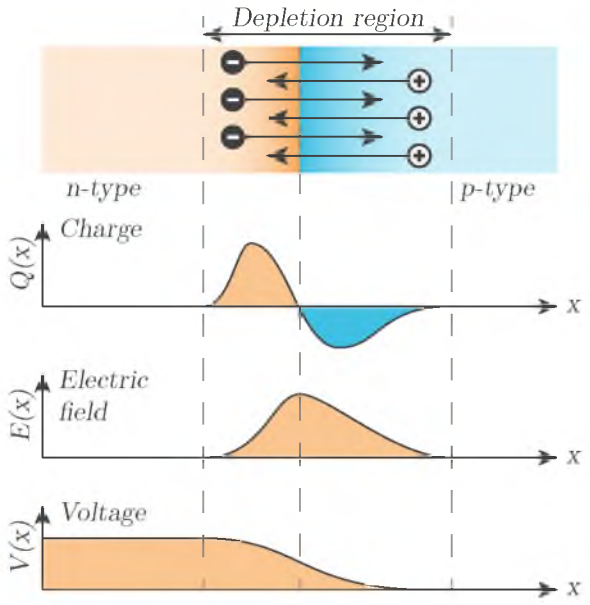

Figure 3.6: The *p-n junction* is an interface which has an inherent voltage potential across the so-called *depletion region*.

swept to the *n*-type side and holes are swept to the *p*-type side. When incident ionising radiation generates an electron-hole pair within the depletion region, the charges are carried out by the inherent electric field, resulting in an electrical signal[163].

The above describes the effect of a *p-n* junction with no externally applied electric field. In practise, this can be an ineffective method of measuring deposited energy (spectroscopy), as a portion of the electron-hole pairs generated will recombine before full charge collection can occur. The yield of the measured charge can be increased by applying an external electric potential across the junction in a process called *reverse biasing*. This occurs as the electric field acts to increase the speed of the electrons, reducing the travel time and, thus, the likelihood of recombination prior to measurement.

In their basic form, *p-n* junctions are called *diodes* and essentially give little resistance when a voltage is applied in one direction, known as a *forward bias*, and very high resistance in the other, known as a *reverse bias*. This process is illustrated in Figure 3.7 where current flow from the device is plotted against applied electric potential, and

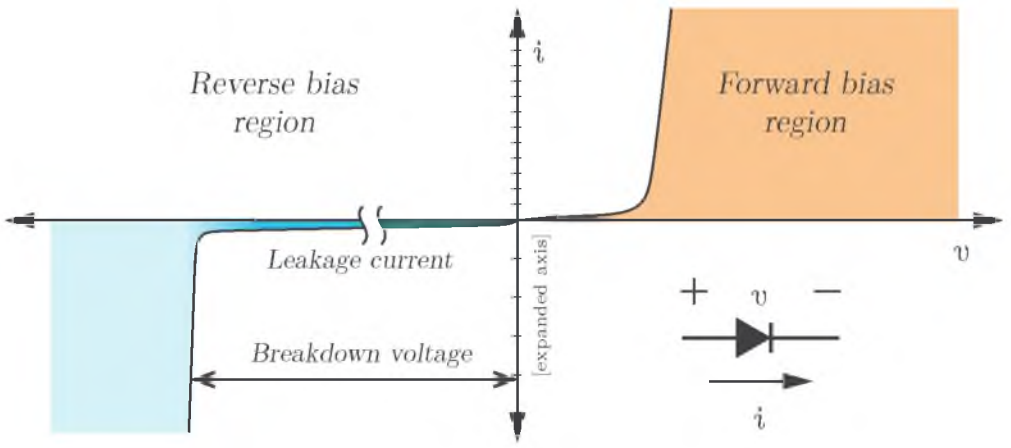

Figure 3.7: The current-voltage curve of a p-n junction, or diode. *Forward biasing* (*orange*) occurs when a voltage is applied across the device with the higher potential at the anode (p-type material). *Reverse biasing* (*blue*) occurs with the lower potential at the anode, and when the magnitude of this potential is large enough, *breakdown* occurs. *Note*: The positive and negative current axes have different scales, and the negative voltage axis contains a break.

is called a current-voltage (I-V) curve. It is a useful measure of the operation of many devices and is used during characterisation in Chapters 4 and 7.

When a diode is forward biased, a voltage is applied across its junction with the positive side of the source connected to the p-type material and the negative to the n-type. By convention, the positive side indicates the point of relatively higher voltage and the direction from which positive charge (holes) moves, towards the lower potential at the negative terminal. The contrary is true for electrons moving towards the point of higher potential. Therefore, a forward biased diode will cause electrons to be forced towards the p-type material and holes to the n-type.

As like charges have a repulsive effect, the forward biasing process effectively reduces the width of the depletion region. When a large enough voltage is applied across the junction in this manner, the depletion region becomes sufficiently thin for the inherent junction resistance to become significantly reduced. This reduction in resistance permits the flow of current.

For a diode operating in reverse bias mode, the higher potential of the supply voltage is connected to the n-type material, and the lower potential to the p-type. The process has the opposite effect of forward biasing and further inhibits the flow of current, increasing the depletion region width. This extended depletion region therefore increases the available sensitive volume in which ionising radiation can be collected. A junction in which the depletion region extends through the entire thickness of the semiconductor wafer is said to be *fully depleted*.

When a reverse bias voltage is applied to a semiconductor junction, even in the absence of an ionising radiation source, a very small amount of *leakage current* will flow. Typically, this is a product of current contributions from both the surface and bulk of the detector.

Bulk current is generated through two means, *a*) continuous transportation of minority carriers across the junction, due to the imposed electric field; and *b*) thermally generated electron hole pairs in the sensitive volume. Both of these sources of current increase proportionally with the geometry of the junction and as a result, larger diodes will yield more leakage current. Surface leakage current occurs at the edges of the junction and while it is effected by surface contamination, it can be reduced with the use of a guard ring[163].

The leakage current of a reverse biased junction is a strong function of temperature, as shown in the following equation[163,164]:

$$i = CT^{3/2} exp\left(-\frac{E_g}{2kT}\right)$$

where i = leakage current, C = proportionality constant characteristic of material, T = absolute temperature, E_g = band-gap energy of material and k = Boltzmann constant.

If the reverse bias voltage is great enough, the electric field is sufficient to strip

electrons from their atomic bonds and accelerate them across the junction. The mobile electrons cause other electrons to break loose, forming more electron-hole pairs and causing *avalanche breakdown* to occur, whereby significant current beings to flow. While this effect is reversible, thermal damage may be disastrous to circuits when unintentional.

3.1.1.4 Diode Detectors

Many variations of the *p*-*n* junction have been developed to improve performance in specific applications, one of which is called the *p*-*i*-*n* diode. The *p*-*i*-*n* diode is commonly used for dosimetric radiation detection, and is characterised by the addition of an undoped, *intrinsic* (*i*) semiconductor layer between the *p*-type and *n*-type materials of the diode junction.

The *p*-type and *n*-type regions are heavily doped and act as ohmic contacts for the device, whilst the *i*-type region is not truly an intrinsic semiconductor material, but is lightly doped. In reality, however, no practical semiconductor is free from impurties and this intrinsic layer is approximated with either lightly doped, high resistivity *p*-type (called π-type) or *n*-type (called ν-type) material.[165,166] The addition of the intrinsic layer makes the diode a poor rectifier but its width gives it a low capacitance when it operates in the reverse biased mode. The larger depletion region also means that the sensitive volume of the detector is larger. Fundamentally, this occurs in three stages:

1. incident radiation causes generation of electron-hole pairs (carriers) within the depletion region;

2. transportation of carriers across the junction by an applied electric field; and

3. output of signal through extraction of carriers at device terminals.

The geometric and electrical properties of the *p-i-n* diode gives it several benefits over the *p-n* diode as a radiation detector, including the following:

- larger in sensitive volume of the detector due to the enlarged width of the depletion layer;
- reduced leakage current, yielding a better signal to noise ratio;
- reduced junction capacitance, C_J, due to the enlarged width of the depletion layer; and
- faster drift processes carry a greater proportion of the generated current due to a reduced ratio between the diffusion length and the drift length of the device.

The increased width of the depletion layer comes at the expense of increased carrier transit time. This increased time limits the readout rate and means charge recombination is more likely to occur, diminishing signal quality.

As it is almost free from impurities and charge carriers, the intrinsic layer of a *p-i-n* diode is nearly fully depleted at zero or low reverse bias voltages. Here, the capacitance per unit area is defined as[163,165]:

$$C_{dep} = \frac{\epsilon_s}{W} \tag{3.1}$$

It can be seen that the depletion capacitance, C_{dep}, is a function of the depletion width of the semiconductor junction, W, and the substrate permittivity, ϵ_s. The depletion width is a function of applied reverse bias voltage, V, doping level, N, and the electron charge, e, as per the following relationship:

$$W \cong \sqrt{\frac{2\epsilon_s V}{eN}} \tag{3.2}$$

The depletion capacitance is thus a function of reverse bias voltage and substrate properties as shown in Equation 3.3.

$$C_{dep} \cong \sqrt{\frac{e\epsilon_s N}{2V}} \tag{3.3}$$

Equation 3.3 shows that the capacitance of the junction is inversely proportional to the reverse bias voltage, $C_{dep} \propto \sqrt{\frac{1}{V}}$, meaning that, whilst below breakdown voltages, the junction capacitance decreases with increasing reverse bias. Practically, the full depletion voltage can be determined by the point at which the capacitance ceases to change significantly with increasing bias voltage. Detector capacitance has a major influence on signal quality and the design of the preamplifier stage in the signal processing chain.

The *p-i-n* diode is compact, relatively rugged and allows for real-time readout, making it well suited for the dose verification needs of eye plaque brachytherapy. When exposed to x-ray or gamma radiation the detector produces pulses from secondary photoelectrons which can be processed through analogue and digital electronics to provide a convenient form of dosimetry.

3.2 Preamplifier

The current pulse collected in the first stage of the signal processing chain is extremely small, requiring a special interface circuit known as a preamplifier (or *preamp*). This circuit acts as an interface between the sensor and the subsequent processing stages. The preamp prepares the signal for subsequent processing by converting the very small current pulse into a relatively large voltage pulse. The primary function of the preamp is to extract the signal from the sensor with minimal degradation of the signal-to-

noise ratio. To do this, the capacitance loading to the preamp should be minimised by placing it as close as possible to the detector and hence shortening the electrical connections.

While there are many designs of preamplifiers, they essentially fall into one of two configurations, voltage-sensitive or charge-sensitive. Voltage-sensitive preamplifiers, see Figure 3.8, generate a low impedance output whose voltage amplitude is proportional to the input current as received from the detector. The relationship between output voltage, V_o, measured charge, Q_i, and the input capacitance, C_i, is $V_o = Q_i/C_i$. The input capacitance is that which is seen by the input terminals of the preamplifier, i.e. from the detector and connections to the preamplifier. This configuration is fine for most detectors; assuming that C_i remains constant, the output voltage is entirely dependant on the input charge. As discussed in Section 3.1.1.4, the capacitance in a semiconductor detector varies with operational parameters, including bias voltage, which means the decoupled relationship between V_o and Q_i does not exist.

This problem can be overcome using charge-sensitive preamplifiers whose output is independent from input capacitance. The output voltage of the ideal charge-sensitive preamplifier, shown in Figure 3.9, is proportional to the input charge deposited in the feedback capacitor. The output voltage of the amplifier is $V_o = -AV_i$, where V_o is the

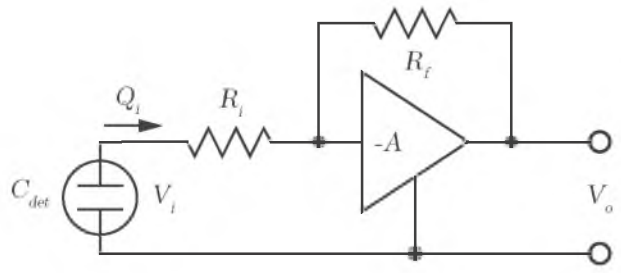

Figure 3.8: Simplified voltage-sensitive preamplifier schematic. The diagram labels the detector, C_{det}, input voltage, V_i, measured charge, Q_i, feedback resistance, R_f, input resistance, R_i, transimpedance gain, A, and the output voltage, V_o. Assuming $A >> R_f/R_i$, then $V_o \cong -(R_f/R_i)V_i$.

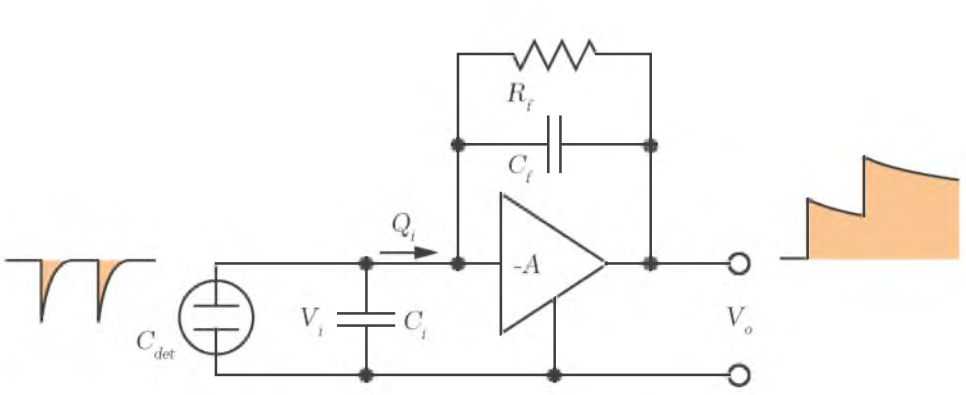

Figure 3.9: Simplified charge-sensitive preamplifier schematic showing the input charge pulses and the corresponding output voltages with long pulse-tails. The diagram labels the detector, C_{det}, input voltage, V_i, input capacitance, C_i, input charge, Q_i, feedback resistance, R_f, feedback capacitance, C_f, transimpedance gain, A, and the output voltage, V_o.

output voltage, A is the amplifier gain and V_i is the input voltage. The voltage across the feedback capacitor is then given by $V_f = V_i(A+1)$. The charge, Q_f, deposited on the feedback capacitor is then $Q_f = C_f V_f = C_f V_i(A+1)$. In an ideal amplifier, there is an infinite input impedance and no current flow in, so Q_f must equal Q_i, giving

$$C_i = \frac{Q_i}{V_i} = \frac{C_f V_i(A+1)}{V_i} = C_f(A+1)$$

The transimpedance of the circuit is the output voltage per input charge as shown in Equation 3.4. By reducing this further, it shows that the output voltage is effectively dependant on the feedback capacitance. In the case of semiconductor detectors this conveniently leads away from the issues with dependency on input capacitance. As long as the time constant, $\tau = R_f C_f$, is sufficiently large with respect to the duration of the input pulse, the output voltage is proportional to the charge measured from ionisation events.

$$\begin{aligned} \frac{V_o}{Q_i} &= \frac{-AV_i}{C_f V_i(A+1)} \\ &\approx \frac{1}{C_f} \quad (\text{if } A \gg 1) \end{aligned} \tag{3.4}$$

One of the most important aspects of preamplifier design is the minimisation of inherent noise. The feedback resistor, R_f, is a significant factor in preamp noise due to its associated Johnson (thermal) noise. This noise decreases with increasing resistance, however this causes an increase in the time constant and thus the tail pulse length of the voltage output.

As shown in Figure 3.9, the output voltage has a very short rise time, but long pulse tail. In most cases, this prevents the output voltage from returning to the baseline before subsequent charge events cause further increases to the output voltage.

The following stage in the signal processing chain after the preamplifier, often a linear amplifier (shaper), is designed to handle these baseline offsets. At some point, pulse pile-up will occur due to large pulses coming too frequently for the baseline drop sufficiently low again. When this happens the output voltage reaches a saturation point where it cannot increase further as it is limited by the voltage rails, and no further pulses can be output from the preamplifier.

At the cost of noise, the feedback resistor can be reduced to increase the pulse tail decay rate. Alternatively, R_f can be removed altogether and replaced with an *active reset* circuit, eliminating its associated Johnson noise altogether.

An active reset circuit provides a means for the preamplifier to prevent pulse overflow by resetting the baseline back to zero. Transistor reset is a popular method of active reset, where the feedback capacitor, C_f, is discharged through a transistor when the output reaches an upper threshold[160,163].

3.3 Analogue Processing

The detector signal is converted by the preamplifier into a more robust form for further amplification and handling during the following stages of the signal processing chain. One of the most common components to follow the preamplifier is the *linear amplifier* which provides pulse shaping and signal amplification. After this stage, it is often necessary to select pulses that fall within a specific energy range using a discriminator.

3.3.1 Linear Amplifiers

Linear amplifiers, or shaper amps, are used to convert the signal from the preamplifier into a form that can be processed easily. The output voltage signal from the preamplifier has an amplitude below practical limits for analysis, typically in the order of millivolts, and is also subject to instability as a result of pile-up of events[163]. The linear amplifier provides this signal with a significant voltage gain to boost it into the range of Volts, and shaping to reduce the pulse width and flatten the peak for greater readability.

Whilst older standards for modular instrumentation were limited in their output voltages, such as the NIM standard[167], which was 0 V – 10 V for microsecond analogue signals, modern designs offer much more flexibility. Using NIM as an example, this means that gains of around 100-5000 are needed to adequately boost the preamp signal. Ideally, the shaped signal output will fall within this 10 V range, if the input signal is too great, peak clipping will occur and the amplification will be non-linear. Pulse gain and shaping occur by passing the signal through filters. A simple pulse shaper, known as a *CR-RC shaper*, is depicted in Figure 3.10. It is made up of a high-pass filter (CR) and a low-pass filter (RC). Whilst real linear amplifiers are made up of more complex and sophisticated systems, the CR-RC shaper shares most of their features and will be used in explanation.

The high-pass or CR filter is a system that simultaneously inhibits low frequencies

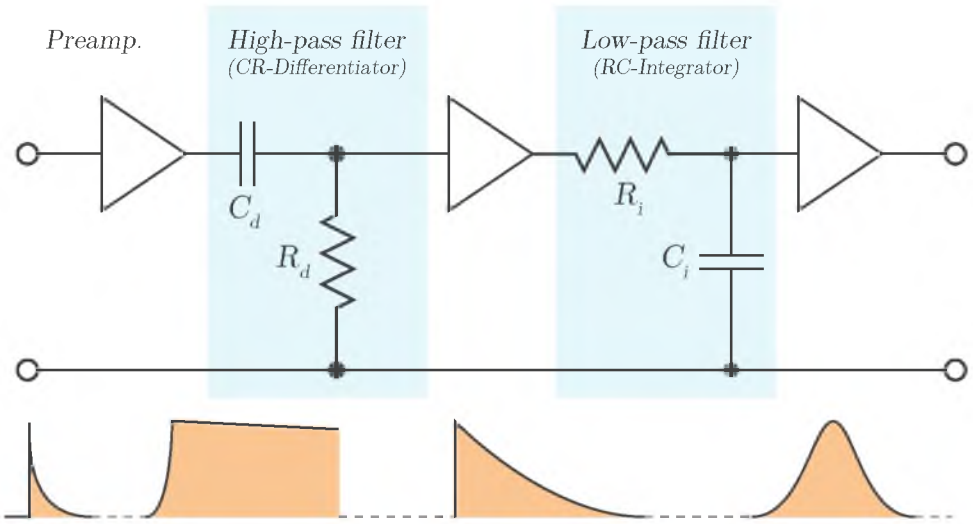

Figure 3.10: A simple CR-RC pulse shaper, comprising of a high-pass filter (CR) and a low-pass filter (RC) in succession. The brief pulse from the detector is passed through the preamplifier where it takes on the shape of a step function before being fed into the high-pass filter which defines a new pulse width, and then the low-pass filter, where it is shaped for ease of measuring.

and allows high frequencies to pass through it. If a step function is considered as the input into the CR filter, with voltage $V_i = Q/C_i$ at $t = 0$, then the output is given as

$$V_{CR} = \frac{Q}{C_i} e^{-\frac{t}{\tau_d}} \qquad \text{for } t > 0 \text{ where } \tau_d = R_d C_d$$

The output signal is represented as an exponential decay, as depicted in Figure 3.10 and has decay time, τ_d. It is impractical to measure the amplitude of such a signal bearing a sharp cusp, as the peak voltage is only present for a short time. In addition to this issue, unwanted high frequency noise components will still remain mixed within the signal, reducing its signal quality.

By passing the signal through a low-pass or RC filter the high frequency noise can be reduced while allowing low frequencies to pass, smoothing out the cusp for ease in signal sampling. The exponential decay shaped response from the CR filter is fed directly into the input of the RC filter. The voltage output from the RC filter alone,

if a step function is applied at the input, with voltage E at time , $t = 0$, is given by

$$V_{RC} = E(1 - e^{-\frac{t}{\tau_i}}) \qquad \text{for } t > 0 \text{ where } \tau_i = R_i C_i$$

This function is analogous to the voltage measured across a charging capacitor with time constant, τ_i and applied voltage E.

The overall system response of the CR-RC filter resembles a semi-gaussian curve. The rise and fall times can be controlled by choosing appropriate values for τ_d and τ_i. The optimal combination of having a flat pulse top (for low ballistic deficit [1]) and a short tail pulse (for minimum pile up) occurs when $\tau_d = \tau_i$. As this condition also results in the maximum signal-to-noise ratio, it is nearly exclusively used[170]. With initial input voltage $V_i = Q/C_i$ at time, $t = 0$, the output voltage from the amplifier is given by:

$$V_{CR-RC} = \frac{Q\tau_d}{C_i(\tau_d - \tau_i)}(e^{-\frac{t}{\tau_d}} - e^{-\frac{t}{\tau_i}}) \qquad \text{for } t > 0 \tag{3.5}$$

$$\text{where } \tau_d = R_d C_d \text{ and } \tau_i = R_i C_i$$

More sophisticated shaper amplifiers are used in practice, such as higher order semi-Gaussian ($CR-(RC)^n$) shapers, double RC differentiation ($(CR)^2 - RC$) shapers, active filter pulse shapers, triangular shapers, trapezoidal shapers and delay line shapers, to name a few[160,163,170].

[1] *Ballistic deficit* is a measure of the fractional loss of pulse height due to inefficiency in integration. It occurs due to variations in rise-time in the detector signal that propogate as amplitude fluctuations after the signals pass through the linear amplifier. In semiconductor detectors, these rise-time variations are often the result of the distribution of charge origins within the detector, field inhomogeneities or charge trapping[168,169]. As noise is independent of input signal, there is a reduction in the signal-to-noise ratio with increasing ballistic deficit[160,170].

3.3.2 Baseline Holders

When a signal is passed through a series capacitor, the capacitor filters out all DC components of that signal. After it has passed through the CR (high-pass) filter, the DC component is removed and the signal takes a baseline that is centred with an average value of zero[160]. The amount by which the output voltage shifts away from its true zero is known as *baseline shift*. Baseline shift offset is greatest when the signal has high pulses at a high rate. When these heights and rates vary, as is the case in a real system, the baseline shift must vary too. This effect is depicted in Figure 3.11.

To mitigate the effect of baseline shift, electronics system known as *baseline restorers* are used. The purpose of a baseline restorer is to recover the true zero value of the signal. There are several types of restorers that can be used depending on the design specifications, these include the simple diode restorer, the Robinson restorer[171] and the Gere-Miller restorer[172] among others[173–176].

3.4 Digitisation and Digital Processing

Once the signal is transformed into a robust and measurable form, it can be further processed so it can be represented digitally. This is a desirable practise for a number of reasons including the immense flexibility and ease of processing along with the efficiency and ease of storage. Each pulse from the detector holds a significant amount of information and, depending what the function of the system is, little or much of this can be extracted.

For simple pulse counting systems, pulses with a voltage peak above a specified level will trigger logic pulses that are recorded by incrementing a counter. When two thresholds levels, a lower and an upper, are specified to create an energy window, only pulses within this region are counted. This type of filter is called a *differential*

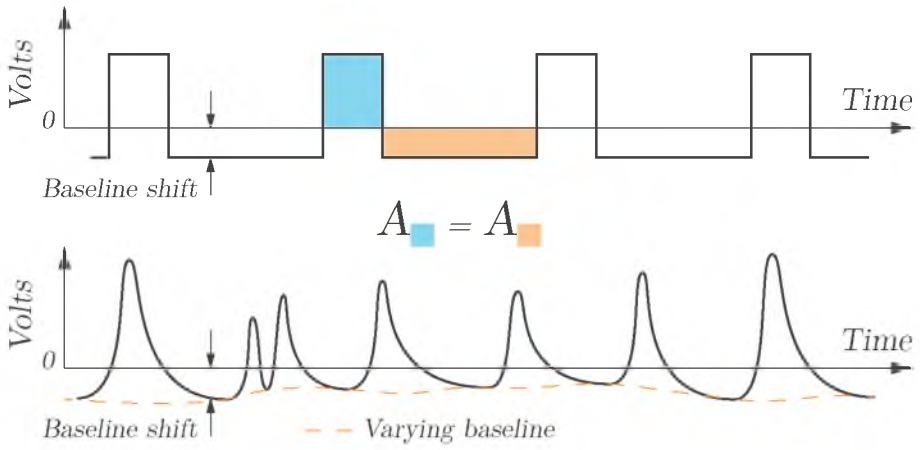

Figure 3.11: Baseline shift occurs when a series capacitor filters out the DC component of a signal. The magnitude of the shift is dictated by the pulse heights and frequency. The average value of the signal must equal zero, e.g. the area above and below the zero value are equal in the top diagram. As a result, variations in pulse heights and frequency create variations in the baseline shift as seen in the bottom diagram. Adapted from Knoll[163].

discriminator or single-channel analyser (SCA).

A combination of multiple SCAs, whose thresholds are contiguously spaced, can be used concurrently to produce a pulse height (energy) histogram and create a multichannel analyser (MCA). By measuring the duration that a pulse's height exceeds a predetermined threshold level using a digital clock, information pertaining to the energy of the pulse can be determined.

3.4.1 Pulse Discriminators

Once the output of the shaper has produced a suitably measurable signal, any pulses that do not fit the criteria of interest can be discarded. From Section 3.3.1 above, the pulse height output from the shaper amplifier (usually 0 V – 10 V) is shown to be proportional to the charge and hence the energy of its input. A discriminator allows for the exclusive selection of pulses that fall in a specified energy range.

3.4.1.1 Integral Discriminators

An *integral discriminator*, or low-level discriminator, is analogous to a high pass filter, in that pulses below a specified energy level will be rejected, and those above will trigger a logic pulse output. By choosing an appropriate threshold level, the low energy noise can be ignored, while the desirable pulses are processed further. This concept is depicted in Figure 3.12 where the blue and oranges pulses are accepted or rejected, respectively.

3.4.1.2 Differential Discriminators

In many situations, it is necessary to select pulses that fall within a specified range, rather than simply above a threshold level. To accommodate this need, a *differential discriminator*, or single-channel analyser, can be used. Here, two separate threshold levels are specified, a lower and an upper, and pulses outside the threshold range are ignored. Figure 3.13 shows the logical function of the differential discriminator, the blue horizontal bar illustrates the region of pulse heights that are accepted. Pulses with an amplitude that is too low are ignored, as are those whose amplitude exceeds the upper threshold.

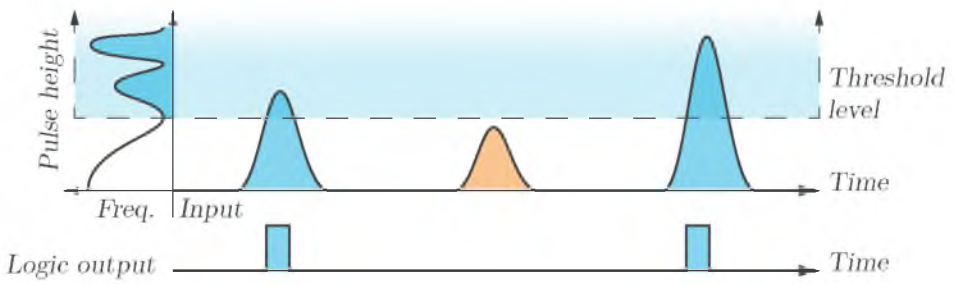

Figure 3.12: Concept of the integral threshold discriminator. Only pulses with a height that lies above the discriminator threshold level (blue) create an output response. The pulse height spectrum illustrates how the pulses of low height (usually low energy noise) can be ignored.

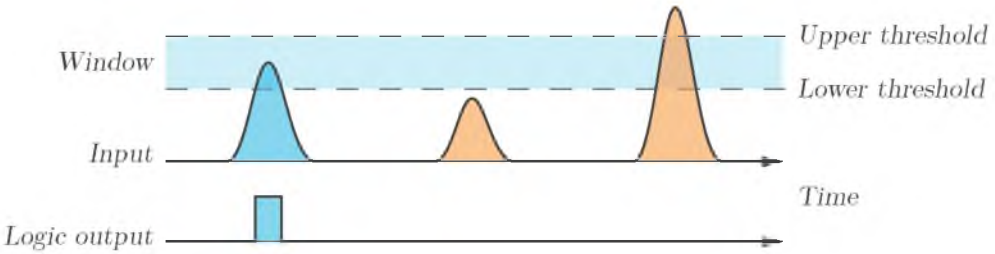

Figure 3.13: Concept of the differential threshold discriminator. Only pulses with a height that falls between the lower and upper energy thresholds (blue pulse) are processed further, other pulses (orange) are ignored.

3.4.1.3 Time Slew

The discriminators described above are subject to an issue known as *time slew* or time walk, where timing differences occur between the input pulse and the logical output pulse[170]. As the input pulses have some finite rise time, the lower threshold level logic of a differential discriminator must trigger prior to the upper threshold logic. The dead time between these stages can be erroneously triggered as a false positive logic output, shown in Figure 3.14. In this case, the input pulse exceeds the acceptable height limit, yet incorrectly produces an output pulse.

In some forms of spectroscopic dosimetry, events that occur within a specified energy threshold window are used to calculate dose. If time slew is present there can be a misrepresentation of energies.

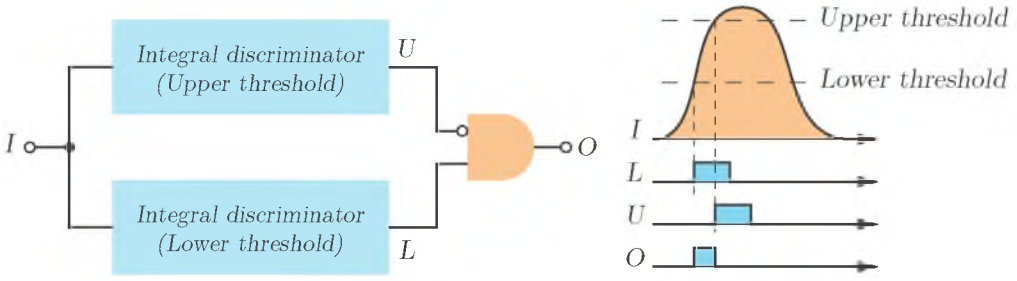

Figure 3.14: Block of the differential threshold discriminator illustrating the effect of time slewing, where the time delay between triggering of the lower threshold discriminator and the upper level discriminator causes an incorrect output response.[170]

The effect of time slewing can be handled in numerous ways, such as delaying and shortening the output pulse from the lower discriminator or using flip-flop based logic circuits[170].

3.4.1.4 Counters

The logical output pulses from the discriminators are temporarily stored in counters. A counter is a device that generally consists of a series of flip-flops and, when enabled, increment a value stored in binary. A counter that uses 12 binary digits is said to have a bit depth of 12, which is equivalent to $2^{12}(4096)$ logical combinations and hence, values. Counters need to be read prior to exceeding their maximum value, or overflowing, so they can be reset although this often causes *dead time* in the overall measurement.

3.4.1.5 Time-Over-Threshold

Although there are many alternatives, one method for measuring the charge of a pulse is using a process called *time-over-threshold* (TOT). TOT is employed by the Timepix detector[143] which was used in this project.

In this type of analogue processing, the width of a pulse (which is proportional to initial signal charge) is digitised at a particular threshold level, using a discriminator and an adjustable analogue threshold. The width of the logical output pulse from the discriminator corresponds to the width of the input pulse. The logical pulse is used to enable a counter that increments based on a fast digital clock, in the order of 100 MHz. The resultant value can then be passed through logical processing or binned using digital comparators. The time-over-threshold process is illustrated in Figure 3.15.

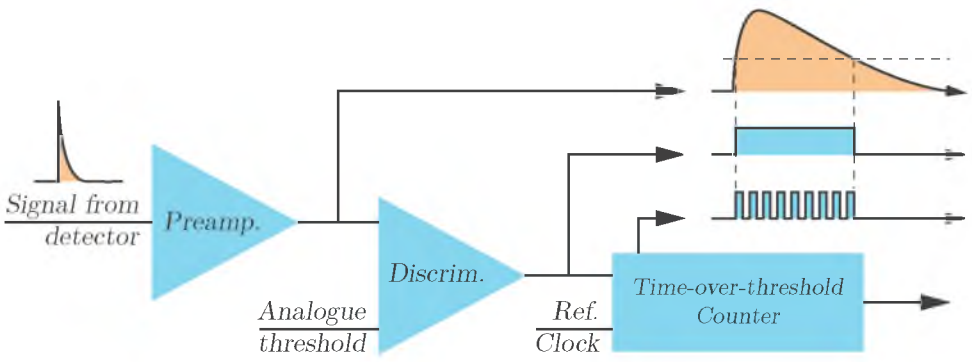

Figure 3.15: The time-over-threshold process; the preamplifier signal is passed through a discriminator, compared with an analogue voltage threshold and the output is timed using a fast reference clock, CLK_{ref}. Adapted from Wong[177]

3.4.2 Digital Processing

The previous stages of the processing chain (signal formation, charge collection, preamplification, and analogue processing) are carried out by the analogue front end electronics. Once the analogue signal has been represented in digital logic there are many potential advantages; it is free to be processed, duplicated or stored as necessary. Digitised data, such as the counter values as measured by discriminators, can easily be stored and presented as desired.

If certain factors, such as the number of detectors, acquisition rate, digital precision, computing power and required processing are within acceptable limits, then data can be handled in *real-time*. Real-time dosimetry requires the conversion of measured signal into user readable doses with sub-second timing.

With growing technology capabilities, digital pulse processing is becoming more viable and offers great advantages. Here, the output from the detector and amplifier are passed through an analogue-to-digital converter where the pulse shape is preserved and represented in the digital domain. Any analogue signal filtering or manipulation is replaced with digital signal processing, which offers endless flexibility. Though this technique is not adopted in the study, its future adoption may provide considerable

opportunity for dosimetry in eye plaque brachytherapy.

3.5 Dose Equivalence

Absorbed dose is defined as the energy deposited in a material per unit mass. The International System of Units defines dose in units of the Gray (Gy) as:

$$1\,\mathrm{Gy} \equiv 1\,\frac{\mathrm{J}}{\mathrm{kg}} = 1\,\mathrm{m}^2/\mathrm{s}^2$$

In treating cancer, it is critical to understand and deliver the correct amount of dose to the treatment target, too little and the threat remains, too much and serious side-effects occur, see Section 2.3. In the context of this study, the term *dosimetry* refers to the measurement and calculation of absorbed dose in a specific medium, at a specific location.

In order to create a system that can accurately determine the dose in a specified area, the interactions of ionising radiation with matter must first be understood. To accomplish this, it is also necessary to be aware of the types of radiation that are present in the treatment and will affect the dosimetry. In plaque brachytherapy, either beta (β) or low energy gamma (γ) radiation is used through a variety of nuclides. The most commonly used radionuclide in the United States and Australia is ^{125}I, whilst ^{106}Ru tends to be more common in Europe. Other, more recently developed sources, such as ^{103}Pd and ^{131}Cs, are also becoming increasingly popular[10,18,178]. Some common radionuclides used in plaque brachytherapy have been provided in Table 2.2 of Chapter 2.

The biological effectiveness of the dose deposited in a material is dependant on the type of radiation. For the same energy deposited per unit mass, heavy charged particles produce greater biological damage than beta-particles.

This occurs because heavy charged particles have a higher *linear energy transfer*, or energy deposition per unit length, than beta-particles. Gamma-rays deposit their energy in the form of beta-particles and, as such, behave in the same manner. The effective biological dose of a type of radiation, called the *dose equivalent*, is accounted for by weighting its absorbed dose. For the energies and radiation types used in context of this study, the absorbed dose is approximately equal to the dose equivalent[163].

3.5.1 Dose in Silicon

It is a challenging task to measure the energy deposited in tissue. However, by using detectors that respond to radiation similarly to tissue, dose can be more accurately measured and calculated as if it were tissue. In addition to this, it is useful to know the radiation interaction processes within the detector and surrounding materials to optimise the design. Figure 3.16 shows the gamma-ray interaction processes that occur within silicon as a function of energy. Around the energies of interest for ^{125}I plaque brachytherapy, $\sim 20\,\text{keV} - 35\,\text{keV}$, photoelectric absorption is the dominant gamma interaction in silicon, meaning less partial deposition of energy is observed as a result of Compton scattering.

Radionuclides that emit beta particles (electrons or positrons), do so over a continuum of energies. For the majority of these energies, the *depth-dose* curves follows an approximately exponential decay, beyond an initial build-up region. This occurs as lower energy electrons are absorbed at a faster rate than those with higher energy. In comparison to gamma-rays, beta particles are more ionising, yet have less range in a material.

As the mass of the beta particles are equal to that of the orbiting electrons they are interacting with, large depositions of energy can often occur in a single interaction. These interactions also cause large deviations in the trajectory of the incident beta

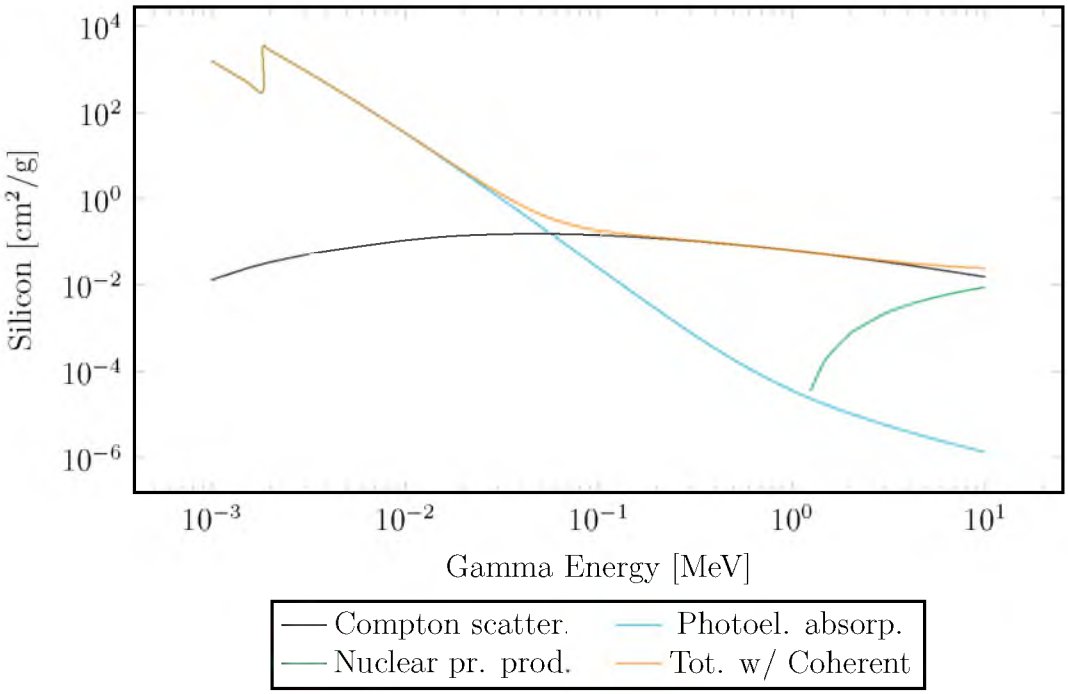

Figure 3.16: Energy dependence of γ-ray interaction processes in silicon including, Compton scattering, photoelectric absorption, nuclear pair production and the summed total including coherent scattering. The dominant process at the low energies used in ophthalmic brachytherapy is photoelectric absorption. *Source*: Berger et al.[179]

particle, known as *scattering*. Scattered electrons only partially deposit their energy and may then exit the material altogether. This effect strongly influences the apparent dose absorbed in a detector. Beta-emitting plaques have less focus than gamma-emitting plaques in this study.

When performing dosimetry for plaque brachytherapy, the appropriate energies and depth-dose curves need to be considered, not only to account for the detector and readout electronics, but the various other materials surrounding the detector.

3.5.2 Anthropomorphic Phantoms

When measuring dose in radiotherapy, it is often not practical or possible to do so during the treatment. In many cases, such as plaque brachytherapy, it is not currently viable to adaptively modify the treatment once it has commenced, consequently there is little point in performing in vivo (in body) dosimetry. Instead, the treatment dosimetry is improved by calculating the expected dose and then modifying where necessary prior to being performed. This is process is called *preoperative dose verification*.

In conducting preoperative dose verification, estimations and assumptions need to be made regarding the physical model of the treatment. It is common practise to use materials which geometrically resemble patient anatomy and have a dosimetric response similar to that of the appropriate type of tissue.

There are many commercially available anthropomorphic phantoms which aim to provide tissue equivalence, though due to its similarities, water is often considered tissue equivalent. Materials used in these phantoms are fabricated to meet the needs of specific energy regimes. Plaque brachytherapy requires a material with water equivalence in response to low energy photons, for the purposes of this study. There are several available options which may be suitable including Plastic Water LR[180], Gammex 457 Solid Water(Gammex Inc., USA), and Virtual Water(Med-Cal Inc., USA) or the less

accurate poly(methyl methacrylate) (PMMA)[181,182].

3.6 Conclusion

Silicon semiconductors are suitable for use in real-time, room temperature radiation detection. The signal processing chain used for such detectors involves measuring the energy deposited from incident radiation and conducting analogue processing which allows it to be represented in the digital domain. The analogue front end electronics and detector play a critical role in determining the quality of the radiation signal measured and hence the dosimetry outcomes. Characterisation of a radiation detector system needs to be undertaken to ensure that its operation is correct and can be optimised.

Given the positive outcomes in the literature and the institutional expertise in the field, the following chapters investigates silicon *p-i-n* diodes as radiation detectors. Several concepts are considered and evaluated starting with a single detector system used for spectroscopic dosimetry. This extended upon through the investigation of pixelated (multi-pixel) silicon detector systems for the improvement of quality assurance in plaque brachytherapy.

Part II

Concept Validation

Chapter 4

Single Detector Concept

The previous chapter provided a background overview on the operation of silicon diode radiation detection systems, while this chapter demonstrates the feasibility in using such a device for plaque brachytherapy. Specifically, the study undertaken in this chapter used a single *p-i-n* diode together with a readout system and water phantom for spectroscopic dosimetry. The detector characteristics were measured and the dosimeter concept was evaluated in terms of dose response and angular dependence. The work presented in this chapter resulted in the development of a prototype plaque brachytherapy dosimeter, and justified the extended development of more complex pixelated detector designs. This was accomplished through the following aims;

- illustrating the dosimetry concept and hardware;
- determining the operational characteristics of the detector; and
- characterising the system and assess its performance.

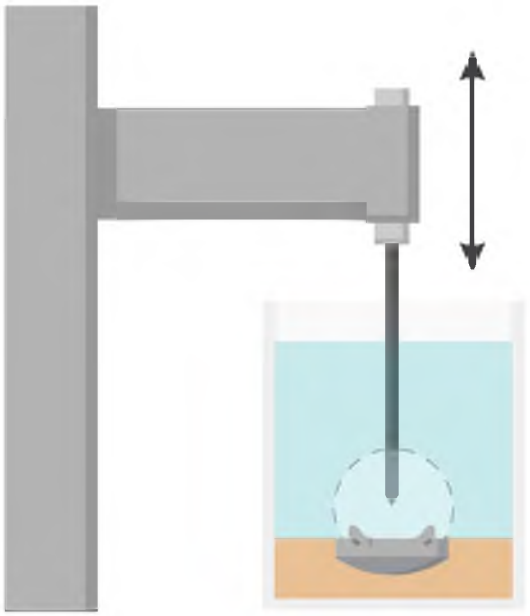

Figure 4.1: A single *p-i-n* diode is lowered towards an inverted eye plaque in increments along the central axis of the plaque. The resulting depth-dose curve is a simple and convenient method of preoperative dose verification.

4.1 Concept and Hardware

Accurate dosimetry can be achieved through observing the spectrum of energies deposited in a detector and calculating dose by considering only those energies which are expected from the source. This ensures that the false events, derived from noise, do not contribute to the calculated dose. The technique is a form of *spectroscopic dosimetry* and has been used in the past in prostate brachytherapy[183]. This section aims to illustrate the proposed and evaluated single detector concept, and to provide an overview of the detection hardware used to perform this. The concept used a water phantom, together with a detector, readout system and positioning system to accurately measure the depth-dose response of a brachytherapy plaque, as shown in Figure 4.1.

The detector, a silicon *p-i-n* diode, was mounted on an elongated printed circuit board (PCB) probe and sealed watertight. By submerging the detector end of the

Figure 4.2: Photograph of the assembled probe (*top*) with the detector located on the tip at the right (*not visible*) and cable running to the readout system (*left*). A sample of the diode detectors are located below the probe.

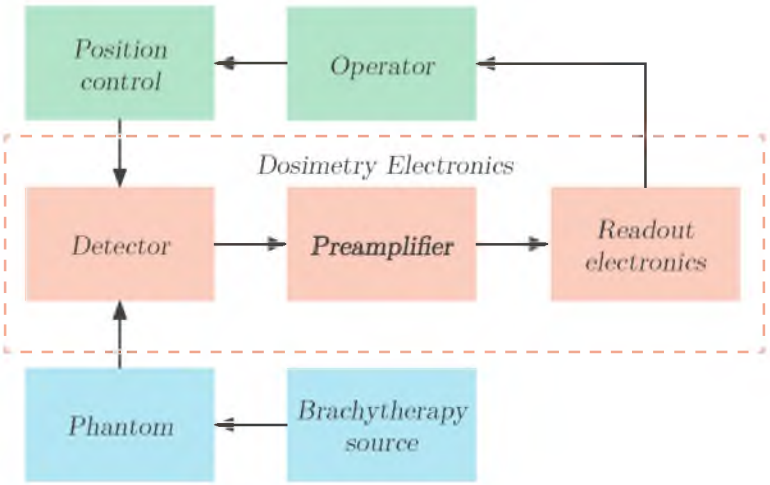

Figure 4.3: A schematic diagram of the single detector system's subsystems

probe in the water phantom, as depicted in Figure 4.1, the dose-rate was measured at the central axis of the plaque loaded with ^{125}I seeds. The opposite end of the probe consisted of the preamplifier electronics which was connected via a cable to a readout system, as seen in Figure 4.2. The readout system was used to provide real-time feedback of dose rate to the operator. The flowchart in Figure 4.3 depicted the subsystem relationships, where the operator controlled the position of the detector, which was used to measure dose from the brachytherapy source via the phantom.

This method allows for depth-dose curves to the surface of the plaque to be measured, which when coupled with lateral movement offers potential for surface dose mapping. The distance between the detector and the plaque is controlled manually, but could easily accommodate computer controlled operation. The system concept shown is in Figure 4.1, where the detector is situated at the end of an extended 'stem' protruding from the preamplifier module. The plaque is inverted within a water phantom with its active side facing up towards the detector and is located centrally within a tissue equivalent phantom. The tip of the detector travels incrementally along a plaque axis, and can be positioned directly against the plaque's surface. During this process, dose measurements are made at user defined locations and intervals.

The detector is one of the most critical factors of the design. The system detailed in this chapter used a *p-i-n* diode, the workings of which are described in Section 3.1.1.4. The external geometry of the diode was 1.0 mm × 1.0 mm × 1.2 mm, and it featured a thin *p+*-type implanted layer (630 µm × 630 µm) on one side and an *n+*-type implantation covering the entire other side. A cross sectional schematic of the diode is detailed in Figure 4.4, showing the *p-i-n* diode topology. The diodes were designed at the Centre for Medical Radiation Physics (CMRP), University of Wollongong and fabricated at the CMRP microelectronics foundry, SPA BIT.

The diode was coated in an epoxy resin to improve its robustness by protecting

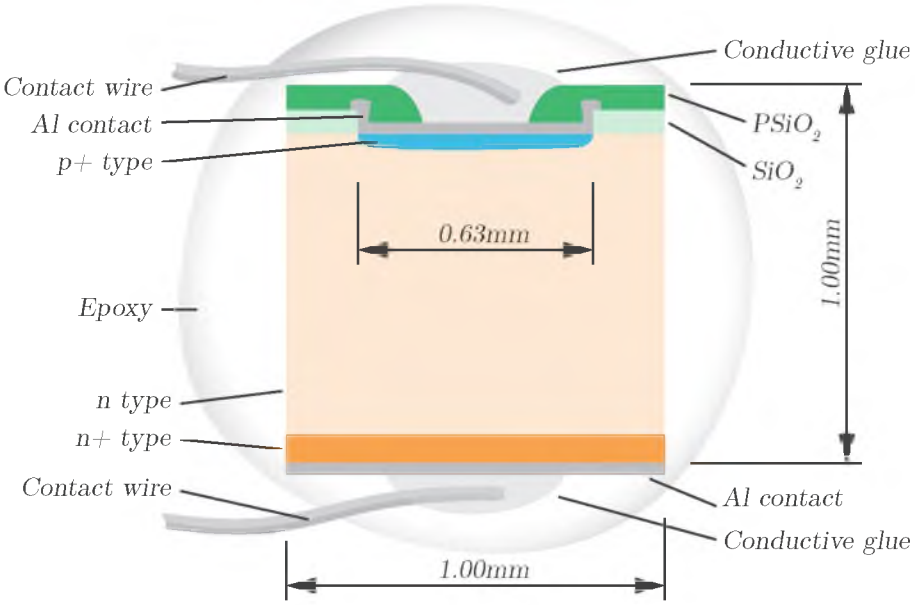

Figure 4.4: A schematic cross section of the single *p-i-n* diode detector. The size of the sensitive volume was primarily governed by the geometry of the p+ region and applied reverse bias voltage. For electrical connectivity, thin aluminium wires were fixed to the device contacts using conductive glue.

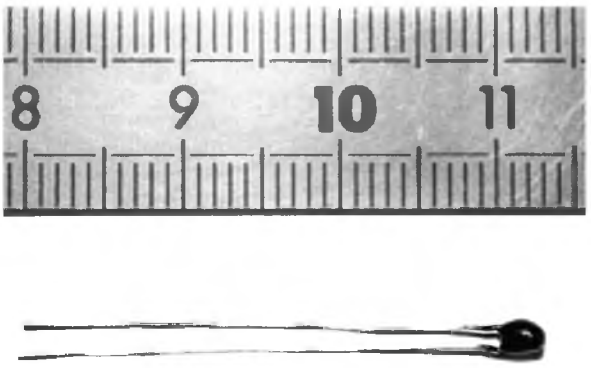

Figure 4.5: A photograph of the single *p-i-n* diode detector used in this study showing the black epoxy coating. The ruler units are in millimetres.

the sensitive wire bonds and creating a seal against water. A sample of diodes with their epoxy coatings can be seen below the probe in Figure 4.2 and in Figure 4.5. The detector was further protected against water with a thin layer of hot-melt glue and shielded from radio frequency (RF) noise with a 70 µm aluminium shrouding once it was mounted to the preamplifier board.

In addition to the detector, the preamplifier formed part of the probe. The preamplifier was mounted within a cylindrical aluminium housing, with the detector at one end, and a cable protruding from the other. This housing was used for shielding the sensitive electronics against electromagnetic interference, see Figure B.1 of Appendix B for schematic designs. The after the signal was enhanced in the preamplifier, it was passed to the readout electronics for dosimetric calculation.

The readout electronics were used for the calculation of dose rate through pulse analysis and counting in a method termed as *spectroscopic dosimetry*[159,183]. In order to calibrate the device for dosimetry, a low level discriminator was set, and the count rate was adjusted to give dose rate. The discriminator value was chosen to ignore low-energy noise events, after observing the output spectrum. The device was calibrated by placing a single ^{125}I seed of known activity (0.0116 mCi) at a known distance (10 mm) in water and adjusting the reader's calibration factor, which acted to ignore pulses randomly at a set rate, to match that given by the TG-43U1 formalism.

To assess the feasibility of a single detector design for plaque brachytherapy, the detectors needed to be characterised and the performance of the assembled system measured.

4.2 Characterisation and Performance

Studying the functional response of the detector and the overall system is important to indicate its suitability for practical dosimetry. This section aimed to characterise

the operation of the detector, and was achieved by measuring current-voltage and capacitance-voltage curves. Measurement of performance of the readout system was carried out through depth-dose curves, energy spectra and angular response.

4.2.1 Detector

Current-voltage curves were taken to determine the typical leakage current in addition to the reverse breakdown voltage of the detector. Capacitance-voltage characteristics were also measured to give an expectation of the signal quality.

4.2.1.1 Current-Voltage Characteristics

Diode leakage current was measured for the detector as a function of reverse bias voltage from 0.0 V – 50.0 V in 1.0 V increments. To achieve this, the diode was placed inside a dark Faraday box from where it was routed through to a Keithley Model 230 Programmable Voltage Source, for applying reverse bias voltage and then to a Keithley Model 614 Electrometer, for measuring the leakage current. The voltage source was controlled through the IEEE-488 interface[184] and a PC with LabView[185]. The measurements were digitised using the same IEEE-488 interface with a Keithley Model 199 System DMM/Scanner connected to the electrometer, see Figure 4.6.

The recorded current-voltage response for the chosen detector is presented in Figure 4.7. Here, the curve shows an initially steep increase in leakage current with applied bias voltage. It then increases linearly, with a least squares fit calculated for values greater than 15 V as m= 6.75 pA V^{-1}, which corresponds to a resistance of $\sim 148\,G\Omega$[1]. Such I-V characteristics are determined primarily by the series resistance of the undepleted region which is long enough (~ 1 mm) to be considered a long-base *p-i-n* diode, in which partial recombination occurs prior to collection at the ohmic contact regions. In

[1] As the gradient of the line is determined to have a conductance of $6.75\,pA\,V^{-1}$ and from Ohm's law ($R = V/I$), the diode junction resistance is $\sim 148\,G\Omega$.

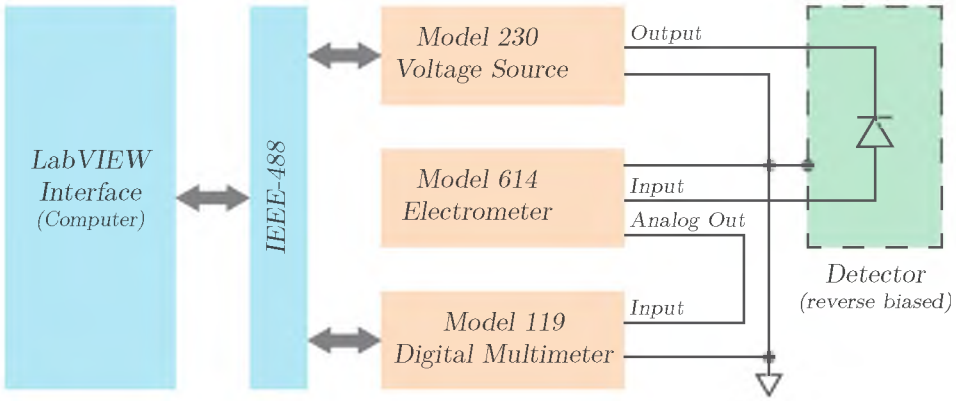

Figure 4.6: Schematic representation of the test circuit used for measuring the leakage current-voltage characteristics of the detector diodes.

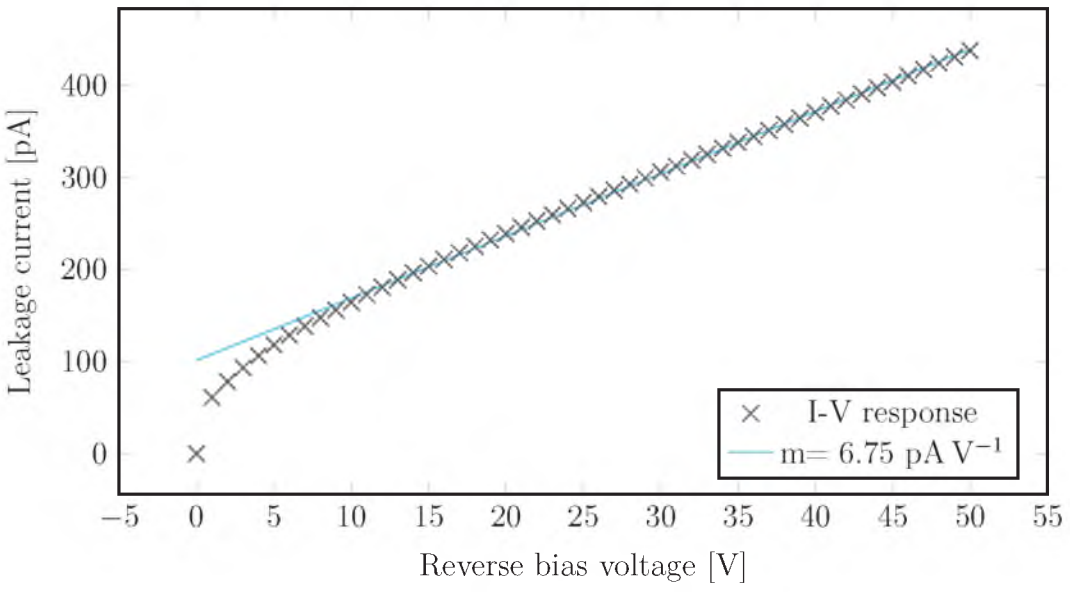

Figure 4.7: Current-voltage characteristics for the single detector. Linear regression, with slope, m, calculated using values 15 V and greater.

a short-base *p-i-n* diode, a $\sqrt{V}$ relationship is usually observed as recombination losses are negligible.

4.2.1.2 Capacitance-Voltage Characteristics

It is important to understand the implications of the junction capacitance of a semiconductor detector. This detector capacitance strongly affects the energy resolution of spectroscopy measurements; if it is too high the device may be unsuitable for radiation detector and dosimetry. Further details regarding diode capacitance are presented in Section 3.1.1.4.

Using a Boonton 7200 Capacitance Meter[186] a reverse bias voltage was applied to the detector and incrementally changed from 0.0 V – 50.0 V (below the breakdown voltage) in 1.0 V steps. Prior to the measurement, the capacitance metre was zeroed to account for the test circuit capacitance. The capacitance was recorded at each step through National Instruments, LabVIEW[185] and the IEEE-488 interface[184]. The electrical connection for the test circuit is diagrammed in Figure 4.8.

The measured capacitance-voltage characteristics of the detector are displayed in Figure 4.9, where $1/C^2$ is plotted against V, a relationship that is usually linear for diodes. This detector has long-base diode geometry and does not exhibit the characteristics of saturation. The *p-i-n* diode capacitance decreased with applied bias voltages greater than 2 V. Given both the increase in leakage current and the decrease in capacitance with increasing bias voltage, 30 V was selected as an acceptable operating voltage that did not require modification of the readout system to achieve. At this voltage, the capacitance was measured to be ~ 1 pF and the leakage current was ~ 300 pA.

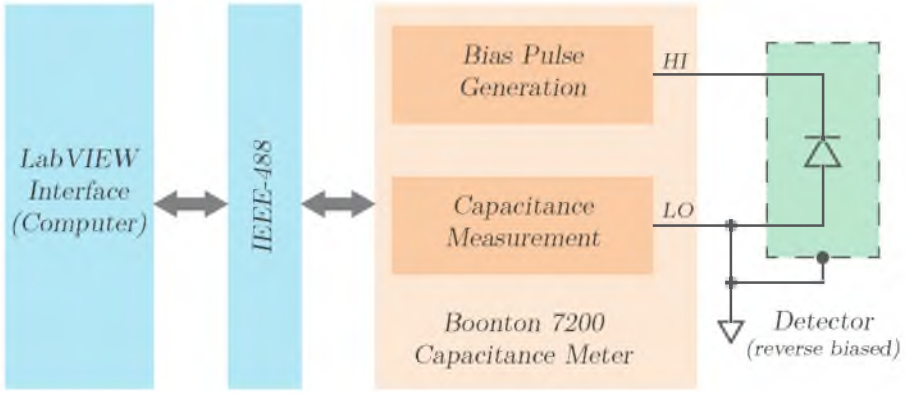

Figure 4.8: Schematic representation of the test circuit used for measuring the capacitance-voltage characteristics of the detector diodes using the Boonton 7200 Capacitance Meter[186]

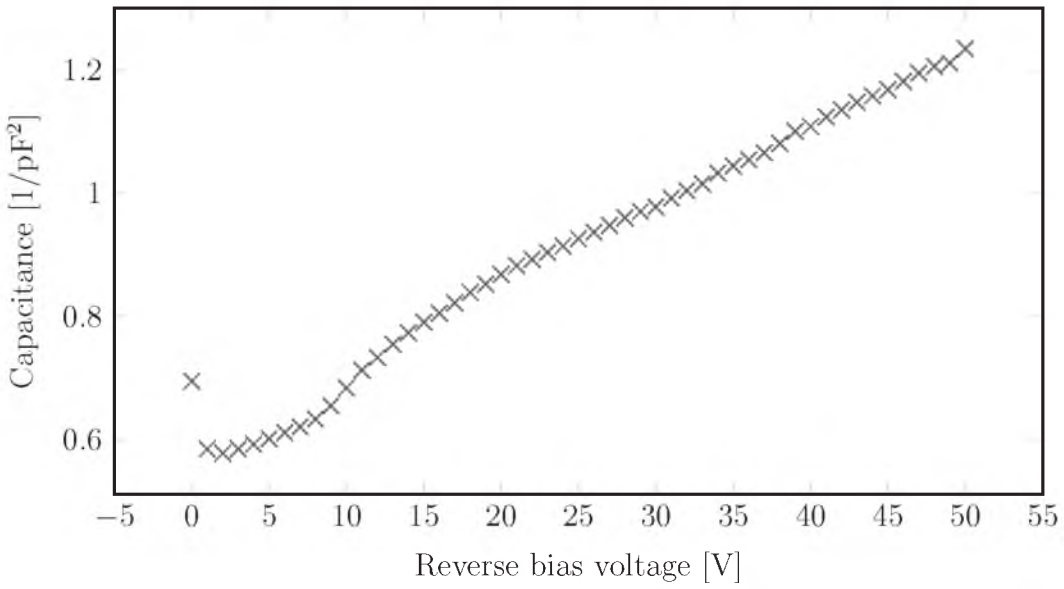

Figure 4.9: Capacitance-voltage characteristics for the single detector.

4.2.2 System

The final aim of the chapter was to characterise the single detector system and assess its performance. Characterisation of the detector, preamplifier and the readout electronics as a whole system included: measuring the energy response through pulse height analysis and measuring the angular dependence of the detector. The performance of the system was assessed through the comparison of a measured depth-dose response, and the TG-43U1 formalism.

Prior to taking measurements with the system it needed to be calibrated and have a low-level discriminator set to exclude noise. The device was calibrated by placing a single ^{125}I seed of known activity (0.0116 mCi) at a known distance (10 mm) from the tip of the detector to the central axis of the seed in water. The reader converted the number of counts that fell within an energy window (corresponding to 22 keV – 35 keV, the major photon peaks of ^{125}I) to absorbed dose in water.

4.2.2.1 Energy Spectrum

The energy spectrum measured and processed by the detector and readout electronics gave an indication of the energy resolution of the system and, thus, dosimetric capabilities. For example, as the ^{125}I spectrum lies within a relatively narrow window ($\sim$ 15 keV wide), a single calibration factor in conjunction with a low level discriminator is sufficient when calculating dose. This has been previously demonstrated through spectroscopic dosimetry[159,183]. When low energy noise can be excluded, the detector can operate in count mode, where the count rate measured is approximately proportionally to the dose rate.

The front of the detector was positioned in close proximity to 5$\times$ ^{125}I seeds and the surrounding medium, air, was used as it had minimal attenuation effects on the spectrum. During measurement, the shaped spectroscopy pulses were output from the

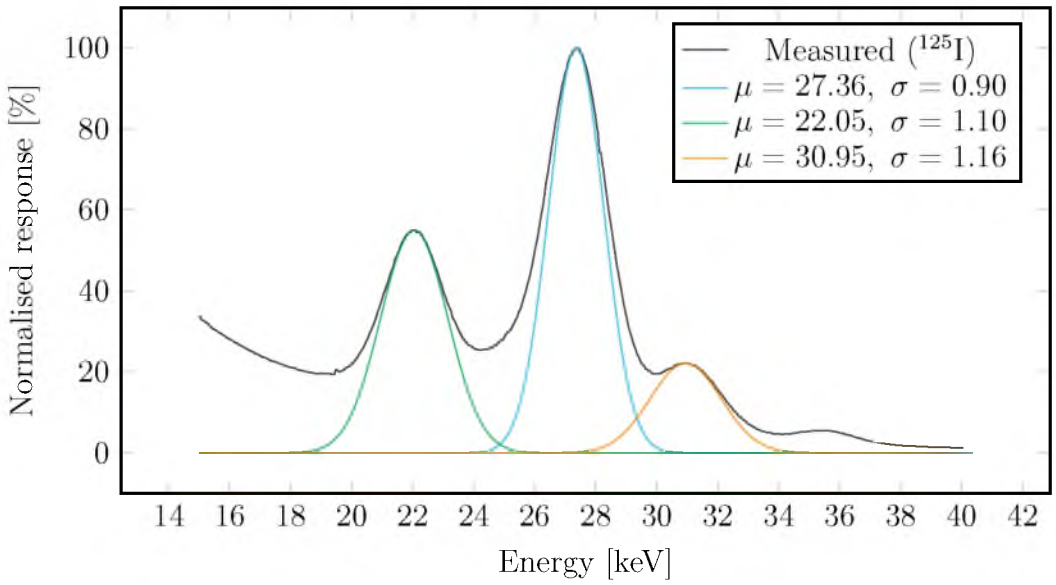

Figure 4.10: The spectrum of $5\times^{125}$I seeds as measured in air by the single detector system. The spectrum was calibrated using the 22.0 keV, 27.0 keV, 31.0 keV and 35.5 keV peaks and their corresponding locations within 1024 energy bins of the MCA. The three dominant peaks where fitted to gaussian curves (illustrated in colour) using the non-linear least squares method.

readout electronics and fed into a 1024 bin multichannel analyser, where a frequency histogram (MCA spectrum) of the pulse heights[2] was generated. A measurement time of about 38 min (2.300 ks) was used to ensure suitable statistics for a low noise spectrum given the seed activity (0.32 mCi).

The energy spectrum measured (Figure 4.10) shows that noise increases with decreasing frequency, close to the lower cut-off threshold. From energies of approximately 19 keV and greater, a set of distinct peaks of differing heights is depicted. These correspond to the ^{125}I seed's 35.5 keV γ transition line, 27.0 keV and 31.0 keV internally converted x-rays and 22.0 keV fluorescent peak from the seed's internal silver rod. At energies greater than the edge of the highest energy peak, no counts are recorded.

[2] The voltage output, measurable as the pulse height is proportional to deposited energy. For further information, see Section 3.2

4.2.2.2 Angular Dependence

The angular response of a detector provides information that is important for assessing the detector's suitability for use in dosimetry. When a detector is considered to have angular dependence, its response will vary in accordance to its orientation with respect to the source. The geometry of the detector and surrounding structures are primary influences on the angular response of a detector. This is due to differences in effective attenuation, and hence measurable spectra deformation, that occurs at different directions of incident radiation.

To conduct this characterisation, the probe was positioned centrally within a cylindrical water phantom using a retort stand and clamp, as seen in Figure 4.11. The phantom had a diameter of 130 mm, a height of 180 mm and a usable volume of approximately 2.0 L. It was placed centrally on a rotary platform which allowed for manual orientation control at sub-degree precision. A single ^{125}I seed of activity 0.101 mCi was fixed vertically to a PMMA holder within the phantom in line with of the detector and at a distance of 20 mm. The rotary platform was zeroed to a reference point on the detector casing. From this point, measurements were made by rotating the platform and seed about the stationary detector in 15° increments until a complete 360° sweep around the detector was made. This motion is shown in the sub-schematic within Figure 4.11. Other rotational axes of the detector were not considered due to the detector always having an 'end-on' orientation with respect to the source during operation. Each measurement consisted of a set of 5×10 s acquisitions. The spatial resolution and integration time selected here were sufficient to illustrate the large dependency effect of the detector, and further detail would not have provided deeper insight.

The results of the angular dependence measurements are shown in Figure 4.12. The data shows the deviation of the mean response at each angle, from the mean response from all measurements. Each datum point is accompanied by error bars of

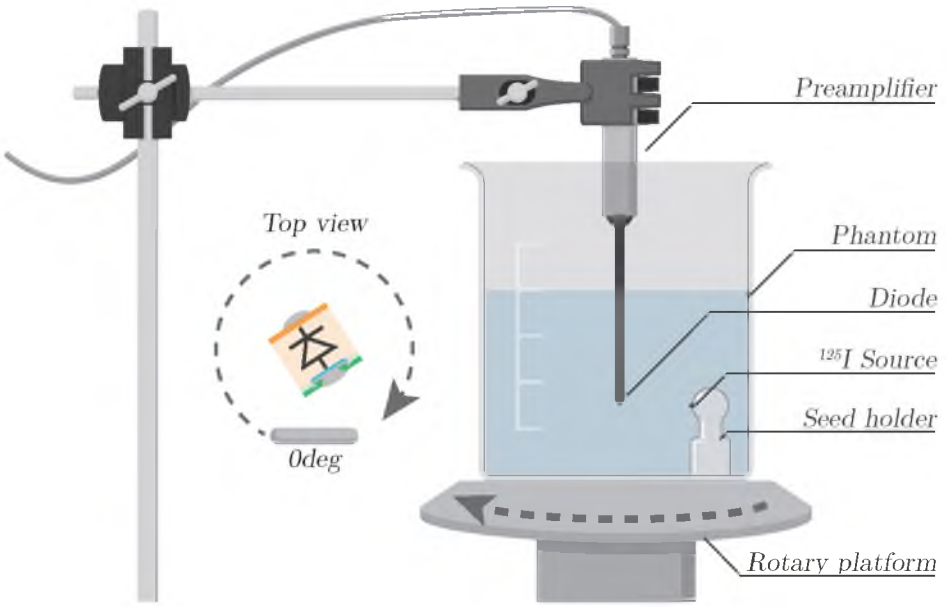

Figure 4.11: Diagram of the angular dependence experiment concept. The detector was vertically aligned with a single ^{125}I seed which was then rotated completely about the detector's axis. The top-down sub-schematic shows the seed-detector orientation.

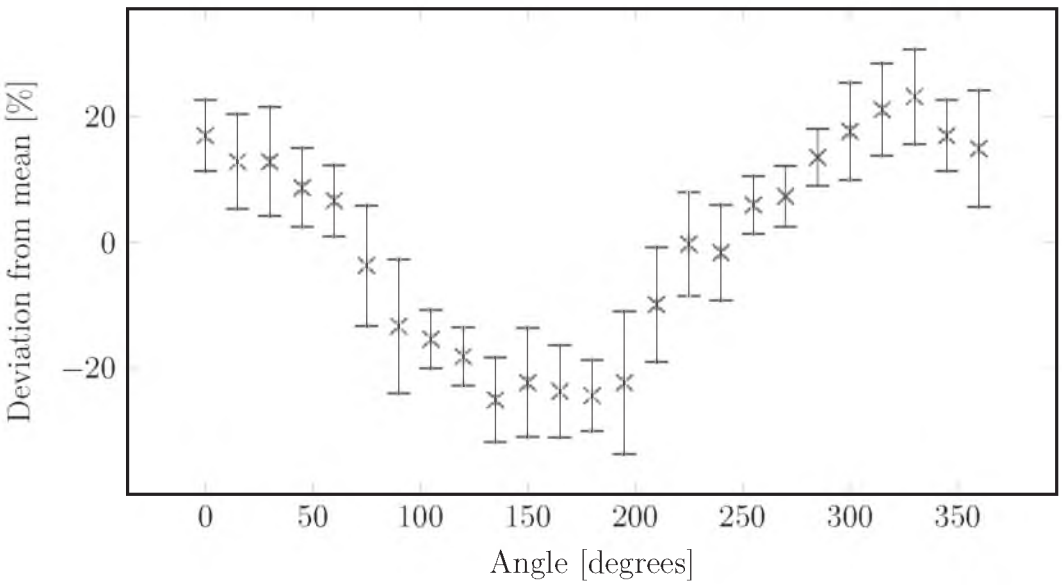

Figure 4.12: Normalised angular dependence of the single detector system measured with a single ^{125}I seed. Each point is the average of five measurements (errors to $\pm 1\sigma$), calculated as the percentage difference from the mean of all measurements.

one standard deviation each way, calculated across the five measurements.

4.2.2.3 Depth-Dose Response

To determine the dosimetric validity of the system, the dose rate of the central axis of a plaque loaded with $10\times^{125}$I seeds, measured from the detector system, was compared to that calculated using the TG-43U1 formalism. The plaque used was a standard ROPES 15 mm model, the insert layout of which is illustrated in Figure 4.13. It was fully loaded with ten Oncoseed 6711 ^{125}I seeds[187], giving a total activity of 0.116 mCi. The vertical detector-plaque distance was varied within a phantom to generate a depth-dose response from the detector system.

The detector probe was fixed to a linear micrometre positioner to allow for alignment over the plaque and phantom and control of the vertical detector-plaque distance. The phantom consisted of a high density polyethylene (HDPE) container filled with water. The container was a 120 mm × 120 mm × 120 mm cube, in which a PMMA plaque holder was placed at the bottom. The plaque holder comprised a machined layer of PMMA, and was used to position the plaque centrally within the phantom. The detector was aligned over the centre of the plaque and zeroed to the plaque's surface prior to starting measurements. See Figure 4.14 for a depiction of the experimental apparatus.

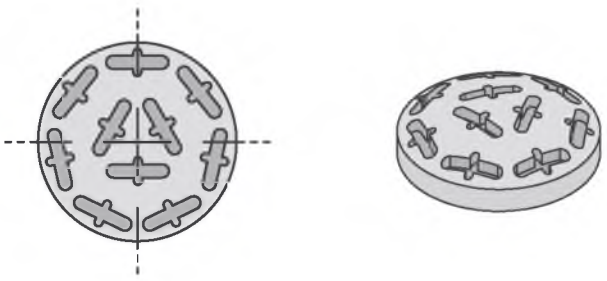

Figure 4.13: An illustration of the acrylic insert for the ROPES 15 mm eye plaque that was used in conjunction with its metal backing (not depicted) to provide a source for the depth-dose curve. All ten seed slots were filled with Oncoseed 6711 ^{125}I seeds[187], giving a total equivalent activity of 0.116 mCi.

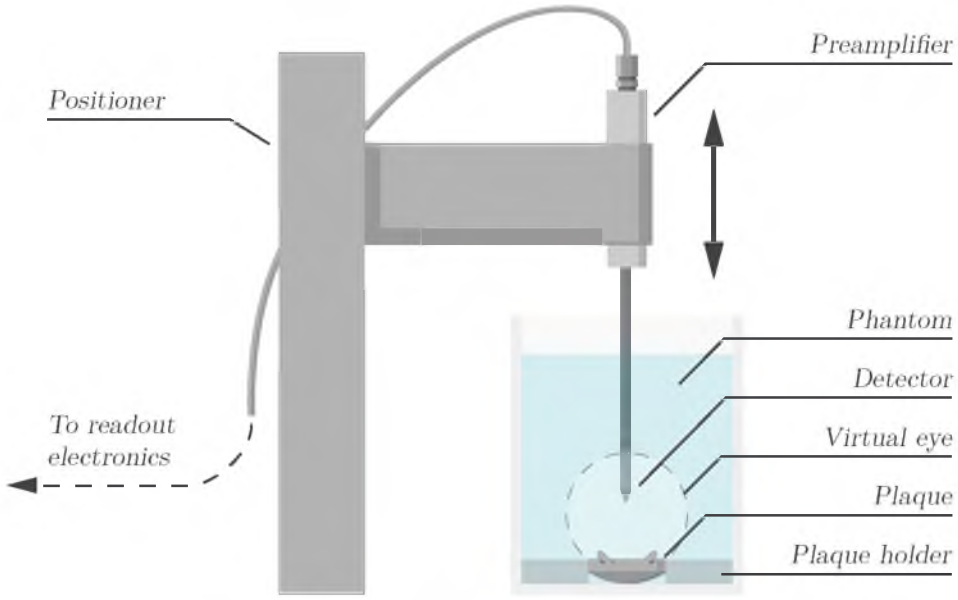

Figure 4.14: Diagram of the depth-dose experimental apparatus. The detector probe was fixed to a linear positioner and aligned centrally over the plaque. The plaque was fully loaded with ten ^{125}I seeds and kept in place with a PMMA insert. The first measurement was taken directly on the surface of the plaque to act as a reference point for subsequent measurements, which were taken with the detector positioned at increasingly greater distances from the plaque. The *Virtual eye* represents the position of the patient's eye relative to the plaque during the actual treatment.

Measurements were taken for detector-plaque distances ranging from 1.0 mm – 22.0 mm and were repeated to reduce error. Each point in the *mean measured dose rate* series in the top plot of Figure 4.15 represents the average of 4×10 s intervals for every given distance. The associated error bars to two standard deviations are displayed for each point in the *measured dose rate* series.

As a comparison to current plaque brachytherapy treatment planning, a calculation of the corresponding TG-43U1 formalism is also displayed in the top plot of Figure 4.15 with the percentage difference at each point from the measured values shown in the bottom plot. In order to determine the dose from the plaque using the TG-43U1 formalism, a software tool was written using C++[188] and Digia's Qt interface libraries[189] to generate the super-positioned total from the ten seeds at their respective orientations and positions within the ROPES plaque.

4.3 Discussion

The concept of using spectroscopic dosimetry for plaque brachytherapy was feasibility tested using a single, silicon *p-i-n* diode. First, the detector was characterised in terms of its current-voltage and capacitance-voltage characteristics. The detector was then tested whilst integrated with the preamplifier and readout electronics in three methods: energy response, angular dependence and depth-dose response.

4.3.1 Current-Voltage Response

Measuring the current-voltage response characteristics is a fundamental test for many electronic structures. The expected current response of the *p-i-n* diode is similar to that of the *p-n* junction shown in Figure 3.7. However, the main region of interest for radiation detection lies between zero volts (unbiased) and the reverse breakdown voltage. The data in Figure 4.7 shows that leakage current increased rapidly from

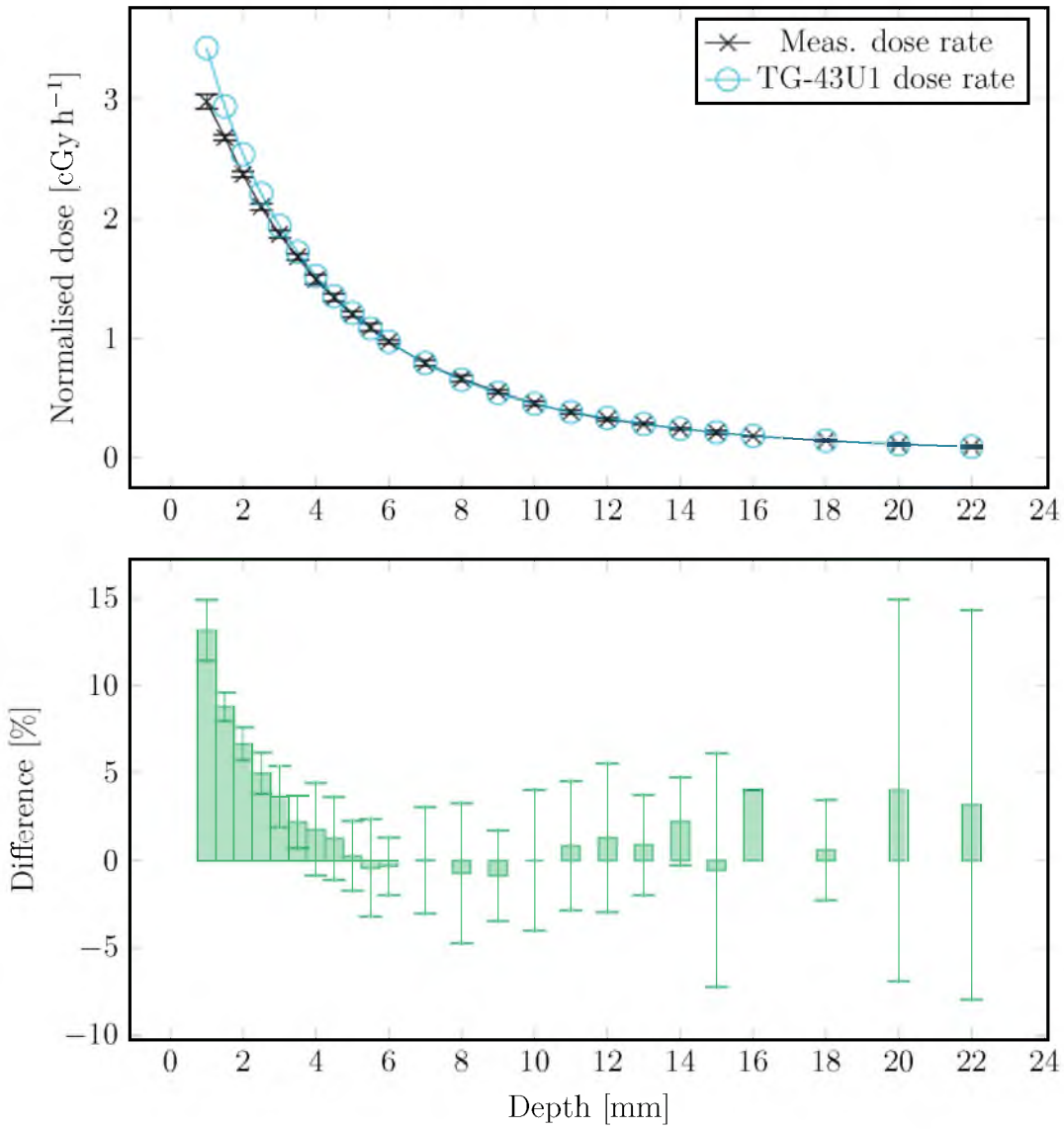

Figure 4.15: Depth-dose plot of the single detector system is compared to the TG-43U1 protocol in the top plot. The percentage difference of TG-43U1/measured dose rates is presented below in the bar graph, along with the corresponding scale errors (2σ). The experiment involved the use of a fully loaded ROPES 15 mm plaque with each ^{125}I seed having an activity of 0.116 mCi.

zero to ten volts, and then linearised to a constant rate of around 6.75 pA V^{-1}. The device demonstrated expected behaviour as the measured IV curve was consistent with that of an undepleted 1.2 mm long-base diode. The operational bias voltage used in the readout electronics was 30 V which pertained to a leakage current value of approximately 300 pA. This lay within acceptable limits because it had not exceeded the reverse breakdown voltage.

4.3.2 Capacitance-Voltage Response

The capacitance-voltage response of the *p-i-n* diode can be used to develop an expectation of the signal quality. As explained in Section 3.1.1.4, a lower detector capacitance helps to improve signal quality by improving the signal-to-noise ratio and more accurate dosimetry. The data displayed in Figure 4.9 shows capacitance (in pF) as a function of reverse bias voltage.

The non-ideal shape of the curve, which should ideally follow a $C \propto \sqrt{1/V}$ relationship, can be attributed to an increase in sensitive area with voltage. This occurred due to an edge effect that was significant as the geometric dimensions of the *p-n* junction were similar to those of the lateral depletion, and lead to an increase in the effective area of the *p-n* junction. This can be explained through the equation of the parallel plate capacitor, $C = \epsilon_r \epsilon_0 A/d$ which shows that capacitance is proportional to sensitive area (A) and inversely proportional to depletion width (d). In addition to this, the wafer thickness was large enough (1 mm) that full depletion could not be reached before breakdown occurred. This effect was seen as capacitance continues to decrease with increasing voltage.

4.3.3 Energy Resolution

Observation of the energy spectrum can give a good indication of the signal quality and how distinguishable it is from low energy noise. Figure 4.10 shows the measured photon spectrum of Oncura model 6711 ^{125}I seeds in air at room temperature with a cut-off threshold energy of 15 keV. Gaussian curves were fitted to the dominant peaks using the nonlinear least squares method. The full-width at half-maximum (FWHM) values were calculated using the relationship FWHM $= 2\sqrt{2ln(2)}\sigma$. The largest of the peaks, at 27 keV, yielded a FWHM of 2.1 keV, or about 8 %, and demonstrated the acceptably low noise of the readout electronics. The 22.1 keV and 25.2 keV peaks were emitted as fluorescent x-rays from the seed's internal silver rod[187].

For this system to be used for practical dosimetry, the cut-off threshold should be set around 19 keV to exclude as much unwanted noise as possible, whilst including the full ^{125}I spectrum. This is only possible through sufficient peak resolution, such as that demonstrated here.

4.3.4 Angular Response

Angular dependence arises as a result of incident radiation becoming attenuated by differing amounts, depending on the angle of arrival due to material type and thickness. Thus, the extent of the attenuation that occurs is strongly dependant on the geometry and topology of the silicon detector.

The angular dependence of the detector is plotted in Figure 4.12. It follows an approximately sinusoidal shape with overall deviations ranging as much as ±30 %. The shape of the data can be explained by the partial depletion of the long-based detector ($\sim$ 1 mm) which lead to strong attenuation of low energy photons emitted by ^{125}I seeds, causing about a 60 % difference in count rates. Additionally, the globular epoxy packaging of the detector may also have been a contributing factor for individual

device asymmetry. This variation in material thickness would have also hindered the correct centralisation of the detector and, hence, the distance between the effective point of measurement and the seed, further affecting outcomes by possible eccentricity in the rotation.

4.3.5 Depth-dose Response

The dosimetric functionality of the single detector system was evaluated by comparing depth-dose measurements with the TG-43U1 formalism. From the literature reviewed in Table 2.4, most dosimetry techniques have an uncertainty of between 8 % – 15 %. The calibrated and normalised depth-dose curve shown in Figure 4.15 matched well, with the TG-43U1 with points coinciding by less than around 4 % for distances $\geq$ 3.0 mm. Distances less than this under-responded due to limitations in the ability of the TG-43U1 algorithm to account for medium heterogeneities. This occurred, as the presence of the metal plaque backing affected the backscattering conditions predicted in the algorithm. Additionally, the uncertainty in the thickness and symmetry of the epoxy packaging of the detector increased the error in small detector-source distances.

There are mixed accounts in the literature regarding the effects of plaque presence, including: under-dosing[108,109], overdosing at short range[110,113], backing material dependent dose changes[114] or no effect at all[122]. Monte Carlo simulations have shown that dose decreases occur at distances of 5 mm – 6 mm from the inner sclera along the eye's central axis in the range of 4 % – 20 % depending on the radionuclide and backing material used. A sound dosimetry treatment planning and verification method is needed to ensure consistency in the clinical community.

4.4 Future Research

The concept of the system and its performance yielded promising results and established justification for extended development into more complex detector designs. Despite this, the single detector system offers for simple dosimetry solutions such as surface dose measurements and depth-dose verification of plaques. A number of aspects of the design could be optimised for future designs, including: the detector design, positioning system and the information interface.

4.4.1 Diode Design

The existing detector design could be improved for dosimetric use by enabling closer surface measurements and having less angular dependence.

In creating a system that is to be used in providing the depth-dose characteristics of an assembled plaque, it is essential that it be capable of measuring most, if not all, regions of interest. The sclera is an area that is subject to extreme dose and, as such, profiling the dose in this region is critical. One limiting factor of the detector investigated is the minimum distance at which dose can be measured from the plaque surface ($\sim 1\,\text{mm}$). By modifying the geometry of the detector and its packaging to reduce unnecessary material, dose closer to the inner surface of the plaque could be measured.

In addition to modifying the size and shape of the detector for positioning purposes, the angular response of the device must also be considered. When vertically depleted, the active implanted region ($p+$-type) should also provide full lateral depletion. A diode with a very small, yet fully depleted, volume ($0.5 \times 0.5 \times 0.1\,\text{mm}^3$) would provide good angular response and spatial resolution. The packaging of the detector and surrounding probe need to be water equivalent minimise angular dependence and waterproof to prevent damage. A suitable implantation and biasing configuration study should also

be conducted to improve detector selection.

4.4.2 Positioning System

The accuracy could be improved in the positioning of both the diode and the plaque, along with their relative distances. Whilst the linear positioner used operated at the micrometre level, aligning the detector to the plaque was difficult as it was a manual process and relied on vision. Using a common base plate, the phantom and positioner could both be fixed and, given their known positions, detector localisation would be inherently accurate. Unique phantom inserts would be required for each style of plaque to ensure correct positioning and orientation of the plaque within the phantom.

Control over the vertical axis should be automated and computer integrated, providing depth-dose curves with little need for attention during measurements. Extension from such single dimensional, vertical measurements, to two or three dimensional positioning could achieved through the computer controlled guidance of lateral positioning systems. Such control would allow for plaque surface scanning and measurements of planes, volumes and regions of interest. Mechanical operation of this system may be much more time consuming and probably not optimal for everyday clinical practice. Accurate detector zeroing could be determined using some form of proximity feedback, such as a force, capacitance or optical sensor.

Some combination of automated and manual control would be suitable for clinical use, depending on costs and dosimetry needs. A prototype positioner featuring automated position control in the vertical direction was proposed and is depicted in Figure 4.16.

Figure 4.16: Future development of a single detector system could include a gantry using modular components. This figure shows an automated vertical positioning system using a stepper motor for depth-dose sweeping functionality.

4.4.3 Software integration

The dosimetry system would benefit from software integration of its output, especially when in conjunction with position controlling. Measured values could be sent to a computer interface for real-time statistical analysis and curve plotting using position values directly. Such software could improve plaque verification efficiency by integrating it either directly, through an application programming interface (API) or through a plug-in into current treatment planning software such as Plaque Simulator. This would provide the opportunity to make comparisons to the treatment plan for plaque modification or acceptance in real-time.

4.5 Conclusion

The single detector concept aimed to provide a simple dose verification tool for use in clinical environments, in addition to determining the feasibility of continuing development into more complex and advantageous detector designs. To do this, a detector system comprising a *p-i-n* diode detector, preamplifier and readout electronics was assembled. The aim to determine the operational characteristics of the detector was achieved through measurement of both current-voltage and capacitance-voltage responses. Furthermore, through the measurement of energy response, angular dependence and depth-dose response of the assembled system, the aim of characterising the system assessing its performance was also fulfilled.

These experiments demonstrated the feasibility of the proposed concept of eye brachytherapy dosimetry on the central axis of the plaque. Despite this, the *p-i-n* diode used was suboptimal for this type of dosimetry. For further improvement, the detector should allow for full depletion of the geometric volume which would reduce the angular dependence of the detector response. The size of the detector should be as small as possible for two reasons:

1. to provide high spatial resolution, which is needed due to the steep dose rate gradient closer to the plaque surface, and

2. to cause negligible perturbation of the radiation field without compromising sensitivity of the detector.

To meet these requirements, the detector should be around $0.5 \times 0.5 \times 0.1\,\mathrm{mm}^3$ in size. Additionally, under full vertical depletion, the active implanted p+ region should provide full lateral depletion. This would reduce attenuation of the low energy photons from ^{125}I seeds positioned laterally from the detector. Unfortunately, doing this would also cause an increase in the surface leakage current as a guard ring cannot be placed

around the p+ region. The packaging of the detector should be water equivalent for minimal effect on dosimetry and waterproof for protection during submersion.

To perform three-dimensional dosimetry, an eye phantom should be fitted with multiple detectors sufficient for reconstruction to be performed.

It is not possible to satisfy all these design requirements simultaneously. For a single detector probe, substrate material is required with pins for wire bonding. The detector can be mounted on a thin waterproof probe and used within a water phantom. The probe is long enough to allow for scattering conditions that resemble infinite water, when used within a water phantom such as that in Figure 4.16.

For 3D dosimetry it would be impractical to use numerous individual detectors due to the connection and interfacing logistics. Pixelated, monolithic silicon detectors offer a solution to this issue, and also provide excellent definition of the pixel geometries. However, the presence of the silicon substrate laterally surrounding each pixel is disadvantageous for dosimetry. The following chapter investigates the concept of spectroscopic dosimetry with pixelated detectors.

Chapter 5

Pixelated Detector Concept

The previous chapter demonstrated the successful use of a single silicon detector for spectroscopic dosimetry in plaque brachytherapy. The study is developed further in this chapter, where pixelated detectors were investigated for their effectiveness in event counting three-dimensional (volumetric) dosimetry of brachytherapy sources.

Two concepts for volumetric dosimetry were explored, both of which involved creating numerous planar dosimetric images, whilst incrementally moving a pixelated detector relative to the plaque. The first concept translated a rectangular detector plane in a linear motion, while the second rotated a semicircular detector plane about its axis. These concepts were tested using existing pixelated detectors from the Medipix family[142,143].

Overall, this chapter aimed to assess the validity of using pixelated silicon detectors for plaque brachytherapy dosimetry, and to offer improvements for detector design. This was achieved through the following specific aims:

- assessing the feasibility of volumetric dosimetry;
- comparing count mode and charge mode dosimetry;
- assessing the activity variance in seeds;

- determining the required spatial resolution;
- determining the affect of back scattering and phantom design; and
- measuring the accuracy of dose measurement of beta sources.

5.1 Pixelated Detectors

Since the early 1980s, planar fabrication processes have provided a means for developing complex semiconductor devices[138,139]. They have since become popular for studying ionising radiation events for dosimetry and many other applications[190,191]. The pixelated semiconductor detector is a device that is fabricated with discreet sensitive elements, or *pixels*, and provides additional two-dimensional spatial information about the measured radiation events. While there are benefits in having small sensitive elements, there are also trade-offs with complexity in areas, including the readout electronics.

With decreasing size of the sensitive volume of a semiconductor detector, there is an associated decrease in junction capacitance and leakage current, as explained in Section 3.1.1.4. The decrease in these parameters leads to a decrease in the inherent noise, thus improving the signal quality and providing more accurate dosimetry. Another advantage of low leakage current is that devices may be operated without cooling at room temperature, where otherwise thermal noise would be too great.

One issue faced when using detectors where pixels are both numerous and small is the increase in complexity of connectivity to the readout electronics. When the geometry of the detector permits, electrical connections using metal tracks on the surface can be made between the individual pixels and the edge of the wafer for wire bonding. However, this method can result in losing too much active area on the detector surface. As an alternative, a double-metal process can be employed where

tracks are formed on two layers separated by an insulating glass layer, allowing for more complex designs[192]. Track length affects the quality of the signal through the increase in input capacitance it causes.

To mitigate these adverse noise effects whilst maximising the active area of the detector, the readout electronics can be connected directly to one side of the detector, forming what is called a *hybrid detector*. This is achieved through designing the readout elements to match the size of the individual detector pixels and bump bonding them together. The design and fabrication of such a device is a relatively complex and expensive process in circumstances when the simpler method of surface track connectivity may suffice. For many applications, however, low noise hybrid detectors such as those in the Medipix family are a very attractive technology.

5.1.1 The Medipix Detector

The Medipix detectors are a family of hybrid detectors that have been in development since the Medipix1 Collaboration was formed in the early 1990s. There have since been a number of successors and offshoots of the technology, including the Medipix2[142] (see Figure 5.1), Timepix[143] and Medipix3[193].

Silicon pixelated detectors such as the Medipix2 and Timepix have been successfully used in radiography, neutronography and micro-tomography[194–196] and are currently being investigated for eye plaque dosimetry at the Centre for Medical Radiation Physics[140,141]. These devices each consist of an array of 256×256 individual pixels with a pitch of $55\,\mu m \times 55\,\mu m$ and are capable of high resolution imaging with low noise.

For deposited charges smaller than $50\,ke^-$, the Medipix2 can operate up to a maximum count rate of 1 MHz per pixel without pile-up[142], which corresponds to a maximum activity of about 1 Ci, far beyond the normal scope of activities used

Figure 5.1: Photograph of the Medipix2, a hybrid, pixelated detector with 256×256 individual pixels of pitch $55\,\mu m \times 55\,\mu m$.

in plaque brachytherapy. Additionally, the Medipix2 detector is very radiation hard, capable of operation at up to 300 krad (3.00 kGy)[142]. Whilst the Medipix2 uses count mode with a windowed discriminator, the Timepix builds on this and includes the capability of effectively measuring charge using a *time-over-threshold* (TOT) mode. This form of spectroscopic dosimetry can provide excellent outcomes, however it is relatively more complex and costly, if otherwise avoidable when count mode could be used.

This chapter investigates the feasibility of using pixelated detectors, through the Medipix2 and Timepix, for the purposes of establishing the feasibility of two separate design concepts for a volumetric detector for plaque brachytherapy.

5.2 Design Concepts

Two design concepts were considered to support the development of a volumetric dosimetry tool for plaque brachytherapy; the first used a rectangular, pixelated detector used in a similar, but inverted, fashion to the single detector concept (see Chapter 4),

the second comprised a semicircular, planar pixelated detector to produce a volumetric dose map in a solid phantom. Both concepts use motors to create controlled, accurate and repeatable positioning between the detector and the plaque.

The dose volume created would be used for clinical preoperative treatment verification by extracting information in regions of interest, as one dimensional (depth-dose), two dimensional (planar slices), or three dimensional (dose volume) data sets. These dosimetric results could be directly compared to existing treatment plans in real-time to provide valuable dose verification to plaque brachytherapy.

5.2.1 Translation Concept

A primitive version of the *translation concept* was seen as the single detector concept in Section 4.1, and is adapted in this chapter for use with a pixelated detector. The concept essentially involves incrementally lowering a brachytherapy plaque to the bottom of a water filled vessel. At each stationary point along the way, the pixelated detector acquires dosimetric data in conjunction with the current position and stores it. The series of recorded measurements can be used to reconstruct volumetric dose distributions, as shown in Figure 5.2b. These distributions provide detailed information for comparison to patient treatment plans. The general hardware configuration of the concept is depicted in Figure 5.2a, where the *Virtual eye* represents the location of a patient eye during treatment. This concept is investigated experimentally with the Medipix2 detector in Section 5.3.1.1.

5.2.2 Rotation Concept

The *rotation concept* uses a semicircular detector, designed to fit closely against the inner surface of an ophthalmic plaque. A tissue equivalent phantom is used to occupy the volume surrounding the detector in a shape and position which corresponds to the

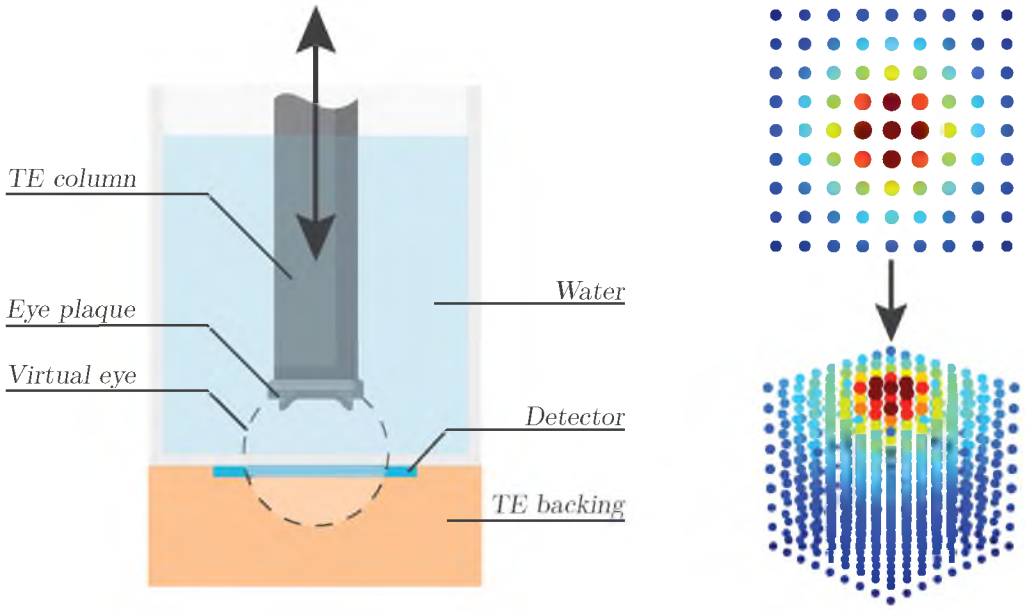

(a) Plaque translation concept (b) Dose volume construction

Figure 5.2: A rectangular pixel detector array, embedded in a tissue equivalent phantom, is positioned below a water filled vessel, where the brachytherapy plaque is lowered towards it in discrete intervals for providing a volumetric set of data.

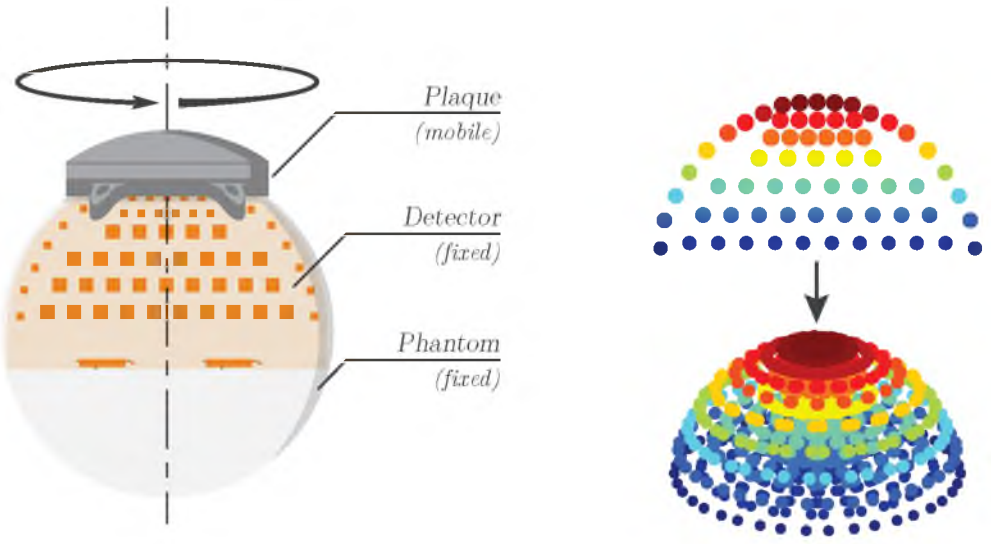

(a) Plaque rotation concept (b) Dose volume construction

Figure 5.3: The ophthalmic plaque is rotated about its central, vertical axis while a semicircular pixel detector array, embedded in a tissue equivalent phantom, remains stationary to provide a volumetric sweep of measurements. Single planar measurements are made for multiple plaque-detector angles and superimposed to create a dose volume.

eye ball in a treatment, as shown in Figure 5.3a. This geometry allows for a planar dose map to be created for a cross-section of the eye that passes through the central axis of the plaque. If the plaque is rotated about this axis, different cross-sectional dose maps can be measured, corresponding to the angle of rotation. When a set of these maps is reconstructed as a whole, a dose volume from the plaque can be produced, as depicted in Figure 5.3b. This concept is investigated experimentally with the Medipix2 detector in Section 5.3.1.2.

5.3 Proof of Concept

In order to evaluate and demonstrate the working principles of the pixel array design, several tests were conducted. This involved using proven silicon pixel detector arrays designed by the Medipix Collaboration, namely the Medipix2[142] and the Timepix detectors[143]. The high resolution capabilities of this family of detectors provided an ideal foundation for determining the system requirements for this study, allowing for volumetric dose reconstruction prototyping, comparison between count and charge modes of operation, detailed seed dosimetry and detector resolution investigation. The detectors were also used to evaluate specifics of preliminary phantom design and effectiveness of measuring beta-emitting plaques.

5.3.1 Volumetric Dosimetry

Volumetric, or three-dimensional, dosimetry plays a useful role in gaining a good understanding of the complex and steep dose fields and gradients within the eye during a plaque brachytherapy treatment. This study looked at two concepts for generating volumetric dose: translation[141] and rotation[140,197].

In order to view the differences in dose distributions and the potential for plaque customisation, two seed configurations were used in the ROPES 15 mm plaque during

(a) Asymmetrically loaded (5 seeds) (b) Fully loaded (10 seeds)

Figure 5.4: The ROPES 15 mm eye plaque loaded with ^{125}I seeds, as indicated by shading. The annotated arrows indicate the direction used for orientation.

the concept evaluations. They comprised an asymmetric configuration of five seeds (Figure 5.4a) and a fully loaded configuration with ten seeds (Figure 5.4b). The seeds used were Oncura model 6711 ^{125}I with an activity of 239 µCi each.

5.3.1.1 Translation Concept Evaluation

If the detector array is structured as a regular grid, converting to a three-dimensional array is trivial. Using the data in this form, it is possible to interpolate between points in 3D space when appropriate. This concept was investigated experimentally with the Medipix2 detector and a layered phantom. The method detailed below was used as the original proof of concept, prior to the revised design in Figure 5.2a which was used from Section 5.3.2 onward.

The layered phantom consisted of a ⌀40 mm, paraffin wax hemisphere cut into 5×4 mm slices, as seen in Figure 5.5. Historically, paraffin wax was commonly used as a tissue substitute and, whilst would not be used in a final design, is more than sufficient for prototyping use[198].

The slices were stacked concentrically atop one another with the plaque positioned at the apex. The plaque was oriented with the insert aligned towards one corner of the detector. The Medipix2 detector had a 4 mm polypropylene protective shroud around it, a polypropylene insert to protect the detector, and a 20 mm slab of tissue equivalent Plastic Water® LR[180] below it. Removing one slice at a time, the detector

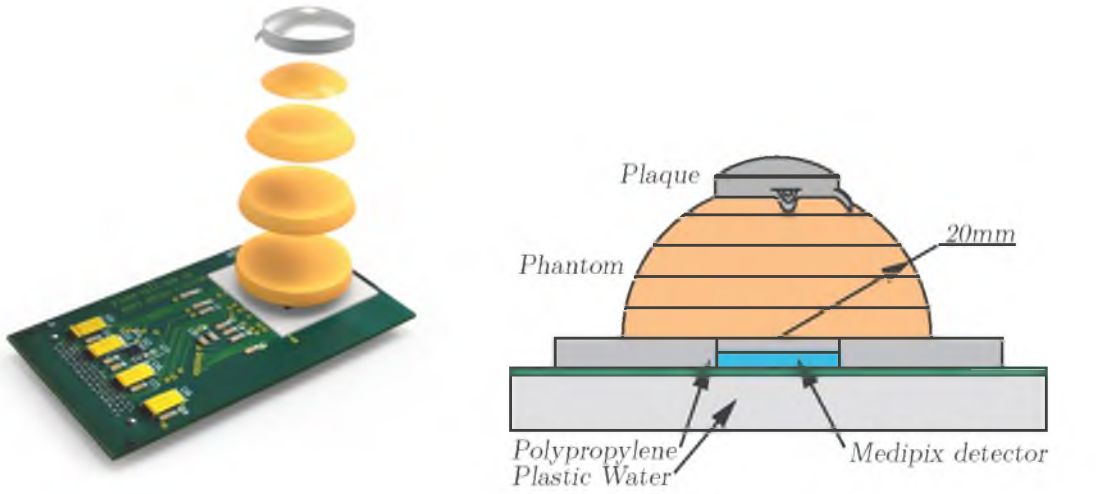

(a) Exploded view (b) Cross section

Figure 5.5: Paraffin wax, layered phantom for testing the translation concept. In the exploded view, the Medipix2 detector is seen below four of the wax phantom slices and the eye plaque.

was used to take a measurement in place of each removed slice. Each measurement corresponded to a different depth within the eye and consisted of the integrated total of $500 \times 1.0\,\mathrm{s}$ acquisitions. The method produced five planar measurements for each plaque configuration set, as seen in Figure 5.6a and Figure 5.7a.

These Medipix acquisition parameters were selected to establish consistancy between measurements conducted in this study and future measurements and to allow for visual feedback at each frame. Event pile-up was not a concern, with the maximum count rate of the Medipix2 at 1 MHz, however, its 13 bit counter depth (allowing up to 8191 events per frame) necessitated multiple frames per acquisition. The 500 s total duration gave a mean event rate of $\mu = 1716$ events per pixel at the lowest intensities (using five seeds with the detector at the farthest layer from the plaque) and a corresponding measurement uncertainty of $\sigma/\mu = 1/\sqrt{\mu} = 2.41\,\%$, demonstrating the statistical suitability of the data. The sampling parameters for the highest intensity measurement are provided in Table 5.1.

The data was stored in a 3D matrix using computational software (Mathworks

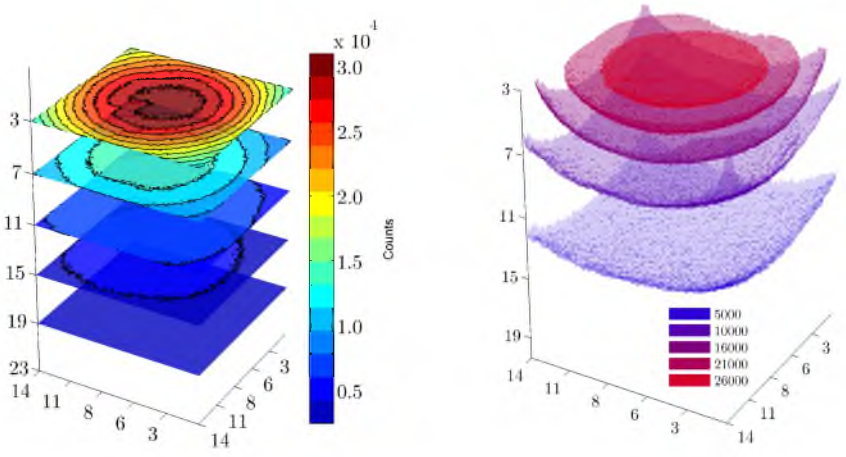

(a) Stacked Layers (b) Isosurfaces

Figure 5.6: Translation concept volumetric dosimetry verification with ten seeds in ROPES 15 mm plaque. The vertical axis shows the distance of the detector from the source in millimetres, and colours depict the number of events counted. The left image illustrates the raw data, and the right image shows an isosurface representation of the interpolated 3D dose volume.

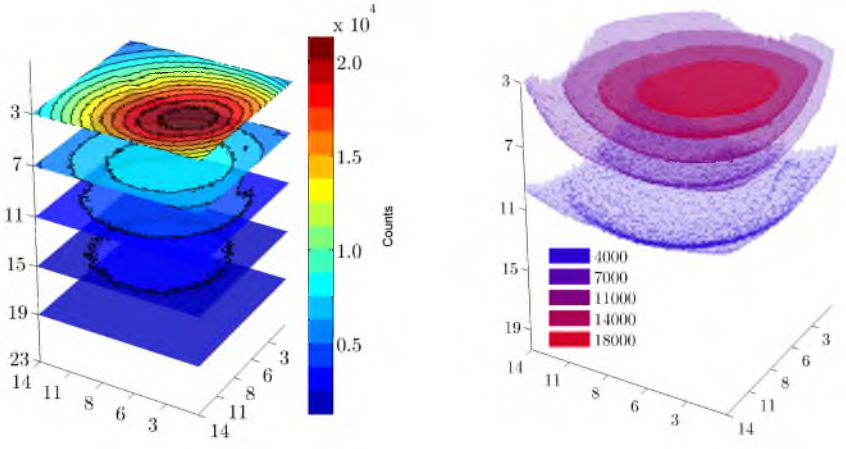

(a) Stacked Layers (b) Isosurfaces

Figure 5.7: Translation concept volumetric dosimetry verification with five seeds in ROPES 15 mm plaque. The vertical axis shows the distance of the detector from the source in millimetres, and colours depict the number of events counted. The left image illustrates the raw data, and the right image shows an isosurface representation of the interpolated 3D dose volume.

Table 5.1: Sampling parameters of the Medipix and Timepix. The measured event rates correspond to the count mode highest intensities where the detector was positioned proximate to the plaque for $10\times^{125}$I seeds configuration. The parameters above the division are generic device specifications, and those below are measurement specific. *Source*: Llopart et al.[142].

Parameter	Value
Acquisition frame time	1.0 s
Bias voltage	100 V
Max pixel count rate	1 MHz
Pixel counter depth	13 bits/pixel
Electronic pixel noise rms (adjusted)	140 e^-
Timepix clock	10 MHz
TOT frame time	498.8 µs
Mean measured event rate	48.3 events/pixel/frame
Max measured event rate	62.0 events/pixel/frame

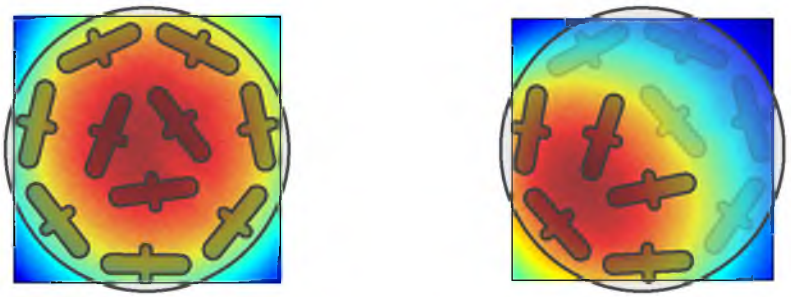

(a) Asymmetrically loaded (10 seeds)

(b) Fully loaded (5 seeds)

Figure 5.8: The approximate ROPES 15 mm plaque orientations for the measurement at the topmost layer of the paraffin wax translation phantom for both 10 and 5 seed configurations. The darkened seed slots indicate the presence of seeds, and the faded slots indicate their absence.

Matlab 2012a[199]). It was then interpolated using the cubic spline method[200] to improve the resolution between slices as needed for volumetric visualisation. The results for this set of experiments are presented in Figure 5.6 and Figure 5.7. The left hand image of each of these Figures shows the Medipix images stacked atop each other, covering the 25 mm vertical span of the measurement, with the plaque located closest to the top layer. The approximate orientation of the plaque with respect to the Medipix detector is depicted for both seed configurations in Figure 5.8.

The corresponding image on the right hand side shows an isosurface plot of the interpolated data. Each isosurface shell represents a dose surface of a constant value, as indicated in their respective legends.

The asymmetric distribution of the five seed results of Figure 5.7 is visible for the shortest plaque distance, but becomes less obvious with increasing distance. The ten seed configuration of Figure 5.6 shows a mostly symmetric result by comparison. It also shows a notch feature present towards the centre of the dose distribution in the topmost layer.

5.3.1.2 Rotation Concept Evaluation

In contrast to creating a stack of parallel dosimetric images, the rotation concept aimed to generate a set of overlaid dose images, rotated about an axis, that form a three-dimensional dose volume. The process involved taking planar dose measurements whilst controlling the angle between the detector plane and the central axis of the brachytherapy plaque. To evaluate feasibility of this concept, the Medipix2 detector was used in conjunction with a hemispherical, a paraffin wax phantom and a ROPES 15 mm brachytherapy plaque with Oncura model 6711, ^{125}I seeds. The activity of the seeds were 238 µCi each.

The plaque was located centrally upon the ⌀ 40 mm phantom and moved to four different positions in a trajectory across the surface of the phantom, as per Figure

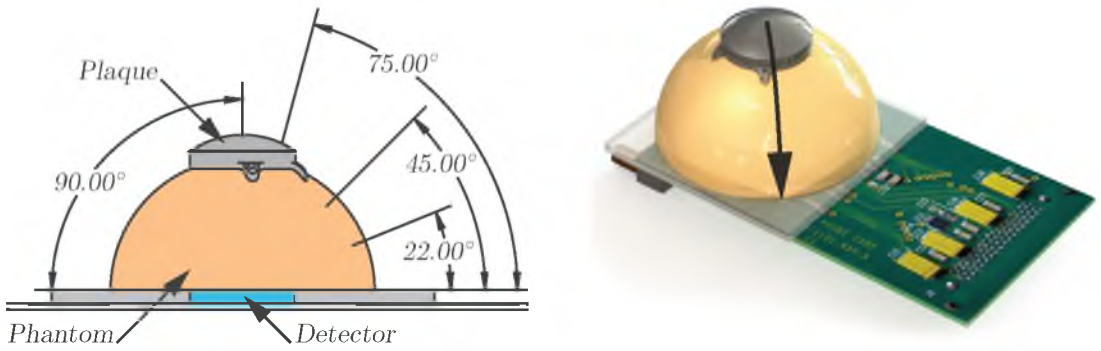

(a) Schematic showing angles

(b) Render showing trajectory

Figure 5.9: The experimental operation of the rotation concept. There were four different angles used in the trajectory of the plaque.

5.9b. The four plaque-detector angles used in the measurements were: 90°, 75°, 45° and 22°, where the plaque axis is defined as 90° and the detector plane is 0°. The orientations and angles are illustrated schematically in Figure 5.9a. Each position was measured as the integrated total of 500 × 1.0 s acquisitions. Two sets of measurements were conducted: one using an asymmetrically loaded five seeds and the second fully loaded with ten seeds, see Figure 5.4.

The individual measurements taken with the ten seed configuration are shown in Figure 5.10. The plaque source was closest to the detector at the 22° measurement and furthest at the 90° measurement. The dose rate of these images was normalised at 100% to the maximum of the set. The separate layers were spatially reconstructed by converting them to a 3D coordinate system and superimposing them, where a sparse dose volume was created, as seen in Figure 5.11.

The spatial reconstruction of the five seed configuration measurements is shown in Figure 5.12. Here, the dose rate values were normalised to the ten seed data for comparison, however, the colour bar is scaled to its local maximum to provide greater contrast. The five seeds were arranged asymmetrically, as shown in Figure 5.4a, and aligned normal to the plaque trajectory. This asymmetry is unclear in the data as the

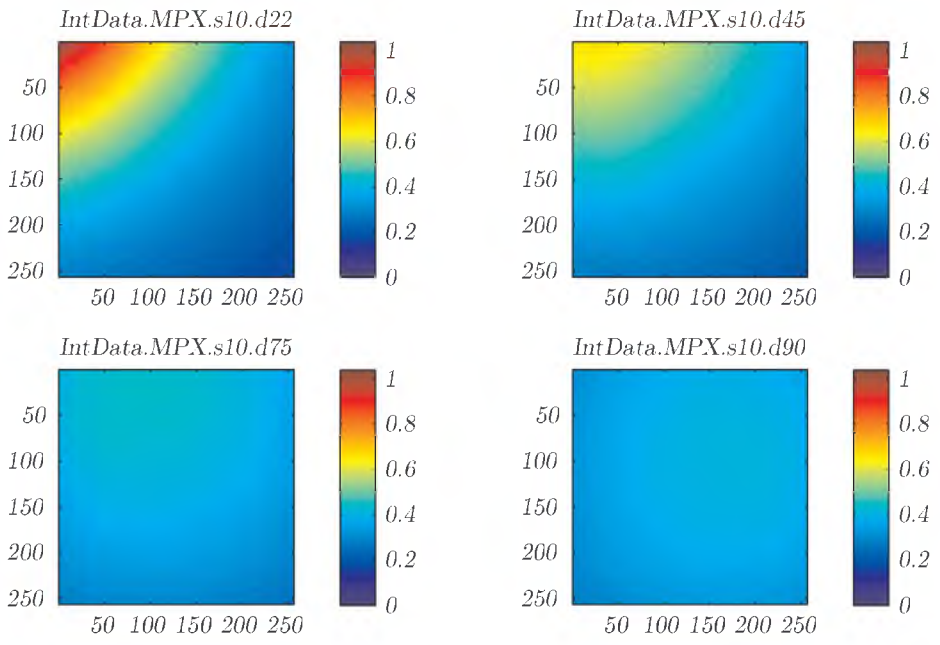

Figure 5.10: Measurements taken using the Medipix2 detector for angular concept verification with $10\times^{125}$I seeds (Oncoseed model 6711) in the ROPES 15 mm plaque. From left to right, top to bottom, the angles used are 22°, 45°, 75° and 90°.

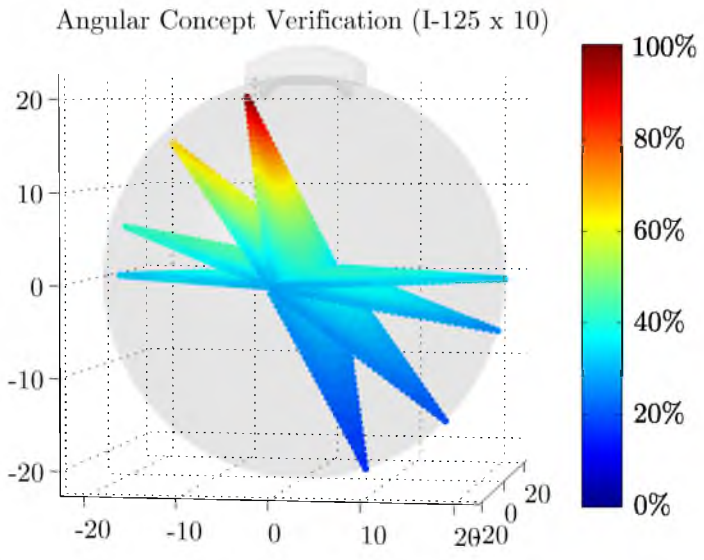

Figure 5.11: Reconstructed volume of the four dosimetric images taken with the Medipix2 with the ROPES 15 mm plaque fully loaded with $10\times^{125}$I seeds (Oncoseed model 6711). Note: plaque and eye phantom not to scale.

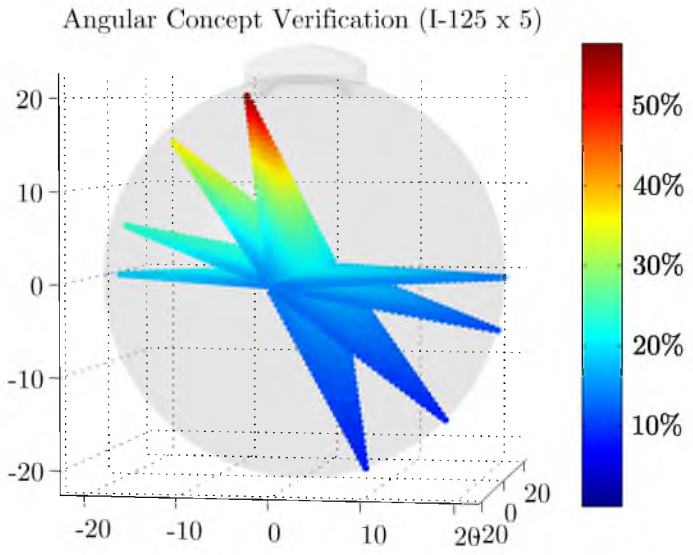

Figure 5.12: Reconstructed volume of the four dosimetric images taken with the Medipix2 with the ROPES 15 mm plaque partially loaded with $5\times^{125}$I seeds (Oncoseed model 6711). Note: plaque and eye phantom not to scale.

minimum plaque-detector distance was inhibited by the phantom size and the inability to measure angles less than 22° due to detector geometry.

5.3.2 Spectroscopic and Counting Operation

Following the proof of volumetric dosimetry, the next aim was to determine whether the event counting operation of the Medipix2 is significantly similar to the time-over-threshold (TOT) (spectroscopy) mode of the Timepix for ^{125}I dosimetry. For verification of the principle, the event mode results are compared to calculations from the TG-43U1 formalism. By providing the equivalent of the total integrated charge generated in each pixel, the operation of the Timepix in TOT mode could be considered to measure charge from the detector in an integral mode by current integration.

Previously, it was established that event counting is sufficient for spectroscopic dosimetry for ^{125}I seed dosimetry in prostate brachytherapy[159]. Due to the ^{125}I spectrum resulting from low energy photons with a relatively narrow energy spread,

radiation hardening[1] effects are not significant across the three major photo peaks, as they undergo similar levels of attenuation. Considering this, a dosimetry system based on an event counting design is feasible and could be developed at a lower cost than would otherwise be possible with a more complex charge measurement (spectroscopy) system.

There was no tissue equivalent material placed below the detector in the first part of this experiment in order to observe the effect of a change in the scattering material present for different orientations of the plaque during a treatment. Placement of the plaque on the eye ball depends on the location of the tumour, for example, posterior or temporal placement. This will result in a relative change in the location and, hence, the effect of the air-eye interface between patient cases. However, tissue equivalent material is used as backing, below the detector, during TG-43U1 comparison.

The translation phantom used in this study improves on the previous, layered design used in Section 5.3.1.1 to result in a design similar to the original concept shown in Figure 5.2a. This improvement gave greater flexibility in plaque-detector distances, rather than being defined by the wax layers, in addition to better tissues equivalence due to the presence of water rather than paraffin wax. Here, the brachytherapy plaque was positioned within a water phantom, with the Medipix detector measuring from below as seen in Figure 5.13. This system used a PMMA column to move the eye plaque through a small, cylindrical water phantom, 100 mm $\times \varnothing$29.5 mm in size. In contrast to the previously investigated method, this system consisted of a stationary detector and a positionable plaque. This allowed the plaque to be surrounded by water for a tissue equivalent environment, whilst keeping the detector and electronics dry and safe. The plaque used was a 15 mm ROPES model fully loaded with $10 \times 390\,\mu Ci$ ^{125}I seeds (Oncoseed Model 6711[187]).

[1] Radiation hardening, or beam hardening, is the process of increasing the mean photon energy of a polyenergic radiation field through the earlier attenuation of the lower energy photons relative to those with higher energies.

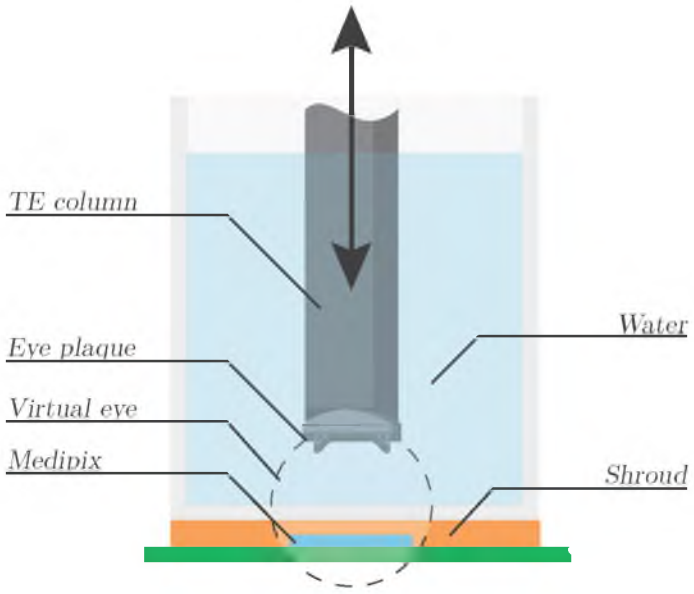

Figure 5.13: A schematic representation of the apparatus configuration including the Timepix detector placement below a water filled vessel.

Fixing the plaque to a linear positioner enabled fine control over the placement of the plaque relative to the detector. It was translated along a vertical axis which was both normal and central to the detector surface. The phantom, a water filled vessel, was placed as close as safely possible to the surface of the detector. The plaque was immersed within the phantom and measurements were taken at discrete intervals between the beginning and final position of the plaque, during which the water volume remained constant. Initially, the plaque was zeroed and aligned at the closest possible point to the detector from within the phantom. Event counting and TOT measurements were taken subsequently at each position using the Timepix, minimising any geometric error between them.

The data collected from the detectors consisted of a 256×256 square array of values for each distance and mode. Each acquisition was taken over a period of 500 s, which was composed of the integration of 500×1.0 s acquisitions. This was sufficient to prevent counter overflow for the given source activity and provided low counting uncertainties (less than $\sim 1\%$).

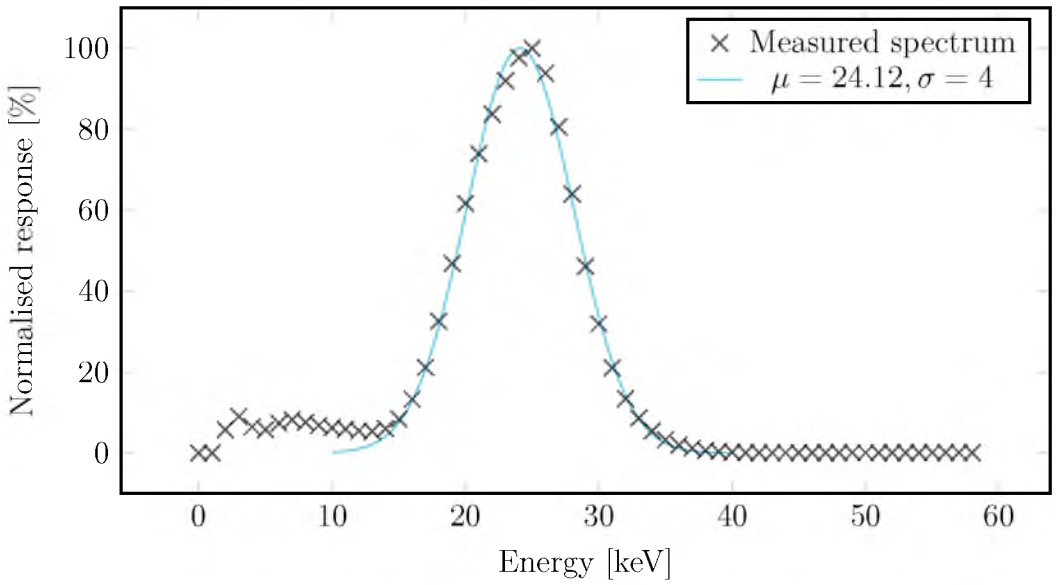

Figure 5.14: Spectrum of 10 $\times^{125}$ I seeds in ROPES plaque taken with Timepix in TOT mode. The phantom included the presence of backing material and the detector was located 2.4 mm from the source. The fitted curve is gaussian and represents the combined peaks of the ^{125}I spectrum.

Since total energy deposition was measured in TOT mode, pile-up events had no detrimental effect on the outcome. Whether a measured charge pulse event originates from a single or multiple incident photons (pile-up) does not effect the integrated TOT value[201]. The source activity gave a count rate of 121 events/pixel/second, which falls far below the maximum count rate (1 MHz) or count depth ($2^{13} - 1 = 8191$) of the Medipix2, and thus neither pile-up nor overflow effects were present in event count mode.

Prior to conducting the measurements, the Medipix detector was calibrated to significantly reduce noise and equalise pixel response. Through the Pixelman software (v1.9.2 working, b.2008-04-03)[202], the dedicated 8 bit global threshold for all pixels and the 3 bit fine tuning threshold for individual pixels were adjusted down to the noise floor[203]. Figure 5.14 shows an example of the ^{125}I plaque spectrum measured within the phantom that used backing material. It was measured using the Timepix in TOT mode and illustrates the lack of a significant presence of low energy noise due to the

threshold equalisation process. The individual spectral peaks of the ^{125}I spectrum in Figure 5.14 have been lost by scattering though the phantom. The sampling parameters for Medipix and Timepix are presented in Table 5.1.

To generate the depth-dose curve for analysis, a 10×10 sample was taken from the centre of each of the matrices and the values were averaged. Each pixel had a square pitch of 55 µm, giving the sample region an area of 550 µm × 550 µm. The two sets of points were then plotted against their corresponding depths to generate the depth-dose curves presented in Figure 5.15. The percentage difference of the two curves is presented in the bar graph below with corresponding error to two standard deviations.

The error associated with the event counting data set ranges from 0.45 % up to 1.33 %, though the error bars cannot be distinguished on the plot. The results show that, for the full range of distances measured (2.4 mm – 15.9 mm), event counting and charge mode (TOT) agree to within less than ±0.45 % error. This error linearly decreases in value with increasing distance with an R^2 value of 0.8668.

To allow comparison between event counting mode and the TG-43U1 formalism, a water equivalent environment surrounding the detector and plaque was needed. This was achieved by placing a tissue equivalent block of Plastic Water® below the detector, as per Figure 5.2a. The resulting set of data is plotted against the TG-43U1 formalism calculations in Figure 5.16. This calculation was performed using a software process with superpositioned dose rates along the central plaque axis taken from the individual seeds of the ROPES plaque. Agreement between the curves falls between +25 % and −5 % for all distances. This error increases most substantially for decreasing distances approaching the plaque, less than around 7 mm.

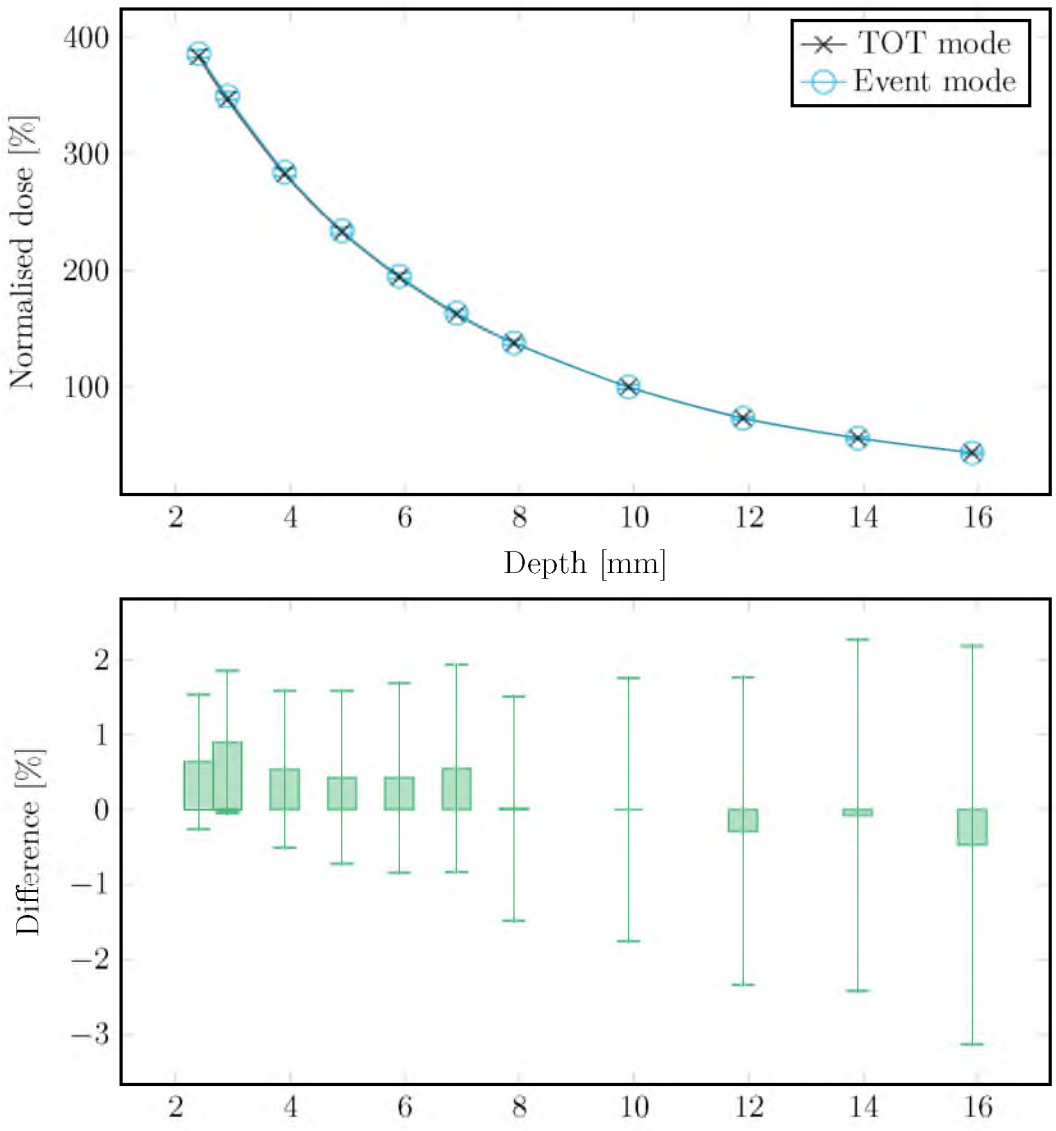

Figure 5.15: The depth-dose curve of both number of events and the total energy of events over 500 s intervals using the Timepix is presented in the top plot. The bar plot at the bottom shows the percentage difference of the event mode / TOT mode and the associated error (2σ). The source was a 15 mm ROPES eye plaque with ten ^{125}I seeds.

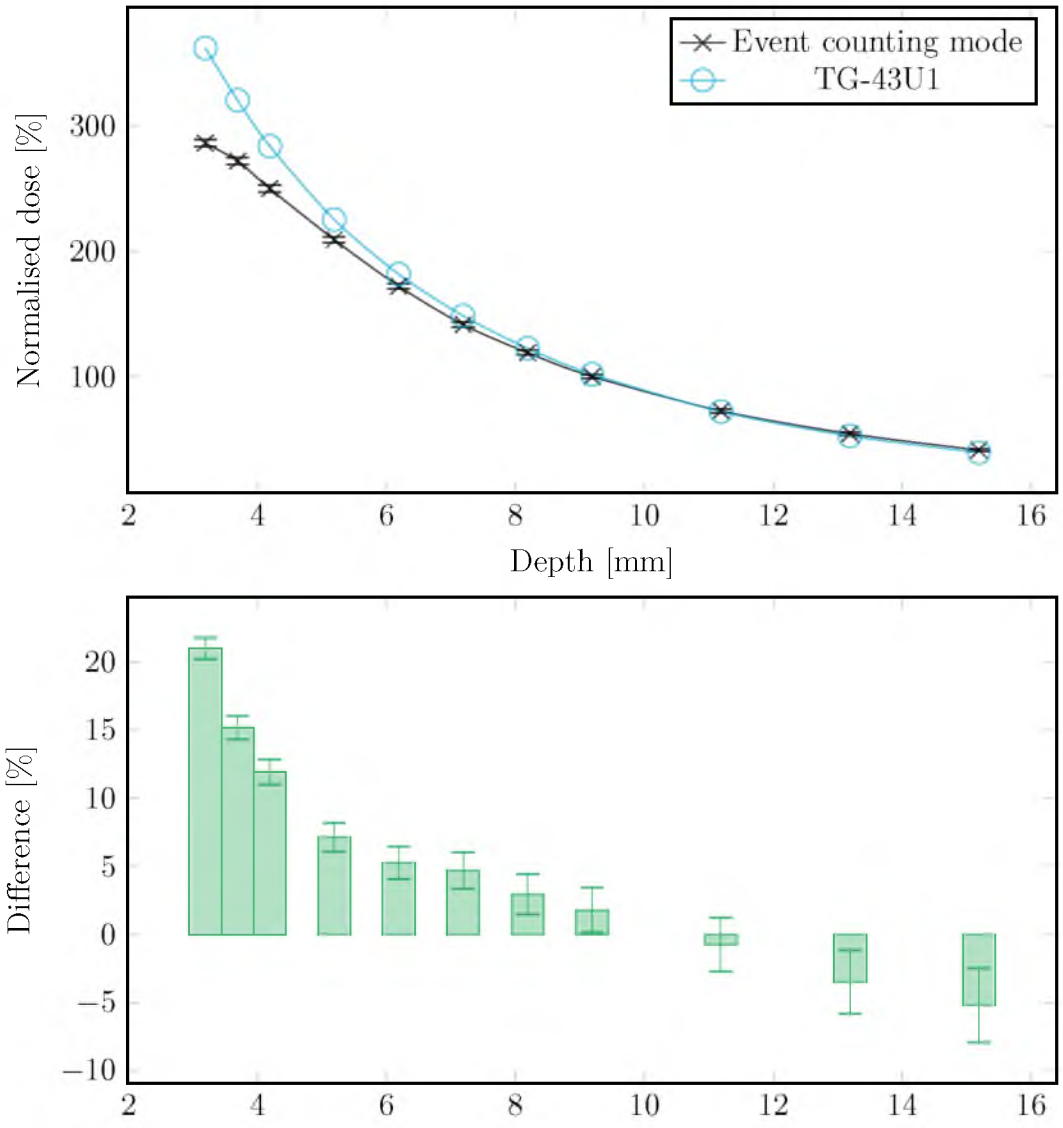

Figure 5.16: The depth-dose curve of event counting mode measurements are compared to the TG-43U1 formalism. The source was a 15 mm ROPES eye plaque with ten ^{125}I seeds. The associated error has a confidence interval of 95 % (2σ).

5.3.3 Seed Variation and Resolution

The next stage of the investigation was to observe the spatial variation in the activity distribution of ^{125}I brachytherapy seeds with the Timepix detector directly. This was conducted to assess the activity variation of seeds between and within two manufacturer seed batches in order to quantify potential uncertainties that may be addressable through a dose verification tool. This study was also used to demonstrate the resolution of the detector to determine its suitability for such a tool.

The seeds were placed on a thin plastic sheet (40 µm thick) on the surface of the Timepix. In order to preserve the anonymity of the manufacturers, they will hence forth be referred to as Manufacturer 1 (M1) and Manufacturer 2 (M2). The sets of measurements consisted of measuring four different seeds for M1 and five different seeds for M2. The seeds were placed on the detector in an approximately vertical alignment, as per Figure 5.17.

The measurements for each seed were conducted in integrating count mode for 500×1.0 s acquisitions. Through image processing in MathWorks Matlab 2012a[199], the seed data was oriented and translated to a common position, vertical and centred. This was achieved through an iterative combination of matrix transformation processes and cross correlation template matching, until an optimal transformation was reached. Once each seed had been reoriented, mean values and standard deviations across the samples were determined for each manufacturer set.

The batch activity of the seeds was 382 µCi for M1 and 215 µCi for M2. The variation in the total activity between seeds was eliminated through the normalisation of the data sets. Given that the average number of counts in the areas of interest was in the order of 250×10^3, the corresponding error is approximately ± 500 counts or ± 0.20 % whilst the mean error in counting across all pixels and measurements was 0.74 %.

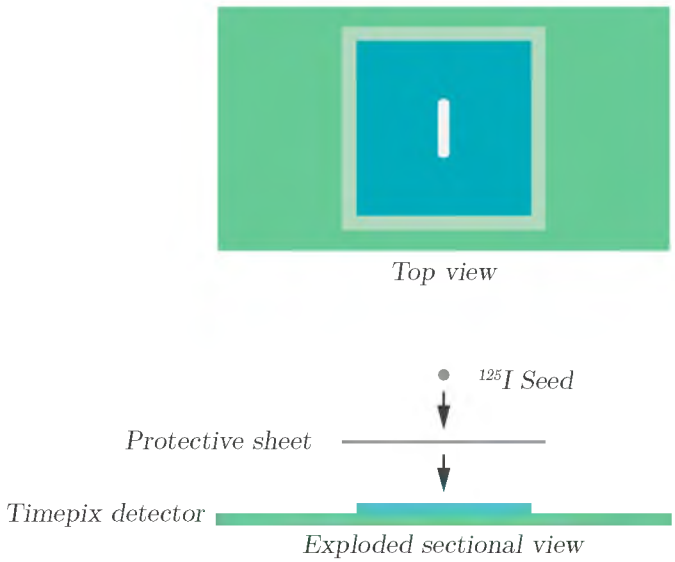

Figure 5.17: A single ^{125}I seed was placed on a thin protective plastic sheet atop the surface of the Timepix detector to measure the dose distribution in count mode.

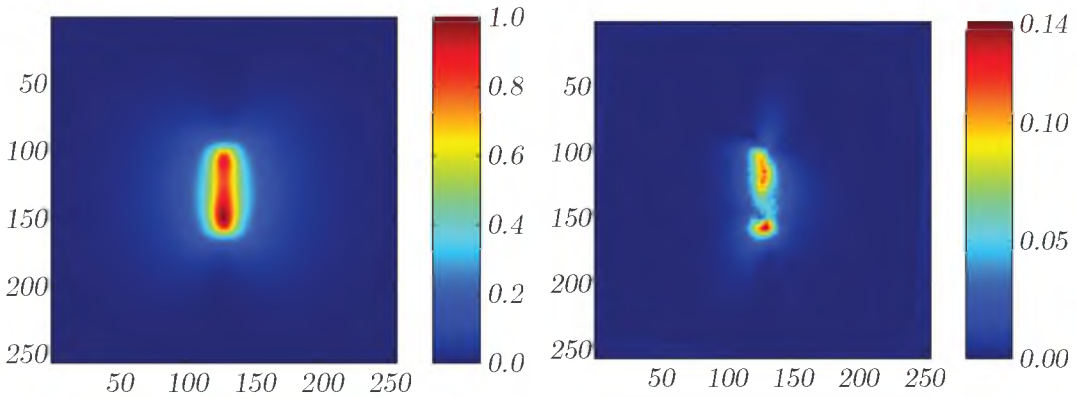

(a) Normalised mean

(b) Std. dev. of normalised seed activities

Figure 5.18: Combined data from four seeds for Manufacturer 1

It can be seen from the plots in Figure 5.18 that the sample of seeds tested from M1 does not yield a uniform activity distribution. The bottom end of the seed ($\sim$ #160 on vertical channels) in the mean activities map for M1 has a significantly higher activity to the top end ($\sim$ #100 on the vertical channels), with a difference of 12.5 %. The section of seed between these points has a relatively lower mean activity. The per pixel standard deviation associated with this sample set indicates a large variation of activity between the seeds, with the greatest discrepancies occurring at the ends of the seed at around 14 %.

The count data measured from M2 in Figure 5.19 on the other hand demonstrates a considerably more uniform seed activity model. There are a lack of obvious activity *hot spots* or *cold spots* occurring anywhere on the mean activities map and the expected anisotropic function is clearly visible. The per pixel standard deviation plot for M2 demonstrates that it features the greatest amount of inter-sample error present at the ends of the seed, and that the sample set overall has a lower error than that of M1 at around 9 %.

The data shown in Figure 5.20 consists of a combination of both manufacturer data sets, giving a total of nine seeds. In the standard deviation map of this data, displayed on the right, it can be seen that the greatest deviations occur at the ends of the seeds at around 21 %. This plot demonstrated the differences in dose distribution that occur between seeds of the same batch and those of different styles. It also demonstrated the potential of high resolution pixelated detectors in dosimetry for plaque brachytherapy.

5.3.4 Resolution Requirements

In terms of retrieving detail from an image, higher resolution generally is preferable. However, image processing complexity, data storage, design complexity and feasibility are less demanding at lower resolutions. Whilst processing power and storage in

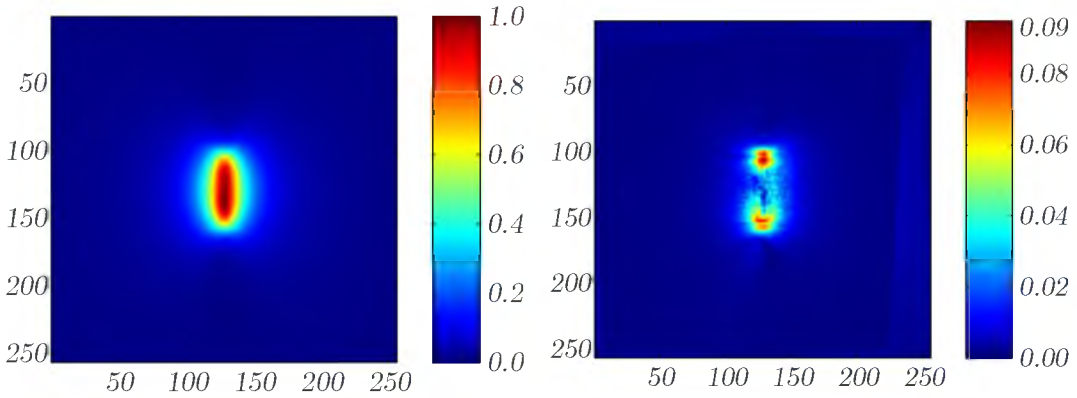

(a) Normalised mean (b) Std. dev. of normalised seed activities

Figure 5.19: Combined data from five seeds for Manufacturer 2.

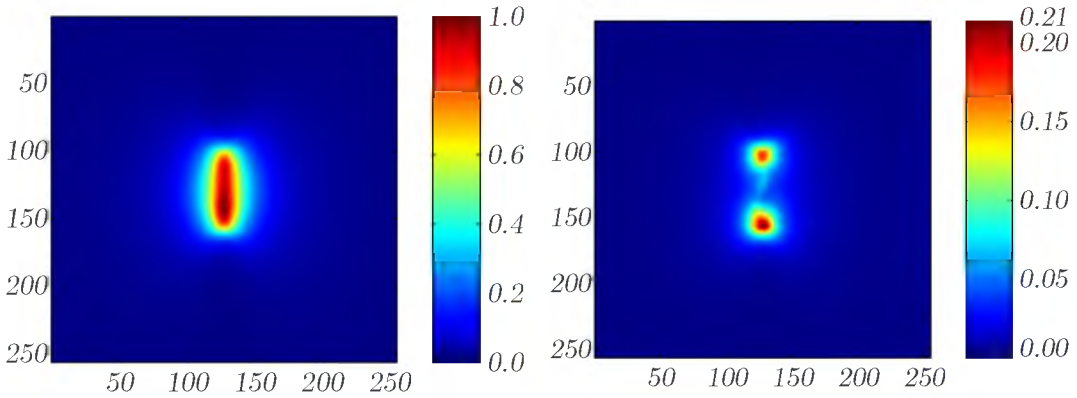

(a) Normalised Mean (b) Std. dev. of normalised seed activities

Figure 5.20: Combined data from nine seeds for both Manufacturers.

current computing technologies are negligible issues for most tasks, limitations can arise regarding design complexity and feasibility. The aim of this study was to estimate and demonstrate the minimum required resolution for use in a dose verification tool for eye plaque brachytherapy.

In this study, a priority of proof of concept and reliability outweigh the need for optimisation and high end system performance. As such, the pixel resolution of the detector need only be adequate enough to resolve the finest details of interest, i.e. dose at the optic nerve ($\sim \varnothing 1.6\,\text{mm}$). According to the Nyquist-Shannon sampling theorem[204], in order to resolve this level of detail a pixel half this size is needed (i.e. 800 µm). This value was selected as an initial design specification and may be refined in later designs.

Data taken from the top and most proximate layer to the plaque in Figure 5.7a was used as an example in Figure 5.21 to indicate the level of detail loss that would occur for a given pixel size. The Medipix2 consisted of 256×256 pixels of $55\,\mu\text{m} \times 55\,\mu\text{m}$ pitch which, considering the sampling theorem, allows resolution of details that are 110 µm in size. As this resolution exceeds the requirements of the system to be designed, downsampling of the image was used to simulate the effect of a lower resolution detector.

Downsampling was achieved by averaging groups of pixels by factors of 8, 16 and 32 to give a new pixel size of 440 µm, 880 µm and 1760 µm, as per Figures 5.21b, 5.21e and 5.21h, respectively. Downsampling an image by a factor of n involved calculating the means of groups of $n \times n$ pixels, at a pitch of $n \times n$.

Table 5.2: Summary of statistics for difference maps generated downsampling with three sampling factors and interpolating back to original size.

Sampling factor	Pixel size (µm)	$\lvert\mu\rvert$	σ %	|max|
×8	440	1.29 %	1.02 %	9.30 %
×16	880	2.59 %	1.87 %	12.85 %
×32	1760	5.03 %	3.66 %	19.37 %

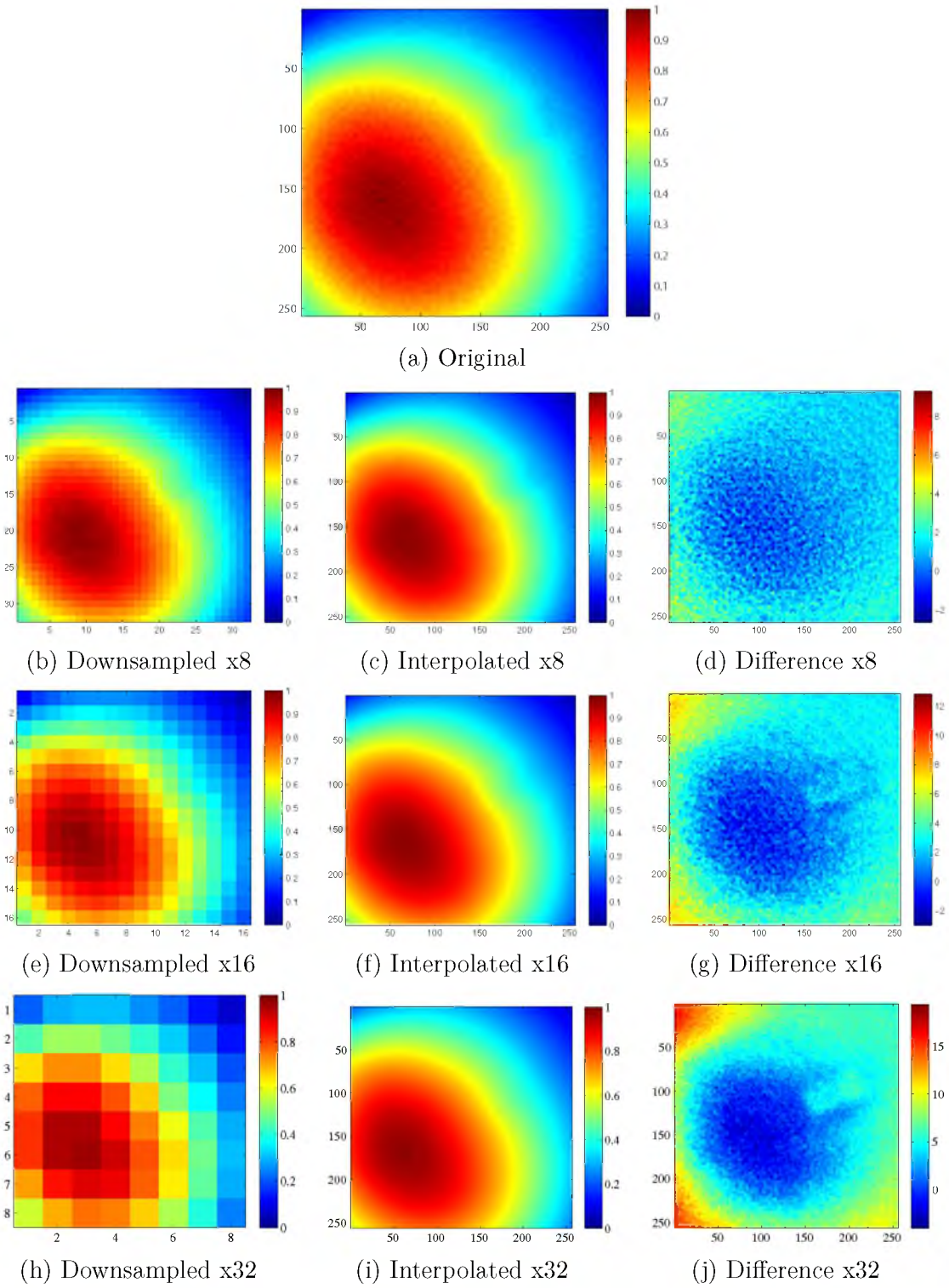

(a) Original

(b) Downsampled x8 (c) Interpolated x8 (d) Difference x8

(e) Downsampled x16 (f) Interpolated x16 (g) Difference x16

(h) Downsampled x32 (i) Interpolated x32 (j) Difference x32

Figure 5.21: Demonstration of the effect of image resampling on a normalised measurement of five ^{125}I seeds. Averaging of pixel groups with three different sampling factors (8, 16 and 32) was used in downsampling and the bicubic method[205] was used for interpolation.

In order to gain some idea of the extent and location of loss of detail from this process, the downsampled images were then interpolated back to original size using the bicubic interpolation method[205] and the differences were shown by subtraction of these from the original image. The interpolated images are shown in Figures 5.21c, 5.21f and 5.21i and their corresponding difference maps are shown in Figures 5.21d, 5.21g and 5.21j, respectively.

Errors between the interpolated and original images are up to approximately 9 %, 13 % and 19 % in localised regions for factors of 8, 16 and 32, respectively. This is particularly prominent in high dose gradient regions around the edge of the images where the interpolation process is less accurate. The mean magnitude of the errors between the images is 1.29 %, 2.59 % and 5.03 % for all pixels, whilst the standard deviation is 1.02 %, 1.89 % and 3.66 % for sampling factors of 8, 16 and 32, respectively. These statistical findings are summarised in Table 5.2.

5.3.5 Backscatter and Phantom Design

The aim of this study was to investigate the effect of backscattering from the material downstream of the detector to better understand the phantom design requirements for the dose verification system being developed as the overall aim of this thesis.

Two sets of measurements were taken with different scattering conditions to determine the effect of eye tissue between the eye-air interface and detector. This was performed using the translation water phantom, the Medipix2 detector, a block of tissue equivalent material and a ROPES 15 mm plaque loaded with ten ^{125}I seeds of activity, 60 µCi each. The apparatus is depicted in Figure 5.22, where the *Virtual eye* represents the equivalent location of the patient's eye during treatment.

Scattering conditions were controlled through the presence of the tissue equivalent material below the detector, labelled *TE backing* in Figure 5.22. The material used was

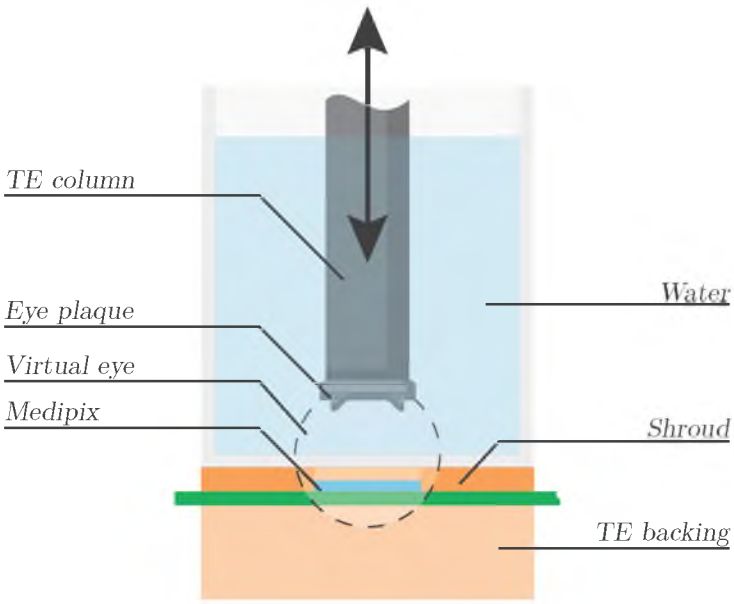

Figure 5.22: A schematic representation of the apparatus configuration for testing the effects of backscattering. The detector is placed below a water filled vessel and above a tissue equivalent (TE) material slab[180].

a 50 mm × 100 mm × 100 mm block of Plastic Water® LR,[180]. A series of measurements were taken for each configuration for plaque-detector distances in the range of 2 mm – 16 mm. Each measurement was the integrated total of 500 × 1.0 s acquisitions.

As per the method used in Section 5.3.2, the central 10 × 10 pixels were averaged for each measured distance and subsequently plotted against their respective distances. This process was performed for both backscatter configurations and the results are displayed in Figure 5.23. In addition to these data series, the percentage increase in counts with the addition of the tissue equivalent material was plotted against the secondary axis in Figure 5.23 for comparison.

Errors in the event count datasets are ±300 µm in distance and range from 0.49 % – 1.29 % and 0.50 % – 1.30 % for configurations with and without backing material, respectively. The addition of backing material caused overall dose enhancement, as expected due to increased backscattering. This enhancement was approximately 3.5 % at 3.5 mm and increased to a maximum of 6.71 % at 5.19 mm. The dose enhancement

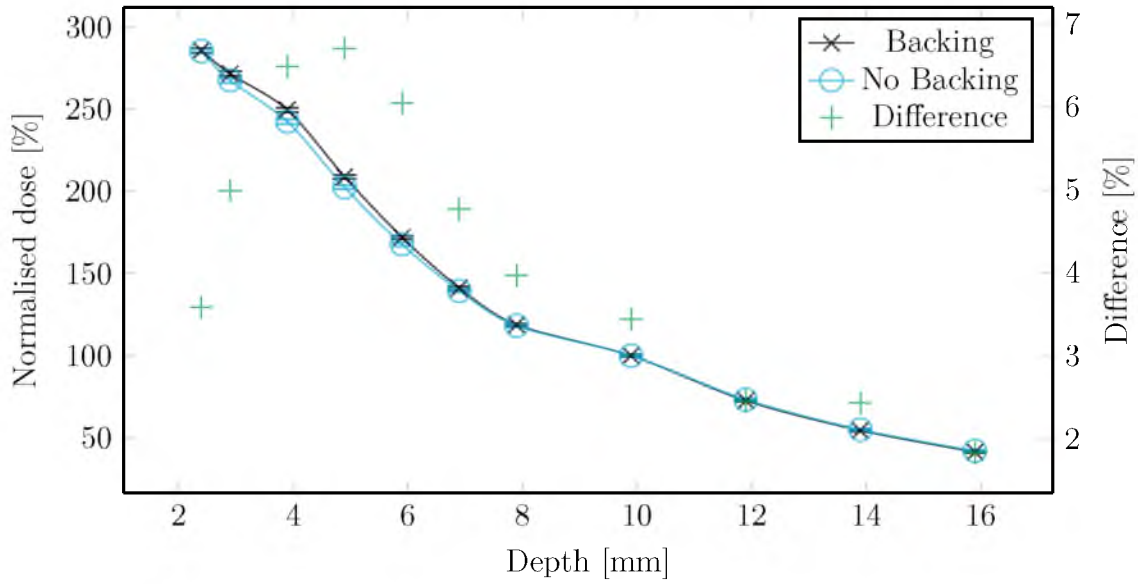

Figure 5.23: The depth-dose response of a 15 mm ROPES eye plaque with and without the presence of a 50 mm tissue equivalent block of Plastic Water® below the detector. The central 10 pixels × 10 pixels of the Medipix2 were averaged for each depth measured.

tapered off towards zero for distances beyond the peak.

5.3.6 Beta Source Evaluation

Ideally, a robust dosimeter for plaque brachytherapy should be able to measure dose from most, if not all, of the different radionuclide sources used in the treatment. Whilst the radionuclide of focus in this study is the low energy gamma emitter, ^{125}I, it was also beneficial to determine the potential and limitations of silicon pixelated detectors for dosimetry of other radionuclides. Therefore, the aim of this study was to measure the accuracy of dose measurement of beta sources using such detectors. The beta emitting plaques from BEBIG[56] are a different style to the ROPES models previously tested, and better suited to small tumours. They consist a of thin layer of ^{106}Ru, electrically deposited on silver foil and encapsulated by a silver backing.

The parent radionuclide, ^{106}Ru has a half-life of 374 d and disintegrates to the

daughter product, ^{106}Rh, via a beta decay (Q value =39.4 keV). The majority of the therapeutic dose is delivered from the unstable ^{106}Rh, which has a maximum energy of 3.54 MeV and a half life of about 30 s.

Using the translation water phantom, described in Sections 5.3.2 and 5.3.5, with Plastic Water[180] placed below the detector as backing material, dose distributions were measured for two types of BEBIG plaques, type CCA and type COB. The CCA-type plaque is circular in shape, with a diameter of 13.5 mm, as depicted in Figure 5.24a. The COB-type plaque is larger at 19.8 mm diameter and has a notch shaped into it, seen in Figure 5.24b.

The measurements involved aligning the plaque normal to the detector plane by, first, resting it on a flat block with the suture eyelets overhanging the corner so as not to impede its orientation. The plaque was then fixed to a vertical PMMA tube using the suction of a vacuum pump to seal against its smooth outer surface. A linear positioner with micrometre precision was used to support the tube over the phantom and detector.

Lateral orientation was achieved by positioning the plaque over the detector as close as the plaque's suture eyelets would allow from within the phantom. With the Medipix detector sampling at a frame rate of about one frame/second the lateral position was

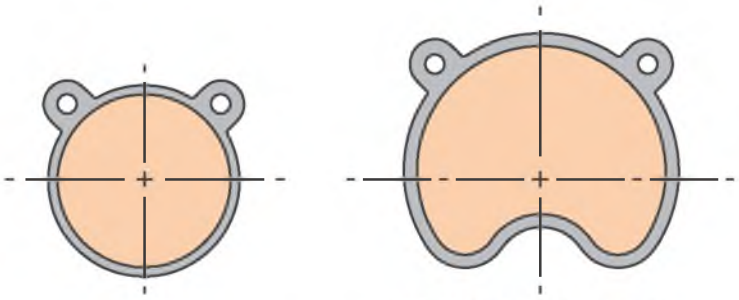

(a) CCA (⌀15.3 mm) (b) COB (⌀19.8 mm)

Figure 5.24: Geometric shape of BEBIG plaques which have a thin film of ^{106}Ru deposited onto a silver backing. The radioactive area is marked in colour. Adapted from Eckert & Ziegler BEBIG GmbH[56].

adjusted accordingly, until centralised.

The Medipix detector was used to take the integral of $500 \times 1.0\,\mathrm{s}$ acquisitions at incrementally increasing depths from within the water phantom. This ensured that enough statistics were taken to obtain uncertainties of less than $\sim 1.5\%$ for regions of interest. There were a total of 17 measurements with absolute distances ranging from 3.0 mm – 28.2 mm ($\pm$500 µm for the group, $\pm$500 nm between individual measurements). After zeroing to the minimum range, the positioner was used to adjust the distance. Figures 5.25a and 5.26a show the dosimetric images at the closest position for CCA and COB type plaques, respectively. The images were normalised to their respective dose maximums.

For comparison, the Plaque Simulator 5.0.0 software by BEBIG[22] was used to generate dosimetric images of both plaque types at a distance of 3 mm. These images are displayed in Figures 5.25b and 5.26b for plaques types CCA and COB, respectively.

The image from the CCA plaque in Figure 5.25a shows that the plaque was centrally aligned to the detector and that the dose distribution increased to a maximum in the centre. In comparison, the dose map produced by the software shows a much more uniform distribution in the central region, with a drop off occurring at around 4 mm – 5 mm.

In Figure 5.26a the dose distribution from the COB type plaque is non-uniform with maximums at two hot spots located symmetrically on either side of the notch. The area between is approximately 70 % – 80 % of the maximum dose. The dose map from the corresponding Plaque Simulator COB-type plaque output is shown in Figure 5.26b. It has a much more uniform coverage in a crescent moon shape ("$\frown$").

At locations centred through the points of interest annotated in Figure 5.25a and Figure 5.26a, the mean value of 10 pixels $\times$ 10 pixels were calculated for each depth. Depth-dose plots were generated for the CCA-type plaque and the COB-type plaque,

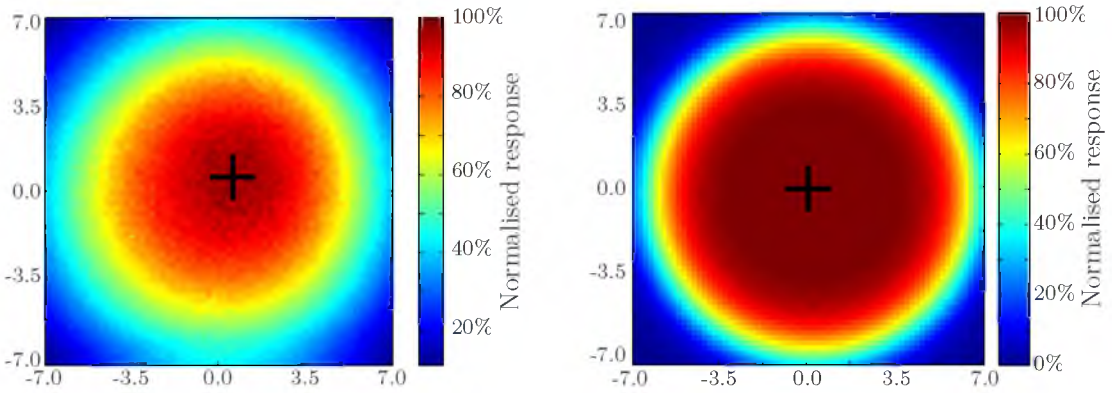

(a) Measured (b) Plaque Simulator

Figure 5.25: Dosimetric images taken at 3 mm for measured and calculated BEBIG CCA-type plaque, with distances in millimetres. The black cross on the measured image indicate the points of interest taken for the depth-dose curve.

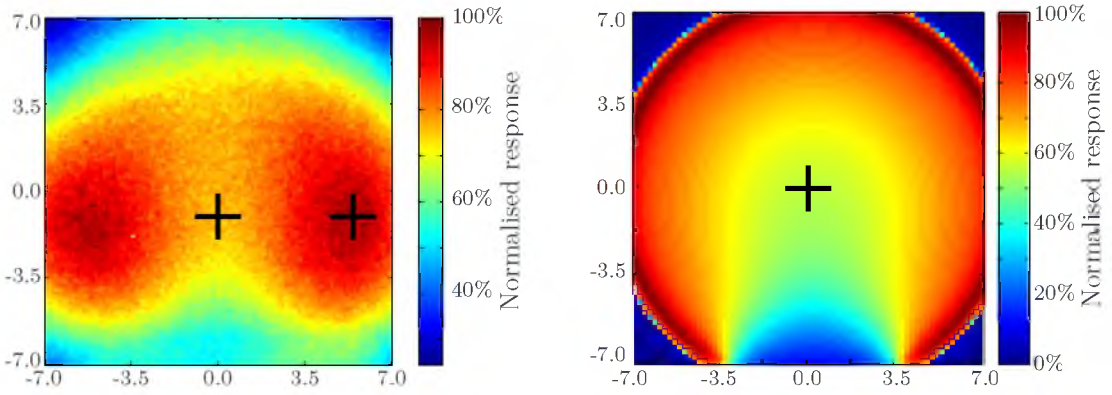

(a) Measured (b) Plaque Simulator

Figure 5.26: Dosimetric images taken at 3 mm for measured and calculated BEBIG COB-type plaque, with distances in millimetres. The measured COB-type plaque shows two hot spots (red) instead of the expected "⌒" shape, resulting from non-uniform deposition of the radionuclide. The black crosses on the measured image indicate the points of interest taken for the depth-dose curve.

respectively. Two depth-dose curves are displayed for the COB type plaque, one through the geometric centre of the plaque and the other through one of the hot spots. Depth-dose curves for each plaque were also generated using Plaque Simulator 5.0.0. The curves were taken through the central axes of each of the two plaques, and were plotted on the same graphs as their corresponding measured plaque types. The manufacturer uncertainty of 20 % (2σ)[206] has also been plotted for each point. The curves were normalised to 100 % at 7.7 mm for the central axes.

Figure 5.27 shows that there is excellent agreement between the measured and calculated CCA-type plaque, within the manufacturer range of error. The overlapping distances between the methods covered the range of 6.5 mm – 12.0 mm, with 12 mm being the centre of the eye.

The divergences are larger between the measured and calculated COB-type plaques, as displayed in Figure 5.28. Here, the difference between the plots exceeds the uncertainties for the data and the curves exhibit dissimilar dose rate gradients. The measured difference between the maximum value of the hot spot recorded and that of the centre of the plaque is approximately 20 %.

5.4 Discussion

The feasibility of using a pixelated silicon detector for plaque brachytherapy dosimetry was tested using the Medipix family of detectors. This was done by evaluating two potential designs, the translation concept and the rotation concept. In addition to this, a number of investigations were undertaken; the suitability of event counting for ^{125}I dosimetry; variation in seed dose distributions; resolution observations; the effect of backing scatter in a phantom; and finally, the dosimetry of beta-emitting plaques.

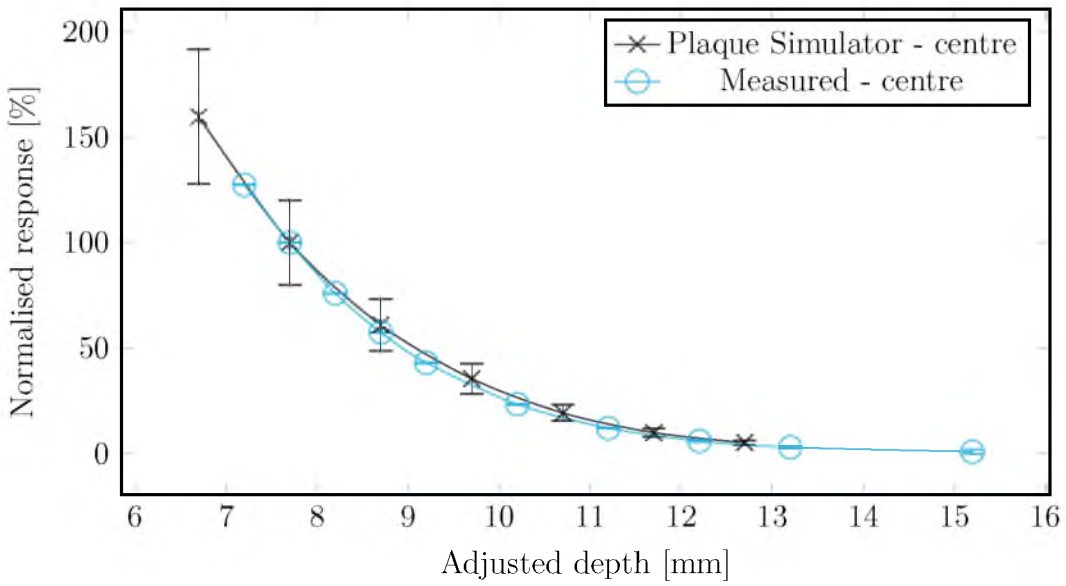

Figure 5.27: Depth-dose curves for measured and calculated CCA-type plaques. The curves are taken through the points of interest marked in Figure 5.25. Distances are measured from the central axis of the inner surface of the plaque.

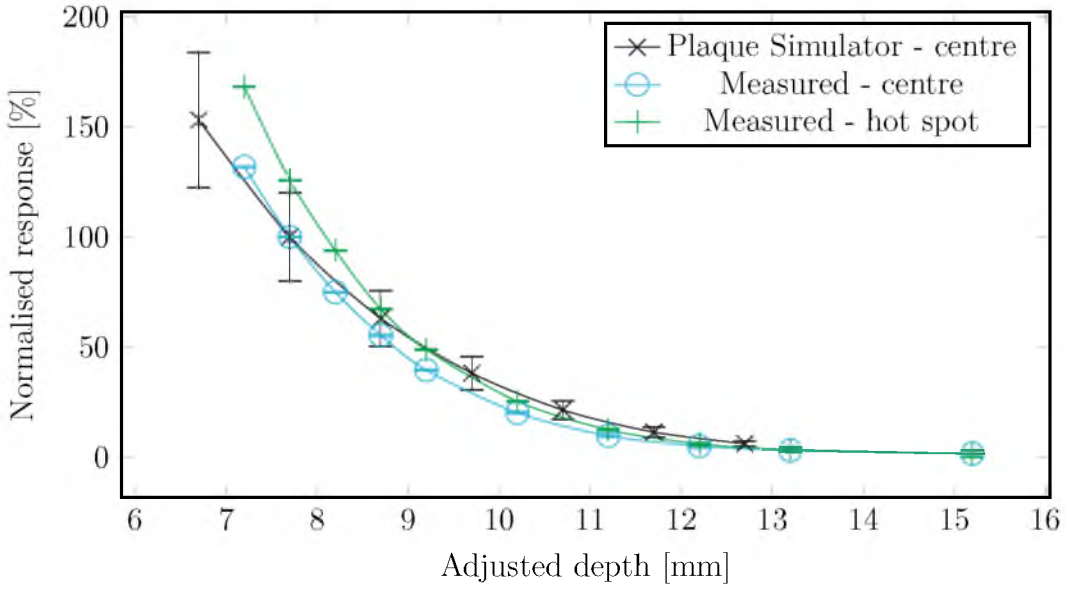

Figure 5.28: Depth-dose curves for measured and calculated COB-type plaques. The curves are taken through the points of interest marked in Figure 5.26. Distances are measured from the central axis of the inner surface of the plaque.

5.4.1 Translation Concept

The translation concept study attempted to determine the suitability of a pixelated detector in generating a dose volume from a collection of planar dose slices with enough resolution and timeliness for practical clinical use.

Pixelated detectors proved to be well suited to volumetric dosimetry. The dose volumes produced were intended as demonstrations of the concept and clearly showed a high level of detail in the detector plane. Beyond simple recognition of asymmetric differences between the two plaque configurations tested, the resolution would enable finer features to be resolved. The phantom only allowed for five measurements, though isosurfaces were generated by interpolating the results. These results indicated that the concept could act as a platform from which a preoperative dose verification system can be designed. Ideally, this three dimensional data would be directly compared to the treatment plan from within a treatment planning system such as BEBIG's Plaque Simulator.

The layered translation phantom required the manual placement of the detector at a specific distance within the phantom layers. This process was labour intensive and as a result was time-consuming and prone to human error. The layered design also limited the plaque-detector distances to discreet values and inherently limited the vertical resolution of the system. In such a system, the number of phantom layers used is proportional to procedural time and increases the likelihood of introducing inter-layer displacement error.

From this early design, it was suggested that future translation phantoms use a water bath and a method of controlling the plaque-detector distance such as that depicted in the original concept in Figure 5.2a. Submersion of the plaque in water, whilst offering excellent tissue equivalence, may be a clinical concern for contamination. Modified sterilisation procedures would need to be adopted as the result of such a design.

Whilst the translation water phantom approach to dosimetry offers a geometrically simple solution, it cannot easily measure critical surface doses of the plaque itself without a significant detector redesign.

5.4.2 Rotation Concept

Images generated from the Medipix detector in the rotation phantom were used to produce a simple dose volume. Whilst the number and orientations of measurements were strictly limited, the overall outcome showed the rotation based volumetric dosimetry of eye plaques is viable. Section 5.3.1.2 also showed that conventional pixelated detector geometry would need to be significantly modified to accommodate the shape of the plaque, as the square Medipix designed used prevented both surface measurements and acceptable coverage.

In some ways, the concept of the rotation phantom, is advantageous over the translation phantom for volumetric plaque dosimetry, despite the limitations of the investigation. The major foreseeable concern with the translation phantom concept is that it lacks the ability to measure dose at the inner surface of the plaque. This is a region of interest for clinicians and the TG-43U1 formalism[20] does not effectively handle it. Additionally, the dose rates closest to the source are those which are both the greatest and have the steepest dose gradients. It is essential to understand the dose to this region of the eye as the outer scleral dose can be many times greater than the prescription dose[207].

The ideal detector design would neatly sweep across the inner surface of the plaque, providing surface dosimetry of the plaque. Further improvements to this rotary phantom design would include a reduced and adjustable plaque-detector angle increment in addition to automated positioning.

5.4.3 Spectroscopic and Event Counting Dosimetry

The TOT and count mode data depicted in Figure 5.16 demonstrate very strong similarities to each other but strongly disagree with the TG-43 protocol for distances less than $5mm$, as expected. The development of a dosimetry system based on the Medipix2's event counting mode would be a cheaper and simpler alternative to one based on the spectroscopic capabilities of Timepix. This is possible because the spectra of ^{125}I does not change considerably with depth.

The discrepancies between the measured data and the TG-43U1 formalism curve can be explained due to the limitations of the TG-43U1 formalism. This is primarily due to its inability to account for material heterogeneities, most significantly, the metal plaque backing. In this case, the backing causes a dose reduction due to its absorption of the otherwise backscattered radiation. This outcome has been reported in the literature[70,84,108–114,149] with mixed results.

5.4.4 Seed Activity Variation and Dosimetry

From this study of the dose distribution of seeds between and within the same manufacturers, it can be seen that the standard deviation of the ends of the seeds is much greater than other areas. Standard deviation was also greater in the seeds from M1 in comparison to those of M2. This could in part be due to the lower numbers of seeds measured or a product of the manufacturing and certification processes.

This study was aimed at illustrating the potential for seed-to-seed variation, both between manufacturers and within manufacturer batches. Whilst the number of seeds measured in this study limits its overall significance, the results of the study show that dose distributions vary within seed batches and between manufacturers; an effect that cannot be accounted for in the TG-43U1 formalism. It stresses that a reliable preoperative dose verification tool capable of measuring close to the plaque surface is

required to reduce these types of uncertainties and ensure better treatment practises.

5.4.5 Resolution Requirements

The Medipix2 detector is a high resolution instrument capable of resolving details down to 110 µm. For the development of a preoperative dose verification system prototype, however, this level of resolution would be superfluous for a new detector design.

Three sampling factors were assessed, namely 8, 16 and 32, and resulted in reconstruction that produced differing levels of recoverable detail. From the summary in Table 5.2, higher factors for sampling led to a greater level of loss in recoverable detail, as expected. The sampling factor that corresponded to pixels of 880 µm (sampling factor 16) was the most clinically achievable considering the trade off between technical challenges, cost and required resolution.

Interpolation was used to restore downsampled images back to their original resolution, albeit at the loss of detail. Figure 5.21g illustrates that for a sample factor of 16 the worse discrepancies ($\sim 12.9\,\%$) in reconstruction occurred at the image edges, where the interpolation boundary points were missing. The mean of the discrepancy magnitudes for this sample factor was relatively low at 2.59 % in comparison to other errors in the treatment process, including seed variation (up to around 9 % – 14 % at 1σ) and planning calculation limitations, meaning that interpolation could be used if needed. These values are strongly dependant on the level of recoverable detail required.

The proposed detector design should have a resolution of around 1 mm and, whilst interpolation of data is possible, there are inherent risks of misrepresentation of data. For the volumetric dosimeter concepts presented in this chapter, resolution would be adjustable in the direction of motion.

5.4.6 Backscatter and Phantom Design

From the similarities observed in the depth-dose responses of the backing investigation, it can be seen that additional material placed below the detector influences the dose received in the detector for small plaque-detector distances. This had maximum effect at a distance of around 5 mm with a difference of close to 7 %.

Due to the likely dominance of pre-existing backscattering through the silicon detector and PCB, differences at close distances are not as large. The data points monotonically decrease for distances greater than 5.19 mm due to the short range of backscattered radiation from the ^{125}I source. In practical dosimetry, the detector should be used in conjunction with a tissue equivalent material to account for the backscatter.

Further study into the geometry of the vessel used for the water phantom should also be undertaken to investigate side scatter. Ideally, the phantom shape in general should be adapted to suit a given tumour location, as the distance and orientation of the eye-air interface will vary between cases. This is a complex problem, however, and Monte Carlo simulation for optimisation and a modifiable or modular design of the phantom for such a dosimetry system would be useful. This is another reason for the discrepancy from the TG-43U1 formalism with experimental measurement because TG-43U1 assumes an infinite water environment, which is clearly not the case during the brachytherapy treatment.

The dose verification system designed as the main aim of this thesis should incorporate tissue equivalent material around the detector in a manner that permits further investigation into backscattering, accounting for the eye-air interface where possible.

5.4.7 Dosimetry of Beta-Emitting Plaques

Beta-emitting plaques are generally the preferred plaque brachytherapy method for treating shallow tumours. The two styles tested in this investigation were the CCA-type and COB-type BEBIG plaques. Dose distributions of the CCA-type plaque, which is circular in shape, are relatively simple in comparison to the COB-type plaque which features a notch enabling it to be used for tumours that are close to the optic nerve.

The CCA-type plaque calculations from Plaque Simulator 5.0.0 correlated well with the measured dose planes. The depth-dose curve matched to within the manufacturers indicated level of uncertainty (20 % 2σ) for all distances measured. The calculated dose plane depicted a dose profile with a much flatter top than that measured, illustrating differences in the dose distributions.

The measured dose map for the notched COB-type plaque showed two distinct hot spots in contrast to simulations from the literature[206] and the dose plane produced using Plaque Simulator, where crescent moon shaped distributions were evident. Measurements by the manufacturer also showed that the dose distribution on the surface of the COB-type plaque was non-uniform[206]. It is likely that this is due to the non-uniform deposition of the radionuclide on the plaque.

The design of plaques require that they feature suture eyelets, making them poorly suited for close measurements with planar detectors. These suture eyelets prevent the detector from being placed normal to the plaque central axis closer than distances of about 6 mm to the central surface. Given that the majority of tumours treated with the ^{106}Ru plaques are less than 5 mm in thickness, the device offers little practical use for them. A refined detector design is needed for the measurement of dose close to the plaque surface, such as that proposed in the rotation concept.

The uncertainty in dose distribution demonstrated in this beta-emitting plaque study show that there is significant benefit to gain from the use of a preoperative dose

verification system that is capable of mapping near surface doses.

5.5 Conclusion

Two concepts were investigated for using pixelated silicon detectors for volumetric dose verification in plaque brachytherapy, the translation and the rotation concepts. Several other aspects were also studied to provide additional design specifications for the ultimate development of a plaque dosimetry tool.

The concept studies demonstrated the feasibility of their physical development and general operation. The translation concept consisted of translating a two-dimensional detector plane normal to its surface to create three-dimensional dose distributions of a plaque. The rotation concept, in contrast, involved the rotation of a detector plane about itself to create three-dimensional dose distributions of a plaque. Both the experimental procedures required a significant amount of handling and their dosimetric coverage was spatially limited in design. Whilst results were promising, both phantom solutions were suboptimal. A water phantom modification was suggested and implemented for further translation based volumetric dosimetry. The rotation based phantom needed to be optimised through the redesign of the detector shape.

Using the modified translation water phantom, the event counting mode of the Timepix detector was compared to its time-over-threshold (charge) mode for the measurement of ^{125}I plaque dosimetry. The depth-dose results showed excellent agreement between the two methods. Event counting mode was used with tissue equivalent backing material and the water phantom and compared to the TG-43U1 dose calculations for a 15 mm ROPES plaque fully loaded with ^{125}I seeds. Dose enhancement occurred at distances close to the plaque due to TG-43U1 not accounting for heterogeneities including the metal plaque backing.

Two batches of seeds from unnamed manufacturers were tested using the Medipix2

detector for the investigation of intra-batch and inter-batch variations. The dose images from the Medipix clearly depicted the anisotropic dose functions of the seeds. The maximum standard deviation of one set of seeds (M1) was about 14 % while the other was about 9 % (M2), and the maximum discrepancies in the seeds occurred at their tips. This study illustrated that benefits could be gained from preoperative dose verification by minimising source uncertainty.

The Medipix family of detectors used in this concept study had very high resolution, and while it could be of great benefit in plaque dosimetry, their design inherently inhibits their use in the rotation concept by preventing scleral measurements at the surface of the plaque. By downsampling, bicubic interpolating and comparing a measurement taken using the Medipix2 to its original, for several sampling factors the loss detail was examined. When optimised by Nyquist theory for resolving dose to the finest features in plaque brachytherapy ($\sim 1.6\,\mathrm{mm}$), 800 µm was considered an acceptable initial resolution for detector design. Though it is image dependant, the mean error in reconstruction for pixels downsampled to a resolution of 880 µm was 2.59 %, and showed that lower resolutions would still be useful.

The effect of the presence of tissue equivalent material below the detector was investigated and shown to strongly effect dose. A block of Plastic Water® increased dose by up to nearly 7 % at around 5 mm from the plaque. This supports the need for the development of reliable dose verification tools for eye plaque brachytherapy, which could measure such discrepancies if plans are incorrect.

Two types of BEBIG, beta-emitting plaques were tested to observe the effectiveness of dosimetry using silicon pixelated detectors. The CCA-type plaque showed agreement within manufacturer uncertainty to the depth-dose curve generated using Plaque Simulator. The COB-type showed an unexpected dose distribution featuring two hot spots and a depth-dose curve that did not correlate well to calculated values. Dose

verification close to the plaque surface would be useful for overcoming the fabrication induced activity uncertainties and non-uniformities.

By incorporating the outcomes of this concept study, the development of a fast, three-dimensional, preoperative dose verification system for plaque brachytherapy is feasible. Details of the design and further development of such a system, called the PANOPTES, are presented in the following chapter.

Part III

The Panoptes

Chapter 6

Design and Development

The previous part of this thesis consisted of two chapters which were used as proof of concept studies for the development of a preoperative dose verification system for plaque brachytherapy. The chapters showed that single silicon *p-i-n* diode detectors were well suited to point based dosimetry and that the further developed concept of pixelated silicon detectors offers much in the way of volumetric dosimetry. In this final part (Part III) of the thesis, the design, development and evaluation of a pixel array detector system, called the PANOPTES (Pixelated, Automated Nuclear Ophthalmic Plaque Treatment Evaluation System) is presented.

The translation and rotation dosimetry concepts investigated in the previous chapter were used as a basis for the PANOPTES design. This chapter details the design and development of the custom pixelated detectors, electronics, phantoms and graphical software interfacing for the PANOPTES. A photograph of the assembled hardware is shown in Figure 6.1. A diagram of the system components and their relationships is provided in Figure 6.2.

The detector design and fabrication was critical for the overall success of the project. It was carried out after the readout electronics had been selected, and prior to the design and development of complementary systems. Specifically, the detector design

Figure 6.1: Photograph of the PANOPTES showing the detector board fixed within the positioning system (*left*) and the main electronics enclosure (*right*) which contains the power supply and interface boards.

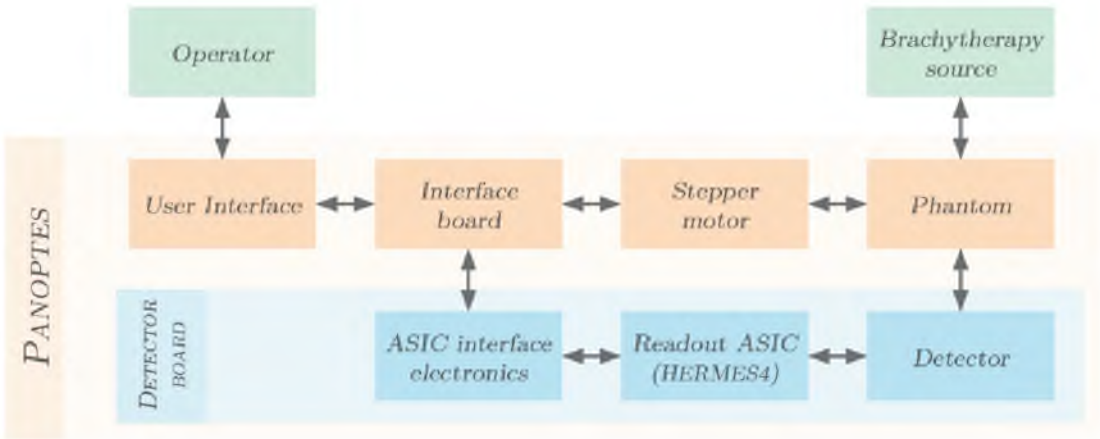

Figure 6.2: Overview of the PANOPTES subsystems

for the PANOPTES was investigated for both of the volumetric acquisition concepts considered in Section 5.2. However, the rotation based concept was pursued exclusively as it demonstrated greater potential for dose volume coverage near the plaque surface.

Design of the electronic systems followed the detector and included the detector board, interfacing board and power supply board. The detector board featured multiple front-end mixed-signal readout ASICs and provided power and signal routing to them. The detector board was interfaced to a central control board which used a field programming gate array (FPGA) for control processing. It managed data handling and controlling acquisitions on the detector board, routed information to and from the software interface and controlled a stepper motor positioning system.

Concurrent to the development of the electronic systems was the phantom design. It consisted of a single piece of 3D printed material shaped as a hemisphere and, beyond its dosimetric purpose, filled the secondary role of protecting the sensitive electronics.

The software interface was written to provide a means for the operator to control all acquisition parameters and take measurements. It allowed for tasks such as controlling sets of automated measurements, single channel analysis of sources and visualisation of measured data.

6.1 Detector Design

The PANOPTES project involved the investigation of two approaches for dose volume acquisition and this required two individual designs of pixelated silicon detectors. The first was designed for the translation based concept and was rectangular in shape and bore 127 pixels. The second was designed to suit the rotation based concept, was semicircular in shape and consisted of 64 pixels comprised of two different sizes. A photograph of the two detector designs is presented in Figure 6.3.

The detector wafer consisted of 300 µm thick, bulk n-type silicon. The detector

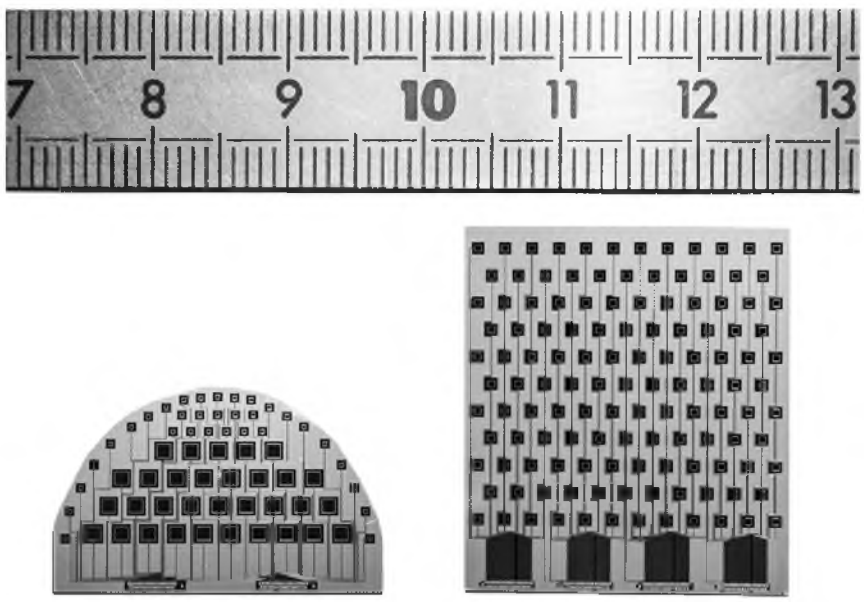

Figure 6.3: Photograph of the silicon pixelated detectors, showing the rotation based design on the left and the translation based on the right. Ruler units are in millimetres.

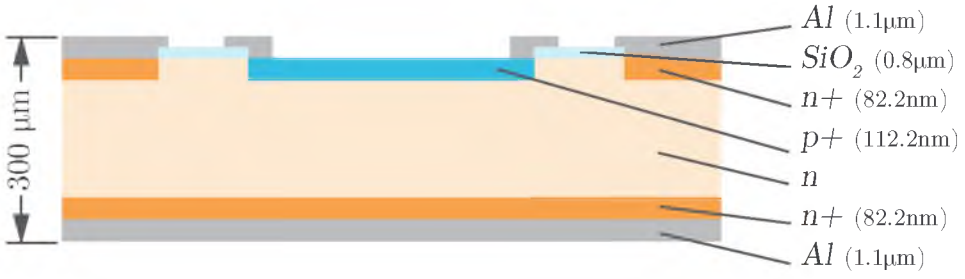

Figure 6.4: Cross-section of a single diode of the detectors

geometry and implantation parameters were designed at the CMRP, University of Wollongong and the masks were produced and the detector fabricated at the CMRP microelectronics foundry, SPA BIT. All of the detectors in both designs were of *p-i-n* diode structure, as depicted by the cross sectional view in Figure 6.4.

The pixels featured *p+*-type silicon implanted with boron at $E = 30\,\text{keV}$ and a dose of 5×10^{15} ions/cm^2, which gave an ionisation depth of 112.2 nm[208]. An *n+*-type silicon layer was present in all other regions on the top and bottom detector surfaces. It was implanted with phosphorus at $E = 60\,\text{keV}$ and a dose of 50×10^{15} ions/cm^2, giving a depth of 82.2 nm[208]. The aluminium metallisation layer had a thickness of 1.1 µm and the silicon oxide, 800 nm. In all cases projection masks were used, and the fabrication processes used 1 µm technology.

Aluminium contacts were used to route the signals to groups of bonding pads at the edge of the detector. The output bonding pads were designed to match the 32 input pads of the front-end mixed-signal ASIC, as discussed later in Section 6.2.1.1. Multiple ASICs were needed to accommodate the number of pixels on each of the detectors; four for the translating detector and two for the rotating detector.

The detectors both featured bonding pads on the top to connect to the aluminium surface, and hence the underlying *n+*-type region, for applying a bias voltage. Similarly, the bottom of the detectors had an aluminium layer, connected to the other *n+*-type silicon region. The bias voltage could be applied through this layer via a conductive glue to a printed circuit board pad.

6.1.1 Rotation Based Detector

The rotation based concept required that the detector be designed with a semicircular shape to allow it to fit closely within the inner radius of an eye plaque, as seen earlier in Figure 5.3a. The silicon detector was cut multiple times from an originally square

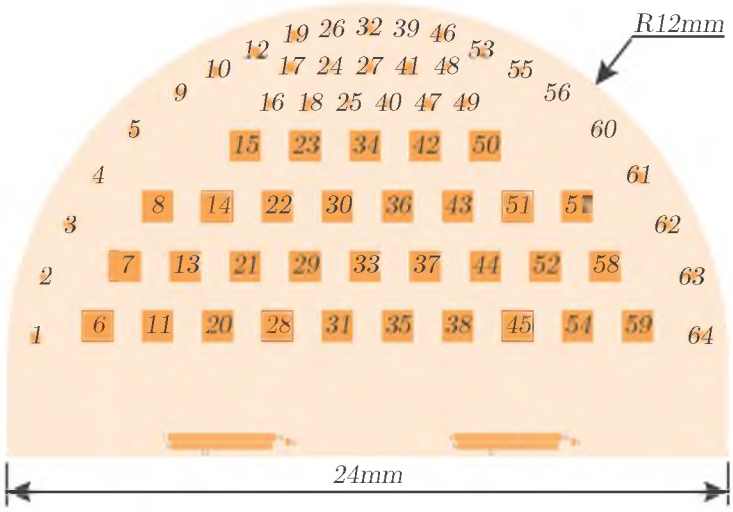

Figure 6.5: Semicircular detector with 64 pixels, designed for the rotating phantom concept. The curvature of the detector was based on the radius of the human eye. The numerical indexing on the pixels was derived from the horizontal placement of the output bonding pads.

shape to form the resulting semicircle. The detector was 24.05 mm wide by 15 mm high and the semicircle had a radius of curvature of 12 mm. Some samples of the fabrication masks used in making the detector are presented in Figures D.1 – D.3 of Appendix D.

The detector featured two sizes of pixels: 32 small pixels measuring 300 µm × 300 µm, and 32 large pixels measuring 1.00 mm × 1.00 mm, shown in the schematic of Figure 6.5. The variation in pixel size allowed a more efficient coverage of the detector plane, by using small pixels to provide a higher resolution at the sclera and around the plaque, and by using large pixels for better signal statistics at larger distances. The large pixel size was also intended to maximise the statistics measured in areas of relatively lower dose.

The numerical indexing of the pixels, shown in Figure 6.5, was based upon the vertical track routing to the bonding pads as they occur from left to right. Pixels ranging from 1 – 32 are routed through the left hand ASIC and the pixels from 32 – 64 are routed to the right hand ASIC.

6.1.2 Translation Based Detector

The rectangular detector was designed to be used with the translation based phantom detailed in Section 5.2.1. It had a width of 24.00 mm and a height of 27.00 mm, large enough to cover the entire diameter of the average human eye. A schematic representation of the detector is provided in Figure 6.6.

The *p-i-n* diode topology of the square detector was the same as that of the semicircular detector, except that all of the 127 diodes are 500 µm × 500 µm in size. The pitch between pixels was 2.00 mm in the horizontal and vertical directions.

The detector was arranged in alternating columns of six and five pixels and the signal outputs from the pixels were routed to four groups of bonding pads for interfacing with the front-end readout ASICs. Some samples of the fabrication masks used in making this detector are presented in Figures D.4 – D.5 of Appendix D.

To best achieve the aims of this study, a single concept needed to be selected for investigation in the PANOPTES. The rotation concept was deemed most appropriate as it allowed measurements closer to the surface of the plaque with relatively lower electronics complexity, compared to the translation concept.

6.2 Electrical Design

The electrical hardware consisted of four main components: the detector board, power supply, the interface board and the stepper motor. The detector board bore the detector and front-end electronics in a low noise environment. The interface board featured a field programmable gate array for logical processing and was used for communication to and from the other electrical components and the user. The power supply was used to provide standard voltage rails for the electronics, in addition to the detector high voltage bias and the stepper motor power rails. The stepper motor was controlled

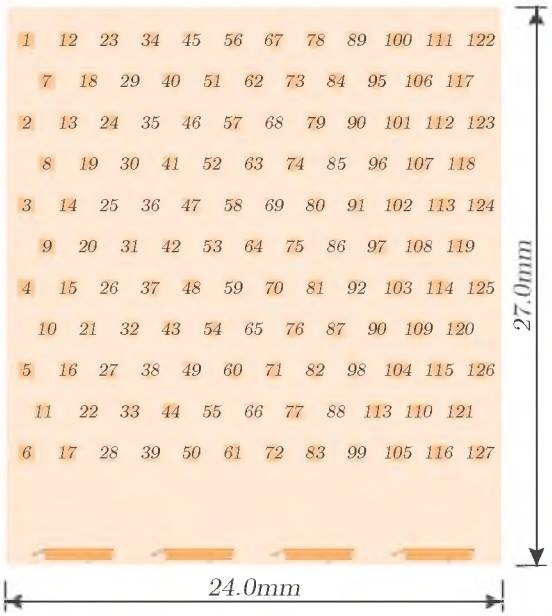

Figure 6.6: Rectangular detector with 127 diodes, designed for the plunge phantom and the channel numbers on the detectors are derived from the horizontal placement of the bonding pads.

using signals from the interface board via a driver circuit. The interconnections of the electrical systems are depicted in a system diagram shown in Figure 6.7.

6.2.1 Detector Board

The detector board was designed with the primary considerations of providing a platform for detector and phantom mounting and also a low-noise environment for the front-end, readout electronics. The board featured the pixelated detector at one end and the electrical interface at the other. The interface provided the bias voltage along with separate digital and analogue +5 V voltage rails, the serial peripheral interface bus, and various control lines. Figure 6.8 shows a photograph of the detector mounted onto the PCB with, and bonded to, the two readout ASICs.

The board used a four layer design, featuring both a multi-net power and a multi-net ground plane as the central two layers. The board was separated into two main regions, digital and analogue, to limit the noise transmitted through to the ASIC.

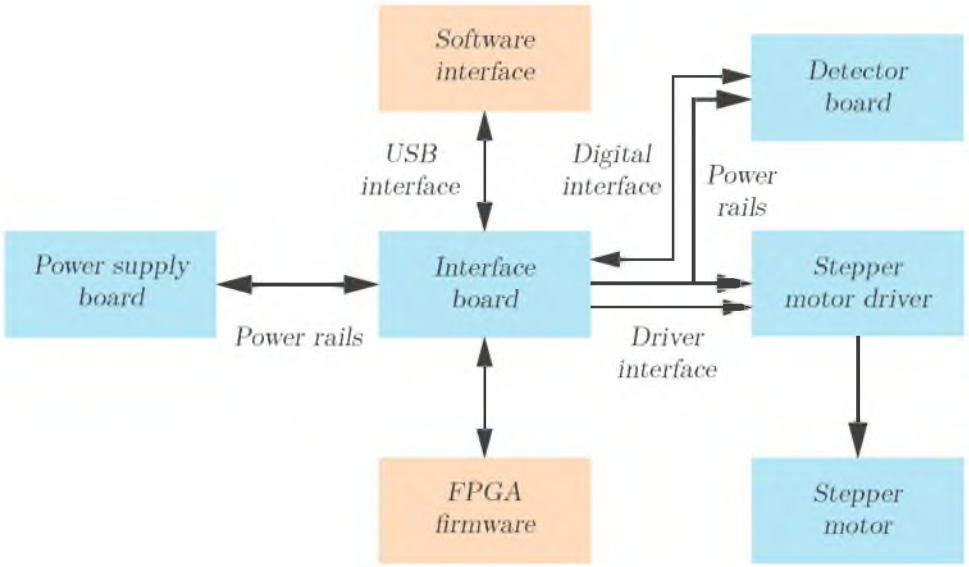

Figure 6.7: Block diagram of the PANOPTES electrical interfaces showing electrical hardware in blue, and the control systems, in orange.

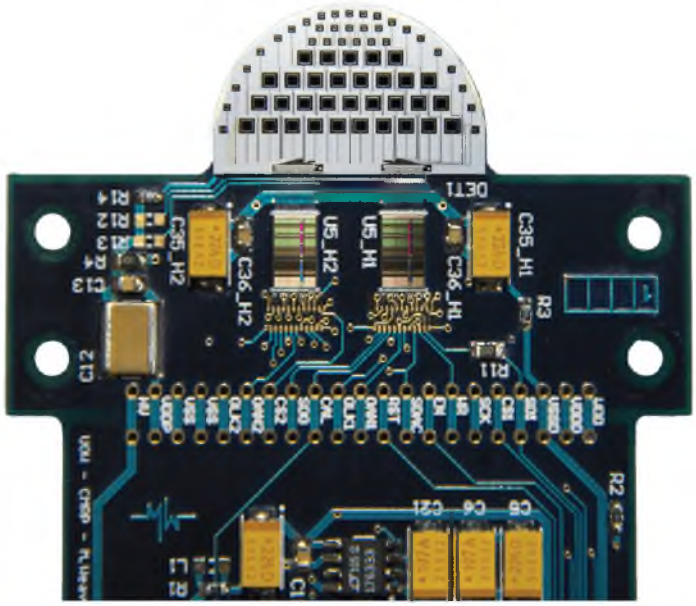

Figure 6.8: The semicircular detector sample N3 was mounted to the detector board (top half shown). Wire bonding joined the detector to the ASIC, and the ASIC to the board.

Several low-noise +3.3 V voltage regulators were used with +5 V inputs to provide stable power rails to the ASIC. The bias voltage supplied to the detector was current limited using a 1 MΩ resistor and stabilised using ceramic capacitors. Operational amplifiers were used to create four voltage followers for reliably routing output signals from the ASICs to the interface board. The detector board was connected to the interface board via a 34 pin header and shielded cable, the connection scheme for which is provided in Table C.1 in Appendix C.

The circuit schematics of the detector board are presented in Figures C.1 to C.3 of Appendix C and the printed circuit board layouts are presented in Figure C.4.

6.2.1.1 Front-End Electronics

The readout ASIC used for the PANOPTES was the HERMES4[209] and was designed at the Instrumentation Division of Brookhaven National Laboratory. It was selected primarily due to its high-rate, high-resolution, moderate complexity, and suitability for ^{125}I dosimetry as used in plaque brachytherapy. This family of ASICs has been used in a number of low-noise applications in the past[210–213].

HERMES4 is a mixed-signal, front-end ASIC fabricated in 350 nm CMOS, dual-poly, four-metal 3.3 V technology. It has 32 analogue input channels, each of which comprises a low-noise preamplifier with continuous reset[214], a high-order shaper with baseline holder (BLH)[175], a single low-level discriminator (Window 0), two window discriminators (Windows 1 – 2) with fine adjustment digital-to-analogue converters (DACs) and one 24-bit counter, as annotated in the photograph in Figure 6.9. Each of the four window thresholds for each channel is individually adjustable with a 6-bit DAC. The power consumption for each channel is reported to be ∼ 8 mW, of which 3 mW is dissipated by the preamplifier. There is no timing information available from the ASIC.

Communication with the HERMES chip was conducted using the serial peripheral

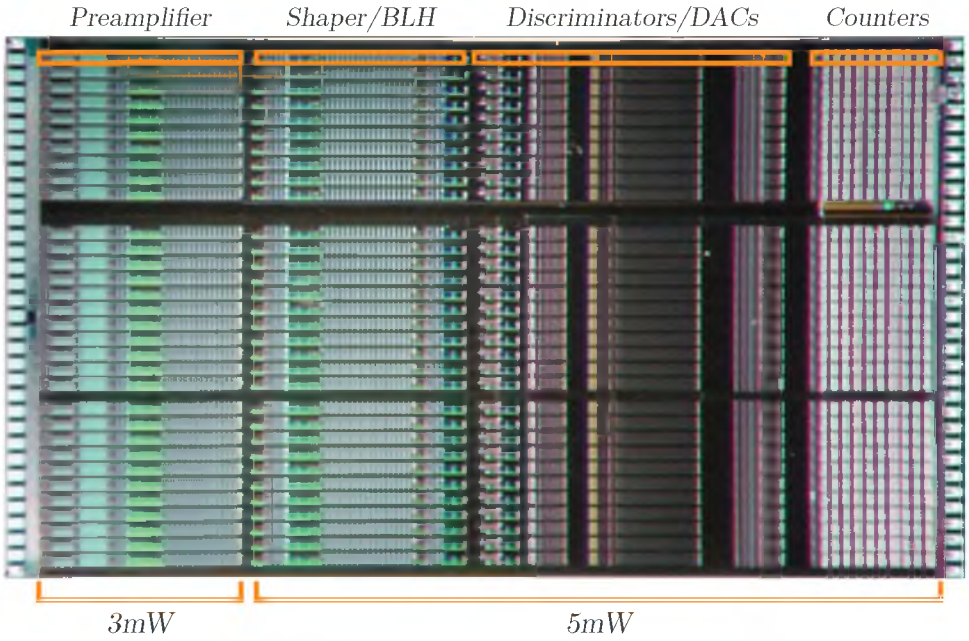

Figure 6.9: Photograph of the HERMES4 ASIC[209] showing various sections of each channel. Each channel counts the number charge pulses that fall within three separate adjustable energy windows and can be subsequently read out digitally.

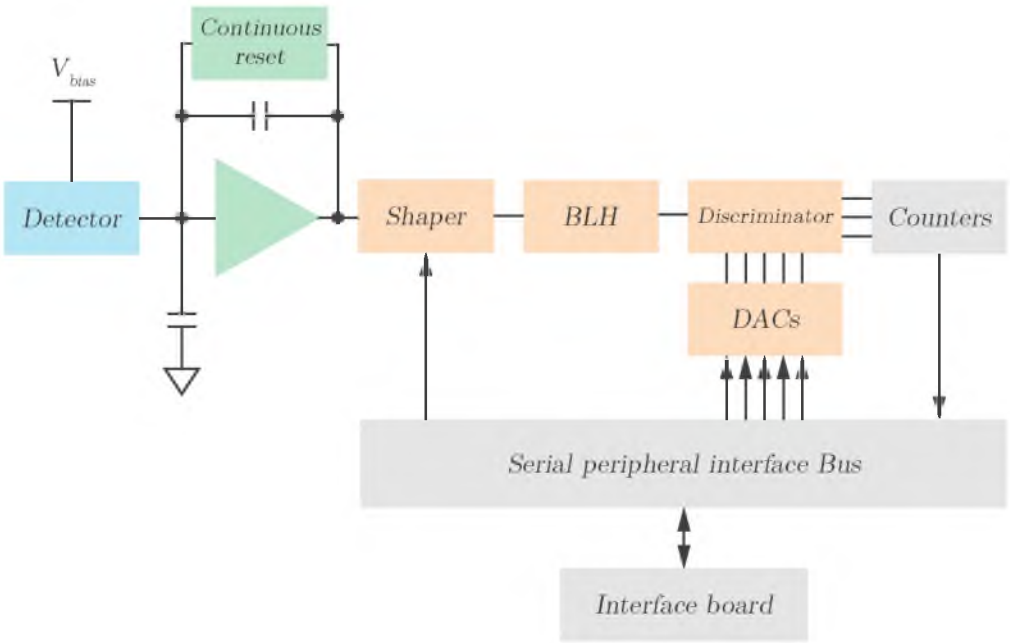

Figure 6.10: Simplified schematic of a single channel of the HERMES4 mixed-signal front-end ASIC[209] and its connections with the FPGA via the serial peripheral interface bus

interface (SPI) bus. The serial data input (SDI) line allowed for some of the analogue processing chain's parameters to be configured, viz. gain [0.75 mV fC^{-1}, 1.50 mV fC^{-1}] and shaper peaking time [0.5 µs, 1.0 µs, 2.0 µs and 4.0 µs]. Upon request from the FPGA processor, the serial data output (SDO) line from the device clocked out the three 24-bit counter values sequentially for each of the 32 channels, totalling the 2304 bits of a data frame. Figure 6.10 shows a simplified diagram of a single channel of the ASIC and its relationship to the interface board through the SPI bus.

6.2.2 Electrical Enclosure

The main electrical enclosure, shown earlier in Figure 6.1, housed the power supply board and the interface board, seen in Figure 6.11. Its steel casing was earthed to the mains supply (240 VAC) through a fused IEC[215] socket and provided electromagnetic shielding. The boards were electrically isolated from the enclosure and the interface board was further protected from power supply interference with a dedicated electromagnetic interference (EMI) shield. The front and back panels of the enclosure were both used as connection and control interfaces, images of which are provided in Appendix B as Figures B.5a and B.5b, respectively.

The front panel featured a power indication LED and sockets for the stepper motor control and power lines, in addition to the interface connection to the detector board. The later used a shielded multi-core cable for all power and control signals. The back panel provided access for power and a USB type-B connection for communication to and from the host computer to the FPGA module. Control of the high voltage biasing system was provided through an enable override switch, manual-remote switch and a voltage adjustment dial.

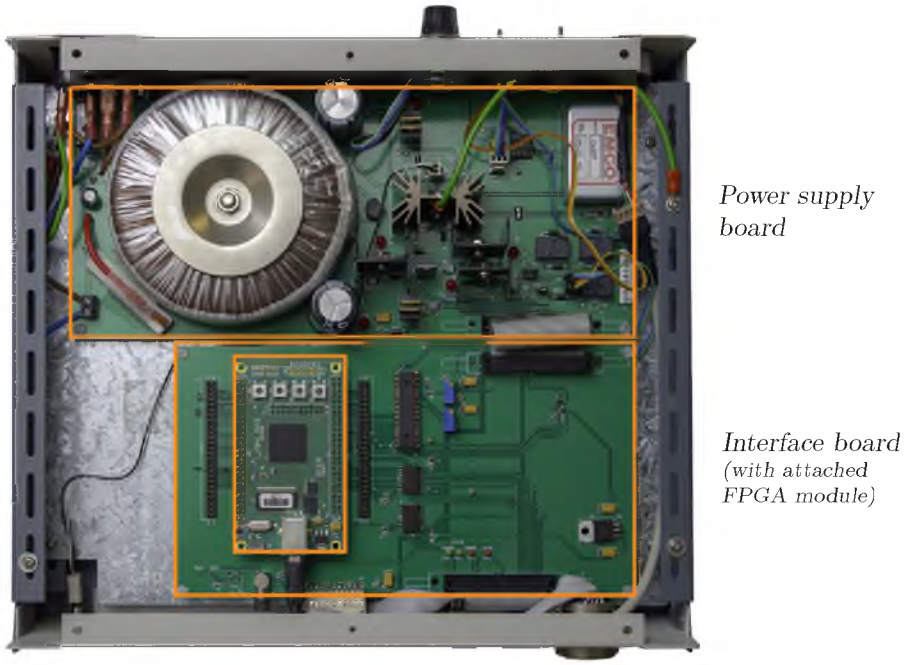

Figure 6.11: The internal circuit boards of the PANOPTES included both the power supply board (*top*) and the interface board (*bottom*) which featured a socketed FPGA module (*all highlighted in orange*). When fully enclosed, the interface board was electromagnetically shielded from the power supply board with a dedicated metal enclosure (not shown).

6.2.3 Power Supply

The power supply system provided rails for +5 VD, +5 VA, and +15 V for various systems including the FPGA, detector board and stepper motor. It also provided an adjustable high voltage (0 V – 200 V) signal with positive polarity to be used for biasing the detector. A series of mechanical relays was used for fail-safe switching of power signals and lines. Circuit schematics and printed circuit board layouts for the power supply are provided in Appendix C as Figures C.5, C.6 and C.7, respectively.

A toroidal step-down transformer with dual secondary windings and a bridge rectifier circuit was used to rectify the input power and provide $\pm \sim 25$ VDC. These lines were then regulated into ±5 VA (DC for analogue line), +5 VD (DC digital line), ±12 V and 15 V using the 78xx and 79xx series linear regulators. The analogue and digital power nets were separated to reduce system noise, though they shared a common ground via a ground-star style filter. The primary side of the transformer featured an in-rush protection circuit consisting of an RC-timed relay and a shunt resistor.

The high voltage bias supply was provided by the very low noise EMCO CA-02T-P[216], which was capable of providing from 0 V – 200 V with a maximum output current of 5 mA. The high voltage adjustment could be set manually using a potentiometer, or through the software interface and a digital-analogue converter. The voltage ripple in the high voltage bias was measured to be ~ 5 mV at the operational voltage (50 V).

The board supplied the +5 VD and +15 V rails to the stepper motor driver via the central acquisition board for logic control and powering the motor coils, respectively.

6.2.4 Interface Board

The interface board was responsible for the logical operation of signals and interfacing to and from the host computer and the detector board, along with the control of the high voltage bias and the motor control for plaque positioning. The power supply and

interface boards comprised the internal circuits of the main PANOPTES electronics box, as shown in Figure 6.11. Circuit schematics for the interface board are provided in Appendix C as Figures C.8 – C.12, and the printed circuit layout in Figure C.13.

The +3.3 VDC voltage rail required for the FPGA module was generated on the interface board using a LD1086 linear voltage regulator. The board featured two separate 34 pin headers for routing voltage rails from the power supply board and to the detector board. The interface board also forwarded the power rails to the stepper motor driver and all power rails to the detector board. Through the FPGA module, the interface board could set a DAC, which was used for setting the input value of the high voltage bias. The SPI signals and CS, EN, WR and RST control lines of the readout ASIC on the detector board were buffered to and from the FPGA module.

6.2.5 Field Programmable Gate Array (FPGA) Firmware

The interface board used a drop-in prototyping module, the Opal Kelly XEM6001[217], for managing communication, clocks and power for the Spartan-6, high gate-count FPGA (XC6SLX16-2FTG256C)[218]. The FPGA was used in the PANOPTES for all logical processing that required time critical hardware interfacing. It acted as an immediate controller between the host computer and the other electric systems, as seen in Figure 6.2.

The XEM6001 featured on-board serial flash memory storage and, upon powering, booted the stored configuration file for immediate operation. It used hardware descriptor language (HDL) libraries on the FPGA side to interface with software using the corresponding application programming interface (API) on the host computer side. This communication used a host interface clock of 48 MHz on the Universal Serial Bus (USB) protocol v2.0[219]. The flexible XEM6001 clocks were generated with an on-board phase-locked loop (PLL).

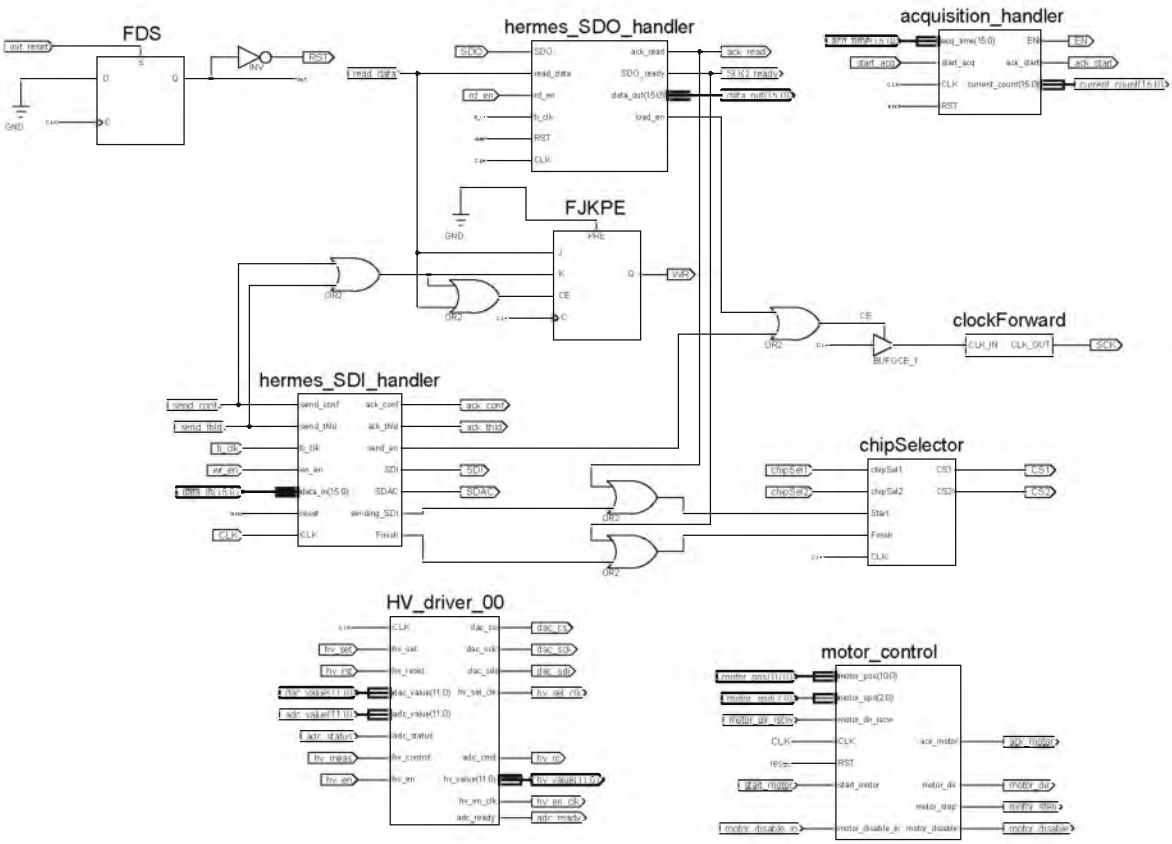

Figure 6.12: The main schematic module of the FPGA firmware showing several of the interconnected sub-modules.

The main FPGA module was responsible for the logical handling and coordination of a collection of sub-modules at the clock cycle timing level and is shown in Figure 6.12. The sub-modules focused on controlling Serial Data In (SDI) and Serial Data Out (SDO) lines, acquisitions, the high voltage bias driver, motor positioning and HERMES chip selection.

The FPGA modules communicated with the two HERMES chips individually, by selecting them via their respective chip select CS lines. The chips were only selected during a transfer process either to or from the HERMES. The host computer was used to coordinate the macro level timing of the chip selection process. The schematic module that handled the chip selection of the two HERMES devices is presented in Figure E.2 of Appendix E.

The front end readout chips were configured with parameters sent from the host computer via the FPGA module. The FPGA module used the SPI interface to send configuration data for gain, peaking time, DAC values for global window thresholds for Windows 0 – 2, individual DAC values for Windows 1 – 2 for each channel, along with some other configuration parameters. The total communication chain was fast enough to permit pre-acquisition configuration for every set of acquisitions, which allowed parameter changes to be made easily. The schematic firmware module that handled the SDI line for configuration to the HERMES is presented in Figure E.3 in Appendix E.

Once the HERMES ASICs had been correctly configured, an acquisition time had been set and the starting trigger had been received from the user interface, the acquisition process was initiated on the FPGA module. The acquisition time variable was 16-bit and represented the time, in clock cycles, that the input event counters were enabled on the HERMES chips, via the EN signal. Given that the clock period was 100 ms, the range of acquisition was from 0.1 s – 6553.5 s, which was sufficiently precise yet large enough for acquisitions of brachytherapy plaque sources. The *enable* signals for the counter inputs were set and reset simultaneously on both ASICs, ensuring that equal and concurrent acquisitions could occur. When the acquisition time had elapsed, the FPGA module flagged a completion trigger and, upon acknowledgement from the host computer, the data from each HERMES chip was clocked out consecutively and forwarded to the host computer for processing. The schematic firmware module that handled the SDO line from the HERMES is presented in Figure E.4 and the Verilog module of the acquisition handler is provided as Listing E.1 in Appendix E.

The EMCO high voltage bias supply was set through a digital-analogue converter that received a value sent serially from the host computer via the FPGA on a SPI bus. The output from this device was monitored using an analogue-digital converter,

which was in turn sent back to the host computer via the FPGA. Additionally, the FPGA and host computer could control the connection of the high voltage supply to the detector circuitry through mechanical relays on the power supply board. The firmware schematics are presented in Figures E.5 to E.7 in Appendix E.

The orientation of the plaque relative to the detector was controlled using a stepper motor, the SANM***O*TION** - 103H7126-0140[220]. The position of motor was handled using three FPGA signals: STEP, DIR and DISABLE for position incrementing, direction, and disabling, respectively. The host computer was used to initiate FPGA signalling for motor movement through the use of three variables to provide information regarding the number of steps, the rotation direction and the step frequency. The stepping resolution was determined from the motor specifications (1.8 °/step) and the motor driver interface[221] (10 microsteps/steps) giving 0.18 °/microstep. The motor coils were powered by the 15 VDC digital rails supplied by the power supply board. The Verilog module of the motor controller is provided as Listing E.2 in Appendix E.

6.3 Phantom and Positioning System

An eye phantom was designed and fabricated to provide tissue equivalence required for accurate dosimetry. It also provided mechanical protection for the sensitive detector and ASICs. For the PANOPTES, the term *phantom* can be considered in two ways: the first includes the material that is used for radiation attenuation, while the second is the entire hardware system needed for measurement. For the purposes of this study, the term *phantom* refers to the tissue-equivalent material object, and the term *positioning system* refers to the remaining hardware, including the stepper motor, shaft, box etc.

The phantom was 3D printed as a single piece of material called VisiJet® Crystal made by 3D Systems[222]. This printing process allowed for the phantom to be produced with much better tolerances (16 µm) than traditional fabrication methods would allow,

Figure 6.13: Photograph of the fully assembled PANOPTES detector board with phantom fixed in place

given the production time and cost.

The use of 3D printing also eliminated otherwise difficult to avoid air gaps, and offered greater flexibility for design modification. The distance between the plaque and the edge of the detector was 500 µm to enhance the capabilities of near-surface dosimetry. A photograph of the detector board with the phantom mounted over the detector is shown in Figure 6.13 and dimensioned drawings for the phantom are provided as Figure B.2 in Appendix B.

Unfortunately, due to the proprietary nature of the available printer material, its exact fractional composition could not be obtained. The material safety data sheet indicated that the composition comprised three main constituents with a range of percentages, as detailed in Table 6.1. This information was not sufficient to perform accurate simulations and it is recommended that future studies investigate the radiation response of this material or seek alternative printable materials.

The positioning system was designed with the aim of providing mechanical position control over the plaque whilst limiting disruption to normal clinical procedure. It

Table 6.1: Composition information for the phantom printed in 3D Systems' VisiJet® Crystal[222] material.

Component	Percent
Urethane acrylate oligomers	20 % – 40 %
Ethoxylated bisphenol A diacrylate	15 % – 35 %
Tripropyleneglycol diacrylate	1.5 % – 3 %

allowed the plaque to be assembled directly on the phantom where it could be measured and verified without double-handling. The position system consisted of a PMMA (poly(methyl methacrylate)) box, stepper motor, lock-down shaft and board holder. A photograph of the positioning system prior to painting is provided in Figure 6.14 and dimensioned drawings of the box and lock-down shaft are provided in Appendix B in Figures B.3 and B.4, respectively.

After assembly of the plaque, the lock-down shaft was used to hold it in place centrally onto the phantom, using a plaque specific seat. The shaft was a telescopic, three part mechanism that could be retracted out of the way during loading and locked down onto the plaque with a spring during operation. The bottommost end of the shaft featured a detachable plaque holder designed to securely fit around the plaque, as shown in Figure 6.15. This feature allows many styles of plaques to be used with limited handling whilst ensuring measurement accuracy. The stepper motor, coupled to the other end of the shaft, acted to rotate the plaque about its axis when changing the plaque-detector angle during acquisition. The board holder was used to orient the detector board vertically, aligning the detector to the axis of the shaft.

The box frame was coated in a conductive nickel based paint that was used to inhibit light and shield the sensitive internal electronics from external EMI. Prior to operation, a panel was magnetically locked into place at the front of the box to complete the shielding.

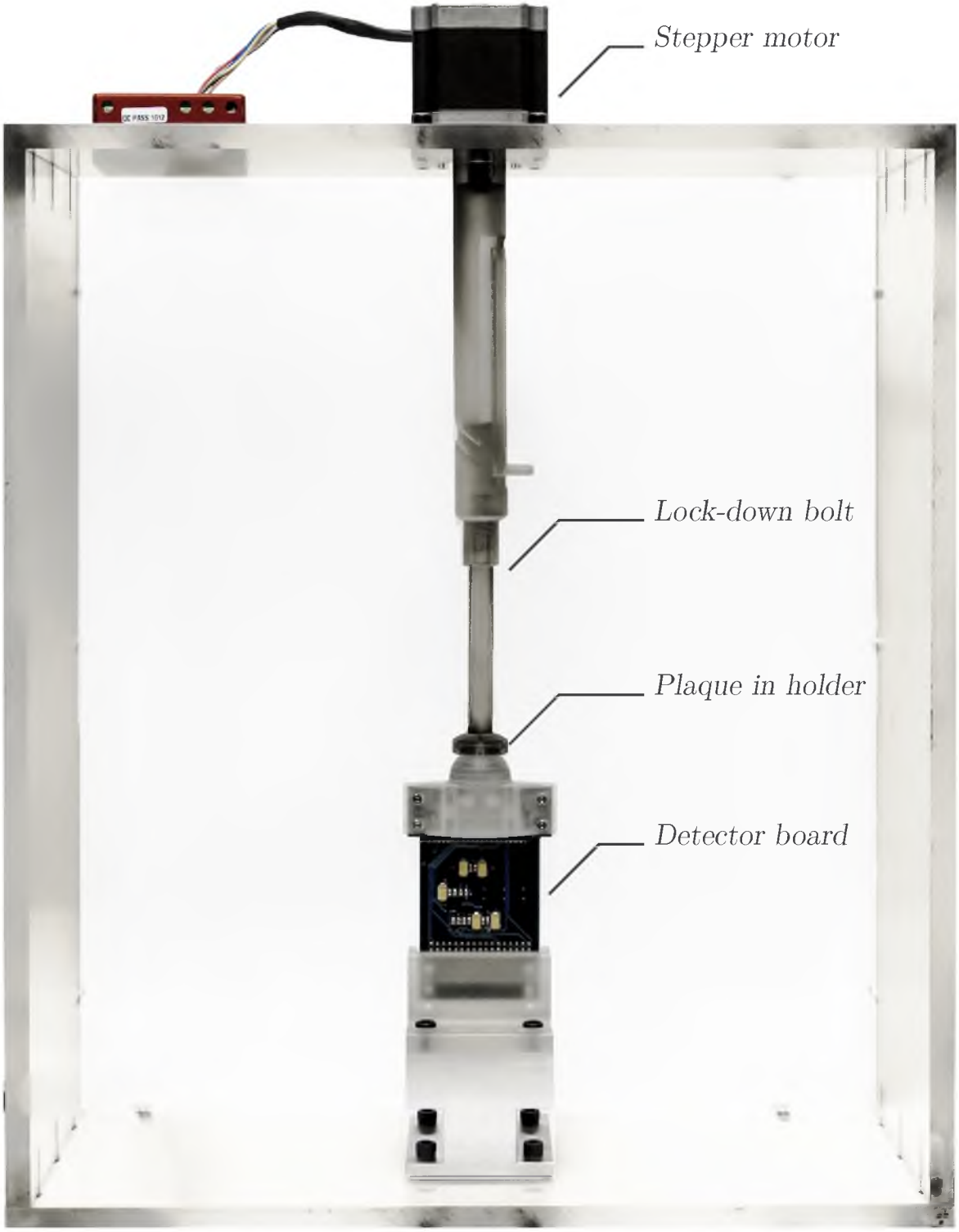

Figure 6.14: Photograph of the entire phantom and positioning system, prior to shielding with metallic paint. The detector board was fixed vertically in the centre and a guide bolt applied a gentle force to the plaque yet allowing it to rotate with the stepper motor whilst the detector took incremental measurements. Within the phantom, the top surface of the detector faced towards the back of the positioning system box.

Figure 6.15: The positioning system could accommodate many styles of plaques by using a detachable plaque holder, illustrated above, which was used to position the plaque in a secure manner and provide control over its orientation.

6.4 Software Interface

The software interface for the PANOPTES, called Panopticon, was designed to provide user control over the system. It was also used to provide fast, visual feedback and data storage from measurements. The interface was written using C++[188] and Digia's Qt interface libraries[189], with the consideration that it should be portable to multiple platforms, namely Windows, Unix and MacOS (on which Plaque Simulator[22] operates). The interface was responsible for handling the communication to and from the XEM6001 FPGA module via the Opal Kelly FrontPanel API[223].

The Panopticon software used the FrontPanel programmer's interface, an Opal Kelly C++ API, to communicate via USB 2.0 with the Opal Kelly XEM6001. The XEM6001 is a prototyping board featuring a SPARTAN-6 FPGA which communicated through a combination of triggers, signals and data pipes to the host interface, Panopticon.

When the plaque, phantom, electronics and software configuration details were prepared, an acquisition process would be ready for initiation. Whilst the interface was in an idle state, an intermittent handshaking signal was used to maintain contact to the FPGA. An acquisition involved first disabling this handshaking to reduce noise, then sending the configuration details to the FPGA, followed by an acknowledged trigger

signal. The user interface then waited for the acquisition time to expire and polled the return triggers to check if the data acquisition was complete. If successful, then data was transferred to the interface and to file if desired. Once the data had been processed, another acquisition may follow or the motor may be repositioned, depending on the acquisition type and status. A screenshot of the main interface of Panopticon is provided in Figure 6.16.

With each measurement taken, the software stored the count data and acquisition details in a PANOPTES data file (*.pdat), as ASCII text to ensure maximum accessibility to the information. Additional details that were stored included any modifiable parameters or notes, such as time and duration of acquisition, bias voltage, front end electronics configuration, motor details, etc. An example output is provided in Listing F.1 in Appendix F.

Once the measured data had been decoded, the 64 data channels were stored in the random access memory. This data was processed further to determine the range of values present, after which it was represented diagrammatically on a detector map graphic where colour was used to indicate count values. The detector map was a schematic representation of the detector's layout and interactively allowed the user to mouse-over pixels of interest and reveal their numeric value in a pop-up overlay, as seen in Figures 6.17a and 6.17b.

Adjacent to the detector map, a histogram chart plotted counts per channel, separated chromatically by large and small diodes. It had been included to allow users to easily assess the dose distribution across the dataset. The histogram offered a customisable number of event bins and the lower and upper trims could be set manually. The colour scaling of the detector map could be used to represent the adjusted values of a trimmed histogram.

Object perceptibility in an imaging system can be enhanced through the improve-

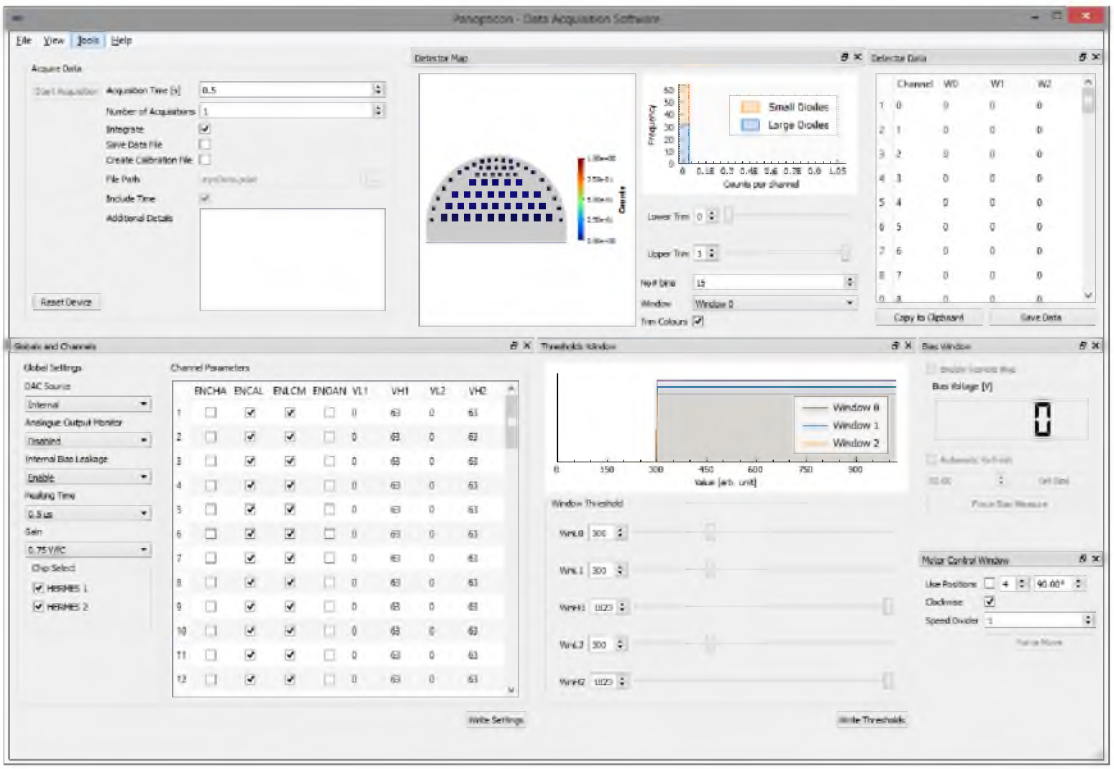

Figure 6.16: Screenshot of the main interface of Panopticon

ment of its signal-to-noise ratio via reducing image noise. The two major contributions of image noise in a system, such as the PANOPTES, are fluctuations in the number of photon events per unit area (entirely stochastic), and those imposed by the imaging system, which can be both stochastic and non-stochastic. Non-stochastic imaging system noise contributions, or fixed-pattern noise, arise from the sensor and the readout electronics.

The origin of noise in the sensor can be attributed to material inhomogeneities which causes non-uniform field distributions, local variations in leakage current and localised reductions in charge collection efficiency. In the readout electronics, the main source of readout-related sensitivity variations are contributed to transistor mismatches introduced during chip production.[224]

To compensate for these inter-pixel variations caused by fixed pattern noise, a so-called flat-field calibration is conducted. This involves taking measurements of a

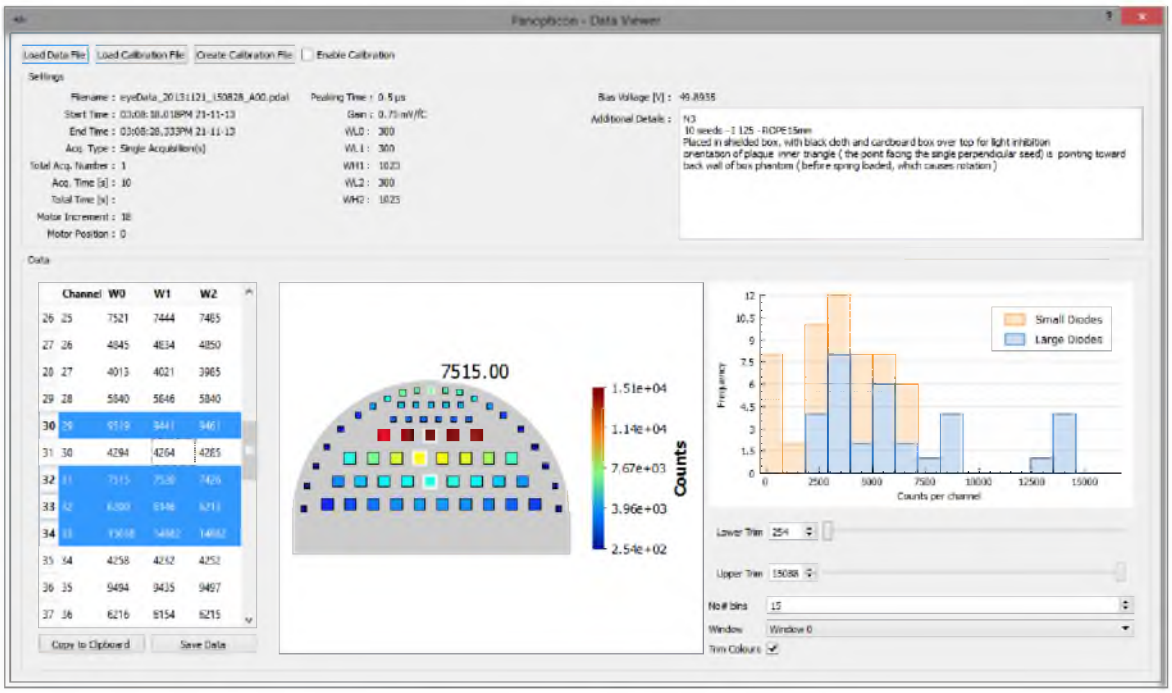

(a) Uncalibrated data

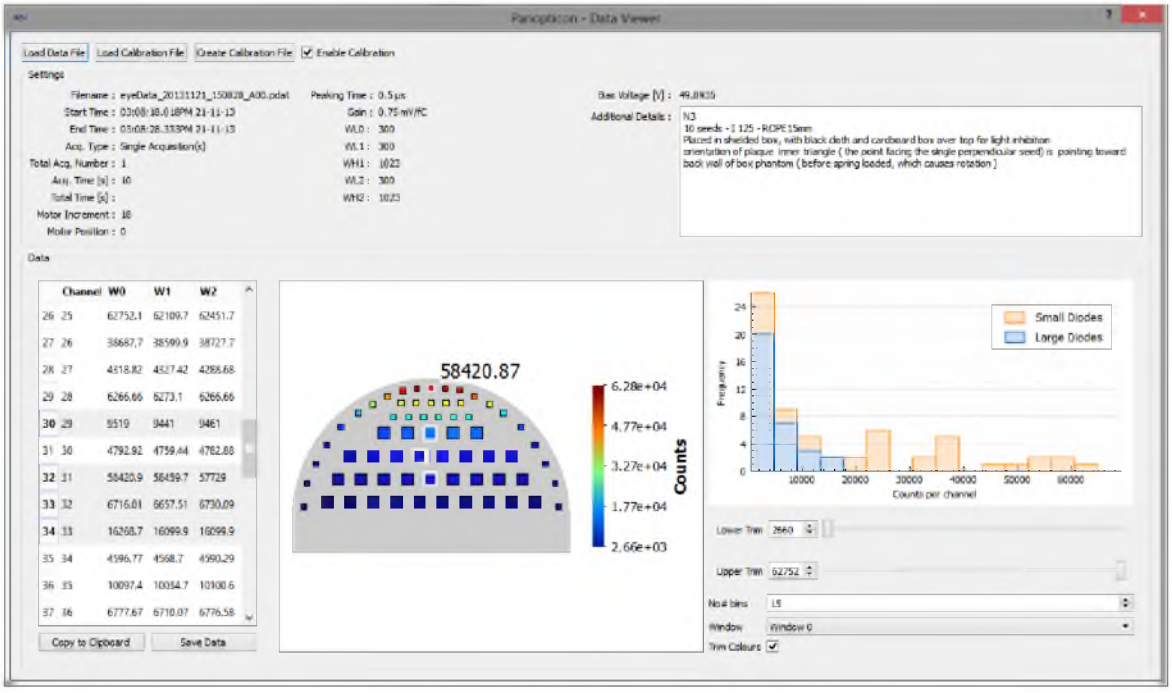

(b) Calibrated data

Figure 6.17: Data could be viewed where count values were colour mapped to the pixels and a histogram of the count distribution provided quick statistical information. The number displayed on the detector map shown is a mouse-over of the value for Pixel #32, see Figure 6.5. Data calibration could be applied using a file generated from a flat field acquisition. The above screenshots show measured data with and without calibration.

uniform field and normalising individual pixel response against the mean of the whole sensitive volume, or some specific pixel. The coefficients generated during this process constitute the flat-field calibration map.

Calibration files could be generated within Panopticon using measured flat-field data and could be applied to any data set. Applying pixel calibration caused the individual calibration factors to scale each pixel value. The factors could be calculated in the software immediately after the system had acquired a flat-field measurement or retroactively, using an existing flat-field measurement. The data values were normalised and the resulting calibration factors were saved to disk in a single calibration file, which could be loaded later. Figure 6.17a shows dose measurement data where the pixels are uncalibrated, in comparison Figure 6.17b shows the same data with calibration applied.

Another useful feature for testing and commissioning of the device was the single channel analyser function (screenshot in Figure 6.18). This tool was used to measure the spectrum of a radiation source by taking multiple measurements and adjusting the three threshold windows, from minimum to maximum. The acquisition time for each energy bin could be adjusted, as could the width of the energy bin. Figure 6.18 shows the results of a scan with the energy bin set to minimum, that is, the lower and upper threshold values were set one increment apart.

During dosimetric measurement only a single threshold is required when ignoring the noise-floor, however utilisation of multiple windows could be used to provide more accurate dosimetry by separating spectral peaks, or reducing electronic noise through taking the mean response. Although they are infrequently used in practice, the spectra of bi-nuclide plaques[132] could be divided into constituent parts for greater dosimetric accuracy when dealing with a range of energies.

An energy threshold histogram could be plotted in real-time and the histogram for

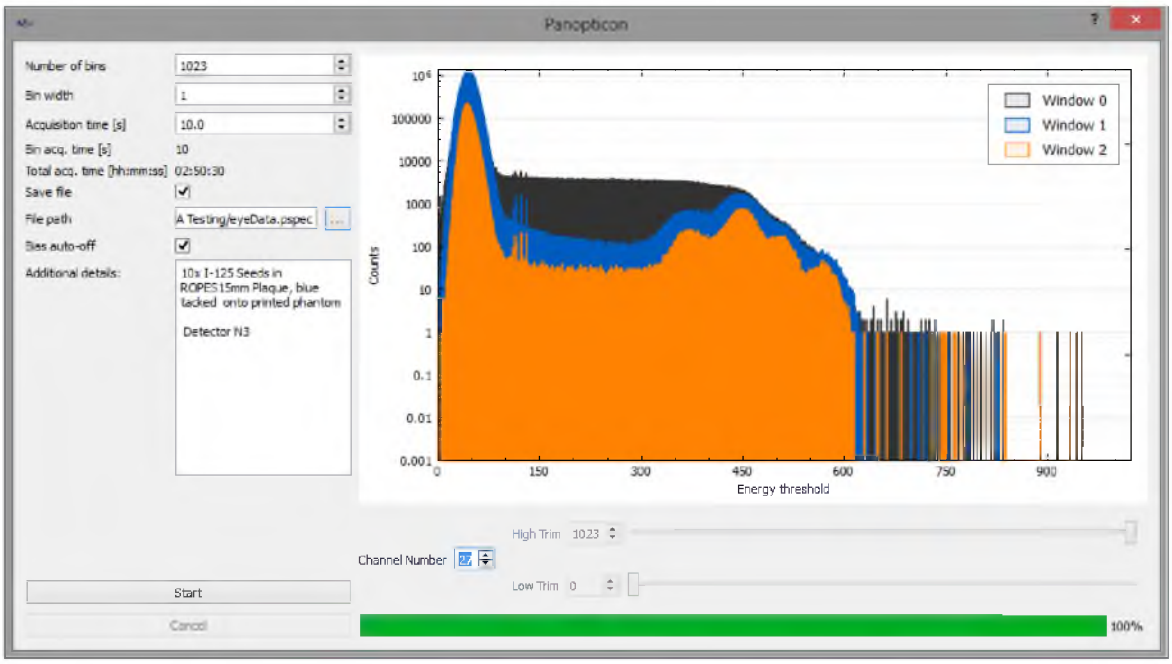

Figure 6.18: Panopticon interface - Single channel analyser. The vertical axis on the plot is in log scale and represents the number of counts measured. The horizontal axis represents the global energy threshold DAC values (0 – 1023) which effectively forms the energy bins when used as a single channel analyser.

any of the pixels could be displayed. An output file could be created upon completion with all relevant acquisition details and the measured spectrum for each of the three energy windows, for all pixels.

The long term aim of Panopticon6 was for use as a complementary tool for the PANOPTES in a clinical environment. Whilst the current software allowed the maximum level of diagnostics and control of the PANOPTES, it included a simplified version of clinical user mode which inhibited unwarranted setting manipulation and included methods for storing patient data and other clinical information. Further development of this system, or integration into an existing dosimetry tool, such as Plaque Simulator[22], would be required prior to clinical implementation.

6.5 Conclusion

The detector, electrical, phantom, positioning and software systems for the PANOPTES were designed, developed and integrated to produce a functioning radiation detection system.

Two types of pixelated silicon *p-i-n* diode detectors were designed and fabricated for the translation and rotation based concepts, respectively. Only the semicircular detector for the rotation based concept was chosen for use with the subsequent design of PANOPTES. Its perimeter was cut with a radius curvature of 12 mm, the average size of a human eye.

Electrical systems were designed, fabricated and assembled for PANOPTES. These included a power supply board, FPGA interface board, detector and readout board and stepper motor circuitry. A mixed-signal, front-end ASIC called HERMES4 was used to handle detector readout. It communicated to a user interface through the interface board which utilised an FPGA based on an Opal Kelly XEM6001 module. The interface board also set the high voltage bias and powered and controlled the stepper motor for orienting the plaque.

A high resolution 3D printer was used to produce an eye phantom, which fitted precisely over the detector. The design allowed the detector to be within 500 µm of the inner surface of a brachytherapy plaque, although the exact composition of the proprietary material could not be obtained from the manufacturer. The material used in this study was selected to allow the continued development of the proof of concept. It is recommended that future studies investigate the radiation response or seek an alternative material. The positioning system developed consisted of a lock-down shaft which was driven by the stepper motor to control the position of the plaque. The detector and phantom were enclosed within an EMI shielded, light-proof box to reduce unwanted noise in the detector.

A software interface, called Panopticon, was written for coordinating acquisitions from the detector. The program could perform a wide variety of functions, such as running multiple, consecutive measurements, with integrable acquisition times ranging from 100 ms to $\sim$ 110 min, saving data to disk upon completion; automatically controlling the plaque position via the stepper motor; visualising measured data with a detector map and histogram; and measuring the energy spectrum of a source by acting as a single channel analyser.

The following chapter details the characterisation of both the semicircular detector in isolation and as an integrated part of the PANOPTES.

Chapter 7

Characterisation

In the second part of this thesis, the concept of using a pixelated detector for plaque brachytherapy dosimetry was shown to be viable. Following on, a semicircular shaped detector was designed, fabricated and implemented as part of a dosimetry system. This chapter details the characterisation that was performed on this detector as an unconnected device and as an integrated part of the PANOPTES.

The detector was tested using current-voltage and capacitance-voltage analysis, as well as alpha spectroscopy and ion beam induced charge collection. This was, in part, useful for determining the energy resolution and geometry of the sensitive volume of the detector. Monte Carlo simulation was used to establish individual silicon response to water dose conversion factors for each pixel in the detector across all angles.

The energy spectra of the pixels was measured by configuring PANOPTES as a single channel analyser. From this, the noise threshold for the pixels was determined for optimisation of ^{125}I dosimetry. Flat-field calibration was performed using a 250 kV photon beam to normalise individual sensitivity. The work in this chapter has resulted in the follow publication:

- M. Weaver, M. Petasecca, D. L. Cutajar, M. L. F. Lerch, G. De Geronimo, D. Pinelli, A. Cullen, D. Prokopovich, V. Perevertaylo, and A. Rosenfeld, "Panoptes:

Calibration of a dosimetry system for eye brachytherapy," *Radiation Measurements*, vol. 71, pp. 310–314, Dec. 2014.

7.1 Detector Characterisation

The electrical performance of the detector was evaluated by measuring its current-voltage and capacitance-voltage characteristics. Charge collection and spectral characterisation of the detector were performed through α-spectroscopy and ion beam-induced charge collection (IBICC) efficiency at the Australian Nuclear Science and Technology Organisation (ANSTO). All physical test measurements were performed with the silicon detector bonded and mounted on to a breakout board, presented in Figure 7.1. The detector sample used for characterisation differed from that used later in the PANOPTES performance testing, although it was from the same fabrication batch. Monte Carlo simulation was used to determine the energy conversion factors for each pixel of the detector by determining and optimising for angle-dependent silicon-water dose conversions.

Figure 7.1: Semicircular detector breakout board prior to the mounting and bonding of the detector.

7.1.1 Current-Voltage Characterisation

Pixel leakage current was measured as a function of reverse bias voltage from 0 V – 50 V in 100 mV increments. To achieve this, the detector on the breakout board was placed inside a dark, shielded box which was electrically connected through to a Keithley Model 230 Programmable Voltage Source for applying reverse bias voltage and a Keithley Model 614 Electrometer for measuring the leakage current. The voltage source was controlled through the IEEE-488 interface[184] and a computer running LabView[185]. The measurements were digitised using a Keithley Model 199 System DMM/Scanner connected to the electrometer and then sent back to the computer on the same interface. This process was identical to that described in Section 4.2.1.1; for a connection diagram see Figure 4.6.

The leakage current-voltage (I-V) curves for 55 pixels were measured, though for clarity only three pixels are presented in Figure 7.2. The selected pixels are Pixel #01, a small pixel with a short track, Pixel #26, a small pixel with a long track, and Pixel #59, a large pixel with a short track.

The median values for leakage current were 1.94 ± 0.49 nA and 430 ± 72 pA for the large and small pixels, respectively. As stated, the leakage current is dependant on the junction geometry and the large and small pixels have areas of 1.00 mm^2 and 0.09 mm^2, respectively. These areas differ by a factor of 11, while the median values of leakage current differ between the large and small pixels by a factor of 3.96. This discrepancy occurs, because the sensitive volume of the small pixels increased relatively more with applied bias than the large pixels. The effect is more clearly depicted later in the charge collection efficiency study of Section 7.1.4. Though not plotted, the breakdown voltage was measured to occur at around 63 V for Pixel #27. Some of the pixels displayed higher leakage currents than expected, which could be attributed to non-uniformity in wafer resistivity, and defects.

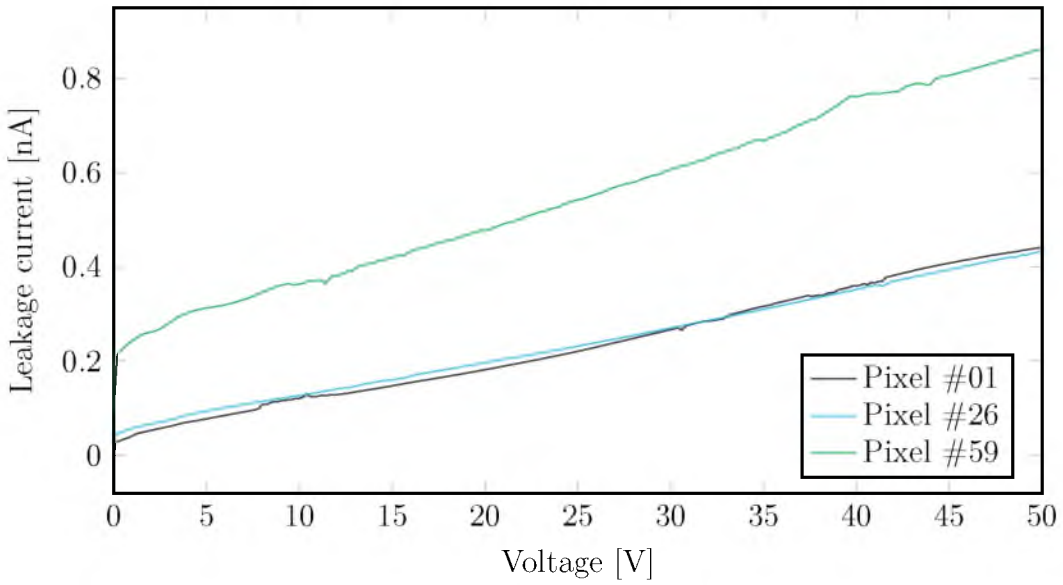

Figure 7.2: Leakage current-voltage characteristics of select pixels showing the large pixel (#59) with a higher current than the small ones (#01 and #26) independent of track length.

7.1.2 Capacitance-Voltage Characterisation

As stated in Section 3.1.1.4, the *p-i-n* diode has a wide, near *n*-type, intrinsic layer that gives a low capacitance and low leakage current under full depletion. To determine a suitable operational voltage and gain a quantitative understanding of the pixel capacitance, the capacitance-voltage (C-V) characteristics of a number of both small and large pixels was measured.

Using a Boonton 7200 Capacitance Meter[186], a reverse bias voltage was applied to the detector, via the breakout board, and was incrementally changed from 0 V – 50 V (below the breakdown voltage) in 100 mV steps. The capacitance was recorded at each step using National Instruments LabVIEW[185] and the IEEE-488 interface[184]. The electrical connection for the test circuit is identical to that diagrammed earlier in Figure 4.8, except that the detector was connected through the breakout board.

The unwanted capacitance of the test circuitry was ignored by connecting an identical, though unpopulated breakout board, zeroing the capacitance meter prior to

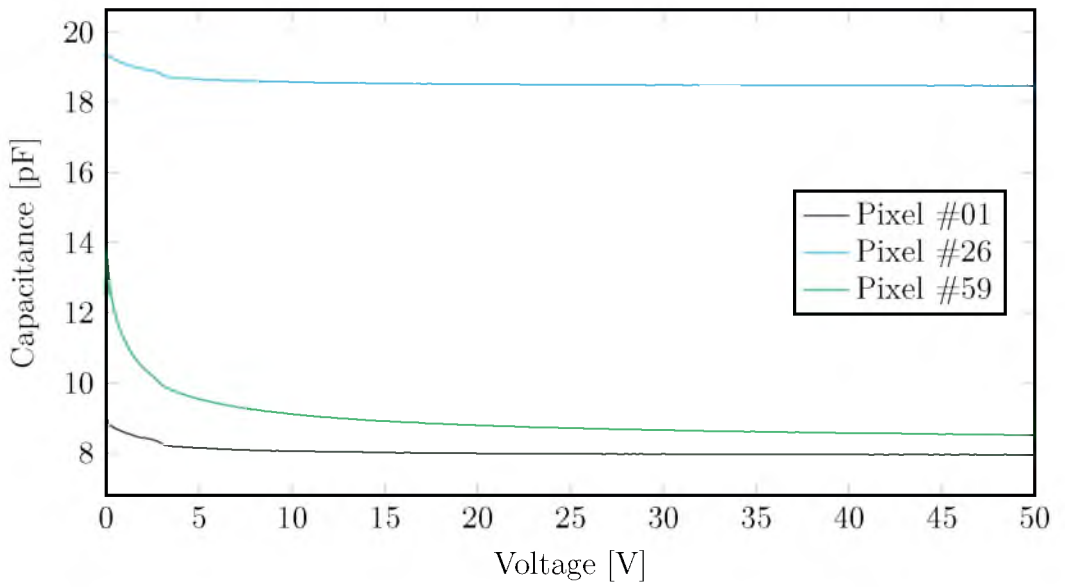

Figure 7.3: Capacitance-voltage characteristics of various pixels. Pixels #01 and #26 are small type, with Pixel #01 having a short track and Pixel #26 having a long track. Pixel #59 is the large and has a short track length.

each pixel measurement and then replacing with the correct, populated breakout board. The data measured for some pixels on the detector sample indicated pixel damage, and were therefore omitted. These performance issues included very low breakdown voltages or unstable and inconsistent response.

A sample of CV curves for both small and large sized pixels are presented in Figure 7.3. As expected, the large pixel features a greater decrease in capacitance with increasing voltage in comparison to the small pixels. Additionally, the difference in capacitance between pixels of differing track lengths is significant with longer tracks resulting in a large capacitance; small Pixels #01 and #26 are extreme examples.

To further analyse the relationship between apparent pixel capacitance and track contribution the capacitance at operational voltage (50 V) was plotted for each pixel against the radial distance from its bonding pad group, see Figure 7.4. Here, a strong correlation can be drawn between track length and observed capacitance, which can only be altered through detector design.

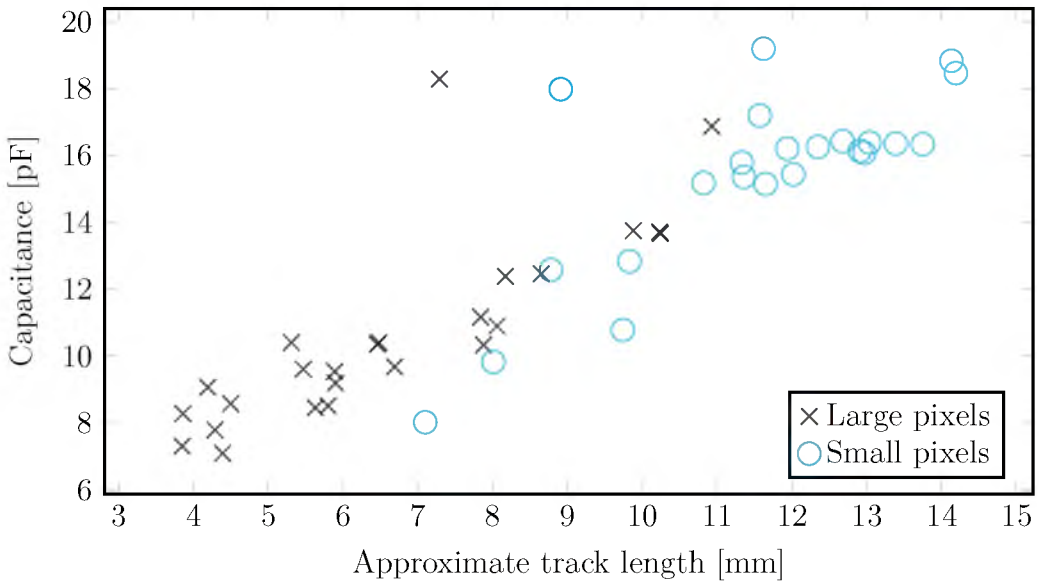

Figure 7.4: Capacitance-track length characteristics of a select number of pixels taken at a reserve bias voltage of 50 V. Note the trend of increasing capacitance with approximate track length (distance from appropriate pixel bonding pad group).

7.1.3 Energy Resolution - Alpha Spectroscopy

Alpha spectroscopy is a very effective method for determining the energy resolution of silicon diodes. The alpha emitter used for this experiment, americium-241 (^{241}Am), has a spectrum of alpha energies with a weighted mean of 5.468 MeV and a projected range in silicon of $\sim 28\,\mu m$ [208]. Given the detector thickness is 300 µm, full energy deposition is expected to occur.

This spectroscopy characterisation aimed to investigate the uniformity of the detector's n-type silicon substrate by observing the energy resolution across various pixels and under differing biasing conditions. Greater substrate uniformity results in higher uniformity in the internal electric field and entrance windows of the pixels and thus indicates the level of quality of the substrate and its fabrication. High uniformity leads to more consistent performance between both pixels and detectors, and infers better energy resolution across all energies which is important for eye plaque dosimetry.

For alpha particles of this energy, the noise contribution from the preamplifier and

electronics can be less significant than the inherent energy resolution of the detector[163]. The theoretical limit of the FWHM observed in silicon at a specific energy can be determined from Equation 7.1, where Fano factor and ionisation energy for silicon are given as $F_{\mathrm{Si}} = 0.11$ and $\epsilon_{\mathrm{Si}} = 3.62\,\mathrm{eV}$, respectively[163].

$$\mathrm{FWMH}|_{lim} = 2.35 \times \sqrt{FE\epsilon} \tag{7.1}$$

As the incident alpha particle energy, E, is 5.486 MeV in this case, the theoretical limit is $\mathrm{FWMH}|_{lim} = 3.47\,\mathrm{keV}$ or 0.063 %.

Alpha spectroscopy was carried out on three pixels, #24, #64 and #59, which were selected based on their position, low capacitive-voltage characteristics and size as mapped in Figure 7.5. An ^{241}Am source and the detector were placed in close proximity within a vacuum chamber in order to both maximise the count rate, and to eliminate the interaction of the α-particles with air. A reverse bias voltage of 50.0 V was applied to the back plane of the detector and, during separate measurements, the pixel of interest was connected to an Amptek A250 preamplifier[225]. The preamplifier was set with gain, $k = 2$, low-level threshold, $LLT = 40$ (320.5 keV), and acquisition time, $t = 600\,\mathrm{s}$. Energy calibration was performed by using a calibrated pulse generator to inject the preamplifier with pulses, with energies of 3.00 MeV, 4.00 MeV, 5.00 MeV and 6.00 MeV. The locations of these were used to scale the output channel accordingly.

The energy spectra measured with the three selected pixels are presented in Figure 7.6. There was good energy resolution for all three with FWHM of the spectral peaks measuring 1.3 % (70 keV), 2.2 % (120 keV) and 1.9 % (100 keV) for pixels #59, #64 and #24, respectively. These peaks coincide relatively well (within 2.2 % of peaks energies) given the differing track lengths for the pixels presented, though it is expected that the resolution will worsen with increasing capacitance. Some fine spectral features are present around the peaks which can be attributed to the presence of the aluminium

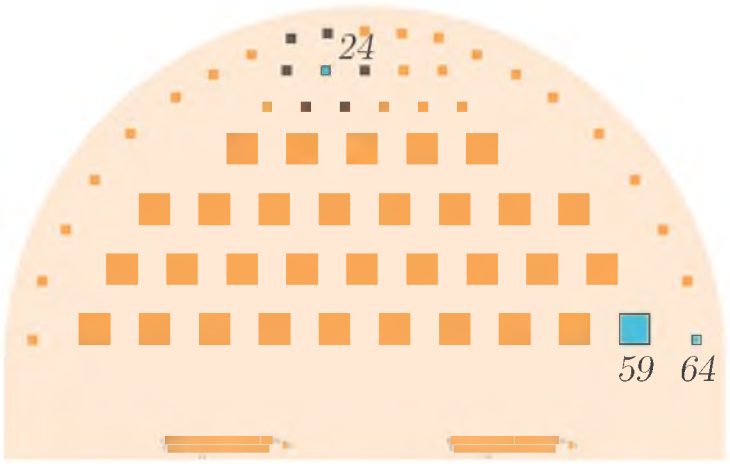

Figure 7.5: Location of three of the pixels used in spectral analysis. Pixels of both sizes and differing track lengths were chosen for comparison. The grey pixels surrounding Pixel #24 indicate those involved in the charge sharing testing.

and the passivated oxide layers over the sensitive volume. This allows for the same energy thresholding in the front-end electronics to be used for all pixels.

The term *charge sharing* describes the process whereby a single particle deposits its charge across multiple pixels. Charge sharing between pixels degrades the quality of the measurable signal. In order to determine whether the PANOPTES detector exhibited charge sharing, the spectrum of a single, centrally located pixel (#24) was measured in two configurations: with the neighbouring pixels connected to ground; and with the neighbouring pixels left floating. By grounding the neighbouring pixels, their collection potential is eliminated and no charge sharing is expected. The floating pixels, by comparison, permit the collection of charge.

The neighbouring pixels included Pixels #17 – # 19 and #25 – #27, and are indicated in gray in Figure 7.5. The energy spectra for both configurations of Pixel #24 are shown in Figure 7.7. While sufficiently indicative of performance, the statistics gathered for these plots were somewhat low due to the limited access to time on facilities and the relatively low activity of the ^{241}Am source used. By fitting first order Gaussian curves to both measurements of Pixel #24 the peaks occur at 5.349 MeV and 5.338 MeV

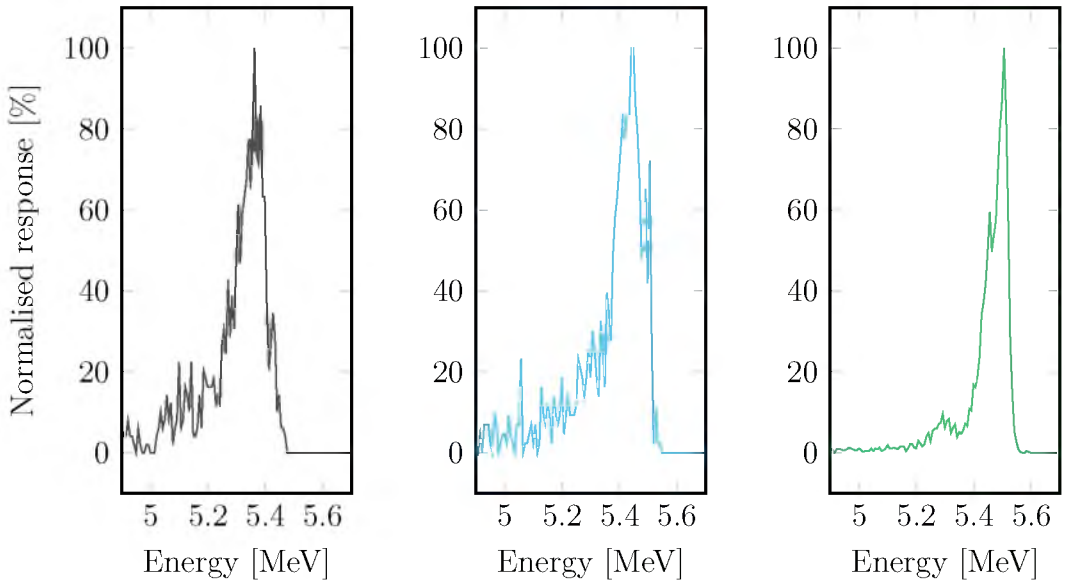

(a) Pixel 24 (b) Pixel 64 (c) Pixel 59

Figure 7.6: Alpha spectroscopy of three select pixels (#24, #59, #64) using ^{241}Am source. Curves have been normalised for comparison.

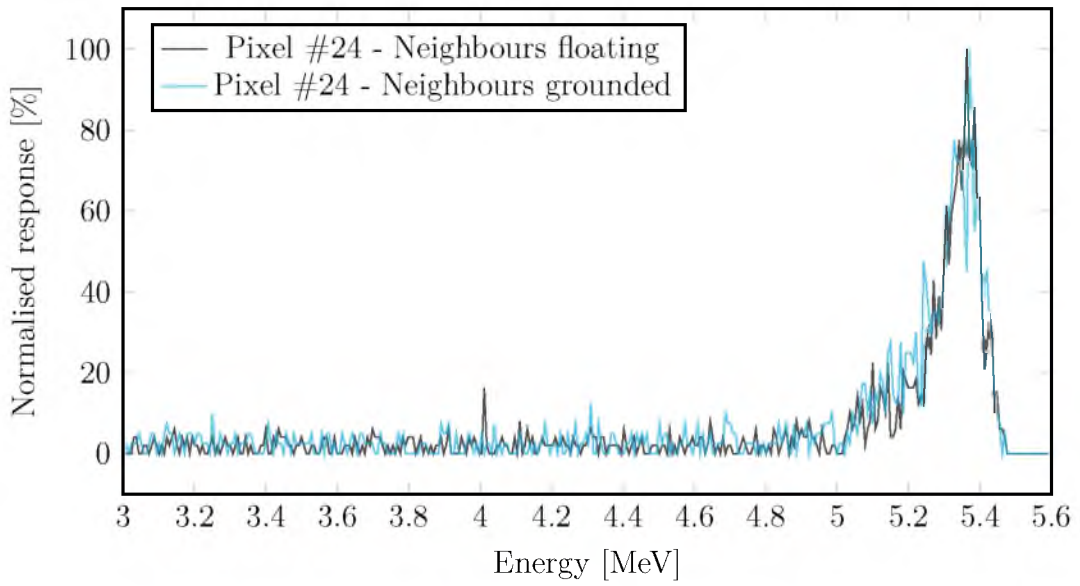

Figure 7.7: Alpha spectroscopy using ^{241}Am source for pixel #24 with and without neighbouring pixels grounded. Curves have been normalised for comparison.

for floating and grounded neighbour connections, respectively. These peaks align to within 99.79 % at these energies, showing that neighbouring pixels have a negligible effect on a given pixel.

More sophisticated methods for measuring the energy response of the detector can be accomplished through ion beam induced charge collection, where ions are raster scanned at a detector sample to provide both charge collection and positional information.

7.1.4 Charge Collection - Ion Beam

Using the heavy ion beam facilities in the ANTARES Accelerator at ANSTO, ion beam induced charge collection (IBICC) was carried out using a 5.5 MeV He^{+2} ion source. Similar to the effect which occurs in alpha spectroscopy, explained above in Section 7.1.3, ion beam measurements are useful in charge response analysis due to the full energy deposition of the particles in the silicon detector. The helium ion has a projected ionisation depth of $\sim 28\,\mu m$ [208] in silicon. The preamplifier used for these sets of experiments was the Amptek A250[225].

The aim of these measurements was to determine the charge collection response of the pixels, the response of applied bias voltage, and to determine the extent of charge sharing. Three pixels of interest were selected to illustrate the results, namely, Pixels #24, Pixel #64 and Pixel #56, see Figure 7.5 for their locations. Median energy maps and the corresponding energy spectra are shown for large and small pixels in Figure 7.8 and Figure 7.9, respectively. The data was calibrated using input from a pulser signal of known energies and curve fitting the channel energies accordingly.

The measured energy resolution of the silicon detector was good, having a FWHM of 20 keV or 0.37 % at the main energy peak. Lower energy events lead to splitting and broadening of the main peak and are more noticeable in the spectra of the small

diodes, as seen in Figure 7.9. This occurred as a small portion of the alpha particle energy was deposited in the non-sensitive silicon oxide and aluminium layers and where ionisation occurred on the edge of the sensitive region causing partial collection, as seen in Figure 7.10.

Charge collection mapping was conducted as a function of bias voltage for both sizes of pixel. The bias voltages used for both pixel sizes were 0.0 V, −10.0 V, −20.0 V, −30.0 V, −40.0 V and −50.0 V and the ion source was 5.5 MeV He^{+2}. The normalised response was plotted as a function of the bias voltage and presented in Figure 7.11. The values for this response curve were taken as the average of 20 pixels × 20 pixels taken at the centroid of the 0.0 V image for each size, respectively.

It can be seen that the charge collection response of both pixel sizes increased substantially between 0.0 V – 10.0 V, after which the response flattened. Nearly full depletion occurred for both pixel sizes, reaching about 96% charge collection efficiency.

To determine whether or not charge sharing occurs between neighbouring pixels, charge collection mapping was conducted for Pixel #24 under two different conditions. This first involved having Pixel #24's nearest neighbouring pixels connected to the test circuitry ground, and the second left them disconnected (floating). Connecting the pixels to ground eliminated any electric field which would act to attract nearby charge to them; leaving them floating did not prevent this from occurring.

The neighbouring pixels included Pixels #17 – # 19 and #25 – #27, and are indicated in grey in Figure 7.5. Charge collection maps were produced using a helium ion source, for neighbours grounded and floating. The resulting energy spectra, normalised to their ion source peaks, are presented in Figure 7.12. No significant changes in spectra occurred due to partial charge collection.

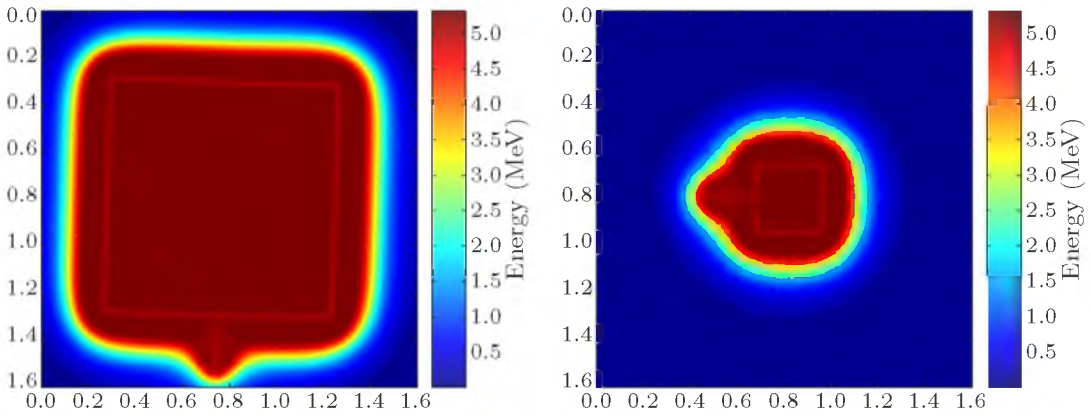

(a) Pixel #59 (b) Pixel #64

Figure 7.8: Median energy map for Pixels #59 and #64; large and small type pixels with a p+type region of area 1.00 mm × 1.00 mm and 300 µm × 300 µm, respectively. The measurements were taken with a bias voltage of −50.0 V. Spatial axes are in units of millimetres.

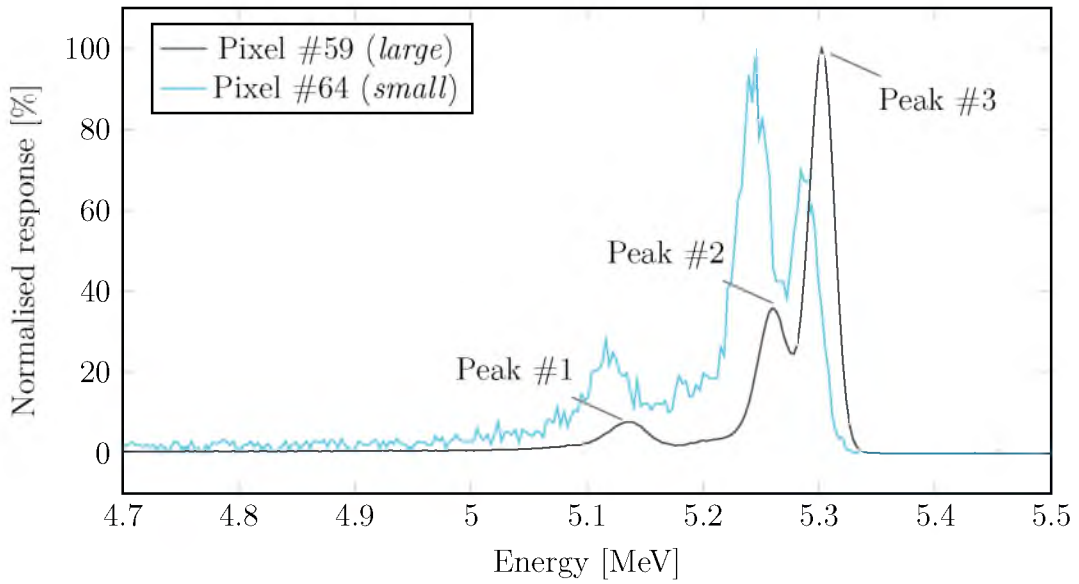

Figure 7.9: Energy spectrum for Pixels #64 and #59, small and large type pixels respectively. The measurements were taken with a bias voltage of −50.0 V. Three prominent peaks are visible and have been labelled. Spatially resolved maps which are thresholded over these peak regions are presented for Pixel #59 in Figure 7.10.

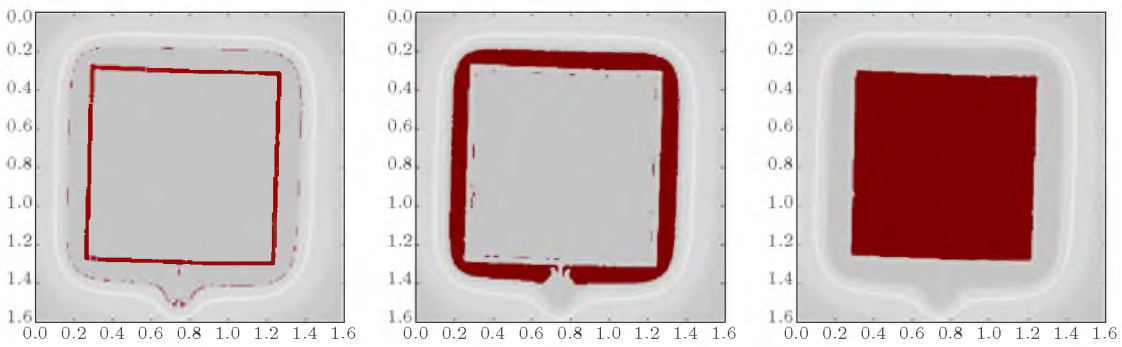

(a) Peak 1 (b) Peak 2 (c) Peak 3

Figure 7.10: Spatially resolved energy windows of the three peaks shown in Figure 7.9 for Pixel #59 with bias voltage of −50.0 V. Peak #1 occurs at the aluminium contact above the $p+$ region, Peak #2 occurs due to the silicon dioxide layer over the edge of the sensitive region, and Peak #3 occurs over the exposed $p+$ region.

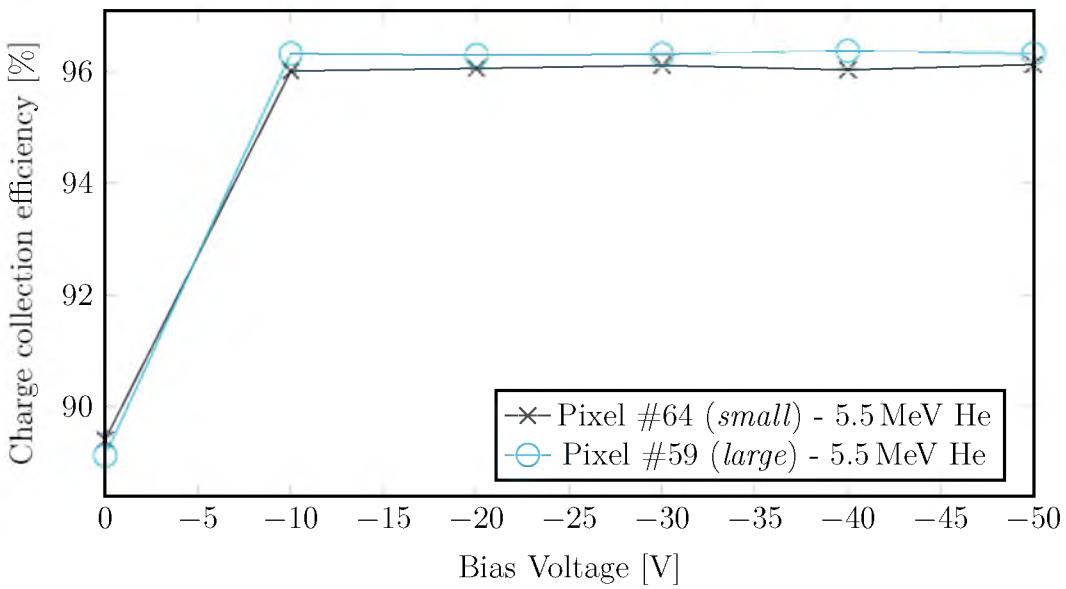

Figure 7.11: Energy spectra with a bias voltage of −50.0 V using 5.5 MeV He^{+2} for Pixel #64 (*small*) and Pixel #59 (*large*). Both datasets are normalised to the 5.5 MeV ion energy.

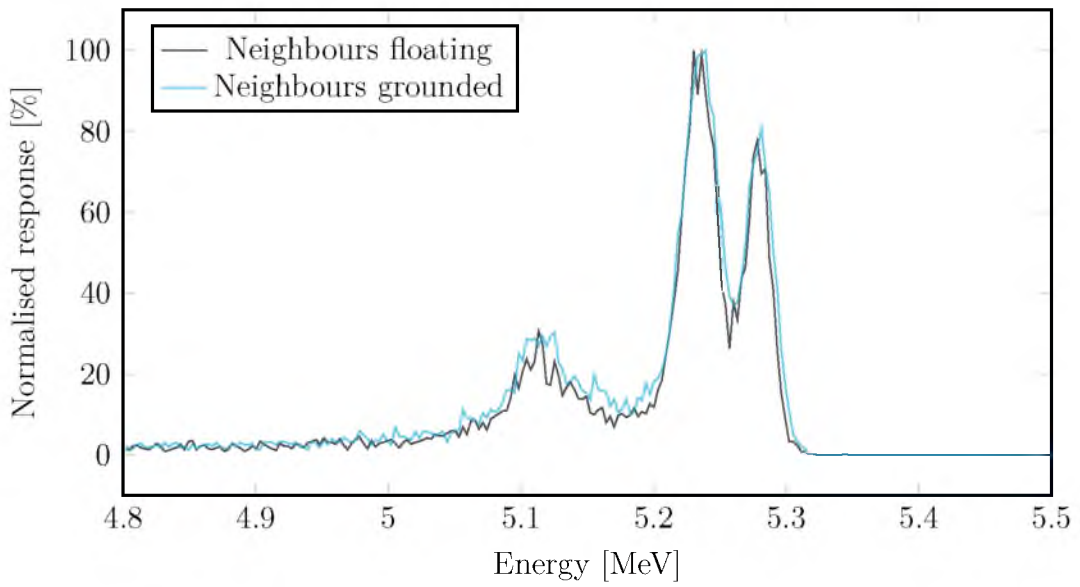

Figure 7.12: Charge sharing comparison of Pixel #24 (*small*) at −50.0 V with neighbouring pixels left floating (disconnected) and with neighbours connected to the test circuit ground. The curves are normalised to their respective ion source peaks. Neighbour pixels include Pixels #17 – # 19 and #25 – #27.

7.1.5 Monte Carlo Dose Response Simulations

In order to convert the values returned by the detector electronics to dose response in tissue, the energy response both in tissue and the detector must be quantified. As described in Section 6.3, the semicircular pixelated detector is located within the spherical eye phantom, such that the detector central axis aligns with the plaque central axis. Despite this, there is still an effect of differences in attenuation of the low energy photons that propagate through the silicon plane compared to water. This effect depends on the angle of the plaque due to differences in the number of seeds crossing the silicon detector plane. As the silicon pixelated detector is thin (300 µm) relative to the size of the eye phantom, the impact of dose conversion factors in spectroscopic dosimetry for each pixel is expected to be low.

The effects of the perturbation of the radiation field by both the silicon detector within the PMMA (poly(methyl methacrylate)) eye phantom and the substitution of

water by PMMA, need to be accounted for. This was performed using conversion factors to convert the detector's spectroscopic pixel response to tissue (water) dose for each pixel. Monte Carlo simulation offers a strong platform for quantifying these details and enabling the use of PANOPTES for dosimetry.

To calculate the conversion factors for PANOPTES, Monte Carlo simulations were performed using the Geant4 Toolkit[226,227]. Here, the full PANOPTES detector, PMMA eye phantom and surrounding air were modelled, below a 15 mm ROPES eye plaque, loaded with ten ^{125}I seeds. The simulation included modelling the full PANOPTES detector where the sensitive volumes corresponded to the individual pixels. The detector was modelled inside a PMMA eye phantom. A 15 mm ROPES eye plaque containing ten Oncura model 6711 ^{125}I seeds was located at the apex of the eye phantom, and the phantom housed the detector, as shown in Figure 7.13.

The Livermore low energy physics models[228] were used with Geant4 version 9.5 patch 01. The individual physics interactions considered in the simulations were the photoelectric effect, Compton scattering and coherent scattering for photon interactions and Bremsstrahlung, ionisation and multiple scattering for electrons, with a 1 µm minimum range set for the generation of secondary particles. The simulations of the eye phantom in the detector were performed in two configurations:

1) the materials used for the detector, phantom and environment were silicon, PMMA and air, respectively; and

2) all materials, except the plaque and seeds were modelled as water.

Each of these configurations consisted of a set of measurements with the plaque-detector angle varying from 0° – 360° in 15° increments. Computational cost was reduced as only 180° needed to be covered in the simulation due to the symmetry of the model. The conversion factors for each pixel were calculated as the ratio of dose

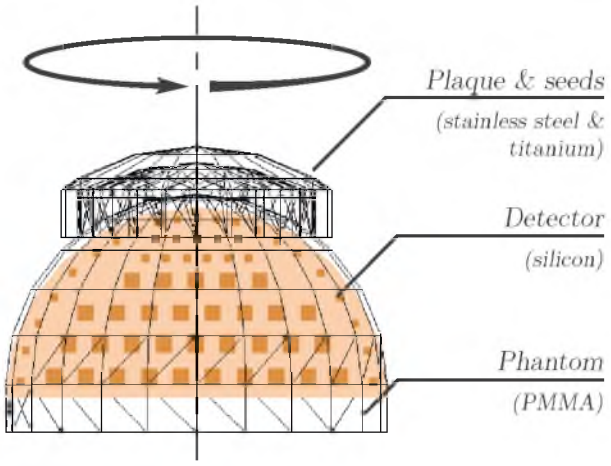

Figure 7.13: Schematic of Monte Carlo model where two material configurations were compared, treatment equivalent (water) and phantom equivalent (silicon, PMMA, etc.). For clarity, the seeds are not displayed.

measured in silicon to dose measured in water averaged, across all angles, as seen in Equation 7.2.

$$k_i = \frac{1}{24} \sum_{\theta=0,15,30,\ldots}^{360} \frac{D_{Si_i}(\theta)}{D_{H_2O_i}(\theta)} \tag{7.2}$$

Equation 7.3 shows the dose, $D_{w_i}(\theta)$ as a function of plaque angle, θ, where N_i is the number of counts per unit area at Pixel #i, and $k_i(\theta)$ is the *conversion factor* for this pixel, at plaque angle, θ.

$$D_{w_i}(\theta) = N_i \times k_i(\theta) \tag{7.3}$$

The conversion factors presented in Figure 7.14 show that the positions of the pixel dictate their energy response; the pixel conversion factors are clustered into groups corresponding to their layout. The closer a given pixel is to the plaque, the higher the proportion of its incident particles that will have deposited energy in silicon, giving it a

more influential conversion factor. These data are tabulated in Table A.2 in Appendix A.

The deviations of the conversion factors calculated for each pixel across all angles are presented as error bars in Figure 7.14 and are plotted in Figure 7.15. These data are tabulated in Table A.2 in Appendix A. The pixels that are positioned closer to the central plaque axis have less deviation across all angles. The mean deviation across all pixels is 1.9 %, while around 96 % of the deviations from all pixels and angle fall within 4.0 % and the absolute maximum deviation from all pixels and all angles is 7.4 %, on Pixel #2, one of the farthest from the plaque.

It can be seen from Figure 7.15 and the pixel map in Figure 6.5 that with decreasing pixel-plaque distance, there is a reduction in angular discrepancy across all angles. This is ideal for dosimetry as these pixels fall in the region of most interest, near the plaque.

7.2 Integrated Detector Characterisation

The systematic response of the PANOPTES was evaluated for calibration and understanding of performance. Using a flat radiation field, the PANOPTES was used to measure the spectral response of an ^{125}I source, and the detector-ASIC sensitivity was normalised.

7.2.1 Energy Resolution and Thresholding

In order to calibrate the readout electronics for energy thresholding, the PANOPTES was configured as a single channel analyser (SCA) and used to measure an ^{125}I source. Energy thresholding is the process of counting only input energies within a given range. This was achieved by setting the global threshold DACs on the readout electronics to compare against input pulse heights (event energies). Only the low-level threshold required tuning, in order to ignore level energy noise. The upper-threshold was set

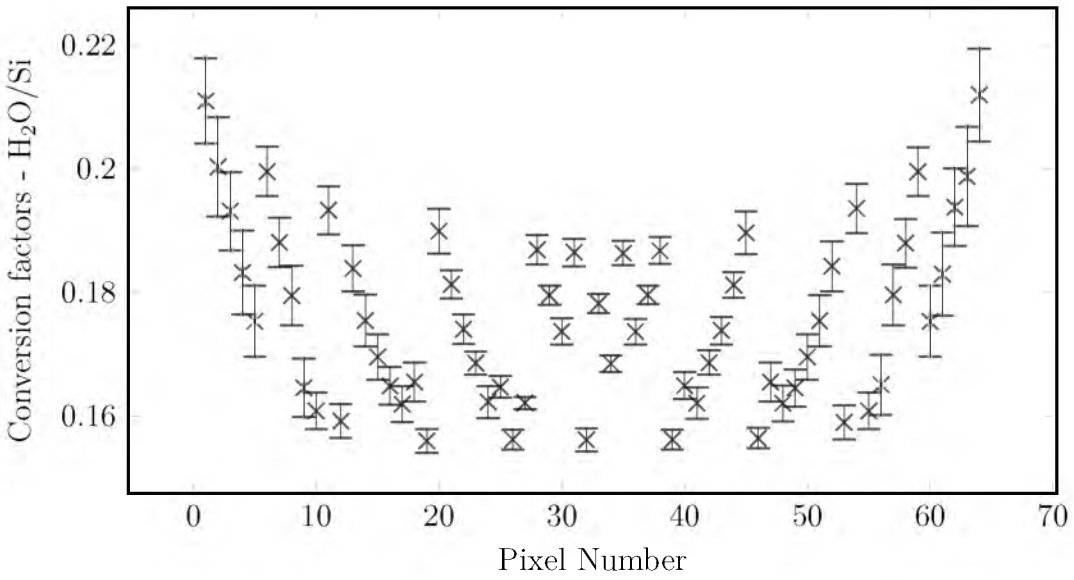

Figure 7.14: Dose to water conversion factors for all pixels, averaged across all angles. The conversion factor value is lower for pixels closer to the plaque. The error bars corresponding to each pixel represent the standard deviation of the conversion factors of all angles for that pixel.

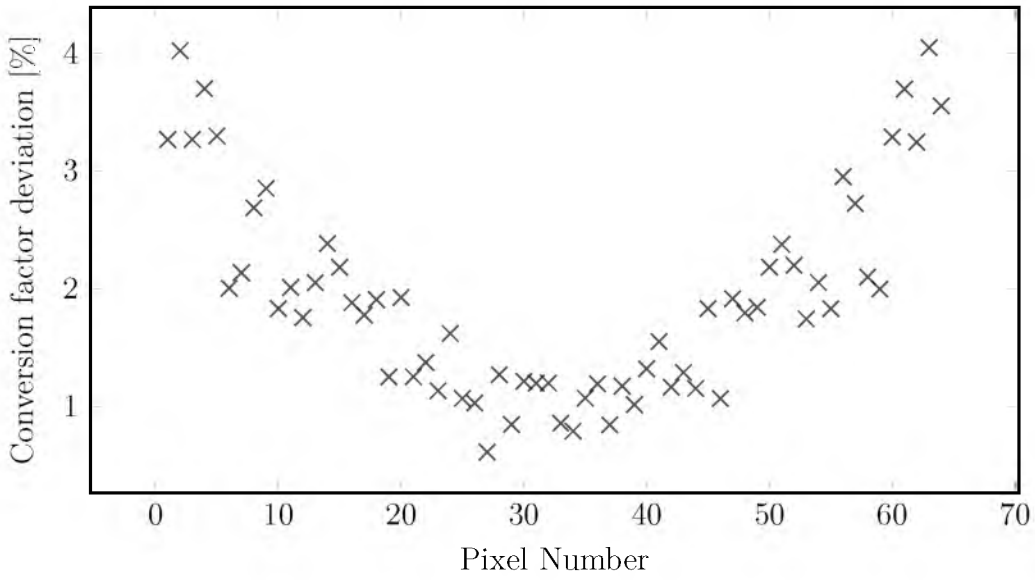

Figure 7.15: Angular discrepancies across all angles for simulated conversion factors of individual pixels. The conversion factor deviation increases with increasing distance from the plaque central axis.

fully open as there was no expected presence of high energy noise. Since the peak energies were known, linear calibration was a simple process. The software interface that was used to handle the analysis procedure is described in Section 6.4.

The device operated as an SCA by setting a small threshold window width and taking multiple acquisitions, incrementing the windows along with each acquisition, from minimum to maximum . This process was carried out for all three windows and all pixels concurrently. For Window 0, this type of windowing is not possible as it is only a one sided, low level discriminator.

Whilst all the pixels were measured, Pixels #27 and #34 were selected for presentation due to their central location, good statistics and difference in size; i.e. small and large types, respectively. The selected pixels are highlighted in Figure 7.16, and were deemed a good representation of the dataset.

For the acquisition shown in Figure 7.17, the bin width was set to the minimum, a single channel, giving a total of 1023 bins. With a bias voltage of 50 V applied, each acquisition was set to run for 10 s, totalling an acquisition time of approximately 3 h and 20 min.

The spectra shown in Figure 7.17 have good resolution and clearly resolvable ^{125}I peaks. The FWHM for Pixel #27 and Pixel #34 are 2.5 keV (9.3 %) and 3.0 keV (11.1 %), respectively. Low energies, not shown on the plot, are dominated by noise. Energy thresholding was used to select only the peaks displayed in Figure 7.17, which improved dosimetric accuracy on the PANOPTES.

7.2.2 System Equalisation

A detector's sensitive volume is determined by its geometry and applied bias voltage, and hence amount of charge collected for a given radiation flux density, see Section 7.1.4. The sensitivity of individual pixels of the same size could differ slightly from

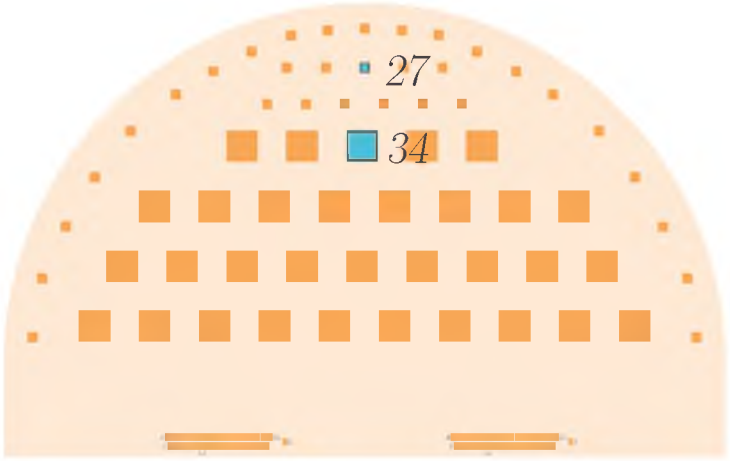

Figure 7.16: Location of Pixels #27 and #34 used in the spectral measurement.

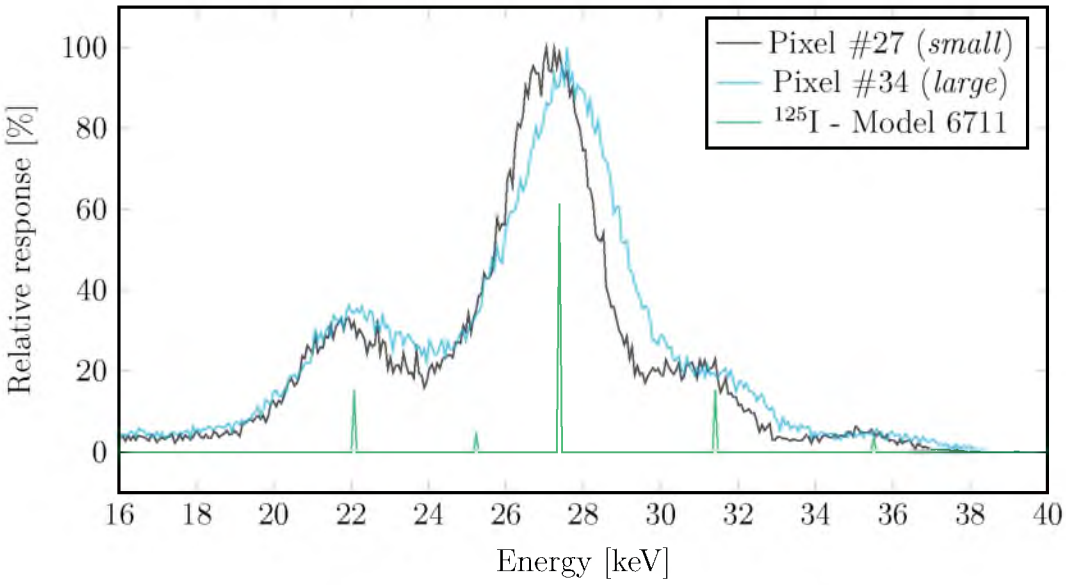

Figure 7.17: Spectrum of $10\times^{125}$I seeds loaded in ROPES 15 mm plaque with phantom. Taken by configuring the readout ASIC to perform single channel analysis using Pixel#27, the location of which is shown in Figure 7.16. The relative emission spectrum of a Model 6711 brachytherapy seed is overlaid for comparison. *Source*: Ling et al.[229], Bé et al.[230]

one another due to the presence of silicon defects and resistivity variations in the pixel and its coupled readout electronics channel. Before the PANOPTES can be used for dosimetry, the pixel response must be equalised through this type of flat-field calibration. The calibration factors determined in this set of tests could be subsequently applied through the Panopticon software, as detailed in Section 6.4.

In order to determine the individual response of each pixel-readout channel couple, measurements were taken using a flat-field x-ray source. This testing was carried out at the Illawarra Cancer Care Centre (ICCC) using a Gulmay D3300, orthovoltage machine. The detector was connected to its readout electronics and aligned at a source-detector distance (SDD) of 3 m from the beam source, see Figure 7.18 for an annotated photograph.

The orthovoltage machine was used with a 10 cm circular applicator with a 50 cm FSD (focus to surface distance). The intensity of profile of the largest available field size (15 cm × 15 cm) is presented in Figure 7.19. The beam shows a flat response for the 150 mm specified region and the region pertaining to the 10 cm applicator used experimentally falls within this. Deviations in this field were diminished when the focal spot was extended to the location of the detector at 3 m, where it became a ⌀60 cm field. Given the active area of the detector is approximately 24 mm × 12 mm, the resulting relative uniformity was sufficient for calibration.

The detector board was mounted within a thin PMMA box and encapsulated in aluminium tape, which was grounded to the digital ground of the electronics. This acted to shield the device from electromagnetic interference and inhibit the transmission of light through the box to the detector. To further limit light exposure, the acquisitions were performed in a dark room.

The readout ASICs were configured with the energy windows set fully open whilst excluding dark noise, gain set to 0.75 mV fC^{-1} and shaping time set to 500 ns. Using a

Figure 7.18: Photograph of flat field calibration experiment undertaken at the Illawarra Cancer Care Centre, showing the source and detector, encapsulated in a shielded, dark box.

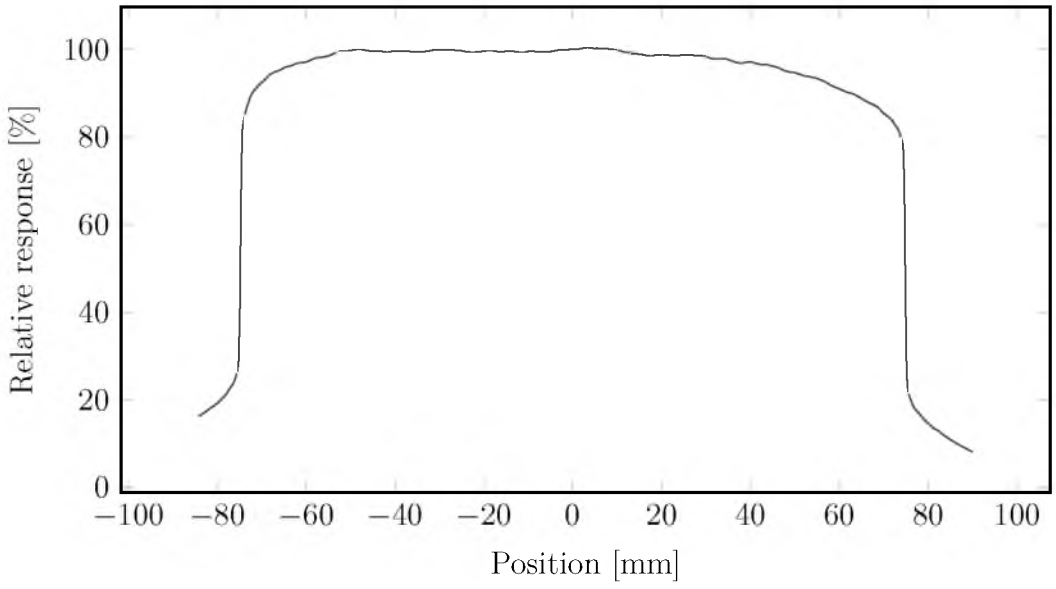

Figure 7.19: Profile of the 250 kV beam used for flat field calibration. This measurement was performed on the surface of a Plastic Water® [180] phantom using a 10 cm circular application with a FSD of 50 cm.

beam voltage of 250 kV, 100 acquisitions of 100 ms were taken and integrated to give a total acquisition frame of 10 s. The dose rate was 68 cGy min^{-1}, calibrated to water at 500 mm. Table A.1 in Appendix A summarises the configuration parameters used in this calibration.

The small and large pixel datasets in Figure 7.20 represent the calibration factors of the individual pixels, normalised to the pixel with highest response (Pixel #30). The mean calibration factor for the small and large pixels is 7.57 ± 0.59 and 1.09 ± 0.05, respectively. From these mean values, the large pixels are approximately 6.9 times more sensitive than the small pixels.

The overall uniformity of similarly sized pixels was good with a standard deviation of 7.8 % and 4.3 % for small (300 µm × 300 µm) and large (1.0 mm × 1.0 mm) pixels, respectively. This overall response implies that the detector substrate is relatively homogeneous and that the performance of the readout channels of the HERMES ASIC are also relatively uniform.

The colour coded pixel map shown in Figure 7.21 was generated with the Pantopicon software interface and provides a visual representation of this information and the number of counts that were recorded for the given calibration. The values presented have been left as raw, showing that the count statistics ranged from about 579×10^3 – 61.4×10^3. The average statistical error to one standard deviation for the large pixels was 0.16 % and for small was 0.41 %. These data are tabulated in Table A.2 in Appendix A.

7.2.3 Combined Conversion and Equalisation

Combining the conversion factors from the Monte Carlo simulation and the calibration factors, the pixel colour map in Figure 7.22 was produced. This plot illustrates the corrections that were applied to the PANOPTES measurements taken in the following

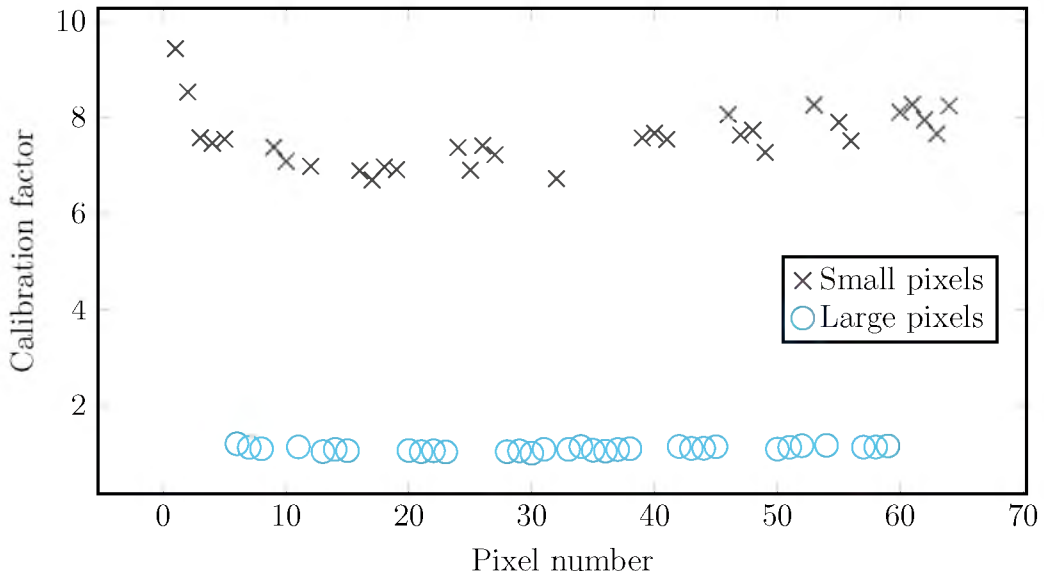

Figure 7.20: Calibration factors derived from flat field experiment plotted for small and large pixels. The high calibration factors on the smaller pixels account for their smaller sensitive volume relative to the larger pixels.

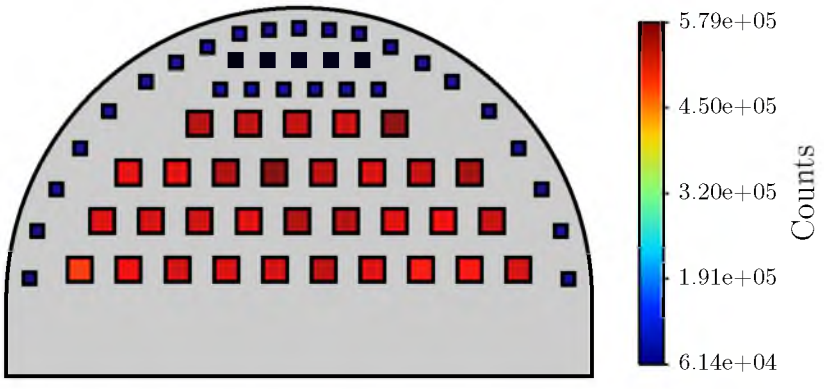

Figure 7.21: Visual representation of detector response from the flat field calibration in raw counts taken as the summation of $100 \times 0.1s$ acquisitions, as detailed in Table A.1

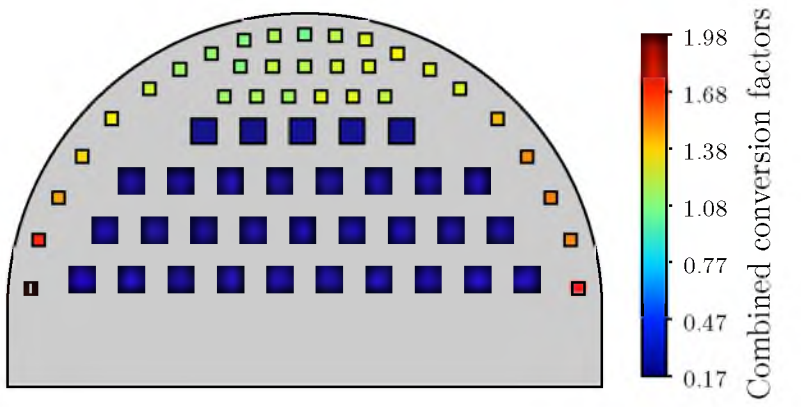

Figure 7.22: Visual representation of the combined flat-field and dose-to-water conversions. Performed using fully loaded ROPES 15 mm. Data are provided in Table A.2 in Appendix A

chapter. These data are tabulated in Table A.2 in Appendix A.

Equation 7.4a was used to calculate the dose to water, $D_{w_i}(\theta)$, at the location of a given pixel, Pixel #i, and for a given angle, θ. Here, $N_i(\theta)$ is the number of counts measured at Pixel #i, b_i is equalisation coefficient normalised to the most sensitive pixel, Pixel #30, $k_{i_{ave}}$ is conversion coefficient for Pixel #i, averaged across all simulated angles.

$$D_{w_i}(\theta) = N_i(\theta) \times b_i \times k_{i_{ave}} \tag{7.4a}$$

$$D_{w_i}(\theta) = N_i(\theta) \times b_i \times k_{i_{ave}} \times a_i \tag{7.4b}$$

A more complete version of this equation, shown in Equation 7.4b, would also include a factor for absolute calibration. In this case, a_i is the conversion factor of the number of counts measured in the detector to the dose in silicon. Determining this calibration would involve placing a single seed in Plastic Water at 1 cm above a central pixel, for example Pixel #34, with the equalisation coefficient equal to 1. The response from each pixel would be recorded and compared to the expected dose at each point

as per the TG-43U1 formalism and verified using Monte Carlo.

7.3 Discussion

The detector, as a standalone device and integrated into PANOPTES, was characterised to determine parameters to prepare it for use in accurate plaque brachytherapy dosimetry. Current-voltage and capacitance-voltage curves were measured to quantify device performance. The energy resolution of the detector was measured using alpha-spectroscopy and ion beam induced charge collection. The latter process was also used for geometric mapping of the sensitive volume of the selected pixels. Monte Carlo simulators of the device were used to accommodate for energy corrections from silicon to water. With the detector integrated into PANOPTES, a spectrum was taken using single channel analysis, and finally, the PANOPTES was calibrated using a flat-field photon beam.

7.3.1 Current-Voltage Characterisation

By measuring its current-voltage characteristics, the detector was shown to behave as expected, with breakdown occurring at approximately 63 V. The large pixels were shown to have a larger leakage current than the small pixels, as expected. This suggests that a greater level of operational signal noise will occur in large pixels, though it will be counter-balanced by their higher sensitivity and thus better count statistics. The relatively low overall leakage current means that the device can be used safely at room temperature which is important for clinical practice.

7.3.2 Capacitance-Voltage Characterisation

Capacitance-voltage curves of many of the detector pixels were measured to get an estimate of the expected signal quality for the device. It was shown that the track length of a pixel had a greater overall contribution to the total pixel capacitance than its geometry. Pixels far from the bonding pads had capacitance values of about twice those that were close to the pads. The fact that this track capacitance is high, relative to the pixel capacitance, makes it difficult to decouple them and determine the full depletion voltage through plotting $1/C^2$ versus bias voltage. However, the capacitance is not required to determine the depletion voltage, only the point when it is saturated. Depletion characteristics of the pixels were investigated later using ion beam analysis.

7.3.3 Energy Resolution - Alpha Spectroscopy

The energy spectra of three pixels measured showed the detector to have good energy resolution between 1.3 % – 2.2 % for the set. This is important in order to ensure that the spectrum can be clearly identified and separated from noise using energy thresholding on the readout electronics. Given the devices all performed with similar energy peaks, common electronics parameters may be used for energy thresholding of the ^{125}I spectrum. It also addresses one of the aims of this study, showing that the detector substrate has good uniformity and fabrication quality and suggests consistency between both pixels and detectors, which is important for eye plaque dosimetry. Energy resolution is also important, given differentiation of the spectral peaks is needed if spectroscopic plaque dosimetry is to be investigated using the separate photopeaks. Charge sharing between pixels was shown to be of negligible effect, ensuring that spatial resolution of the detector is not effected, which is very important for the measurement of steep dose gradients in plaque brachytherapy.

7.3.4 Charge Collection - Ion Beam

Charge collection of the pixels of both sizes was uniform over the sensitive volumes of the tested samples. The surrounding contact pad is discernible in the charge collection maps for the 5.5 MeV H^{+2} ions, due to energy loss in the aluminium and silicon oxide over-layers around the periphery of the pixels. This has no effect in ^{125}I ($\sim$ 22 keV – 35 keV γ) and ^{106}Ru (3.54 MeV β) isotopes commonly used in ophthalmic plaque radiotherapy.

Charge collection efficiency was measured as a function of bias voltage to determine an acceptable operating voltage for PANOPTES. The increase in bias voltage only caused a marginal increase in collection efficiency between 10.0 V – 50.0 V. Despite this, it is advantageous to operate the device at this voltage to ensure that capacitance induced noise is minimised and collection rates are maximised at no significant detriment. The leakage current at this voltage for a single pixel, was within about 1 nA, and no over-heating effects were observed during the testing.

The sensitive volumes of the pixels measured were well defined spatially. This provides accurate dose correction when converting from dose in silicon to dose in water. In addition to this, during charge sharing tests, neighbouring diodes were not visible on the median energy maps. Supporting the conclusions of the tests performed using alpha-spectroscopy in Section 7.3.3, there was no significant charge sharing effect present.

7.3.5 Monte Carlo Dose Response Simulations

Critical for dosimetry, calculating the energy correction factors for each pixel needed to be performed over a range of angles. The dosimetry of the eye plaque is inherently difficult due to the steep dose gradients, small overall size and low energy photons, and is only worsened when angular dependence in detection is also considered. Through

the Panopticon software, this angular dependence can be accounted for, as correction factors can easily be applied to dose measurements made.

The angular response deviation for all pixels falls within around 4 % for the ROPES 15 mm plaque loaded with $10\times^{125}$I seeds. In relation to other current systematic errors in plaque brachytherapy, such as source activity variation and plaque placement, this level of uncertainty is within similar limits.

The energy correction factors were calculated through simulation using a ROPES 15 mm eye plaque model. A generic correction factor for each pixel, accounting for all plaques and angles, is not the optimal solution. The accuracy of said model will determine the ultimate accuracy of the calculated silicon pixel response to dose in water conversion. Plaque and angle specific conversion factors could be developed and evaluated for other types of plaque, but would still be limited by simulation accuracy and such optimisation is beyond the scope of this project.

The Monte Carlo simulations were performed, both to serve as a proof of concept for the operation of the PANOPTES as a dose verification tool, and to generate the dose to water conversion factors for use with the measured PANOPTES data.

7.3.6 Energy Resolution and Thresholding

The spectra taken for the pixels by the PANOPTES illustrates that the resolution is good enough to identify individual peaks on the ^{125}I spectrum. By observing the spectra from all the pixels, the global low energy cut-off could be determined as the distinct minimal point between the low energy noise and the beginning for the first ^{125}I peak. Based on this, the value was selected to be at Channel #300 or 17 keV.

The measurement taken is not ideal in providing the original ^{125}I spectrum, as it used the PANOPTES phantom. While it gives an indication of the level of photopeak identification possible, it was not used for energy calibration of the device. Instead, a

phantomless calibration was performed.

7.3.7 System Equalisation

Equalisation was carried out using a flat-field calibration with a photon beam. This enabled normalisation of the sensitivity of individual pixels and the amplification gain by their corresponding readout electronics channels. The deviation in the calibration factors of the small pixels was greater than that of the large pixels. This could be due to the small pixels being located closer to the perimeter of the detector where crystal defects, caused by cutting, are more likely. This simple calibration process would need to be performed for the commissioning of any newly constructed PANOPTES device. For correct calibration, these flat-field factors clearly need to be used in conjunction with the silicon pixel response to water dose conversion factors. The calibration factor map is dependant on specific detector and ASIC sensitivity, in addition to the silicon detector response to water dose conversions.

7.4 Conclusion

The custom designed, semicircular, pixelated silicon detector was characterised as an independent device and then also integrated in the rest of the PANOPTES. Characterisation of the device was done through generating I-V and C-V curves, alpha spectroscopy and Monte Carlo simulation. The PANOPTES was characterised through spectroscopy and flat-field calibration.

Measurements of current-voltage curves showed that the detector was functioning correctly, with leakage currents around less than 1 nA for most pixels. It also showed that the breakdown voltage was around 63 V, so further testing and operation should be done below this level.

The capacitance of the pixels was influenced more by the pixel track length, than

the size of the pixel. The two capacitances were difficult to decouple, and as a result, the full depletion voltage could not be determined from this. The overall capacitance of the pixels was relatively low and should allow good signal quality.

The energy resolution of the detector was measured through alpha-spectroscopy. The process showed the small and large pixels have similar energy responses and there was negligible effect of charge sharing from neighbouring pixels, which is important in energy preservation.

Extending upon the alpha-spectroscopy measurements, ion beam induced charge collection showed that the detector pixels had well defined geometry, uniform charge collection and, again, no influence from neighbouring pixels in regards to charge sharing. The greatest observed charge collection efficiency occurred at a bias voltage of 50 V. These factors are important to verify the accuracy of dose conversion factors.

These dose conversion factors were calculated using Monte Carlo simulations on Geant4. The dose-to-water, energy conversion factors were calculated for each pixel, averaged for all angles from 0° to 360° in 15° increments. The angular deviation of the conversion factors fell to within about 4% for all pixels while the maximum deviation across all pixels and angles was 7.4%.

The single channel analyser configuration of the PANOPTES is a useful tool in commissioning the device. It allowed the energy threshold cut off to be determined across all channels, accounting for individual device characteristics. The lower level threshold cut off determined for operational use was Channel #300 (17 keV).

The deviations in sensitive volume of the individual pixels and readout channels were measured using the flat-field from an orthovoltage machine. Pixel geometry was the major factor in dictating the sensitive volume for the detector. These values were then normalised and used to apply calibration factors to the individual pixels through the software interface.

Characterisation of the PANOPTES has allowed for operational parameters to be determined and to gain an understanding of the expected behaviour of the system during the subsequent performance testing.

Chapter 8

Early Performance Testing

The previous chapters of Part III detailed the design and characterisation of the PANOPTES. These characterisations demonstrated the capabilities of the design, and the completion of the dosimetry system. In this chapter, dosimetry measurements were taken with the complete PANOPTES using symmetric and asymmetric seed configurations to produce depth-dose plots and dose maps, and assess the potential of interpolating these into dose volumes.

These planar dose map measurements were converted to dose in water, and represented as isodose plots and three-dimensional sliced dose volumes. For clinical significance, comparisions to the depth-dose plots and dose maps were carried out against the primary dose calulation methods used in eye brachytherapy. These included Monte Carlo simulations, the Plaque Simulator software, and the TG-43U1 formalism.

8.1 System Measurements

The PANOPTES was tested using a ROPES 15 mm plaque loaded with Model 6711 ^{125}I seeds. The activity of each seed was 45 µCi. For all measurements conducted in this chapter the plaque was assembled normally using the acrylic insert and stainless steel

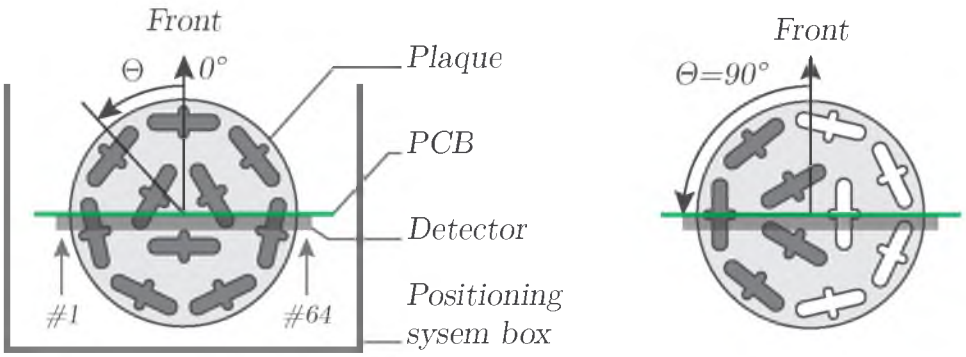

(a) Fully loaded (10 seeds, shown at 0°)

(b) Asymmetrically loaded (5 seeds, shown at 90°)

Figure 8.1: The ROPES 15 mm eye plaque loaded with ^{125}I seeds. The orientation angle, θ, is normal to the detector plane, and indicates the amount which the plaque was rotated with respect to the detector plane. The grey box and the adjacent green line indicate the orientation of the detector and PCB, respectively. The numbers #1 and #64 represent the location those pixels on the detector. These diagrams are not drawn to scale.

backing. Two seed configurations were used for the plaque in measuring planar and volumetric doses across range of plaque-detector angles. These plaque configurations are shown in Figure 8.1 and comprised:

- a symmetric ten seed layout (Figure 8.1a), and;
- an asymmetric five seed layout (Figure 8.1b).

The PANOPTES electronics hardware was configured with a 50 V bias voltage, for full depletion as measured in Section 7.1.4. A shaping time of 500 ns was selected for optimal resolution at the high count rates of imposed by the treatment. To ensure events occurred within a measurable energy range, a gain of 0.75 mV fC^{-1} was selected. All energy windows were set with a lower threshold of 17 keV, and the upper thresholds at maximum ($\sim$ 66 keV).

The acquisitions were each taken in single measurements and had a duration ranging from 30.0 s – 100.0 s. As activity of the seeds was low, this ensured that measured counts had a statistical uncertainty within 1% for all pixels. In addition, the detector

was light sensitive, and the entire positioning system was concealed within a box to eliminate external light sources.

The plaques were configured with the *front*, corresponding to $\theta = 0.0°$ as per Figure 8.1a. The plaques were loaded into the positioning system with the front facing outward from the box, after the positioning shaft had been locked down. The top surface of the detector was facing towards the back of the box, as shown earlier in Figure 6.14.

The dose distribution seen in Figure 8.2 shows an example response of a 100.0 s acquisition using ten ^{125}I seeds, orientated at $\theta = 90.0°$ as a colour scaled, pixel map output from the software interface. The response of each silicon pixel was adjusted with the flat-field equalisation data and silicon-to-water dose conversion to give a corrected response, as per Equation 7.4a, repeated below.

$$D_{w_i}(\theta) = N_i(\theta) \times b_i \times k_{i_{ave}} \tag{7.4a}$$

The pixel count values range from around 26.2×10^3 – 553×10^3 counts, giving a statistical error of 0.1 % – 0.6 %[1]. From this measurement the dose distribution can clearly be seen to diminish with increasing distance from plaque, and takes a generally symmetric, circular shape, originating from the apex of the detector. The top central pixel, Pixel #32, appears to slightly under-respond relative to its neighbours. This is most likely related to the seed distribution of the ROPES 15 mm plaque.

The colour scaled, pixel map shown in Figure 8.3 shows the converted response for five seeds, with an axial alignment of 90.0°. Dose conversions were achieved using Equation 7.4a. Across all pixels, the count magnitude ranges from 9.66×10^3 – 395×10^3 and their corresponding statistical errors, 0.2 % – 1.0 %. The detector plane bisects the

[1]Using the Poisson distribution, where it is assumed $\sqrt{s^2} \approx \sigma = \sqrt{x}$, which gives the fractional standard deviation to be $1/\sqrt{N}$.

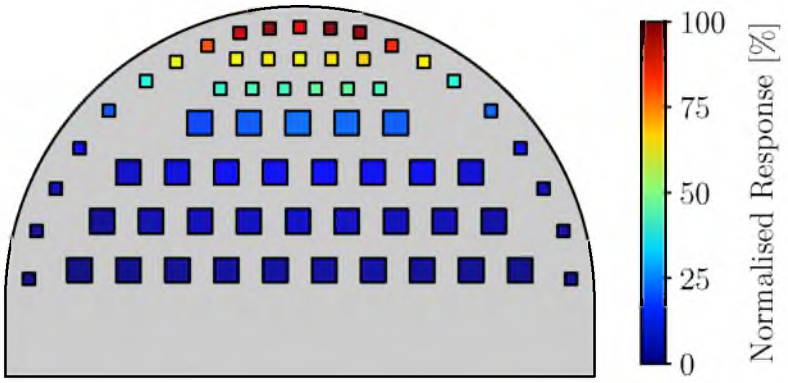

Figure 8.2: Converted dose to water measurement taken with the PANOPTES using a fully loaded ROPES 15 mm eye plaque. The acquisition time was 100.0 s and the detector plane was at 90° to the plaque angle. Counts are normalised to 100% relative to the maximum pixel value, Pixel #39.

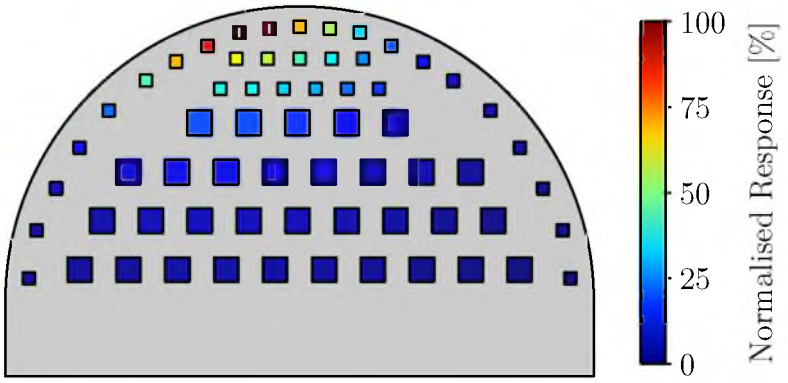

Figure 8.3: Converted dose to water measurement taken with the PANOPTES using a ROPES 15 mm eye plaque loaded with five seeds, as showing in Figure 8.1b. The acquisition time was 100.0 s and detector plane was at 90.0° to the plaque angle. Counts are normalised to 100% relative to the maximum pixel value, Pixel #19

seed configuration symmetrically, resulting in the asymmetric dose distribution seen in the pixel map. The dose gradient is steep, with an approximately 50 % reduction in dose occurring between some pixels in high dose regions.

8.1.1 Planar Reconstruction

Whilst the individual pixel values are useful for point-wise dosimetry, a continuous plot provides a better basis for dose distribution evaluation and comparison. Isodose plots were calculated through MathWorks Matlab 2012a[199] after using bicubic interpolation process on the pixel values and locations.

An isodose plot for the ten seed plaque configuration was generated for the orientation angle of 90° and is shown in Figure 8.4. This plot illustrates the presence of two possible hot spots to either side of the axis at the apex of the detector as a result of the response of Pixel #32, seen in Figure 8.2. The distribution depicts a reduction of dose by half at about 3 mm. The plot features a distinct perturbation near the dose periphery on the mid-right side, matching the calibration map from Figure 7.22 in Chapter 7, and another near the bottom left. For comparison, an additional plot at a plaque orientation of 0° is provided in Figure A.1 in Appendix A. The two plots are very similar in dose distribution.

An isodose plot using the five seed configuration was also created for a 90° plaque orientation and displayed in Figure 8.5. The 90° orientation shows strong asymmetry towards the left side of the detector. The plot depicts a small non-uniform distribution in the area of high activity, under the location of the seeds. An additional isodose plot at a plaque orientation of 0° is provided in Figure A.2 in Appendix A, which is symmetric by comparison.

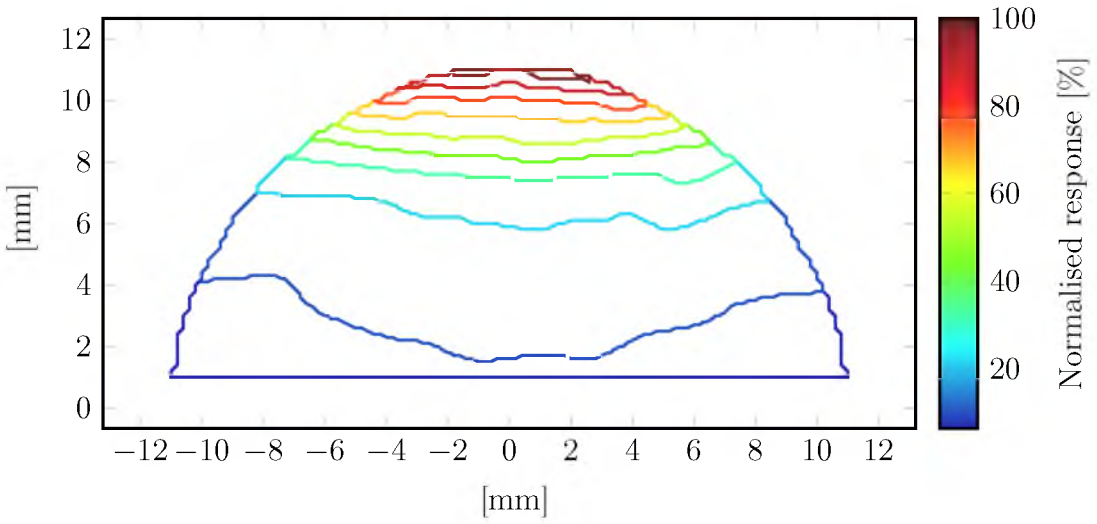

Figure 8.4: Interpolated isodose curves of PANOPTES measurement converted to dose in water with ten ^{125}I seeds at 90°. Dimensions are in millimetres and dose is normalised to 100% at the maximum value.

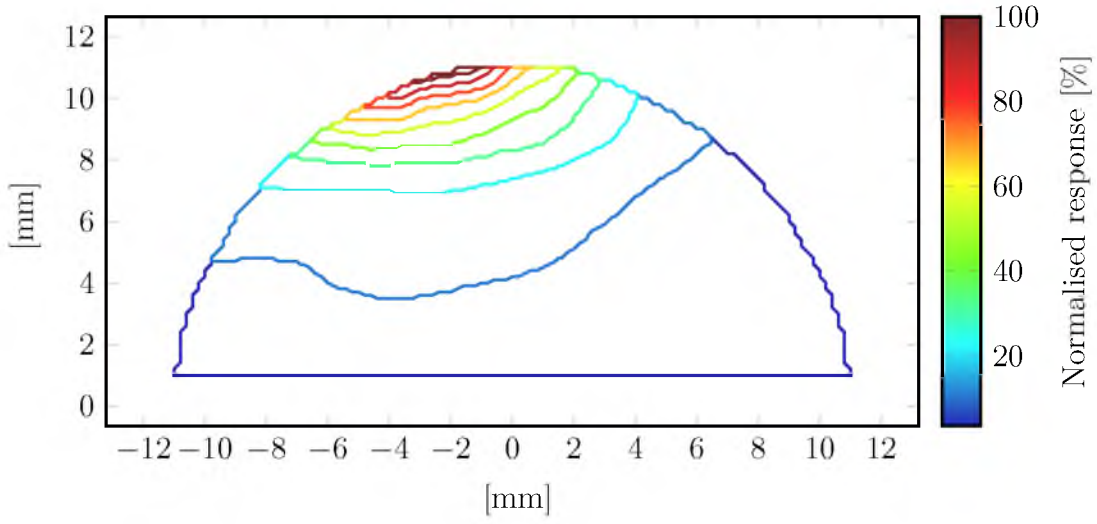

Figure 8.5: Interpolated isodose curves of PANOPTES measurement converted to dose in water with five ^{125}I seeds at 90°. Dimensions are in millimetres and dose is normalised to 100% at the maximum value.

8.1.2 Volumetric Reconstruction

For every angle measured with the PANOPTES, a dose distribution map, such as the isodose plots used in Figures 8.4 and 8.5, can be produced. This form of presentation is useful in its own right, though for an overview of the dose distribution of the entire plaque, it provides the intended foundation for three dimensional, or volumetric, dosimetry. To meet the aim of assessing the potential of interpolation for plaque dosimetry, volumetric slicing was preferable overly purely 2D representation.

The PANOPTES was used to measure a 360° sweep of the plaque in small increments. Varying the number of angle increments gives a trade-off between axial resolution, θ_i, on one side, and acquisition time and processing complexity on the other. The volumetric datasets presented here used either θ_i =18.0° or 9.0° degree increments, but the PANOPTES is capable of a resolution of θ_i =0.18°. However, for clinical applications this resolution may be superfluous and still limited by the xy resolution of the detector.

By collating the individual pixel values, their corresponding detector positions and acquisition angles, three dimensional matrix operations were used to calculate and convert from the original $xy\theta$ to an xyz coordinate system. These data sets were then linearly interpolated in three dimensions to produce a matrix of values. To improve the interpolation outcomes, only one half of the detector pixels (Pixels #1 – #34) were used in the spatial mapping. Using both halves simultaneously produced artefacts due to attenuation induced variations in the measured dose at a point in space. This was because symmetrically located pixels measured differently attenuated dose for similar locations when the plaque was rotated 180°.

Using a *slice* function, values falling on specified planes were be plotted for visualisation of the volumetric data. Acquisitions were taken for 30.0 s at each angle, which allowed for sufficiently low statistical counting error ($<\sim$ 1%) based on the seed activity.

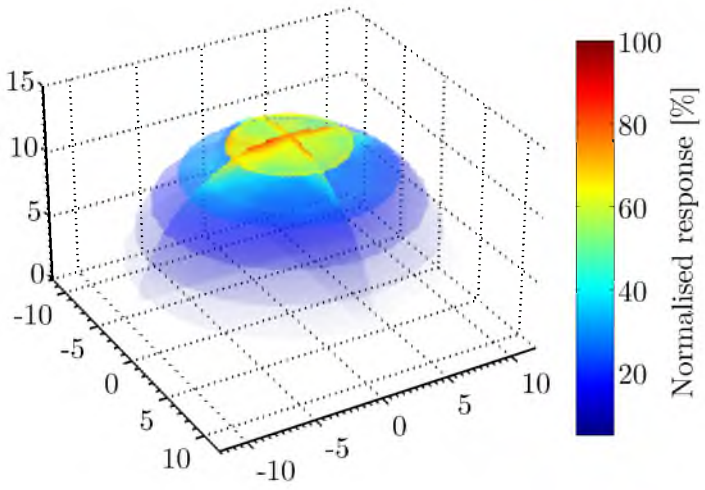

Figure 8.6: Volumetric slice plot of ten ^{125}I seeds in a ROPES 15 mm plaque using the PANOPTES acquired over 20 measurements. The slices are separated vertically by 2 mm increments. Dimensions are in millimetres and dose is normalised to 100% at the maximum value.

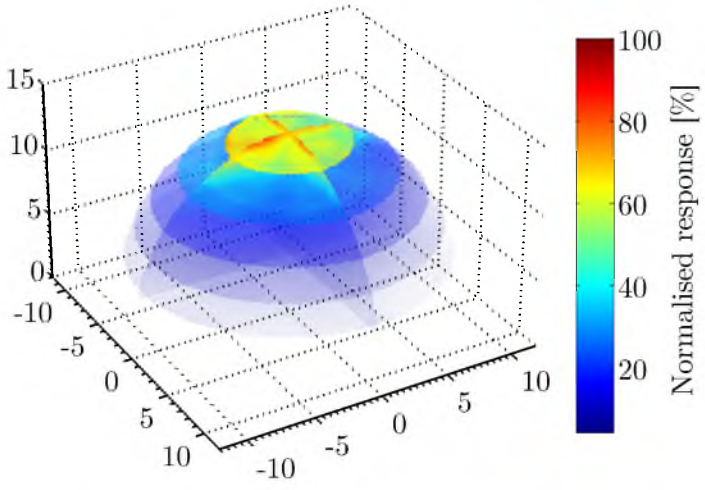

Figure 8.7: Volumetric reconstruction of PANOPTES data taken with ten seeds and 40 angles, with an increment of 9.0°. The slices are separated vertically by 2 mm increments. Dimensions are in millimetres and dose is normalised to 100% at the maximum value.

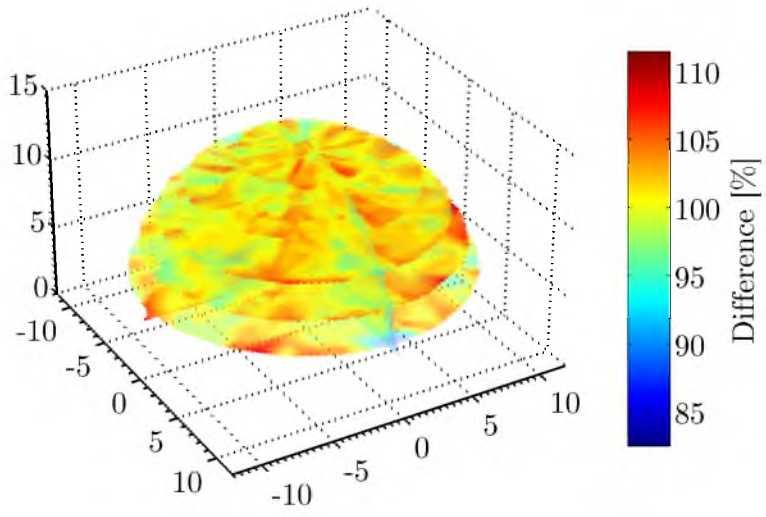

Figure 8.8: Mapped response difference between angular increments of $\theta = 9°$ and $\theta = 18°$. The difference in response is calculated using Figure 8.6 (I_{20}) and Figure 8.6 (I_{40}) as Diff $= I_{20}/I_{40}$. The slices are separated vertically by 2 mm increments. Dimensions are in millimetres.

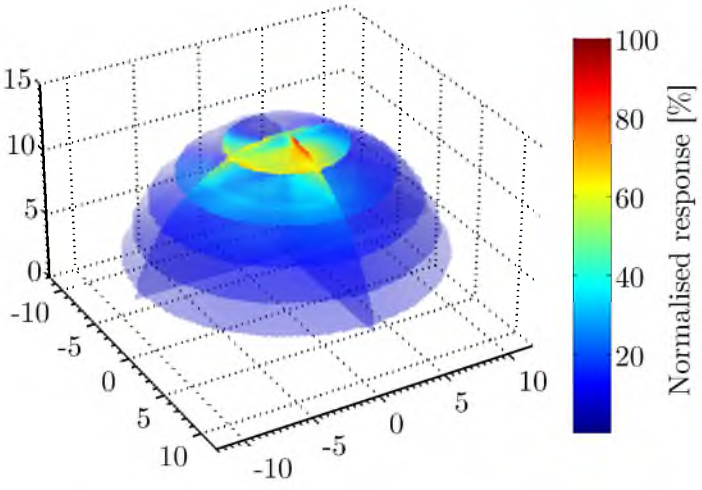

Figure 8.9: Volumetric slice plot of five ^{125}I seeds in a ROPES 15 mm plaque using the PANOPTES configured with 20 angles. The slices are separated vertically by 2 mm increments. Dimensions are in millimetres and dose is normalised to 100% at the maximum value.

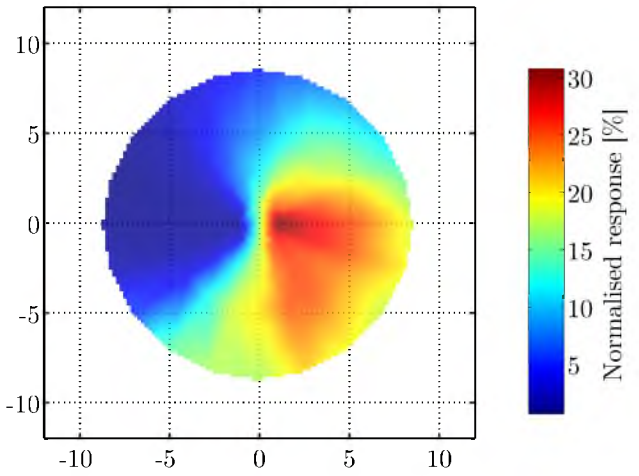

Figure 8.10: Volumetric slice in the xy plane 2 mm from the volume apex of five ^{125}I seeds in a ROPES 15 mm plaque using the PANOPTES configured with 20 angles. Dimensions are in millimetres and dose is normalised to 100% at the maximum value.

The ten seed configuration was measured with $\theta_i = 18°$ and is presented in Figure 8.6. The volume has been sliced in the xy plane at every 2.0 mm and axially at planes xz and yz. It shows a dose volume which is maximal at the apex and quickly drops off to less than 20 % after around 6 mm.

Better coverage of a three dimensional space can lead to more accurate and useful interpolation results. The dose volume in Figure 8.7 was created using twice the angular resolution, at a total of 40 acquisitions and $\theta = 9.0°$. Figure 8.8 shows that differences occur as a function of angle. These differences have a mean of $\mu = 100.6\,\%$, a standard deviation of $\sigma = 2.7\,\%$ and an absolute maximum of 118.5 %.

The dose volume for the five seed configuration is depicted in Figure 8.9 and a slice through the xy plane at 2 mm is shown in Figure 8.10. The dose distribution of the five seed data was generated from 20 angles, with an increment of 18°. On one side of the central plaque axis, the dose reaches a maximum in a relatively small volume; the other side of the axis exhibits a larger, lower intensity dose volume. The xy plane in Figure 8.10 clearly shows this feature and illustrates the usefulness of a dose volume

in generating dose planes in otherwise unavailable orientations. This xy plane also reveals the steep dose gradients that can occur in plaque brachytherapy which, in this case, may be partially attributed to dose attenuation through the detector board.

8.2 Verification

Dose verification of the PANOPTES prototype was investigated through a comparison with Monte Carlo simulations, Plaque Simulator[22] and the TG-43U1 formalism[20], as they offered the most relevance to current clinical practice. This study was conducted using the ten seed plaque configuration, also selected for clinical relevance, and involved a comparison of planar dose contours and depth-dose curves.

8.2.1 Plaque Simulator Calculations

The BEBIG Plaque Simulator[22] was used to generate planar dose maps and depth-dose data for the ROPES 15 mm plaque with ten seeds. The dose maps consisted of a 32.0 mm × 32.0 mm dose field with increments of 200 µm, centred about the centre of the eye. The plaque orientation used for the calculations was $\theta = 90°$, and was cropped to the area of the detector, as displayed in Figure 8.11. The dose map was processed with MathWorks Matlab 2012a[199] to calculate pixel equivalent values, which was interpolated to generate the isodose plot, displayed in Figure 8.12. The pixel value calculations involved taking the mean of the values that fell within the area and location of the pixels.

The dose distribution map generated through Plaque Simulator provides coverage up to the brachytherapy seeds and extends out beyond the eye. The collimation effects of the plaque are clear and the bisection of two seeds can been seen to match the plaque configuration shown in Figure 8.1a.

The PANOPTES equivalent pixel values, taken from the calculated dose map, were

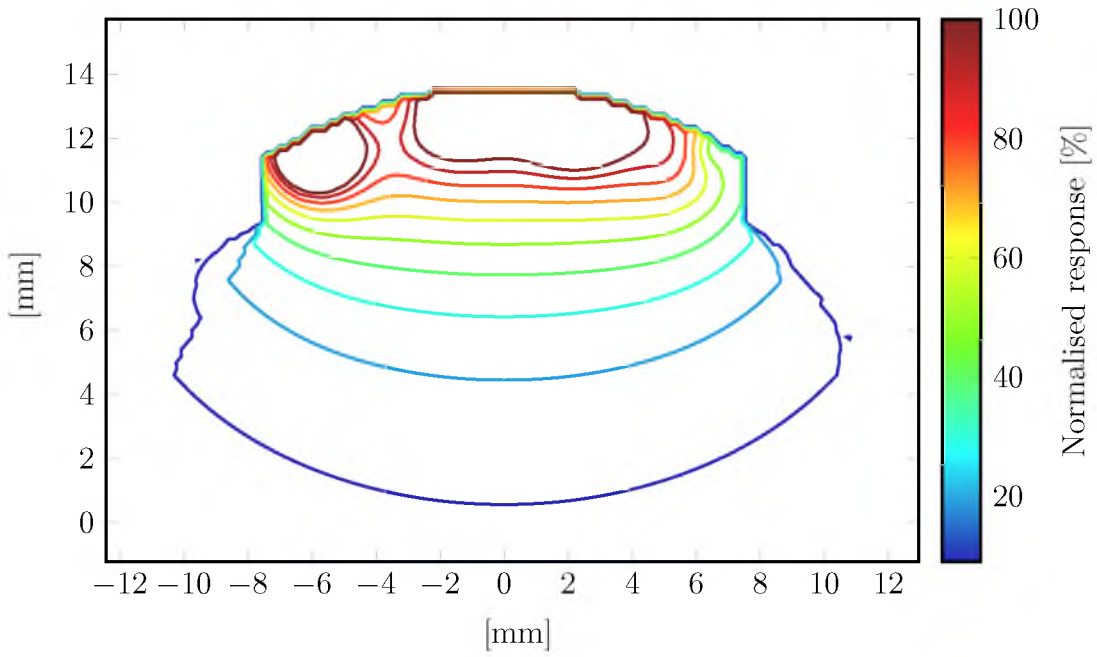

Figure 8.11: Plaque Simulator calculation at 90° on plaque axis. The plaque was a ROPES 15 mm with 10 $\times^{125}$I seeds. Dimensions are in millimetres and dose is normalised to 100% at the maximum value.

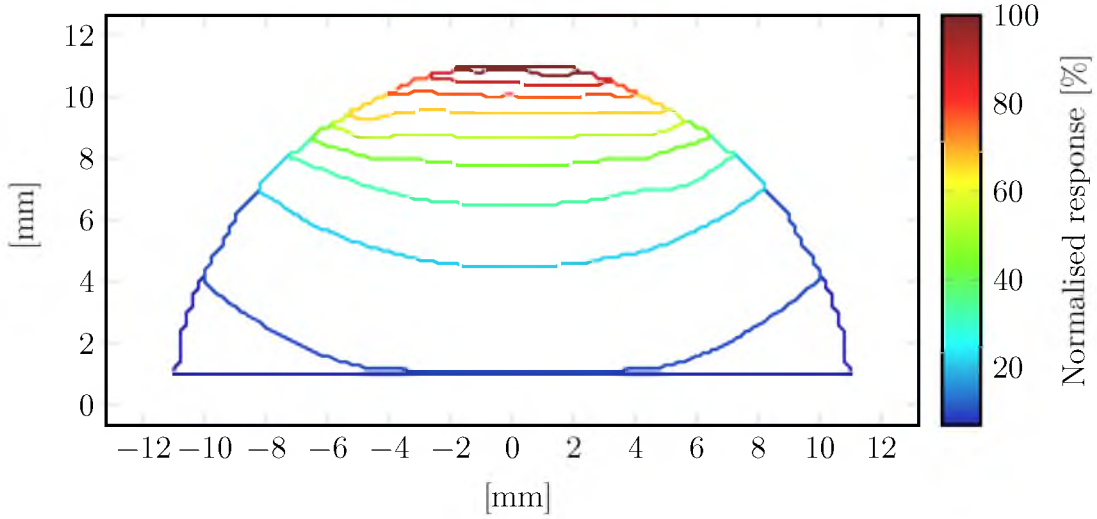

Figure 8.12: The equivalent pixel values from Figure 8.11 were taken to match the PANOPTES detector and then interpolated to provide an isodose curve. Dimensions are in millimetres and dose is normalised to 100% at the maximum value.

used to recalculate the isodose plots for demonstration purposes, and is shown in Figure 8.12. A relative difference comparison of the calculated image matrix with the original image showed good correlation, within 5% which was primarily located at the image edges. There are no distinguishable seeds at the apex of the virtual detector, in agreement with the original Plaque Simulator. This is because this region lies within the plaque boundary and the seeds are simply out of the field of view. For later comparison, the direct mean calculated pixel equivalent values were used, rather than the interpolated map from Figure 8.12.

8.2.2 Monte Carlo Simulations

Using the Monte Carlo model and simulations detailed earlier in Section 7.1.5, the pixel data for the 0.0° orientation was used to produce additional isodose plots for comparison, as shown in Figure 8.13. The model used an acrylic phantom, with a silicon detector, metal backing and an environment of air. Pixel data was taken as the total accumulated energy deposition in the sensitive volume of each pixel, with dose normalised to 100% at the maximum value. The conversion factors from Section 7.1.5 were applied to convert to dose in water.

To gain an understanding of the effectiveness of the conversion factors, the simulated detector response in water was compared to the dose converted detector response at plaque-detector angle, $\theta = 90°$. The resulting differences are plotted in Figure 8.14 and show that most values fall within $\pm 2\,\%$ difference. This lies within some existing uncertainties for plaque brachytherapy such as source activities uncertainty (see Section 2.2.4.3).

The overall distribution of the plot consists of a series of relatively uniform isodose curves originating from the plaque region, shown in Figure 8.13. The Monte Carlo isodose plot shows a similar dose profile to that seen in the reconstructed Plaque

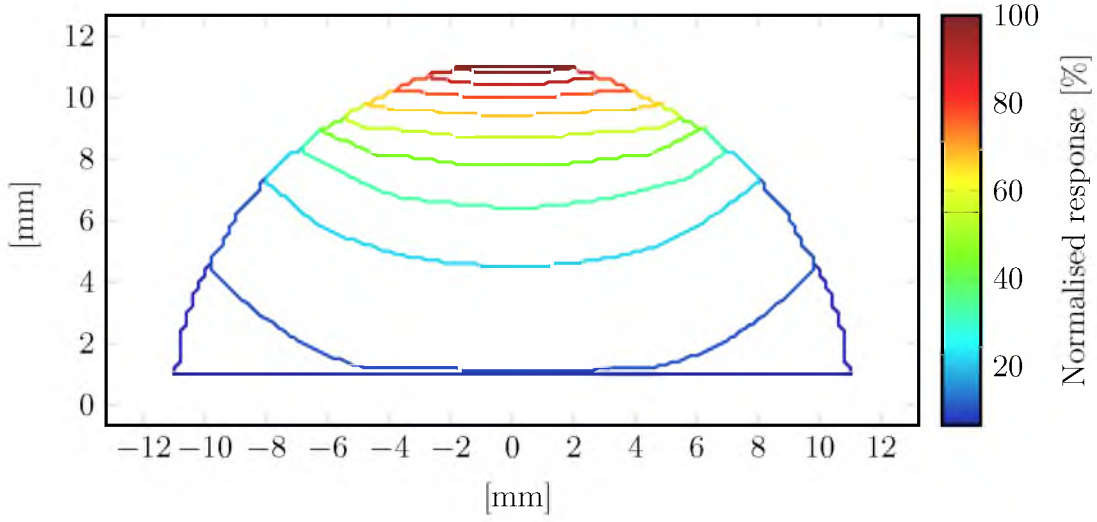

Figure 8.13: Monte Carlo calculation at 90° on plaque axis. The plaque was a ROPES 15 mm with 10 $\times^{125}$I seeds. Dimensions are in millimetres and dose is normalised to 100% at the maximum value.

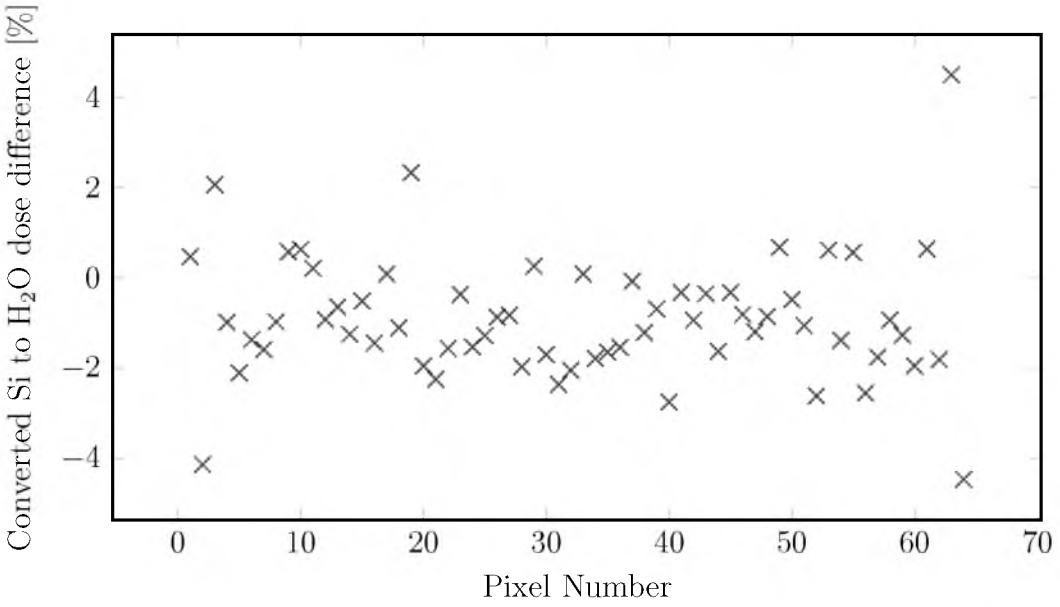

Figure 8.14: Through Monte Carlo simulations, the dose in silicon was converted to dose in water, using the conversion factors from Figure 7.14. The plot shows the percentage difference for a ROPES 15 mm with 10 $\times^{125}$I seeds at $\theta = 90°$.

Simulator plot.

8.2.3 Comparison

Evaluation of the simulated, calculated and measured planar dose images in a *water* eye was performed using a depth-dose comparison and a pixel-by-pixel comparison. The depth-dose comparison consisted of using the four pixels on the central axis of the detector (Pixels #32, #27, #34 and #33) for the PANOPTES data, the corresponding Monte Carlo simulation, Plaque Simulator and TG-43U1 formalism data. The resulting plots are presented together in Figure 8.15 where the data was normalised to 100% at 5.15 mm (Pixel #34).

The Plaque Simulator and the TG-43U1 correlated very well along the available range. The Monte Carlo simulation and the converted PANOPTES measured data also agreed well, falling within approximately 3.5 % for the four points in the curve. The PANOPTES dataset features a greater change in dose rate in comparison to the other datasets, with a maximum discrepancy of less than 4% for any one of them. This discrepancy falls within the uncertainties of low energy brachytherapy sources[116] (Section 2.2.4.3).

For a pixel-by-pixel response comparison for the different means tested, the flat-field and energy calibrated pixel values were calculated and plotted against each other in Figure 8.16. The values were normalised to the central pixel, Pixel #34. In addition to this, the percentage differences between each pixel in the normalised PANOPTES measurement and the other three data sets were plotted and are presented in Figure 8.17.

The plots illustrate that overall, the PANOPTES dataset deviates from the Monte Carlo simulation, the Plaque Simulator data and the TG-43U1 formalism. Discrepancies are largest for pixels that are close to the apex of the detector in comparison to

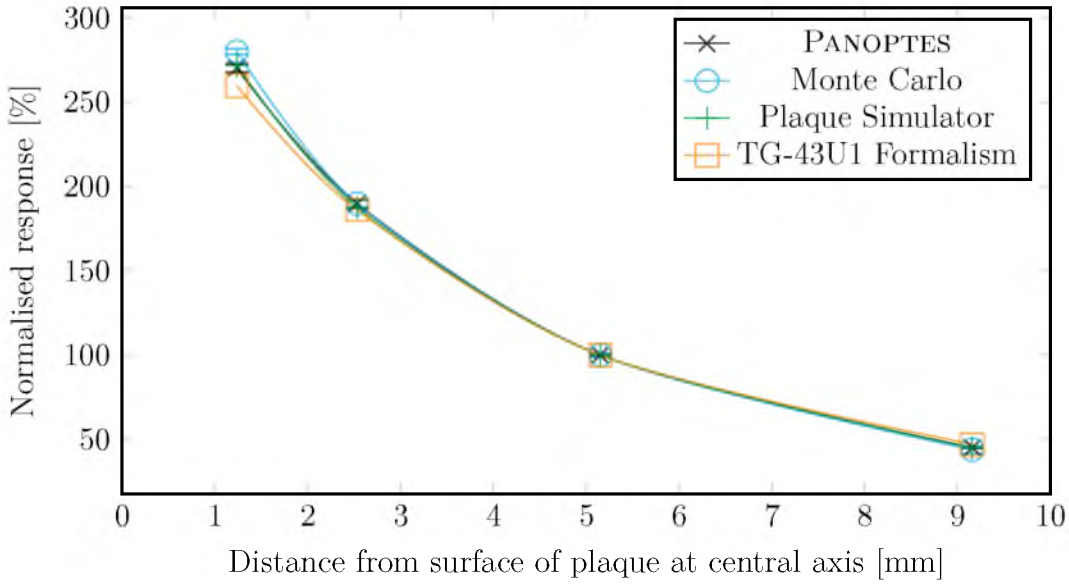

Figure 8.15: Depth-dose comparison of PANOPTES against several calculation methods for the ten seed configuration of the ROPES 15 mm plaque at 90° orientation. For the measured data, the central pixels were used, namely Pixels #32, #27, #34 and #33. All datasets are normalised at 5.15 mm (Pixel #34) to 100 % and error bars on the PANOPTES and Monte Carlo datasets are shown to 2σ.

those at the base. In the PANOPTES data, the three topmost pixels on each side of Pixel #32 (top-central pixel) over-respond compared to the other data. The Monte Carlo simulation and TG-41U1 formalism over-responded with respect to the PANOPTES data, whilst the Plaque Simulator data was most similar to the PANOPTES.

The response differences between the Monte Carlo dataset and the PANOPTES had a mean value of 4.4 % and a standard deviation of 7.5 %, though the majority of pixels fell to within ±15%. For the Plaque Simulator dataset, the mean response difference was 0.0 % and the standard deviation was 5.3 %. Finally, the mean response difference for the TG-43U1 formalism calculations was 4.3 % with a standard deviation of 10.6 %.

The differences in normalised response for each simulation method from Figure 8.17 are also presented on a spatially resolved detector map in Figures 8.18, 8.19 and 8.20 for Monte Carlo, Plaque Simulator and the TG-43U1 formalism, respectively. These plots illustrate that deviation from the PANOPTES dataset occurs dominantly on the

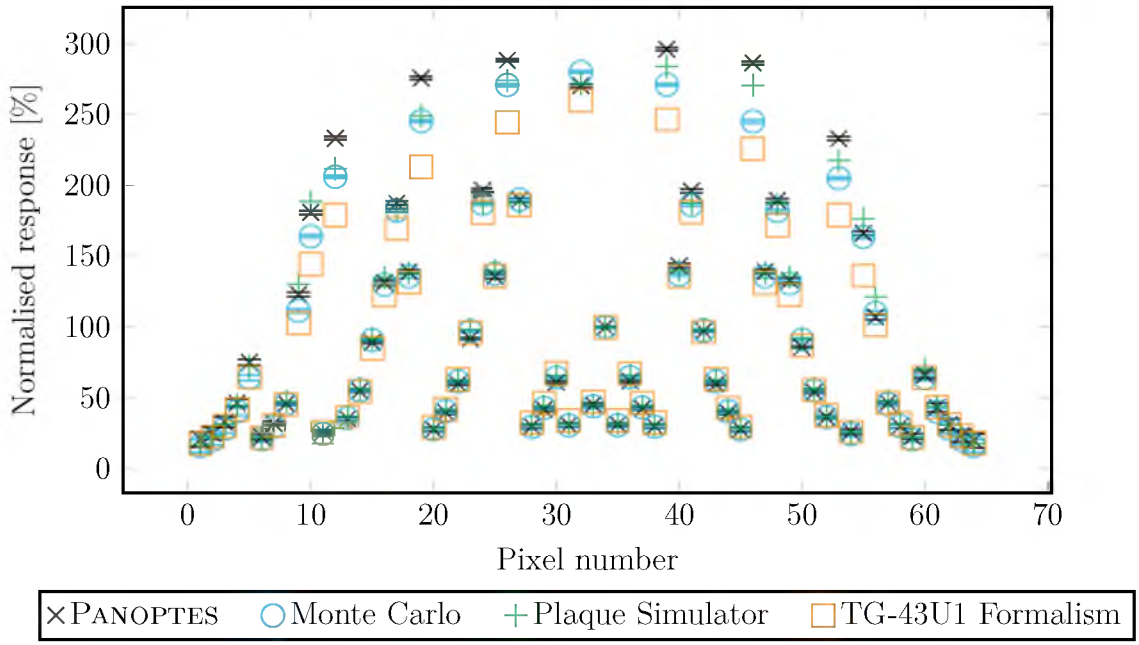

Figure 8.16: Pixel-by-pixel comparison of the normalised response of Panoptes against calculated methods for the ten seed configuration of the ROPES 15 mm plaque at 90° orientation. Plaque Simulator values were taken as the mean value of the dose under the area of each pixel. The error bars for Panoptes and Monte Carlo datasets are shown to 2σ.

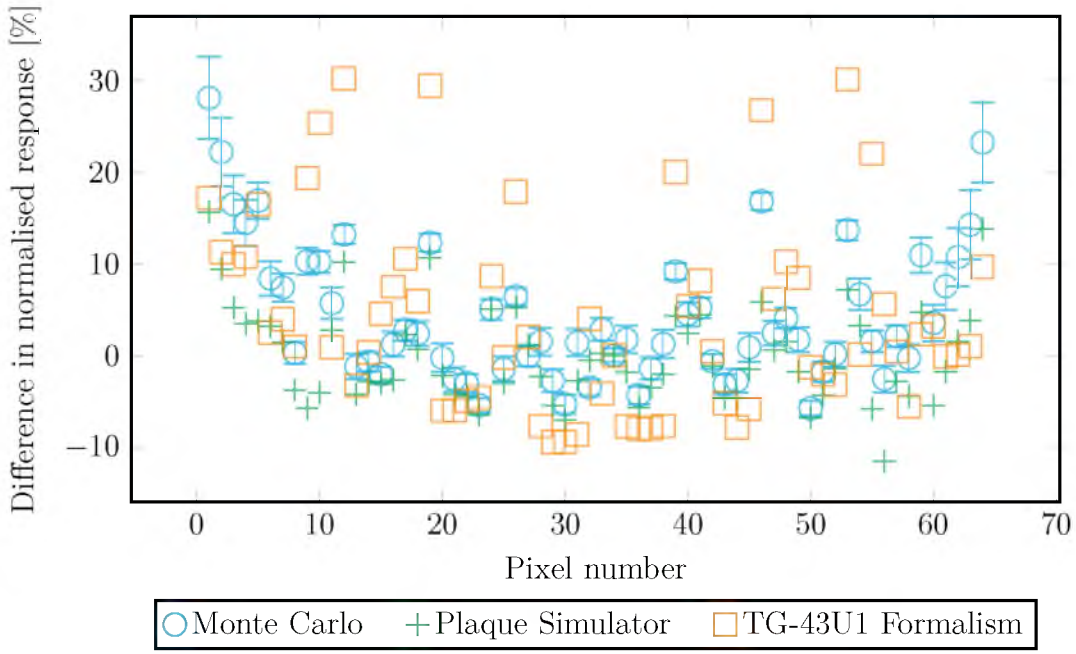

Figure 8.17: The percentage difference for each pixel for Monte Carlo and Plaque Simulator data with respect to the Panoptes data; based on the data presented in Figure 8.16. Error bars on the Monte Carlo dataset are shown to 2σ.

periphery of the detector, especially for the Monte Carlo and TG-43U1 datasets.

8.3 Discussion

The performance of the PANOPTES was observed and evaluated against calculated datasets. Planar and volumetric visualisation demonstrated the potential of the device and options that may be considered for clinical use. A dosimetry tool, such as the PANOPTES, would allow for real-time treatment verification in clinical environments that have no alternative. It would also provide the ability to verify optimised treatment solutions that use methods such as plaque customisation and multiple seed activities. The comparisons were made through depth-dose curves and on a pixel-by-pixel level, and showed that there was some deviation between expected and measured results.

8.3.1 Planar Reconstruction

The isodose plots for the ten seed configuration in Figures 8.4 and A.1 show a low response for Pixel #32. While it seems that it may be the result of individual seeds causing hot spots, the Plaque Simulator and Monte Carlo results depict no indication that the seeds could be discernible. The mid-right side of these isodose plot shows a somewhat abrupt change in dose gradient. This feature occurred at the location of lowest pixel density, where interpolation would be less accurate and more likely to introduce such artefacts.

The two isodose plots for the five seed configuration in Figures 8.5 and A.2 clearly demonstrate the asymmetry of the layout. This illustrates how modification of the plaque seed configurations may be used to create dose distributions to meet patients needs, and that they are clearly detectable in the measured data from the PANOPTES.

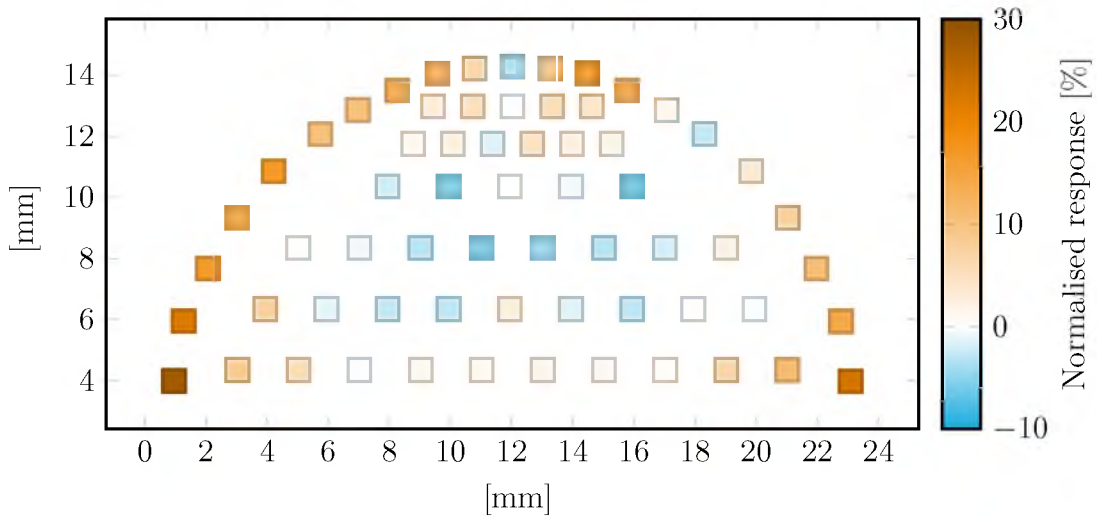

Figure 8.18: Spatially resolves differences in pixel-by-pixel response of PANOPTES versus Monte Carlo simulations; based on the data presented in Figure 8.17.

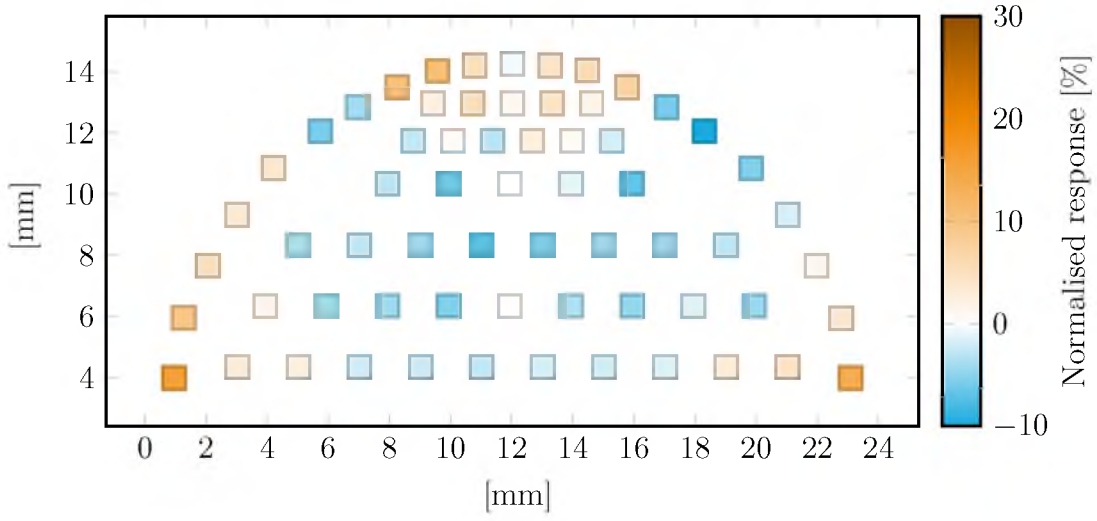

Figure 8.19: Spatially resolves differences in pixel-by-pixel response of PANOPTES versus Plaque Simulator; based on the data presented in Figure 8.17.

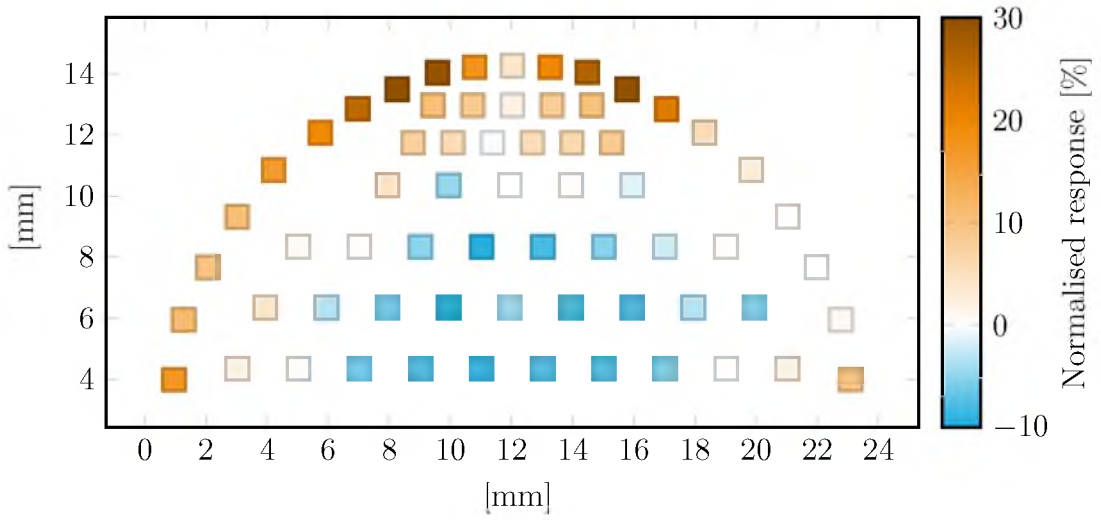

Figure 8.20: Spatially resolves differences in pixel-by-pixel response of PANOPTES versus TG-43U1; based on the data presented in Figure 8.17.

8.3.2 Volumetric Reconstruction

The volumetric plots produced from the PANOPTES data showed that reconstruction of the five and ten seed plaque configurations yielded expected dose distributions. When producing these dose volumes only about one half of the detector pixels (Pixel #1 – #34) were used in the interpolation process. Using all pixels gave rise to unwanted artefact effects that originated when two dose points (spatially mapped pixel values) from spatially symmetric pixels occupied a proximate space, but had different values. When the interpolation algorithm attempted to map the points, an undesirable artefact was produced due to these inhomogeneities. The variation in the values measured by these symmetrically corresponding pixel pairs originated from the flipped detector orientation (i.e. the pixels faced opposite directions when located in the same position) and its impact on the dose attenuation.

In order to resolve the issue of these artefact effects while utilising the entire pixel array, symmetrically corresponding pixel pairs could be averaged in space and magnitude, reducing the angular dependance. However this would also act to reduce

spatial resolution.

The *xy* slice in Figure 8.10 shows a low response in the region opposite the seeds (left of image) which is expected due to the asymmetric five seed configuration. The feature is exaggerated, however, due to attenuation effects through the silicon wafer and detector board. These angular dependence effects could potentially be reduced through the pixel pair averaging described above.

A comparison between the two angular resolutions measured showed radial wedge features that may have been a function of angle due to interpolation. For the two angle increments tested, the mean difference was 100.6 % and the standard deviation of the differences was relatively small, at 2.7 %. The greatest differences occurred in localised regions at the periphery of the dose volume and were most likely the result of interpolation inaccuracies. Further optimisation of the PANOPTES by performing a detailed comparison across a range of angles would be useful to determine the ideal angular resolution for clinical use.

Interpolated dose volumes derived from planar dose maps were shown to have good potential for use in plaque dosimetry. Volumetric dose data used in this manner provides an encompassing set of information across the volume of the eye. Here, dose from essentially any region of interest can be utilised. Whilst other volumetric representations of the data are possible, such as isosurfaces, it is inherently difficult or computationally expensive to compare entire 3D datasets visually. To gain the most out of volumetric data, it should be used in conjunction with 1D and 2D representations for viewing dose slices or profiles.

8.3.3 Verification

The primary measure of clinical suitability for a dosimetry system is comparison against existing systems. As currently there are no methods used for dose verification in plaque

brachytherapy, comparison with clinical dose calculation methods was used. These methods included Monte Carlo, Plaque Simulator and the TG-43U1 formalism.

The Plaque Simulator dose contour, reconstructed from the PANOPTES detector equivalent pixels, illustrated the resolution capabilities of the detector. The original plot depicted uniform, concentric isodose lines, which matched remarkably well with the reconstructed data. This demonstrates that the cubic interpolation process used is suited to this form of image reconstruction, though artefacts seen in the calibration isodose plot may suggest the sparse pixel regions are potentially problematic.

As the edge of the detector was not considered flush against the inner surface of the plaque, but rather 500 µm from it, as per the phantom design, the details of individual seeds are indistinguishable in the reconstruction. This could potentially be improved if necessary, with refined and reduced phantom and detector tolerances.

The depth-dose curve taken through the central pixels of the PANOPTES detector correlated well with the equivalent Monte Carlo simulation results. This form of comparison is useful and common practise for assessing the clinical suitability of dosimeters. The TG-43U1 data and the Plaque Simulator data also correlate well with each other, though this is expected as Plaque Simulation uses calculations adapted from the TG-43U1 formalism. The PANOPTES and Monte Carlo data both incorporated an eye phantom, and the dose-to-water conversion used for both was calculated based on PMMA. The actual phantom, however, was fabricated from a proprietary acrylic material for which details were limited, reducing the correlation between PANOPTES and the Monte Carlo data. Dose correction to water would be improved with more accurate simulation models.

The PANOPTES detector showed deviation from data produced with both the Monte Carlo simulation and the Plaque Simulator. The data was normalised against the top central pixel, which showed an under-response in the measurement, compared

to calculations. The phantom material may have contributed substantially to the deviations seen in the pixel comparison of Figure 8.17. Furthermore, improving the accuracy of the simulation model would account for the attenuation effects caused by surrounding features that were not modelled. These features include the PCB materials, which included a high Z_{eff} gold detector mounting pad, and the HERMES ASICs. The response of the TG-43U1 deviated by up to 30%, however, this was expected due to the presence of the plaque backing and printed phantom material.

8.3.4 Potential Issues and Caveats

In addition to explanations provided above, there are several further issues that should be considered in this study.

One potential issue with the PANOPTES in its current state, is plaque alignment. Should the plaque be off axis from the shaft, its observable dose distribution will be incorrect and greatest in the direction of the offset. Due to the design of the plaque holder on the tip of the shaft, the plaque can only slot in concentrically and thus cannot be off axis, with respect to the shaft. However, plaque misalignment may still have occurred to some extent as the result of shaft eccentricity.

A flaw in the fabrication of the shaft meant it was not true. The components of the lock-down shaft, shown in Figure B.4 of Appendix B were printed in the same process as the phantom. Unfortunately, due to the physical length of the component, it needed to be printed on horizontally, which caused distortion during the heated wax removal process. The distortion caused slight eccentricity of the shaft which may have lead to, what appeared as, an asymmetrically loaded plaque.

The sensitive volume of the detector did not perfectly align with the central plaque axis within the phantom. This design oversight lead to an offset of up to 950 µm from the centre of the sensitive volume to the plaque central axis. The issue was accounted

for in the three-dimensional dose volumes, as the offset was included in the geometric transformations. Discrepancies in the two-dimensional comparisons presented may be attributed, in part, to this offset.

8.4 Conclusion

Throughout this thesis, the primary aim was to develop a preoperative dose verification system for plaque brachytherapy. This chapter brought the research and work together from literature, concepts, design, development and characterisation to finally present results on the function and performance of the PANOPTES as a whole. Two dimensional dose maps were created through single measurements, whilst dose volumes were generated through the collation of multiple measurements.

The PANOPTES was not intended to replace the role of calculation based treatment planning systems, but rather to supplement them through dose verification. For clinical relevance, the outcomes were compared to Monte Carlo simulation, the Plaque Simulator TPS and TG-43U1.

Dosimetric pixel maps were generated with the PANOPTES and its software interface. Using the data in this form, isodose plots were generated, and provided an improvement on the representation of dose distributions. Extending upon this further, the individual pixel values taken from multiple angles covering 360° were translated to an xyz coordinate system and interpolated using three dimensional linear interpolation. The data was then plotted as volume slices for more advanced representation of dose distribution, which showed good results from the five and ten seed configurations. Dose distribution shapes may have been effected by angular dependence, shaft eccentricity, plaque slipping or possibly cross-talk between channels.

Isodose curves were also interpolated based on both pixel equivalent values for data taken from the Plaque Simulator TPS and from Monte Carlo simulation. The

interpolation of calculated data gave distributions which showed excellent correlation to the original data.

The depth-dose response through the central axis of the detector was compared to Monte Carlo, Plaque Simulator and the TG-43U1, showing agreement within 4% for most points. The clinical implications of this are likely to be inconsequential as source uncertainties have been shown to be up to 8.7%[116]. The pixel-by-pixel comparisons demonstrated that there were off-axis discrepancies generally within ±15% between the PANOPTES simulations, Plaque Simulator calculations and the TG-43U1 formalism, especially on the pixels closest to the source. This can be explained, in part, due to slight geometric misrepresentation and inaccuracies in the simulation modelling. These outcomes can be further improved with refined simulations and the subsequent calibrations, as suggested in this chapter.

Through comparison against clinical dose calculation tools, the PANOPTES was shown to be capable of measuring dose using automated position control and while some discrepancies remain against theoretical values, the prototype design showed great potential for producing a preoperative dose verification system for plaque brachytherapy.

Chapter 9

Contributions and Recommendations

The primary aim of this thesis was to design, develop and evaluate the prototype of a dose verification system for plaque brachytherapy. This was conducted in three major parts: conducting a review of the current literature; proof of concepts for single and pixelated detectors; and the design, development and testing of the PANOPTES dose verification tool. This chapter presents a summary of the major contributions of the thesis and offers some recommendations for future research and direction of the project.

9.1 Summary of Contributions

After the introduction, the second chapter provided a review of the current literature in the field. It began by presenting a summary of the anatomy of the eye for the benefit of understanding the terms used in the study. It then covered the prevalence and impact of ocular cancer and several of the current treatments, with a focus on plaque brachytherapy. Building on this, the current clinical outcomes and limitations of plaque

brachytherapy were also investigated. A comprehensive literature search on previously used methods for plaque dosimetry was conducted, concluding that silicon detector technology was suitable for pursuing as an eye brachytherapy dosimetry solution.

Following the literature review, Chapter 3 gave a brief background regarding semiconductor technology and its application in dosimetry. The chapter covered material that was relevant to the physics and electronic systems used throughout the study. It outlined the generic model of a semiconductor radiation detection system and gave details on the constituent parts. Finally, a discussion on dose equivalence was presented along with its importance in this study.

Part II began with Chapter 4, which evaluated the concept of using a miniature detector, about 1 mm^3, to measure the depth-dose distribution of an eye plaque. The aim of this single detector concept was to determine the feasibility of continued development into more complex and advantageous detector designs, in addition to providing a simple dose verification tool for use in clinical environments. To do this, a detector system comprising of a *p-i-n* diode detector, preamplifier and readout electronics was developed. The detector was characterised through measurement of both current-voltage and capacitance-voltage responses, whilst for the assembled system, the energy response, angular dependence and depth-dose response were measured. The overall performance of the technology suggested that continued development towards volumetric plaque brachytherapy dosimetry should be undertaken, whilst there was room for optimisation in the current single detector design.

Building upon the success of the single detector concept, Chapter 5 investigated two concepts for volumetric dosimetry, the translation and the rotation concepts. These were tested using the Medipix family of detectors, which had a 256 × 256 array of pixels each 55 µm × 55 µm. The detectors were used to generate 3D dose volumes and investigate several other plaque dosimetry aspects. This was conducted using a variety

of eye phantoms, including a hemispherical, layered, PMMA phantom and a columnar water phantom with movable plaque. Event counting above a threshold in each pixel using the Medipix detector was compared to charge measurement, or deposited energy in each pixel, using the TimePix detector running in TOT mode. The results showed a strong correlation, to within 1 % in relative depth-dose measurements in the phantom and within 5 % of the TG-43U1 formalism at up to 5 mm from the plaque. This demonstrated that event counting with energy windows of 17 keV – 45 keV for ^{125}I would be effective in the subsequent PANOPTES design. Measurements of single seeds in count mode on the surface of the Medipix detector showed that intra-batch activity variation was around 11.5 %, which was worst at the ends of the seeds.

Tissue equivalent material was placed downstream from the Medipix detector in the water phantom to model additional tissue outside the eye. It showed to influence dose by up to nearly 7 % at 5 mm from the plaque, though the air-eye interface location would vary relative to the plaque from case to case, making phantom design challenging. Despite the advantages of the high spatial resolution in detectors, such as the Medipix, it was demonstrated that a reduction in spatial resolution to a pixel size of $\sim 800\,\mu m \times 800\,\mu m$ would provide sufficient information for 2D dosimetry and lower production costs. The effectiveness of silicon pixelated detectors in measuring beta emitting plaques was also considered and showed radionuclide deposition to be non-uniform in the COB-type plaque, while the depth-dose response of the CCA-type plaque correlated well to Plaque Simulator outputs.

Finally, the concept of spectroscopic dosimetry using pixelated silicon detectors was introduced and the 3D volumetric dose reconstruction based on 2D dose images sets was demonstrated. Using the Medipix detector as a model, customised pixelated detectors with 64 and 127 pixels respectively, were proposed for use in the eye plaque dose verification instrument, the PANOPTES.

The final part of the thesis focused on the PANOPTES, starting with Chapter 6, where the customised pixelated detector, data acquisition, phantom, positioning and software systems for the PANOPTES were designed, developed and integrated to produce the pixelated dosimetry system. Two detectors, rectangular and semicircular in shape, were designed and fabricated to meet the needs of the translation and rotation volumetric dosimetry concepts, respectively. Ultimately, the semicircular detector with the rotation concept was chosen for use in the prototype design as it offered better dose measurement near the plaque surface and simpler implementation. The semicircular detector featured 64 pixels of two sizes, $300\,\mu m \times 300\,\mu m$ and $1.00\,mm \times 1.00\,mm$.

The PANOPTES data acquisition system consisted of a multi-rail power supply, FPGA interface board, detector board and stepper motor circuitry. The front-end readout electronics used on the detector board were mixed-signal, low noise, 32-channel ASICs called, HERMES4 and were bonded directly to the detector. A 3D printed, hemispherical eye phantom was developed to encapsulate the detector, locate the plaque during acquisitions and provide near tissue equivalence. The orientation of the plaque was controlled using a stepper motor was via a spring loaded shaft. The host computer software interface and FPGA interfaces coordinated all acquisitions, data handling and control signals.

The semicircular, ion-implanted, passivated detector was designed, fabricated and then characterised, both in isolation, and as an integrated part of the PANOPTES. Investigation of I-V and C-V curves for the detector showed the breakdown voltage to be $\sim 63\,V$, operational voltage leakage current was less than $\sim 1\,nA$ for all pixels, and capacitance values had a mean of $13 \pm 4\,pF$ and were strongly dependant on track length. Alpha spectroscopy was performed with ^{241}Am and demonstrated that pixels at different locations had similar energy responses and that charge sharing between neighbours was not significant. Monte Carlo simulation of the detector and phantom

was performed to establish PMMA-to-water conversion factors for each pixel, with the assumption the phantom was made from PMMA. Ion beam induced charge collection showed that the detector pixels had well defined sensitive volumes, maximum charge collection occurred at 50 V bias and charge sharing between pixels was very low.

The PANOPTES was characterised through spectroscopy and flat-field calibration. Operating the PANOPTES as a single channel analyser showed that the ^{125}I peaks were clearly resolvable, enabling well defined energy thresholding. Using an orthovoltage machine, flat-field calibration was conducted to equalise readout of the pixel response across the detector.

Measurements were taken with the PANOPTES using a ROPES 15 mm eye plaque and ^{125}I seeds. The plaque was loaded in both ten and five seed configurations to observe differences in dose distribution responses. Isodose curves were produced for corrected PANOPTES data, reconstructed Monte Carlo simulation and Plaque Simulator data. These were used in addition to the TG-43U1 formalism for a depth-dose comparison of the central axis of the detector with ten seeds, which showed to be within 4%. Results showed the PANOPTES correlated within around 15% for most values, though given uncertainties in phantom material, these deviations could be expected.

Software was developed for the reconstruction of multiple 2D doses slices taken over a series of angles for 3D volumetric doses of plaques loaded with both five and ten seeds. Despite the remaining room for optimisation, the PANOPTES shows great potential for providing fast, dose verification in plaque brachytherapy.

The overall aim of this thesis was to address the current lack of preoperative treatment verification in plaque brachytherapy, which was achieved through:

- determining issues in current treatment planning systems,
- experimentally assessing the validity of using a single silicon diode detector for plaque brachytherapy dosimetry,

- experimentally assessing the validity of using a pixelated silicon detector for plaque brachytherapy dosimetry through the Medipix detector family,
- design and fabrication of pixelated detectors for two plaque brachytherapy dosimetry concepts; translational and rotational,
- integration of the detector into a full dosimetry system, called the PANOPTES, for real-time, automated measurements, and
- evaluation of the PANOPTES dosimetry system in plaque brachytherapy treatments.

9.2 Recommendations for Future Work

The PANOPTES project essentially focused around the design of a prototype to act as a proof of concept and offer a platform to determine areas for improvement. The following includes several recommendations that could be adopted to improve the outcomes of the dose verification process or PANOPTES:

1. *Further calibration and characterisation*

   Further characterisation and improvements could be used to increase the performance of the PANOPTES. By performing simulations with a more accurate representation of the detector in the phantom, including the circuit board with the gold contacts, the measured silicon to tissue dose response conversion could be determined with greater accuracy. A primary consideration would be to correctly represent the 3D printer phantom material, rather than using PMMA in simulations to determine the conversion factors from detector response to dose in water. The flat-field response of an electron beam could also be measured for comparison to the existing data. Channels of windows 1 and 2 of the HERMES

front-end electronics could be individually threshold trimmed to ensure more accurate event counting for the desired sources.

2. *Phantom design*

   Design of a generic phantom for plaque brachytherapy is challenging. As tumour location dictates plaque orientation, the relative position of the eye-air interface can change between treatments. The effects of backscatter from tissue in and around the eye have been shown to be significant. The development of a phantom that is able to accommodate these needs would be of benefit in improving the treatment accuracy. The effect on current clinical work flows should be consideration when making such a modification to the existing system.

3. *Software integration*

   The PANOPTES aimed to support treatment verification processes and the process would be more streamlined if the efforts required for data handling were reduced. The integration of the Panopticon acquisition interface, presented in this thesis, into software such as Plaque Simulator would allow for treatment planning and verification within the same software package and hence improve time efficiency.

4. *Customised plaques*

   The plaque prescription needs of each patient vary depending on tumour location, size and geometry. Dose distributions are currently limited to discreet plaque configurations and are not optimised for individual patients. The current state of 3D printing technologies and materials, along with the implementation of the PANOPTES would allow custom designed plaques to be developed and verified at low cost. Further research and development could involve the development of an automated plaque designer based on patient geometry and its subsequent dose verification with the PANOPTES.

In summary, a single detector dose verification system was developed, and pixelated dosimetry was deemed feasible through the design, development and testing of the PANOPTES. Despite the room for further optimisation, the PANOPTES demonstrated strong potential as a viable tool for addressing the current lack of preoperative dose verification in plaque brachytherapy.

Part IV

References and Appendices

References

[1] C. M. Vajdic, A. Kricker, M. Giblin, J. McKenzie, J. Aitken, G. G. Giles, and B. K. Armstrong, "Incidence of ocular melanoma in Australia from 1990 to 1998." *International Journal of Cancer*, vol. 105, no. 1, pp. 117–22, May 2003.

[2] S. a. Callejo, E. Antecka, P. L. Blanco, C. Edelstein, and M. N. Burnier, "Identification of circulating malignant cells and its correlation with prognostic factors and treatment in uveal melanoma. A prospective longitudinal study." *Eye (London, England)*, vol. 21, no. 6, pp. 752–9, Jun. 2007.

[3] B. Damato, "Treatment of primary intraocular melanoma." *Expert Review of Anticancer Therapy*, vol. 6, no. 4, pp. 493–506, Apr. 2006.

[4] D. H. Char, J. M. Quivey, J. R. Castro, S. Kroll, and T. Phillips, "Helium ions versus iodine 125 brachytherapy in the management of uveal melanoma. A prospective, randomized, dynamically balanced trial." *Ophthalmology*, vol. 100, no. 10, pp. 1547–54, Oct. 1993.

[5] D. Char, S. Kroll, T. Phillips, and J. Quivey, "Late radiation failures after iodine 125 brachytherapy for uveal melanoma compared with charged-particle (proton or helium ion) therapy," *Ophthalmology*, 2002.

[6] B. Damato, A. Kacperek, M. Chopra, I. R. Campbell, and R. D. Errington, "Proton beam radiotherapy of choroidal melanoma: the Liverpool-Clatterbridge

experience." *International Journal of Radiation Oncology Biology Physics*, vol. 62, no. 5, pp. 1405–11, Aug. 2005.

[7] R. Dendale, L. Lumbroso-Le Rouic, G. Noel, L. Feuvret, C. Levy, S. Delacroix, A. Meyer, C. Nauraye, A. Mazal, H. Mammar, P. Garcia, F. D'Hermies, E. Frau, C. Plancher, B. Asselain, P. Schlienger, J. J. Mazeron, and L. Desjardins, "Proton beam radiotherapy for uveal melanoma: results of Curie Institut-Orsay proton therapy center (ICPO)." *International Journal of Radiation Oncology Biology Physics*, vol. 65, no. 3, pp. 780–7, Jul. 2006.

[8] Collaborative Ocular Melanoma Study Group, "The COMS randomized trial of iodine 125 brachytherapy for choroidal melanoma: V. Twelve-year mortality rates and prognostic factors: COMS report No. 28." *Archives of Ophthalmology*, vol. 124, no. 12, pp. 1684–93, Dec. 2006.

[9] Collaborative Ocular Melanoma Study - Quality of Life Study Group, "Quality of life after iodine 125 brachytherapy vs enucleation for choroidal melanoma: 5-year results from the Collaborative Ocular Melanoma Study: COMS QOLS Report No. 3." *Archives of Ophthalmology*, vol. 124, no. 2, pp. 226–38, Feb. 2006.

[10] S. Nag, J. M. Quivey, J. D. Earle, D. Followill, J. Fontanesi, and P. T. Finger, "The American Brachytherapy Society recommendations for brachytherapy of uveal melanomas." *International Journal of Radiation Oncology Biology Physics*, vol. 56, no. 2, pp. 544–55, Jun. 2003.

[11] Collaborative Ocular Melanoma Study Group, "Design and methods of a clinical trial for a rare condition: the Collaborative Ocular Melanoma Study. COMS Report No. 3." *Controlled Clinical Trials*, vol. 14, no. 5, pp. 362–91, Oct. 1993.

[12] Collaborative Ocular Melanoma Study Group, "The COMS randomized trial of iodine 125 brachytherapy for choroidal melanoma: IV. Local treatment failure

and enucleation in the first 5 years after brachytherapy. COMS report no. 19." *Ophthalmology*, vol. 109, no. 12, pp. 2197–206, Dec. 2002.

[13] Collaborative Ocular Melanoma Study Group, "Incidence of cataract and outcomes after cataract surgery in the first 5 years after iodine 125 brachytherapy in the Collaborative Ocular Melanoma Study: COMS Report No. 27." *Ophthalmology*, vol. 114, no. 7, pp. 1363–71, Jul. 2007.

[14] K. Gündüz, C. L. Shields, J. A. Shields, J. Cater, J. E. Freire, and L. W. Brady, "Radiation Complications and Tumor Control After Plaque Radiotherapy of Choroidal Melanoma With Macular Involvement," *American Journal of Ophthalmology*, vol. 127, no. 5, pp. 579–589, 1999.

[15] S. Packer, S. Stoller, M. L. Lesser, F. S. Mandel, and P. T. Finger, "Long-term results of iodine 125 irradiation of uveal melanoma." *Ophthalmology*, vol. 99, no. 5, pp. 767–73; discussion 774, May 1992.

[16] P. T. Finger, K. J. Chin, and G. Duvall, "Palladium-103 ophthalmic plaque radiation therapy for choroidal melanoma: 400 treated patients." *Ophthalmology*, vol. 116, no. 4, pp. 790–6, 796.e1, Apr. 2009.

[17] K. L. Leonard, N. L. Gagne, J. E. Mignano, J. S. Duker, E. A. Bannon, and M. J. Rivard, "A 17-year retrospective study of institutional results for eye plaque brachytherapy of uveal melanoma using (125)I, (103)Pd, and (131)Cs and historical perspective." *Brachytherapy*, vol. 10, no. 4, pp. 331–9, 2011.

[18] P. T. Finger, "Radiation therapy for choroidal melanoma." *Survey of Ophthalmology*, vol. 42, no. 3, pp. 215–32, 1997.

[19] A. W. Jensen, I. a. Petersen, R. W. Kline, S. L. Stafford, P. J. Schomberg, and D. M. Robertson, "Radiation complications and tumor control after 125I

plaque brachytherapy for ocular melanoma." *International Journal of Radiation Oncology Biology Physics*, vol. 63, no. 1, pp. 101–8, Sep. 2005.

[20] M. J. Rivard, B. M. Coursey, L. a. DeWerd, W. F. Hanson, M. Saiful Huq, G. S. Ibbott, M. G. Mitch, R. Nath, and J. F. Williamson, "Update of AAPM Task Group No. 43 Report: A revised AAPM protocol for brachytherapy dose calculations," *Medical Physics*, vol. 31, no. 3, p. 633, 2004.

[21] M. J. Rivard, W. M. Butler, L. a. DeWerd, M. S. Huq, G. S. Ibbott, A. S. Meigooni, C. S. Melhus, M. G. Mitch, R. Nath, and J. F. Williamson, "Supplement to the 2004 update of the AAPM Task Group No. 43 Report," *Medical Physics*, vol. 34, no. 6, p. 2187, 2007.

[22] Eckert & Ziegler BEBIG GmbH, "Plaque Simulator," 2013. [Online]. Available: http://www.bebig.eu/fileadmin/bebig/pdf/Factsheet-PlaqueSimulator.pdf

[23] D. Soulières, A. Rousseau, M. Tardif, M. Larochelle, M. Tremblay, L. Vaillancourt, and G. Pelletier, "The radiosensitivity of uveal melanoma cells and the cell survival curve." *Graefe's archive for clinical and experimental ophthalmology = Albrecht von Graefes Archiv fur klinische und experimentelle Ophthalmologie*, vol. 233, no. 2, pp. 85–89, 1995.

[24] R. Pötter and E. V. Limbergen, "Uveal melanoma: Location, size, cell type, and enucleation as risk factors in metastasis," *The GEC ESTRO Handbook of Brachytherapy*, vol. 13, no. 12, pp. 591–610, Dec. 2002.

[25] S. E. Skalicky, P. E. Holt, M. Giblin, S. Taylor, and R. M. Conway, "Australian Cancer Network clinical practice guidelines for the management of ocular and periocular melanoma: an evidence-based literature analysis." *Clinical & Experimental Ophthalmology*, vol. 36, no. 7, pp. 646–58, Oct. 2008.

[26] K. M. Egan, J. M. Seddon, R. J. Glynn, E. S. Gragoudas, and D. M. Albert, "Epidemiologic aspects of uveal melanoma." *Survey of Ophthalmology*, vol. 32, no. 4, pp. 239–51, 1988.

[27] L. Bergman, S. Seregard, B. Nilsson, U. Ringborg, G. Lundell, and B. Ragnarsson-Olding, "Incidence of uveal melanoma in Sweden from 1960 to 1998." *Investigative Ophthalmology & Visual Science*, vol. 43, no. 8, pp. 2579–83, Aug. 2002.

[28] B. Damato, "Detection of uveal melanoma by optometrists in the United Kingdom," *Ophthalmic and Physiological Optics*, vol. 21, no. 4, pp. 268–271, 2001.

[29] A. D. A. D. Singh, M. E. Turell, and A. K. Topham, "Uveal melanoma: trends in incidence, treatment, and survival." *Ophthalmology*, vol. 118, no. 9, pp. 1881–5, Sep. 2011.

[30] P. De Potter, "Ocular manifestations of cancer," *Current Opinion in Ophthalmology*, vol. 9, no. 6, pp. 100–104, 1998.

[31] A. Stang, D. M. Parkin, J. Ferlay, and K.-H. Jöckel, "International uveal melanoma incidence trends in view of a decreasing proportion of morphological verification." *International Journal of Cancer*, vol. 114, no. 1, pp. 114–23, Mar. 2005.

[32] G. Virgili, G. Gatta, L. Ciccolallo, R. Capocaccia, A. Biggeri, E. Crocetti, J.-M. Lutz, and E. Paci, "Incidence of uveal melanoma in Europe." *Ophthalmology*, vol. 114, no. 12, pp. 2309–15, Dec. 2007.

[33] A. D. Singh, "Uveal melanoma: implications of tumor doubling time." *Ophthalmology*, vol. 108, no. 5, pp. 829–31, May 2001.

[34] A. Y. Bedikian, "Metastatic uveal melanoma therapy: current options." *International Ophthalmology Clinics*, vol. 46, no. 1, pp. 151–66, Jan. 2006.

[35] E. Kujala and T. Ma, "Very Long-Term Prognosis of Patients with Malignant Uveal Melanoma," *Investigative Ophthalmology & Visual Science*, vol. 44, no. 11, pp. 4651–4659, Nov. 2003.

[36] A. D. Singh and E. C. Borden, "Metastatic uveal melanoma." *Ophthalmology Clinics of North America*, vol. 18, no. 1, pp. 143–50, ix, Mar. 2005.

[37] M. Diener-west, B. Hawkins, S. Barbara, J. A. Markowitz, and A. P. Schachat, "A review of mortality from choroidal melanoma: II. A meta-analysis of 5-year mortality rates following enucleation, 1966 through 1988," *Archives of Ophthalmology*, vol. 110, pp. 245–250, 1992.

[38] P. K. Lommatzsch and R. Lommatzsch, "Treatment of juxtapapillary melanomas." *British Journal of Ophthalmology*, vol. 75, no. 12, pp. 715–717, Dec. 1991.

[39] P. K. Lommatzsch, W. Alberti, R. Lommatzsch, and F. Rohrwacher, "Radiation effects on the optic nerve observed after brachytherapy of choroidal melanomas with 106Ru/106Rh plaques." *Graefe's Archive for Clinical and Experimental Ophthalmology*, vol. 232, no. 8, pp. 482–7, Aug. 1994.

[40] C. L. Shields, M. Naseripour, J. Cater, J. A. Shields, H. Demirci, A. Youseff, and J. Freire, "Plaque Radiotherapy for Large Posterior Uveal Melanomas (>8-mm thick) in 354 Consecutive Patients," *Ophthalmology (Rochester, Minn.)*, vol. 109, no. 10, pp. 1838–1849, 2002.

[41] E. S. Gragoudas and A. Marie Lane, "Uveal melanoma: proton beam irradiation." *Ophthalmology Clinics of North America*, vol. 18, no. 1, pp. 111–8, ix, Mar. 2005.

[42] A. D. Singh and A. Topham, "Incidence of uveal melanoma in the United States: 1973-1997." *Ophthalmology*, vol. 110, no. 5, pp. 956–61, May 2003.

[43] C. L. Shields and J. A. Shields, "Ocular melanoma: relatively rare but requiring respect." *Clinics in Dermatology*, vol. 27, no. 1, pp. 122–33, 2009.

[44] J. A. Shields and C. L. Shields, *Intraocular Tumours: An Atlas and Textbook*, 2nd ed. Lippincott Williams & Wilkins, a Wolters Kluwer business, 2008.

[45] B. Damato, C. Groenewald, J. McGalliard, and D. Wong, "Endoresection of choroidal melanoma." *The British journal of Ophthalmology*, vol. 82, no. 3, pp. 213–8, Mar. 1998.

[46] B. E. Damato, J. Paul, and W. S. Foulds, "Predictive factors of visual outcome after local resection of choroidal melanoma." *British Journal of Ophthalmology*, vol. 77, no. 10, pp. 616–623, Oct. 1993.

[47] B. E. Damato, J. Paul, and W. S. Foulds, "Risk factors for residual and recurrent uveal melanoma after trans-scleral local resection." *British Journal of Ophthalmology*, vol. 80, no. 2, pp. 102–108, Feb. 1996.

[48] D. Char, S. Kroll, and J. Castro, "Ten-year follow-up of helium ion therapy for uveal melanoma," *American Journal of Ophthalmology*, vol. 125, no. 1, pp. 81–89, 1998.

[49] E. S. Gragoudas, K. M. Egan, P. G. Arrigg, J. M. Seddon, R. J. Glynn, and J. E. Munzenrider, "Cataract extraction after proton beam irradiation for malignant melanoma of the eye." *Archives of Ophthalmology*, vol. 110, no. 4, pp. 475–9, Apr. 1992.

[50] W. J. Meecham, D. H. Char, S. Kroll, J. R. Castro, and E. A. Blakely, "Anterior segment complications after helium ion radiation therapy for uveal melanoma. Radiation cataract." *Archives of Ophthalmology*, vol. 112, pp. 197–203, 1994.

[51] P. K. Lommatzsch and I. H. Kirsch, "106Ru/106Rh plaque radiotherapy for malignant melanomas of the choroid. With follow-up results more than 5 years." *Documenta Ophthalmologica. Advances in Ophthalmology*, vol. 68, no. 3-4, pp. 225–38, 1988.

[52] L. Lumbroso-Le Rouic, M. Charif Chefchaouni, C. Levy, C. Plancher, R. Dendale, B. Asselain, S. Solignac, a. Mazal, and L. Desjardins, "125I plaque brachytherapy for anterior uveal melanomas." *Eye (London, England)*, vol. 18, no. 9, pp. 911–6, Sep. 2004.

[53] M. W. Wilson and J. L. Hungerford, "Comparison of episcleral plaque and proton beam radiation therapy for the treatment of choroidal melanoma." *Ophthalmology*, vol. 106, no. 8, pp. 1579–87, Aug. 1999.

[54] E. S. Gragoudas, A. M. Lane, J. Munzenrider, K. M. Egan, and W. Li, "Long-term risk of local failure after proton therapy for choroidal/ciliary body melanoma." *Transactions of the American Ophthalmological Society*, vol. 100, pp. 43–8; discussion 48–9, Jan. 2002.

[55] E. Egger, a. Schalenbourg, L. Zografos, L. Bercher, T. Boehringer, L. Chamot, and G. Goitein, "Maximizing local tumor control and survival after proton beam radiotherapy of uveal melanoma." *International Journal of Radiation Oncology Biology Physics*, vol. 51, no. 1, pp. 138–47, Sep. 2001.

[56] Eckert & Ziegler BEBIG GmbH, "Ru-106 Eye Applicators," 2013. [Online]. Available: http://www.bebig.eu/fileadmin/bebig/pdf/FactSheet_Ru-106_Eye_Applicators_Englisch.pdf

[57] C. Karolis, R. B. Frost, and F. A. Billson, "A thin I-125 seed eye plaque to treat intraocular tumors using an acrylic insert to precisely position the sources,"

International Journal of Radiation Oncology Biology Physics, vol. 18, no. 5, pp. 1209–1213, May 1990.

[58] C. Karolis, C. Amies, R. B. Frost, and F. A. Billson, "The development of a thin stainless steel eye plaque to treat tumours of the eye up to 15 mm in diameter." *Australasian Physical & Engineering Sciences in Medicine*, vol. 12, pp. 172–177, 1989.

[59] R. B. Frost, C. A. Karolis, and F. A. Billson, "The Development of a Scleral Applicator for the Irradiation of Choroidal Melanoma," *Engineering in Medicine*, vol. 17, no. 2, pp. 77–80, 1988.

[60] J. Earle, R. W. Kline, and D. M. Robertson, "Selection of iodine 125 for the Collaborative Ocular Melanoma Study." *Archives of Ophthalmology*, vol. 105, no. 6, pp. 763–4, Jun. 1987.

[61] N. L. Gagne and M. J. Rivard, "Quantifying the dosimetric influences of radiation coverage and brachytherapy implant placement uncertainty on eye plaque size selection," *Brachytherapy*, Mar. 2013.

[62] The Collaborative Ocular Melanoma Study Group, "Accuracy of diagnosis of choroidal melanomas in the Collaborative Ocular Melanoma Study. COMS report no. 1." *Archives of Ophthalmology*, vol. 108, no. 9, pp. 1268–73, Sep. 1990.

[63] A. J. Mueller, W. R. Freeman, U. C. Schaller, A. Kampik, and R. Folberg, "Complex microcirculation patterns detected by confocal indocyanine green angiography predict time to growth of small choroidal melanocytic tumors: MuSIC Report II." *Ophthalmology*, vol. 109, no. 12, pp. 2207–14, Dec. 2002.

[64] D. H. Char, "Ocular melanoma." *The Surgical clinics of North America*, vol. 83, no. 2, pp. 253–74, vii, Apr. 2003.

[65] R. Nath, L. L. Anderson, G. Luxton, K. A. Weaver, J. F. Williamson, and A. S. Meigooni, "Dosimetry of interstitial brachytherapy sources: recommendations of the AAPM Radiation Therapy Committee Task Group No. 43. American Association of Physicists in Medicine." *Medical Physics*, vol. 22, no. 2, pp. 209–34, Feb. 1995.

[66] N. L. Gagne, K. L. Leonard, and M. J. Rivard, "Radiobiology for eye plaque brachytherapy and evaluation of implant duration and radionuclide choice using an objective function." *Medical Physics*, vol. 39, no. 6, pp. 3332–42, Jun. 2012.

[67] A. Krintz, W. F. Hanson, G. S. Ibbott, and D. S. Followill, "Verification of plaque simulator dose distributions using radiochromic film," *Medical Physics*, vol. 29, pp. 1220–1221, 2002.

[68] J. Poder and S. Corde, "I-125 ROPES eye plaque dosimetry: Validation of a commercial 3D ophthalmic brachytherapy treatment planning system and independent dose calculation software with GafChromic EBT3 films," *Medical Physics*, vol. 40, no. 12, p. 121709, 2013.

[69] S. Knutsen, R. Hafslund, O. R. Monge, H. Valen, L. P. Muren, B. L. Rekstad, J. Krohn, and O. Dahl, "Dosimetric verification of a dedicated 3D treatment planning system for episcleral plaque therapy." *International Journal of Radiation Oncology Biology Physics*, vol. 51, no. 4, pp. 1159–66, Nov. 2001.

[70] M. A. Astrahan, G. Luxton, Q. Pu, and Z. Petrovich, "Conformal episcleral plaque therapy," *International Journal of Radiation Oncology Biology Physics*, vol. 39, no. 2, pp. 505–519, Sep. 1997.

[71] S.-T. Chiu-Tsao, M. a. Astrahan, P. T. Finger, D. S. Followill, A. S. Meigooni, C. S. Melhus, F. Mourtada, M. E. Napolitano, R. Nath, M. J. Rivard, D. W. O. Rogers, and R. M. Thomson, "Dosimetry of (125)I and (103)Pd COMS eye

plaques for intraocular tumors: report of Task Group 129 by the AAPM and ABS." *Medical Physics*, vol. 39, no. 10, pp. 6161–84, Oct. 2012.

[72] P. De Potter, C. L. Shields, J. A. Shields, J. R. Cater, and L. W. Brady, "Plaque Radiotherapy for Juxtapapillary Choroidal Melanoma," *Archives of Ophthalmology*, vol. 114, pp. 1357–1365, 1996.

[73] K. Gündüz, C. L. Shields, J. A. Shields, J. Cater, J. E. Freire, and L. W. Brady, "Radiation Retinopathy Following Plaque Radiotherapy for Posterior Uveal Melanoma," *Archives of Ophthalmology*, vol. 117, no. 5, pp. 609–14, May 1999.

[74] K. Gündüz, C. L. Shields, J. A. Shields, J. Cater, J. E. Freire, and L. W. Brady, "Plaque Radiotherapy of Uveal Melanoma With Predominant Ciliary Body Involvement," *Archives of Ophthalmology*, vol. 117, no. 2, pp. 170–7, Feb. 1999.

[75] P. T. Finger, "Tumour location affects the incidence of cataract and retinopathy after ophthalmic plaque radiation therapy," *British Journal of Ophthalmology*, vol. 84, no. 9, pp. 1068–1070, Sep. 2000.

[76] I. Puusaari, J. Heikkonen, and T. Kivelä, "Ocular complications after iodine brachytherapy for large uveal melanomas." *Ophthalmology*, vol. 111, no. 9, pp. 1768–77, Sep. 2004.

[77] P. T. Finger, K. J. Chin, G.-P. Yu, and N. S. Patel, "Risk factors for cataract after palladium-103 ophthalmic plaque radiation therapy." *International Journal of Radiation Oncology Biology Physics*, vol. 80, no. 3, pp. 800–6, Jul. 2011.

[78] C. Groenewald, L. Konstantinidis, and B. Damato, "Effects of radiotherapy on

uveal melanomas and adjacent tissues." *Eye (London, England)*, vol. 27, no. 2, pp. 163–71, Feb. 2013.

[79] J. Krohn, O. R. Monge, T. N. Skorpen, S. J. Mø rk, and O. Dahl, "Posterior uveal melanoma treated with I-125 brachytherapy or primary enucleation." *Eye (London, England)*, vol. 22, no. 11, pp. 1398–403, Nov. 2008.

[80] I. Puusaari, J. Heikkonen, P. Summanen, A. Tarkkanen, and T. Kivelä, "Iodine brachytherapy as an alternative to enucleation for large uveal melanomas." *Ophthalmology*, vol. 110, no. 11, pp. 2223–34, Nov. 2003.

[81] J. Fontanesi, D. Meyer, S. Xu, and D. Tai, "Treatment of choroidal melanoma with I-125 plaque." *International Journal of Radiation Oncology Biology Physics*, vol. 26, no. 4, pp. 619–623, 1993.

[82] P. T. Finger, A. Berson, T. Ng, and A. Szechter, "Palladium-103 plaque radiotherapy for choroidal melanoma: an 11-year study." *International Journal of Radiation Oncology Biology Physics*, vol. 54, no. 5, pp. 1438–45, Dec. 2002.

[83] M. S. Sagoo, C. L. Shields, A. Mashayekhi, J. Freire, J. Emrich, J. Reiff, L. Komarnicky, and J. A. Shields, "Plaque radiotherapy for choroidal melanoma encircling the optic disc (circumpapillary choroidal melanoma)." *Archives of Ophthalmology*, vol. 125, no. 9, pp. 1202–9, Sep. 2007.

[84] M. J. Rivard, S.-T. Chiu-Tsao, P. T. Finger, A. S. Meigooni, C. S. Melhus, F. Mourtada, M. E. Napolitano, D. W. O. Rogers, R. M. Thomson, and R. Nath, "Comparison of dose calculation methods for brachytherapy of intraocular tumors," *Medical Physics*, vol. 38, no. 1, p. 306, 2011.

[85] Collaborative Ocular Melanoma Study Group, "Mortality in patients with small

choroidal melanoma. COMS report no. 4. The Collaborative Ocular Melanoma Study Group." *Archives of Ophthalmology*, vol. 115, no. 7, pp. 886–93, Jul. 1997.

[86] Collaborative Ocular Melanoma Study Group, "The Collaborative Ocular Melanoma Study (COMS) randomized trial of pre-enucleation radiation of large choroidal melanoma II: initial mortality findings. COMS report no. 10." *American Journal of Ophthalmology*, vol. 125, no. 6, pp. 779–96, Jun. 1998.

[87] M. Diener-West, J. D. Earle, S. L. Fine, B. S. Hawkins, C. S. Moy, S. M. Reynolds, a. P. Schachat, and B. R. Straatsma, "The COMS randomized trial of iodine 125 brachytherapy for choroidal melanoma, III: initial mortality findings. COMS Report No. 18." *Archives of Ophthalmology*, vol. 119, no. 7, pp. 969–82, Jul. 2001.

[88] F. L. Greene, D. L. Page, I. D. Fleming, A. G. Fritz, C. M. Balch, D. G. Haller, and M. Morrow, Eds., *AJCC Cancer Staging Manual*. New York, NY: Springer New York, 2002.

[89] L. M. Heindl, M. Lotter, V. Strnad, R. Sauer, G. O. H. Naumann, and H. L. J. Knorr, "[High-dose 106Ruthenium plaque brachytherapy for posterior uveal melanoma. A clinico-pathologic study]." *Der Ophthalmologe : Zeitschrift der Deutschen Ophthalmologischen Gesellschaft*, vol. 104, no. 2, pp. 149–57, Feb. 2007.

[90] S. Seregard, E. aft Trampe, I. Lax, E. Kock, and G. Lundell, "Results following episcleral ruthenium plaque radiotherapy for posterior uveal melanoma. The Swedish experience." *Acta Ophthalmologica Scandinavica*, vol. 75, no. 1, pp. 11–6, Feb. 1997.

[91] P. K. Lommatzsch, "Results after beta-irradiation (106Ru/106Rh) of choroidal melanomas: 20 years' experience." *The British journal of Ophthalmology*, vol. 70, no. 11, pp. 844–51, Nov. 1986.

[92] R. Correa, J. Pera, J. Gómez, A. Polo, C. Gutiérrez, J. M. Caminal, I. Modolell, V. Navarro, and F. Guedea, "(125)I episcleral plaque brachytherapy in the treatment of choroidal melanoma: a single-institution experience in Spain." *Brachytherapy*, vol. 8, no. 3, pp. 290–6, 2009.

[93] S. Nag, D. Wang, H. Wu, C. J. Bauer, R. B. Chambers, and F. H. Davidorf, "Custom-made "Nag" eye plaques for 125I brachytherapy." *International Journal of Radiation Oncology Biology Physics*, vol. 56, no. 5, pp. 1373–80, Aug. 2003.

[94] R. Jones, E. Gore, W. Mieler, K. Murray, M. Gillin, K. Albano, and B. Erickson, "Posttreatment visual acuity in patients treated with episcleral plaque therapy for choroidal melanomas: dose and dose rate effects." *International Journal of Radiation Oncology Biology Physics*, vol. 52, no. 4, pp. 989–95, Mar. 2002.

[95] J. M. Quivey, J. Augsburger, L. Snelling, and L. W. Brady, "125I plaque therapy for uveal melanoma. Analysis of the impact of time and dose factors on local control." *Cancer*, vol. 77, no. 11, pp. 2356–62, Jun. 1996.

[96] J. M. Quivey, D. H. Char, T. L. Phillips, K. A. Weaver, J. R. Castro, and S. M. Kroll, "High intensity 125-iodine (125I) plaque treatment of uveal melanoma." *International Journal of Radiation Oncology Biology Physics*, vol. 26, no. 4, pp. 613–8, Jul. 1993.

[97] Z. Petrovich, M. A. Astrahan, G. Luxton, R. Green, B. Langholz, and P. Liggett, "Episcleral plaque thermoradiotherapy in patients with choroidal melanoma." *International Journal of Radiation Oncology Biology Physics*, vol. 23, no. 3, pp. 599–603, Jan. 1992.

[98] P. T. Finger, S. Reddy, and K. Chin, "High-frequency ultrasound characteristics of 24 iris and iridociliary melanomas: before and after plaque brachytherapy." *Archives of Ophthalmology*, vol. 125, no. 8, pp. 1051–8, Aug. 2007.

[99] E. K. Lean, D. M. Cohen, P. E. Liggett, G. Luxton, B. Langholz, R. Lau, M. a. Astrahan, E. C. Hyden, and Z. Petrovich, "Episcleral radioactive plaque therapy: initial clinical experience with 56 patients." *American Journal of Clinical Oncology*, vol. 13, no. 3, pp. 185–90, Jun. 1990.

[100] Collaborative Ocular Melanoma Study Group, "Comparison of clinical, echographic, and histopathological measurements from eyes with medium-sized choroidal melanoma in the collaborative ocular melanoma study: COMS report no. 21." *Archives of Ophthalmology*, vol. 121, no. 8, pp. 1163–71, Aug. 2003.

[101] S. F. Byrne, H. C. Boldt, L. Cathy, and S. Mark, "Echography (ultrasound) procedures for the Collaborative Ocular Melanoma Study (COMS), Report no. 12, Part I." *Journal of Ophthalmic Nursing & Technology*, vol. 18, no. 4, pp. 143–9, 1999.

[102] C. W. DiBernardo and E. F. Greenberg, *Ophthalmic Ultrasound: A Diagnostic Atlas*, 2nd ed. Thieme Medical Publishers, Inc, 2006.

[103] Ellex Medical Pty. Ltd., "Eye Cubed - Specifications," 2012. [Online]. Available: http://www.ellex.com/assets/files/brochures/Nov2012/Ellex-Eyecubed-Brochure_2012.pdf

[104] J. M. Romero, P. T. Finger, R. B. Rosen, and R. Iezzi, "Three-dimensional ultrasound for the measurement of choroidal melanomas." *Archives of Ophthalmology*, vol. 119, no. 9, pp. 1275–82, Sep. 2001.

[105] T. H. Pettit, A. Barton, R. Y. Foos, and R. E. Christensen, "Fluorescein Angiography of Choroidal Melanomas," *Archives of Ophthalmology*, vol. 83, no. 1, pp. 27–38, Jan. 1970.

[106] U. Schneider, F. Gelisken, W. Inhoffen, and I. Kreissig, "Indocyanine green

videoangiography of malignant melanomas of the choroid using the scanning laser ophthalmoscope." *German Journal of Ophthalmology*, vol. 5, no. 1, pp. 6–11, Jan. 1996.

[107] P. T. Finger, J. M. Romero, R. B. Rosen, R. Iezzi, R. Emery, and A. Berson, "Three-dimensional ultrasonography of choroidal melanoma: localization of radioactive eye plaques." *Archives of Ophthalmology*, vol. 116, no. 3, pp. 305–12, Mar. 1998.

[108] K. A. Weaver, "The dosimetry of 125I seed eye plaques." *Medical Physics*, vol. 13, no. 1, pp. 78–83, 1986.

[109] G. Luxton, M. A. Astrahan, and Z. Petrovich, "Backscatter measurements from a single seed of 125I for ophthalmic plaque dosimetry." *Medical Physics*, vol. 15, no. 3, pp. 397–400, 1988.

[110] A. Wu, E. S. Sternick, and D. J. Muise, "Effect of gold shielding on the dosimetry of an 125I seed at close range." *Medical Physics*, vol. 15, no. 4, pp. 627–8, 1988.

[111] S. T. Chiu-Tsao, L. L. Anderson, K. O'Brien, L. Stabile, and J. C. Liu, "Dosimetry for 125I seed (model 6711) in eye plaques." *Medical Physics*, vol. 20, no. 2 Pt 1, pp. 383–389, 1993.

[112] A. de la Zerda, S. T. Chiu-Tsao, J. Lin, L. L. Boulay, I. Kanna, J. H. Kim, and H. S. Tsao, "125I eye plaque dose distribution including penumbra characteristics." *Medical Physics*, vol. 23, no. 3, pp. 407–18, Mar. 1996.

[113] J. Cygler, J. Szanto, M. Soubra, and D. W. Rogers, "Effects of gold and silver backings on the dose rate around an 125I seed." *Medical Physics*, vol. 17, no. 2, pp. 172–8, 1990.

[114] J. A. Meli and K. A. Motakabbir, "The effect of lead, gold, and silver backings on dose near 125I seeds." *Medical Physics*, vol. 20, no. 4, pp. 1251–6, 1993.

[115] W. M. Butler, W. S. Bice, Jr., L. a. DeWerd, J. M. Hevezi, M. S. Huq, G. S. Ibbott, J. R. Palta, M. J. Rivard, J. P. Seuntjens, and B. R. Thomadsen, "Third-party brachytherapy source calibrations and physicist responsibilities: Report of the AAPM Low Energy Brachytherapy Source Calibration Working Group," *Medical Physics*, vol. 35, no. 9, p. 3860, 2008.

[116] L. a. DeWerd, G. S. Ibbott, A. S. Meigooni, M. G. Mitch, M. J. Rivard, K. E. Stump, B. R. Thomadsen, and J. L. M. Venselaar, "A dosimetric uncertainty analysis for photon-emitting brachytherapy sources: Report of AAPM Task Group No. 138 and GEC-ESTRO," *Medical Physics*, vol. 38, no. 2, p. 782, 2011.

[117] T. Kron, "Medical Radiation Dosimetry: Concepts and Needs," *AIP Conference Proceedings*, vol. 1345, pp. 24–35, 2011.

[118] J. V. Trapp and T. Kron, *An Introduction to Radiation Protection in Medicine*. Taylor & Francis, 2008.

[119] P. T. Finger, "Finger's "slotted" eye plaque for radiation therapy: treatment of juxtapapillary and circumpapillary intraocular tumours." *The British journal of Ophthalmology*, vol. 91, no. 7, pp. 891–4, Jul. 2007.

[120] R. M. Thomson, K. M. Furutani, J. S. Pulido, S. L. Stafford, and D. W. O. Rogers, "Modified COMS plaques for 125I and 103Pd iris melanoma brachytherapy." *International Journal of Radiation Oncology Biology Physics*, vol. 78, no. 4, pp. 1261–9, Nov. 2010.

[121] P. T. Finger, K. J. Chin, and L. B. Tena, "A five-year study of slotted eye plaque

radiation therapy for choroidal melanoma: near, touching, or surrounding the optic nerve." *Ophthalmology*, vol. 119, no. 2, pp. 415–22, Feb. 2012.

[122] A. N. Harnett and E. S. Thomson, "An iodine-125 plaque for radiotherapy of the eye: manufacture and dosimetric considerations." *The British Journal of Radiology*, vol. 61, no. 729, pp. 835–8, Sep. 1988.

[123] W. Alberti, B. Pothmann, P. Tabor, K. Muskalla, K. P. Hermann, and D. Harder, "Dosimetry and physical treatment planning for iodine eye plaque therapy." *International Journal of Radiation Oncology Biology Physics*, vol. 20, no. 5, pp. 1087–92, May 1991.

[124] C. G. Soares, S. Vynckier, H. Jarvinen, W. G. Cross, P. Sipila, D. Fluhs, B. Schaeken, F. A. Mourtada, G. A. Bass, and T. T. Williams, "Dosimetry of beta-ray ophthalmic applicators: Comparison of different measurement methods," *Medical Physics*, vol. 28, no. 7, p. 1373, 2001.

[125] P. Bilski, M. Waligórski, and M. Budzanowski, "Miniature Thermoluminescent Detectors For Dosimetry in Radiotherapy," *Radiation Protection Dosimetry*, vol. 101, pp. 473–476, 2002.

[126] P. Olko, B. Marczewska, L. Czopyk, M. a. Czermak, M. Klosowski, and M. P. R. Waligórski, "New 2-D dosimetric technique for radiotherapy based on planar thermoluminescent detectors." *Radiation Protection Dosimetry*, vol. 118, no. 2, pp. 213–8, Jan. 2006.

[127] P. Olko, L. Czopyk, M. Klosowski, and M. P. Waligorski, "Thermoluminescence dosimetry using TL-readers equipped with CCD cameras," *Radiation Measurements*, vol. 43, no. 2-6, pp. 864–869, Feb. 2008.

[128] M. F. Chan, a. Y. Fung, Y. C. Hu, C. S. Chui, H. Amols, M. Zaider, and

D. Abramson, "The measurement of three dimensional dose distribution of a ruthenium-106 ophthalmological applicator using magnetic resonance imaging of BANG polymer gels." *Journal of Applied Clinical Medical Physics / American College of Medical Physics*, vol. 2, no. 2, pp. 85–9, Jan. 2001.

[129] A. Wu and F. Krasin, "Film dosimetry analyses on the effect of gold shielding for iodine-125 eye plaque therapy for choroidal melanoma." *Medical Physics*, vol. 17, no. 5, pp. 843–6, 1990.

[130] A. S. Kirov, J. Z. Piao, N. K. Mathur, T. R. Miller, S. Devic, S. Trichter, M. Zaider, C. G. Soares, and T. LoSasso, "The three-dimensional scintillation dosimetry method: test for a 106Ru eye plaque applicator." *Physics in Medicine and Biology*, vol. 50, no. 13, pp. 3063–81, Jul. 2005.

[131] H. Acar, "Verification of plaque simulator dose distributions using GAFCHROMIC EBT film," *Türk Onkoloji Dergisi*, vol. 25, no. 4, pp. 150–156, 2010.

[132] D. Flühs, G. Anastassiou, J. Wening, W. Sauerwein, and N. Bornfeld, "The design and the dosimetry of bi-nuclide radioactive ophthalmic applicators," *Medical Physics*, vol. 31, no. 6, p. 1481, 2004.

[133] D. Fluhs, M. Heintz, F. Indenkampen, C. Wieczorek, H. Kolanoski, and U. Quast, "Direct reading measurement of absorbed dose with plastic scintillators — The general concept and applications to ophthalmic plaque dosimetry," *Medical Physics*, pp. 428–435, 1996.

[134] M. Eichmann, D. Flühs, and B. Spaan, "Development of a high precision dosimetry system for the measurement of surface dose rate distribution for eye applicators." *Medical Physics*, vol. 36, no. 10, pp. 4634–43, Oct. 2009.

[135] A. B. Rosenfeld, D. Cutajar, M. L. F. Lerch, G. Takacs, I. M. Cornelius, M. Yudelev, and M. Zaider, "Miniature semiconductor detectors for in vivo dosimetry," *Radiation Protection Dosimetry*, vol. 120, no. 1-4, pp. 48–55, Jan. 2006.

[136] A. B. Rosenfeld, "Electronic dosimetry in radiation therapy," *Radiation Measurements*, vol. 41, pp. S134–S153, Dec. 2006.

[137] P. A. Jursinic, "Implementation of an in vivo diode dosimetry program and changes in diode characteristics over a 4-year clinical history," *Medical Physics*, vol. 28, no. 8, p. 1718, 2001.

[138] J. Kemmer, "Improvement of detector fabrication by the planar process," *Nuclear Inst. and Methods in Physics Research, A*, 1984.

[139] J. Kemmer, "Fabrication of low noise silicon radiation detectors by the planar process," *Nuclear Instruments and Methods*, vol. 169, no. 3, pp. 499–502, Mar. 1980.

[140] M. Weaver, J. Green, M. Petasecca, M. Lerch, D. Cutajar, D. Franklin, J. Jakubek, M. Carolan, M. Conway, S. Pospisil, T. Kron, P. Metcalfe, M. Zaider, and A. Rosenfeld, "Three-dimensional dosimetry imaging of I-125 plaque for eye cancer treatment," *Nuclear Instruments and Methods in Physics Research Section A: Accelerators, Spectrometers, Detectors and Associated Equipment*, vol. 633, pp. S276–S278, May 2011.

[141] M. Weaver, M. Petasecca, M. Lerch, D. Cutajar, J. Jakubek, S. Pospíšil, and A. Rosenfeld, "Dosimetry verification in eye brachytherapy using silicon pixelated detectors," *Radiation Measurements*, vol. 46, no. 12, pp. 2010–2013, Dec. 2011.

[142] X. Llopart, M. Campbell, R. Dinapoli, D. San Segundo, and E. Pernigotti,

"Medipix2: A 64-k pixel readout chip with 55-μm square elements working in single photon counting mode," *IEEE Transactions on Nuclear Science*, vol. 49, no. 5, pp. 2279–2283, Oct. 2002.

[143] X. Llopart, R. Ballabriga, M. Campbell, L. Tlustos, and W. Wong, "Timepix, a 65k programmable pixel readout chip for arrival time, energy and/or photon counting measurements," *Nuclear Instruments and Methods in Physics Research Section A: Accelerators, Spectrometers, Detectors and Associated Equipment*, vol. 581, no. 1-2, pp. 485–494, Oct. 2007.

[144] B. Chan, M. Rotman, and G. J. Randall, "Computerized dosimetry of 60 Co ophthalmic applicators." *Radiology*, vol. 103, no. 3, pp. 705–7, Jun. 1972.

[145] G. Luxton, M. A. Astrahan, P. E. Liggett, D. L. Neblett, D. M. Cohen, and Z. Petrovich, "Dosimetric calculations and measurements of gold plaque ophthalmic irradiators using iridium-192 and iodine-125 seeds," *International Journal of Radiation Oncology Biology Physics*, vol. 15, no. 1, pp. 167–176, Jul. 1988.

[146] J. Hokkanen, J. Heikkonen, and P. Holmberg, "Theoretical calculations of dose distributions for beta-ray eye applicators." *Medical Physics*, vol. 24, no. 2, pp. 211–3, Feb. 1997.

[147] M. A. Astrahan, "Improved treatment planning for COMS eye plaques," *International Journal of Radiation Oncology Biology Physics*, vol. 61, no. 4, pp. 1227–1242, 2005.

[148] D. Granero, J. Pérez-Calatayud, F. Ballester, E. Casal, and J. M. de Frutos, "Dosimetric study of the 15 mm ROPES eye plaque." *Medical Physics*, vol. 31, no. 12, pp. 3330–6, Dec. 2004.

[149] R. M. Thomson, R. E. P. Taylor, and D. W. O. Rogers, "Monte Carlo dosimetry

for 125I and 103Pd eye plaque brachytherapy." *Medical Physics*, vol. 35, no. 12, pp. 5530–43, Dec. 2008.

[150] C. S. Melhus and M. J. Rivard, "COMS eye plaque brachytherapy dosimetry simulations for 103Pd, 125I, and 131Cs," *Medical Physics*, vol. 35, no. 7, p. 3364, 2008.

[151] S. T. Chiu-Tsao, K. O'Brien, R. Sanna, H. S. Tsao, C. Vialotti, Y. S. Chang, M. Rotman, and S. Packer, "Monte Carlo dosimetry for 125I and 60Co in eye plaque therapy." *Medical Physics*, vol. 13, no. 5, pp. 678–82, 1986.

[152] W. G. Cross, J. Hokkanen, H. Jarvinen, F. Mourtada, P. Sipila, C. G. Soares, and S. Vynckier, "Calculation of beta-ray dose distributions from ophthalmic applicators and comparison with measurements in a model eye," *Medical Physics*, vol. 28, no. 7, p. 1385, 2001.

[153] F. Mourtada, N. Koch, and W. Newhauser, "106Ru/106Rh plaque and proton radiotherapy for ocular melanoma: a comparative dosimetric study." *Radiation Protection Dosimetry*, vol. 116, no. 1-4 Pt 2, pp. 454–60, Jan. 2005.

[154] R. M. Thomson and D. W. O. Rogers, "Monte Carlo dosimetry for 125I and 103Pd eye plaque brachytherapy with various seed models." *Medical Physics*, vol. 37, no. 1, pp. 368–76, Jan. 2010.

[155] H. Zhang, D. Martin, S.-T. Chiu-Tsao, A. Meigooni, and B. R. Thomadsen, "A comprehensive dosimetric comparison between (131)Cs and (125)I brachytherapy sources for COMS eye plaque implant." *Brachytherapy*, vol. 9, no. 4, pp. 362–72, 2010.

[156] K. Gifford, S. Kirsner, J. Horton, T. Wareing, and F. Mourtada, "TU-C-AUD-06: Calculation of the Dose Distribution Around a Commercially Available 125I

Brachytherapy Source Via a Multi-Group Discrete Ordinates Method," *Medical Physics*, vol. 34, no. 6, p. 2550, 2007.

[157] J. R. Bristol, "Comparison of eye plaque dosimetry using deterministic and Monte Carlo methods," Master of Science, Oregon State University, 2010.

[158] A. B. Rosenfeld and M. Zaider, "Method and apparatus for real time dosimetry," 2003. [Online]. Available: http://patentscope.wipo.int/search/en/WO2003062855

[159] D. L. Cutajar, G. J. Takacs, M. L. F. Lerch, T. Braddock, J. A. Bucci, J. Brady, L. J. Duggan, K. E. Enari, M. Zaider, M. Zelefsky, A. B. Rosenfeld, and S. Member, "Intraoperative Solid-State Based Urethral Dosimetry in Low Dose Rate Prostate Brachytherapy," *IEEE Transactions on Nuclear Science*, vol. 53, no. 3, pp. 1408–1412, 2006.

[160] H. Spieler, *Semiconductor Detector Systems*, 1st ed. New York, United States: Oxford University Press, Oct. 2005, vol. 3, no. 4.

[161] G. Bertolini and A. Coche, Eds., *Semiconductor Detectors*. Amsterdam: Elsevier-North Holland, 1968.

[162] P. A. Tipler and G. Mosca, *Physics for Scientists and Engineers*, 5th ed. W. H. Freeman, 2003.

[163] G. F. G. Knoll, *Radiation Detection and Measurement*, 3rd ed. John Wiley & Sons, Inc., 2000.

[164] B. M. Wilamowski, "Semiconductor Diode," in *Industrial Electronics Handbook, vol. 1 - Fundamentals of Industrial Electronics*, 2nd ed., B. M. Wilamowski and J. D. Irwin, Eds. CRC Press, 2011, ch. 8, pp. 8–1 to 8–15.

[165] S. M. Sze and K. K. Ng, *Physics of Semiconductor Devices*, 3rd ed. Hoboken, New Jersey: John Wiley & Sons, Inc., 2007.

[166] A. S. Khan, *Microwave Engineering: Concepts and Fundamentals.* CRC Press, 2014.

[167] U.S. NIM Committee, "Standard NIM instrumentation system," Technical Information Center, U.S. Department of Energy, Tech. Rep., May 1990.

[168] B. W. Loo, F. S. Goulding, and D. Gao, "Ballistic Deficits in Pulse Shaping Amplifiers." *IEEE Transactions on Nuclear Science*, vol. 35, no. 1, pp. 114–118, 1987.

[169] F. S. Goulding and D. A. Landis, "Ballistic Deficit Correction In Semiconductor Detector Spectrometers," *IEEE Transactions on Nuclear Science*, vol. 35, no. 1, pp. 119–124, 1987.

[170] P. W. Nicholson, *Nuclear Electronics.* John Wiley & Sons, Ltd., 1974.

[171] L. B. Robinson, "Reduction of Baseline Shift in Pulse-Amplitude Measurements," *Review of Scientific Instruments*, vol. 32, no. 9, p. 1057, 1961.

[172] E. A. Gere and G. L. Miller, "Active D-C Restoration in Nuclear Pulse Spectrometry," *IEEE Transactions on Nuclear Science*, vol. 14, no. 1, pp. 89–95, 1967.

[173] E. Fairstein, "Gated Baseline Restorer with Adjustable Asymmetry," *Nuclear Science, IEEE Transactions on*, vol. 22, no. 1, pp. 463–466, 1975.

[174] M. Kuwata, H. Maeda, and K. Husimi, "New baseline restorer based on feedforward differential compensation," *IEEE Transactions on Nuclear Science*, vol. 41, no. 4, pp. 1236–1239, 1994.

[175] G. De Geronimo, P. O'Connor, and J. Grosholz, "A CMOS baseline holder (BLH) for readout ASICs," in *1999 IEEE Nuclear Science Symposium. Conference Record. 1999 Nuclear Science Symposium and Medical Imaging Conference (Cat. No.99CH37019)*, vol. 1. IEEE, 1999, pp. 370–374.

[176] H. Li, C. Wang, H. Baghaei, Y. Zhang, R. Ramirez, S. Liu, S. An, and W.-H. Wong, "A New Statistics-Based Online Baseline Restorer for a High Count-Rate Fully Digital System." *IEEE Transactions on Nuclear Science*, vol. 57, no. 2, pp. 550–555, Apr. 2010.

[177] W. Wong, G. Anton, R. Ballabriga, M. Böhnel, M. Campbell, E. Heijne, X. Llopart, T. Michel, I. Münster, R. Plackett, P. Sievers, P. Takoukam, L. Tlustos, and P. Valerio, "A pixel detector asic for dosimetry using time-over-threshold energy measurements," *Radiation Measurements*, vol. 46, no. 12, pp. 1619–1623, Dec. 2011.

[178] M. J. Rivard, C. S. Melhus, S. Sioshansi, and J. Morr, "The impact of prescription depth, dose rate, plaque size, and source loading on the central axis using 103Pd, 125I, and 131Cs." *Brachytherapy*, vol. 7, no. 4, pp. 327–35, 2008.

[179] M. Berger, J. Hubbell, S. Seltzer, J. Chang, J. Coursey, R. Sukumar, D. Zucker, and K. Olsen, "XCOM: Photon Cross Section Database (version 1.5)," p. [Online] Available: http://physics.nist.gov/xcom, 2010. [Online]. Available: http://physics.nist.gov/xcom

[180] Computerized Imaging Reference Systems Incorporated, "Plastic Water LR," Norfolk, VA, USA.

[181] B. Reniers, F. Verhaegen, and S. Vynckier, "The radial dose function of low-energy brachytherapy seeds in different solid phantoms: comparison between

calculations with the EGSnrc and MCNP4C Monte Carlo codes and measurements," *Physics in Medicine and Biology*, vol. 49, no. 8, pp. 1569–1582, Apr. 2004.

[182] R. Hill, Z. Kuncic, and C. Baldock, "The water equivalence of solid phantoms for low energy photon beams." *Medical Physics*, vol. 37, no. 8, pp. 4355–63, Aug. 2010.

[183] D. Cutajar, "Spectroscopic dosimetry : the development of the urethral minidosimetry system," Doctor of Philosophy, University of Wollongong, 2011.

[184] IM/AI - TC8 - Automated Test Systems and Instrumentation, "488.2-1992 - IEEE Standard Codes, Formats, Protocols, and Common Commands for Use With IEEE Std 488.1-1987, IEEE Standard Digital Interface for Programmable Instrumentation," 1992. [Online]. Available: http://standards.ieee.org/findstds/standard/488.2-1992.html

[185] National Instruments, "LabVIEW System Design Software," 2013. [Online]. Available: http://www.ni.com/labview/

[186] Wireless Telecom Group Inc., "Boonton 7200 Series Capacitance Meter," p. 4, 2010. [Online]. Available: http://boonton.com/~/media/Boonton/Datasheets/7200_Datasheet_WEB.ashx

[187] GE Healthcare Medi-Physics Inc., "OncoSeed (Iodine-125 Seeds)," Oncura Inc., Tech. Rep., 2009.

[188] International Organization for Standardization, "ISO/IEC 14882:2014," 2014.

[189] Digia, "Qt," Helsinki Finland, 2013. [Online]. Available: http://qt.digia.com/

[190] P. Lecoq, "Spin-off from particle detectors in the field of medicine and biology," *Nuclear Instruments and Methods in Physics Research Section A: Accelerators,*

Spectrometers, Detectors and Associated Equipment, vol. 581, no. 1-2, pp. 1–11, Oct. 2007.

[191] J. Jakubek, "Semiconductor Pixel detectors and their applications in life sciences," *Journal of Instrumentation*, vol. 4, no. 03, pp. P03 013–P03 013, Mar. 2009.

[192] W. T. Lin, Y.-H. Chang, A. E. Chen, S. R. Hou, C.-H. Lin, P. Kulinich, J. Ryan, P. Steinberg, B. Wadsworth, and B. Wyslouch, "Development of a double metal, AC-coupled silicon pad detector," *Nuclear Instruments and Methods in Physics Research Section A: Accelerators, Spectrometers, Detectors and Associated Equipment*, vol. 389, no. 3, pp. 415–420, Apr. 1997.

[193] R. Ballabriga, M. Campbell, E. H. M. Heijne, X. Llopart, and L. Tlustos, "The Medipix3 Prototype, a Pixel Readout Chip Working in Single Photon Counting Mode With Improved Spectrometric Performance," *IEEE Transactions on Nuclear Science*, vol. 54, no. 5, pp. 1824–1829, Oct. 2007.

[194] J. Jakubek, C. Granja, T. Holy, E. Lehmann, V. Linhart, S. Pospisil, V. Rypar, J. Uher, J. Vacik, D. Vavrik, Z. Vykydal, and M. Cevallos, "Neutron imaging and tomography with Medipix2 and dental micro-roentgenography," *Nuclear Instruments and Methods in Physics Research Section A: Accelerators, Spectrometers, Detectors and Associated Equipment*, vol. 569, no. 2, pp. 205–209, Dec. 2006.

[195] J. Jakubek, "Data processing and image reconstruction methods for pixel detectors," *Nuclear Instruments and Methods in Physics Research Section A: Accelerators, Spectrometers, Detectors and Associated Equipment*, vol. 576, no. 1, pp. 223–234, Jun. 2007.

[196] J. Jakubek, J. Dammer, C. Granja, T. Holy, S. Pospisil, and J. Uher, "Compact system for high resolution X-ray transmission radiography, in-line phase

enhanced imaging and micro CT of biological samples," in *IEEE Nuclear Science Symposium Conference Record*, vol. 2, no. 106, 2006, pp. 1077–1080.

[197] M. Weaver, M. Petasecca, D. L. Cutajar, M. L. F. Lerch, G. De Geronimo, D. a. Pinelli, a. J. Cullen, D. a. Prokopovich, V. L. Perevertaylo, and a. B. Rosenfeld, "Panoptes: Calibration of a dosimetry system for eye brachytherapy," *Radiation Measurements*, vol. 71, pp. 310–314, 2014.

[198] D. R. White, "Tissue substitutes in experimental radiation physics." *Medical physics*, vol. 5, no. 6, pp. 467–479, 2010.

[199] MathWorks, "Matlab," 2012. [Online]. Available: http://www.mathworks.com.au/products/matlab/

[200] H. S. Hou and H. C. Andrews, "Cubic splines for image interpolation and digital filtering," *IEEE Transactions on Acoustics, Speech, and Signal Processing*, vol. 26, pp. 508–517, 1978.

[201] F. Krejci, J. Jakubek, M. Kroupa, P. Bruza, and D. Panek, "Pixel detector Timepix operated in pile-up mode for pulsed imaging with ultra-soft X-rays," *Journal of Instrumentation*, vol. 7, no. 12, pp. C12013–C12013, 2012.

[202] T. Holy, J. Jakubek, S. Pospisil, J. Uher, D. Vavrik, and Z. Vykydal, "Data acquisition and processing software package for Medipix2," *Nuclear Instruments and Methods in Physics Research, Section A: Accelerators, Spectrometers, Detectors and Associated Equipment*, vol. 563, no. 1, pp. 254–258, 2006.

[203] L. Tlustos, R. Ballabriga, M. Campbell, E. Heijne, K. Kincade, X. Llopart, and P. Stejska, "Imaging properties of the medipix2 system exploiting single and dual energy thresholds," *IEEE Transactions on Nuclear Science*, vol. 53, no. 1, pp. 367–372, 2006.

[204] C. Shannon, "Communication in the Presence of Noise," *Proceedings of the IRE*, vol. 37, no. 1, pp. 10–21, Jan. 1949.

[205] R. Keys, "Cubic convolution interpolation for digital image processing," *IEEE Transactions on Acoustics, Speech, and Signal Processing*, vol. 29, no. I, pp. 1153–1160, 1981.

[206] J. Šolc, "Monte Carlo calculation of dose to water of a 106 Ru COB-type ophthalmic plaque," *Journal of Physics: Conference Series*, vol. 102, p. 012021, Feb. 2008.

[207] D. A. Wilkinson, M. Kolar, P. A. Fleming, and A. D. Singh, "Dosimetric comparison of 106Ru and 125I plaques for treatment of shallow (<or=5 mm) choroidal melanoma lesions." *The British Journal of Radiology*, vol. 81, no. 970, pp. 784–9, Oct. 2008.

[208] J. F. Ziegler, M. Ziegler, and J. Biersack, "SRIM - The stopping and range of ions in matter (2010)," *Nuclear Instruments and Methods in Physics Research Section B: Beam Interactions with Materials and Atoms*, vol. 268, no. 11-12, pp. 1818–1823, Jun. 2010.

[209] G. De Geronimo, P. O'Connor, R. Beuttenmuller, Z. Li, A. Kuczewski, and D. Siddons, "Development of a high-rate high-resolution detector for EXAFS experiments," *IEEE Transactions on Nuclear Science*, vol. 50, no. 4, pp. 885–891, Aug. 2003.

[210] P. Yoon and M. Siddons, "Photodiode-based X-ray Beam Position Monitor with High Spatial-resolution for the NSLSII Beamlines," *Proceedings of DIPAC09*, pp. 13–15, 2009.

[211] C. Ryan, D. Siddons, G. Moorhead, R. Kirkham, P. Dunn, a. Dragone, and

G. De Geronimo, "Large detector array and real-time processing and elemental image projection of X-ray and proton microprobe fluorescence data," *Nuclear Instruments and Methods in Physics Research Section B: Beam Interactions with Materials and Atoms*, vol. 260, no. 1, pp. 1–7, Jul. 2007.

[212] K. Lee, J. W. Martin, A. B. Garson III, M. Beilicke, Q. Guo, Q. Li, G. De Geronimo, M. Groza, A. Burger, and H. Krawczynski, "Development of x-ray and gamma-ray CZT detectors for homeland security applications," in *Detection and Sensing of Mines, Explosive Objects, and Obscured Targets XV*, R. S. Harmon, J. H. Holloway, Jr., and J. T. Broach, Eds., vol. 7664, Apr. 2010, pp. 766 423–766 423–9.

[213] D. P. Siddons, A. Dragone, G. De Geronimo, A. Kuczewski, J. Kuczewski, P. O'Connor, Z. Li, C. G. Ryan, G. Moorhead, R. Kirkham, and P. Dunn, "A High-speed Detector System for X-ray Fluorescence Microprobes," in *2006 IEEE Nuclear Science Symposium Conference Record.* IEEE, 2006, pp. 725–728.

[214] G. De Geronimo and P. O'Connor, "A CMOS fully compensated continuous reset system," in *1999 IEEE Nuclear Science Symposium. Conference Record. 1999 Nuclear Science Symposium and Medical Imaging Conference (Cat. No.99CH37019)*, vol. 2. IEEE, 1999, pp. 584–588.

[215] International Electrotechnical Commission, "IEC 60320-2-2 ed2.0," 2014. [Online]. Available: http://webstore.iec.ch/webstore/webstore.nsf/artnum/023204

[216] EMCO High Voltage Corporation, "CA-T Series Datasheet," pp. 1–7, 2013. [Online]. Available: http://www.emcohighvoltage.com/pdfs/ca-tseries.pdf

[217] Opal Kelly Incorporated, "XEM6001 User's Manual," pp. 1–16, 2010. [Online]. Available: http://assets00.opalkelly.com/library/XEM6001-UM.pdf

[218] Xilinx Incorporated, "Spartan-6 Family Overview Summary of Spartan-6 FPGA Features," pp. 1–11, 2011. [Online]. Available: http://www.xilinx.com/support/documentation/data_sheets/ds160.pdf

[219] USB Implementers Forum Incorporated, "Universal Serial Bus Revision 2.0 Specification," 2000. [Online]. Available: http://www.usb.org/developers/docs/usb_20_040413.zip

[220] SANMOTION - SANYO DENKI Co. Ltd., "2-Phase Stepping Systems," Japan, 2013. [Online]. Available: http://www.sanyo-denki.com/Data/Servo/catalogs/F2_ver1.pdf

[221] Gecko Drives Motor Controls, "G203V Stepper Drive Datasheet," 2010.

[222] 3D Systems, "ProJet 3500 SD & HD Professional 3D Printer Series," Darmstadt, Germany, 2013. [Online]. Available: http://www.3dsystems.com/sites/www.3dsystems.com/files/projet_3500_plastic_uk.pdf

[223] Opal Kelly Incorporated, "FrontPanel User's Manual," pp. 1–110, 2012. [Online]. Available: http://assets00.opalkelly.com/library/FrontPanel-UM.pdf

[224] L. Tlustos, "Dissertation Performance and limitations of high granularity single photon processing X-ray imaging detectors," p. 177, 2005.

[225] Amptek Incorporated, "A250 Charge Sensitive Preamplifier - Specifications," Bedford, USA, pp. 1–4, 2013. [Online]. Available: http://www.amptek.com/pdf/a250.pdf

[226] S. Agostinelli, J. Allison, K. Amako, J. Apostolakis, H. Araujo, P. Arce, M. Asai, D. Axen, S. Banerjee, G. Barrand, F. Behner, L. Bellagamba, J. Boudreau, L. Broglia, A. Brunengo, H. Burkhardt, S. Chauvie, J. Chuma, R. Chytracek,

G. Cooperman, G. Cosmo, P. Degtyarenko, A. Dell'Acqua, G. Depaola, D. Dietrich, R. Enami, A. Feliciello, C. Ferguson, H. Fesefeldt, G. Folger, F. Foppiano, A. Forti, S. Garelli, S. Giani, R. Giannitrapani, D. Gibin, J. J. Gomez Cadenas, I. Gonzalez, G. Gracia Abril, G. Greeniaus, W. Greiner, V. Grichine, A. Grossheim, S. Guatelli, P. Gumplinger, R. Hamatsu, K. Hashimoto, H. Hasui, A. Heikkinen, A. Howard, V. Ivanchenko, A. Johnson, F. W. Jones, J. Kallenbach, N. Kanaya, M. Kawabata, Y. Kawabata, M. Kawaguti, S. Kelner, P. Kent, A. Kimura, T. Kodama, R. Kokoulin, M. Kossov, H. Kurashige, E. Lamanna, T. Lampen, V. Lara, V. Lefebure, F. Lei, M. Liendl, W. Lockman, F. Longo, S. Magni, M. Maire, E. Medernach, K. Minamimoto, P. Mora de Freitas, Y. Morita, K. Murakami, M. Nagamatu, R. Nartallo, P. Nieminen, T. Nishimura, K. Ohtsubo, M. Okamura, S. O'Neale, Y. Oohata, K. Paech, J. Perl, A. Pfeiffer, M. G. Pia, F. Ranjard, A. Rybin, S. Sadilov, E. di Salvo, G. Santin, T. Sasaki, N. Savvas, Y. Sawada, S. Scherer, S. Sei, V. Sirotenko, D. Smith, N. Starkov, H. Stoecker, J. Sulkimo, M. Takahata, S. Tanaka, E. Tcherniaev, E. Safai Tehrani, M. Tropeano, P. Truscott, H. Uno, L. Urban, P. Urban, M. Verderi, A. Walkden, W. Wander, H. Weber, J. P. Wellisch, T. Wenaus, D. C. Williams, D. Wright, T. Yamada, H. Yoshida, and D. Zschiesche, "GEANT4 - A simulation toolkit," *Nuclear Instruments and Methods in Physics Research, Section A: Accelerators, Spectrometers, Detectors and Associated Equipment*, vol. 506, no. 3, pp. 250–303, Jul. 2003.

[227] J. Allison, K. Amako, J. Apostolakis, H. Araujo, P. A. Dubois, M. Asai, G. Barrand, R. Capra, S. Chauvie, R. Chytracek, G. a. P. Cirrone, G. Cooperman, G. Cosmo, G. Cuttone, G. G. Daquino, M. Donszelmann, M. Dressel, G. Folger, F. Foppiano, J. Generowicz, V. Grichine, S. Guatelli, P. Gumplinger, A. Heikkinen, I. Hrivnacova, A. Howard, S. Incerti, V. Ivanchenko, T. Johnson, F. Jones,

T. Koi, R. Kokoulin, M. Kossov, H. Kurashige, V. Lara, S. Larsson, F. Lei, F. Longo, M. Maire, A. Mantero, B. Mascialino, I. McLaren, P. M. Lorenzo, K. Minamimoto, K. Murakami, P. Nieminen, L. Pandola, S. Parlati, L. Peralta, J. Perl, A. Pfeiffer, M. G. Pia, A. Ribon, P. Rodrigues, G. Russo, S. Sadilov, G. Santin, T. Sasaki, D. Smith, N. Starkov, S. Tanaka, E. Tcherniaev, B. Tomé, A. Trindade, P. Truscott, L. Urban, M. Verderi, A. Walkden, J. P. Wellisch, D. C. Williams, D. Wright, H. Yoshida, and M. Peirgentili, "Geant4 Developments and Applications," *IEEE Transactions on Nuclear Science*, vol. 53, no. 1, pp. 270–278, 2006.

[228] D. E. Cullen, J. H. Hubbell, and L. Kissel, "EPDL97: the evaluated photo data library '97 version," Lawrence Livermore National Laboratory, University of California, Tech. Rep., 1997.

[229] C. C. Ling, E. D. Yorke, I. J. Spiro, D. Kubiatowicz, and D. Bennett, "Physical dosimetry of 125I seeds of a new design for interstitial implant." *International journal of radiation oncology, biology, physics*, vol. 9, no. 11, pp. 1747–1752, 1983.

[230] M.-M. Bé, V. Chisté, C. Dulieu, X. Mougeot, V. Chechev, N. Kuzmenko, F. Kondev, A. Luca, M. Galán, A. Nichols, A. Arinc, A. Pearce, X. Huang, and B. Wang, *Table of Radionuclides*. Pavillon de Breteuil, F-92310 SÈVRES, France: Bureau International des Poids et Mesures, 2011, vol. 6.

Appendix A

Additional Data

Table A.1: Flat-field experimental details

Property	Value	Units
Beam voltage	250	kV
Dose rate[a]	68	$\mathrm{cGy\,min^{-1}}$
Frame time	100	ms
Number of frames	100	Frames
Total exposure time	10.0	s
FSD	3	m
Detector bias voltage	50.0	V
Shaping time	0.5	µs
Amplifier gain	0.75	$\mathrm{mV\,fC^{-1}}$

[a] Surface dose to water at 500 mm

Table A.2: Dose to water conversion and equalisation factors combined

Pixel #	Dose to Water	Equalisation	Combined factors
1	0.2110	9.4312	1.9898
2	0.2003	8.5261	1.7081
3	0.1931	7.5698	1.4619
4	0.1832	7.4600	1.3665
5	0.1753	7.5431	1.3223
6	0.1995	1.1956	0.2386
7	0.1881	1.1206	0.2107
8	0.1794	1.0911	0.1958
9	0.1645	7.3769	1.2137
10	0.1608	7.0813	1.1384
11	0.1933	1.1305	0.2185
12	0.1591	6.9788	1.1104
13	0.1839	1.0334	0.1900
14	0.1754	1.0798	0.1894
15	0.1695	1.0524	0.1784
16	0.1648	6.8867	1.1350
17	0.1619	6.6901	1.0829
18	0.1654	6.9657	1.1523
19	0.1559	6.9090	1.0772
20	0.1899	1.0567	0.2007
21	0.1813	1.0328	0.1872
22	0.1740	1.0502	0.1827
23	0.1685	1.0257	0.1728
24	0.1622	7.3696	1.1953
25	0.1646	6.8973	1.1355
26	0.1561	7.4071	1.1565
27	0.1621	7.2177	1.1698
28	0.1869	1.0321	0.1929
29	0.1795	1.0479	0.1881
30	0.1736	1.0000	0.1736
31	0.1864	1.0805	0.2015
32	0.1561	6.7174	1.0485
33	0.1781	1.0786	0.1921
34	0.1684	1.1391	0.1919
35	0.1863	1.0611	0.1977
36	0.1736	1.0444	0.1813
37	0.1796	1.0765	0.1933
38	0.1867	1.0933	0.2041
39	0.1561	7.5689	1.1816
40	0.1649	7.6678	1.2642
41	0.1620	7.5399	1.2216
42	0.1686	1.1401	0.1922
43	0.1738	1.0997	0.1911
44	0.1812	1.1025	0.1997
45	0.1896	1.1344	0.2151
46	0.1563	8.0607	1.2603
47	0.1654	7.6296	1.2623
48	0.1620	7.7287	1.2521
49	0.1645	7.2703	1.1959
50	0.1695	1.0852	0.1840
51	0.1754	1.1241	0.1971
52	0.1842	1.1559	0.2129
53	0.1589	8.2578	1.3121
54	0.1936	1.1637	0.2253
55	0.1608	7.8888	1.2683
56	0.1650	7.5050	1.2384
57	0.1796	1.1257	0.2021
58	0.1879	1.1283	0.2121
59	0.1995	1.1514	0.2297
60	0.1753	8.1111	1.4216
61	0.1829	8.2638	1.5115
62	0.1938	7.9509	1.5409
63	0.1988	7.6569	1.5220
64	0.2120	8.2422	1.7471

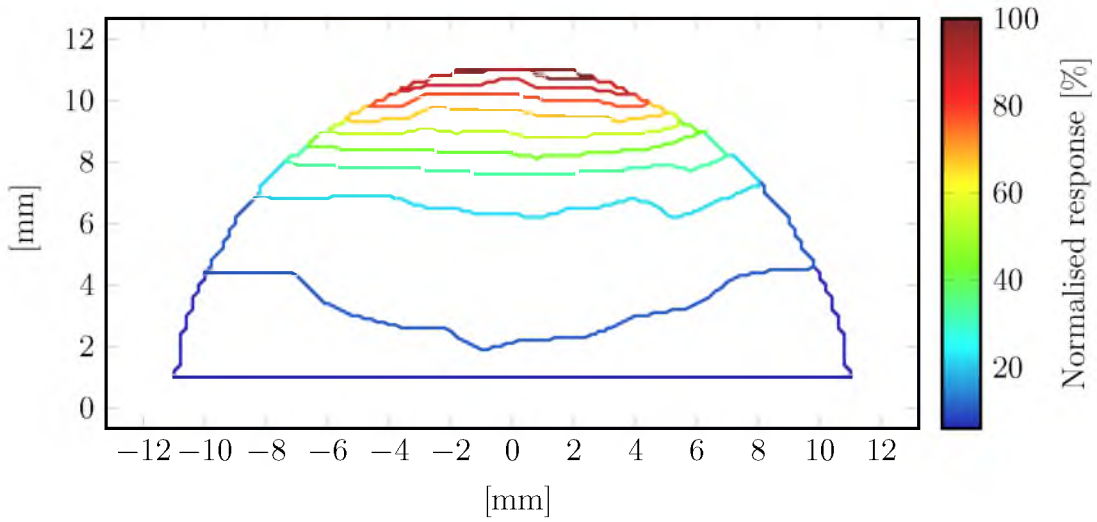

Figure A.1: Interpolated isodose curves of PANOPTES measurement converted to dose in water with ten ^{125}I seeds at 0.0°. Dimensions are in millimetres and dose is normalised to 100% at the maximum value.

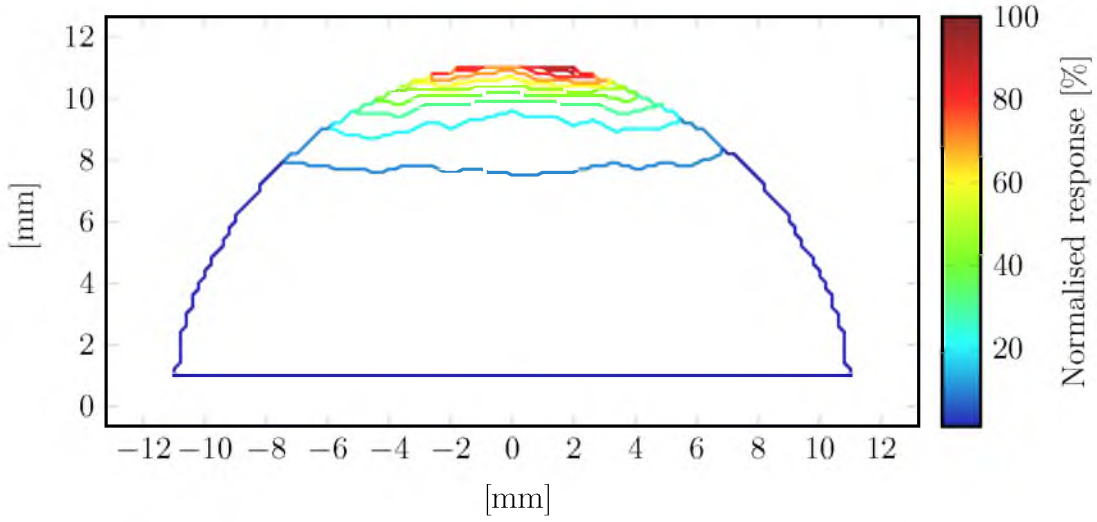

Figure A.2: Interpolated isodose curves of PANOPTES measurement converted to dose in water with five ^{125}I seeds at 0.0°. Dimensions are in millimetres and dose is normalised to 100% at the maximum value.

Appendix B

Mechanical Design

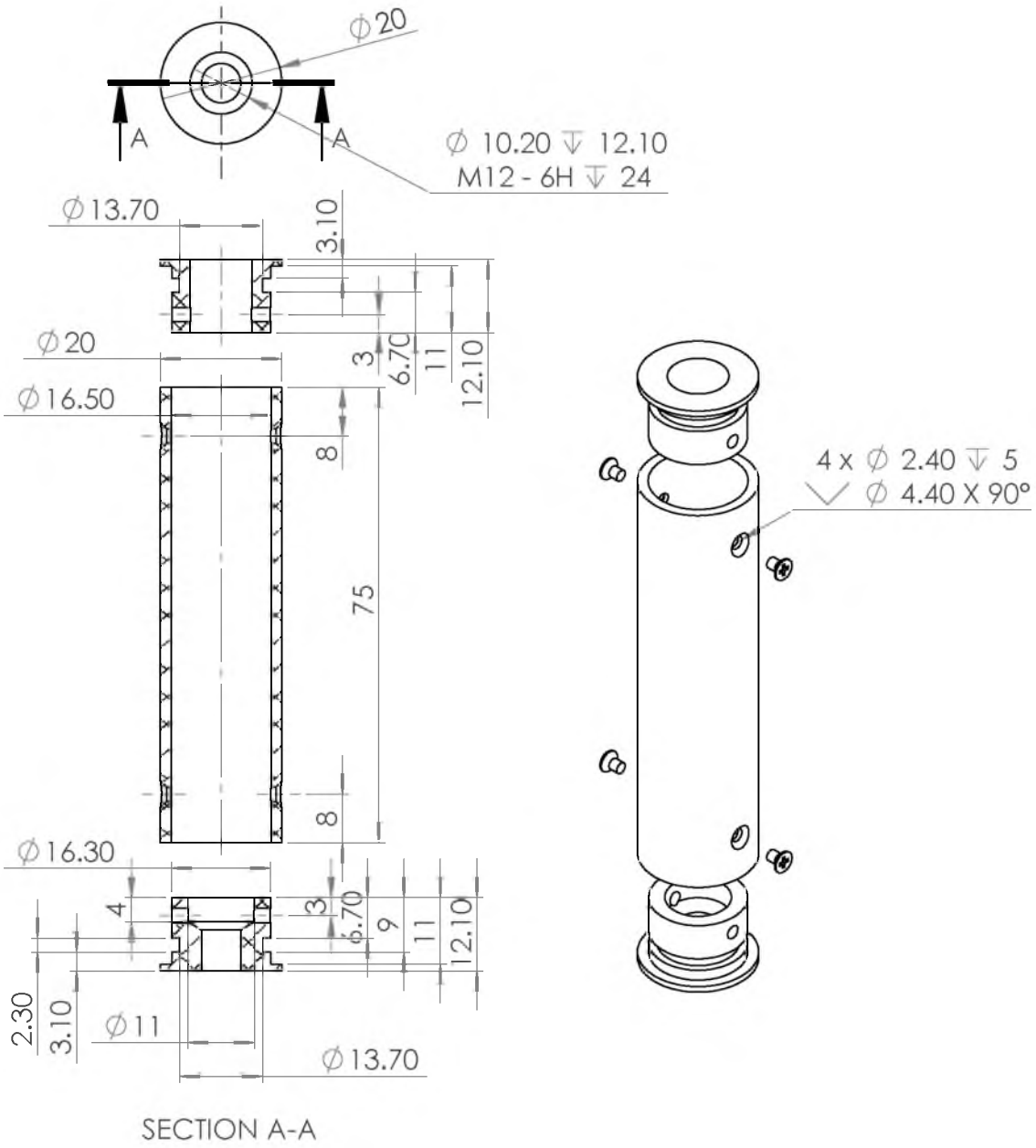

Figure B.1: Dimensioned drawings of the preamplifier housing for the single detector concept.

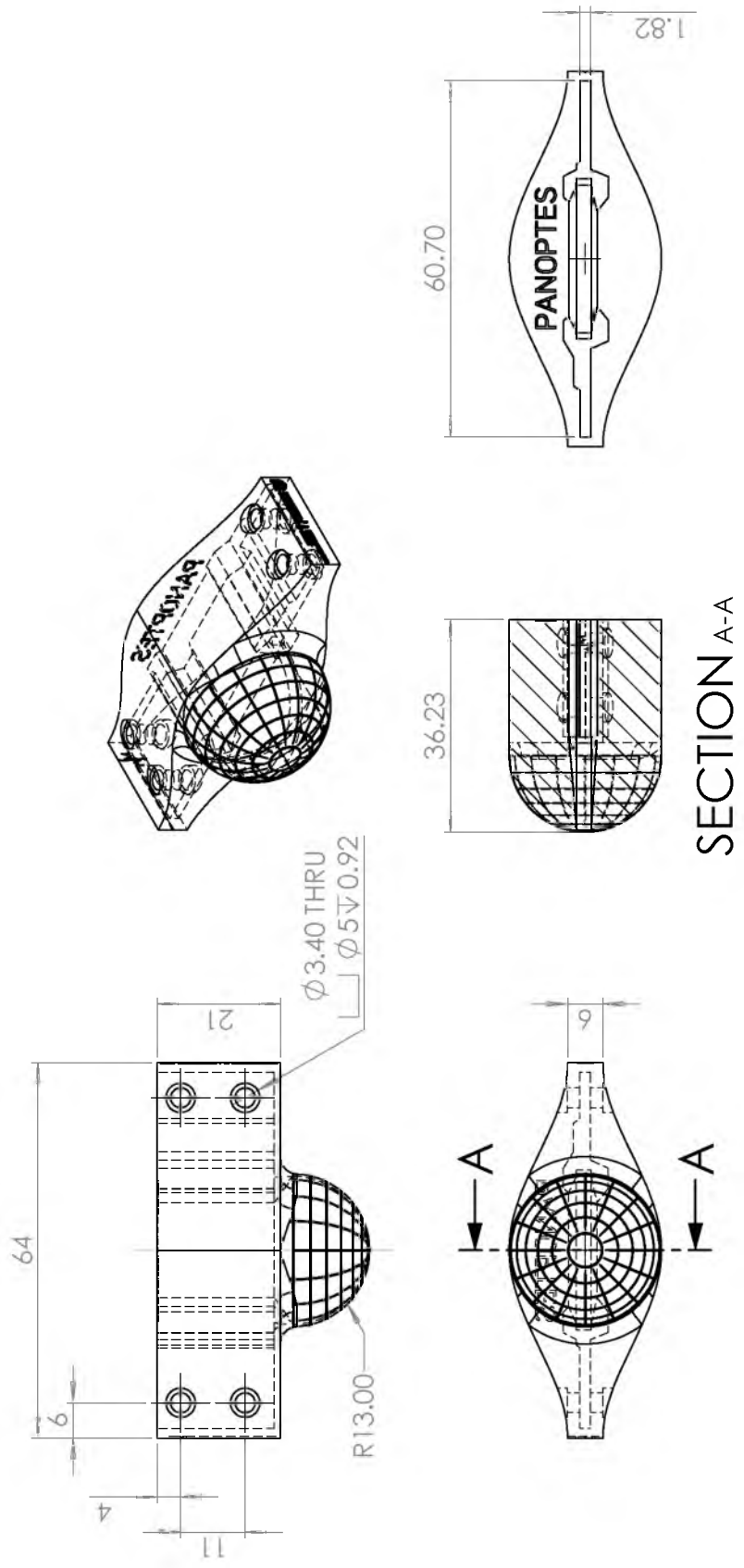

Figure B.2: Dimensioned drawing of the phantom 3D printed for the cut version of the semicircular detector. Dimensions are in millimetres.

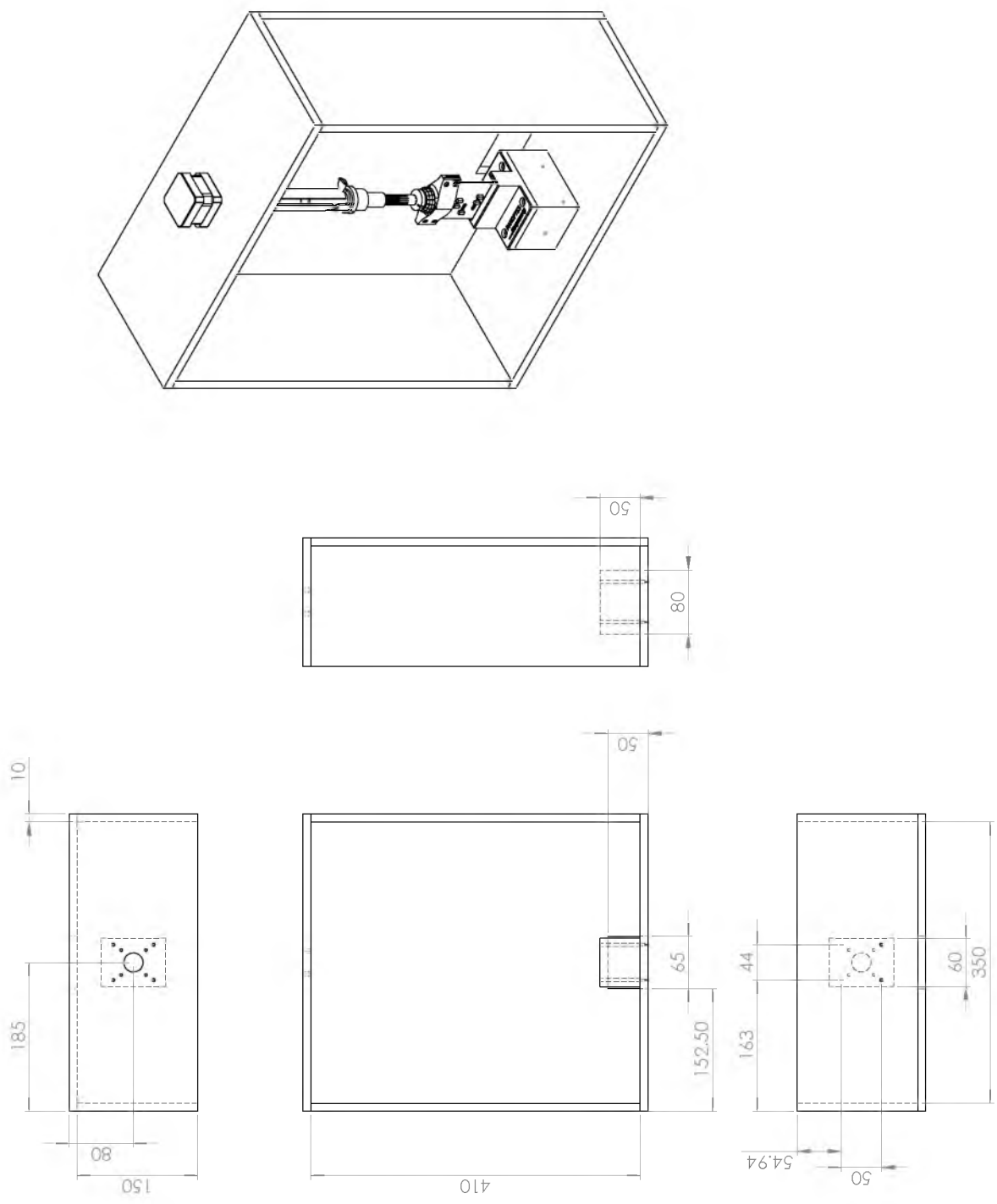

Figure B.3: Dimensioned drawing of the positioning system box and isometric render of the assembled system included the detector board and phantom. Though not shown, a front panel is also used to complete the box and block external noise sources. Dimensions are in millimetres.

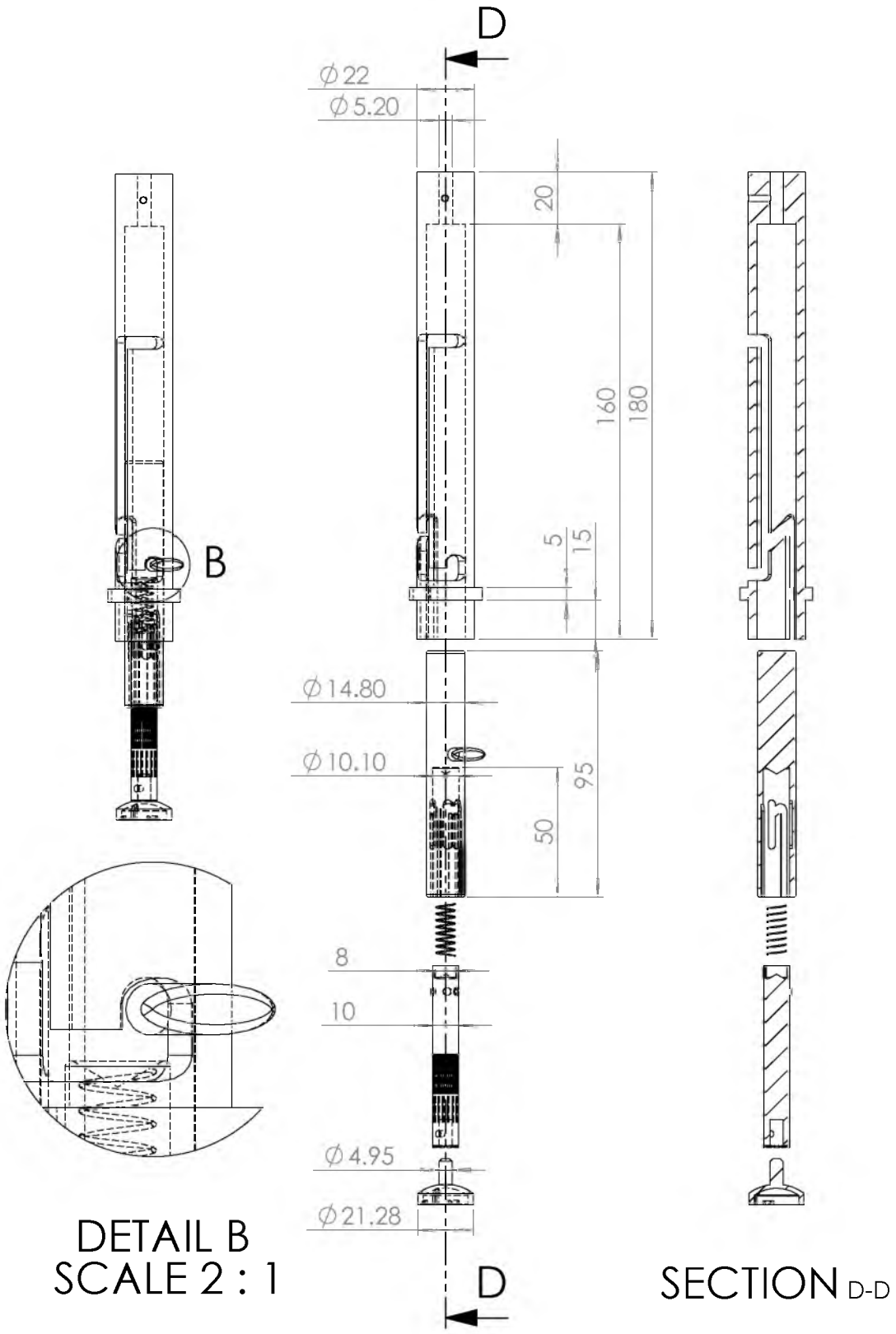

Figure B.4: Dimensioned drawing of the lock-down shaft showing that a spring is used to exert downward force onto the plaque, keeping it firmly in place during acquisitions. Dimensions are in millimetres.

(a) Front panel

(b) Back panel

Figure B.5: The front and back panels of the main electronics box. The top panel features (from *left*) a power indication LED, stepper motor socket and detector board interface. The back panel features (from *left*) a USB B socket for connection to the host computer, high voltage enable override switch, a high voltage manual-remote control switch, a high voltage adjustment dial and a fused IEC[215] power socket.

Appendix C

Electrical Circuits and Schematics

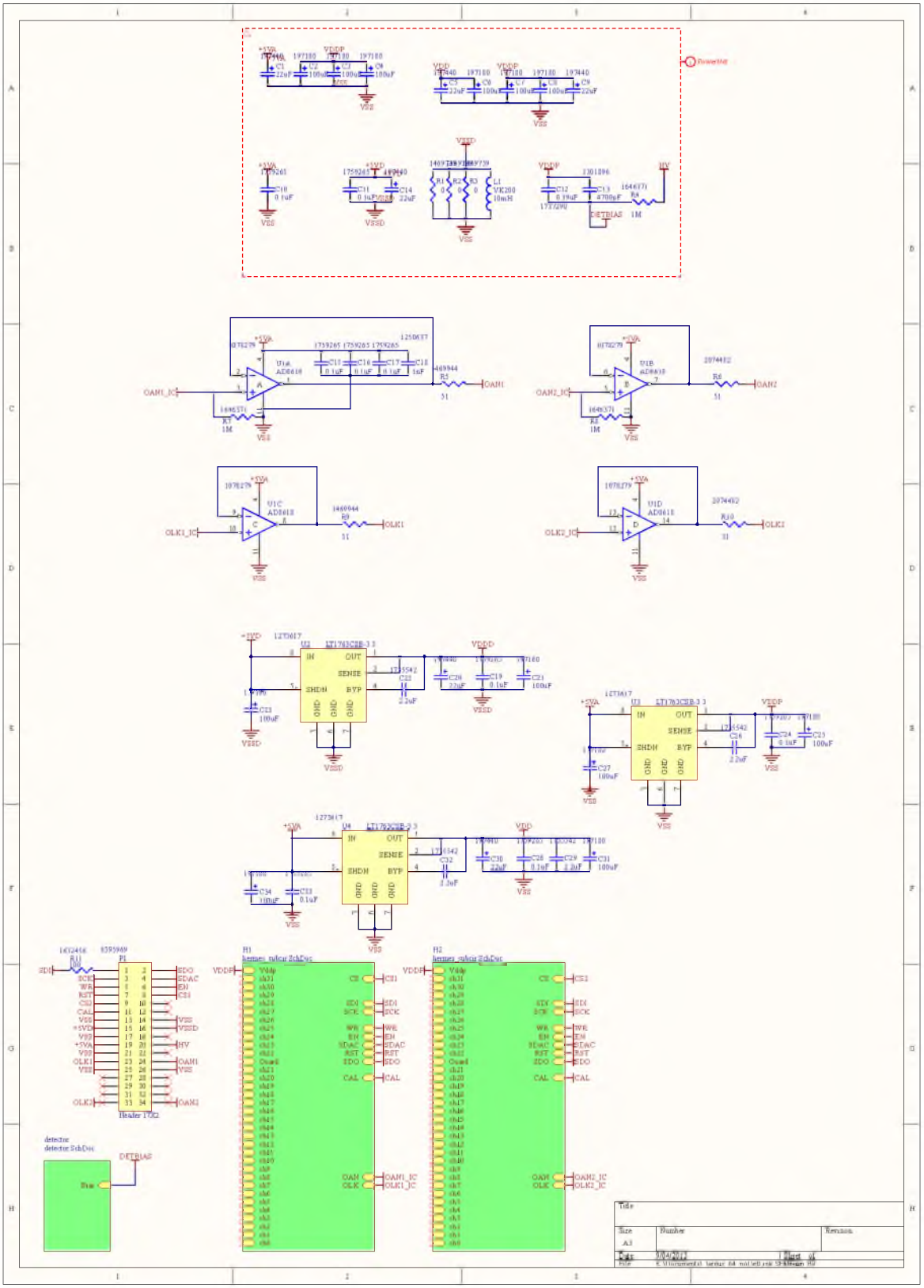

Figure C.1: Circuit schematic of the detector board showing main circuit. (1 of 3)

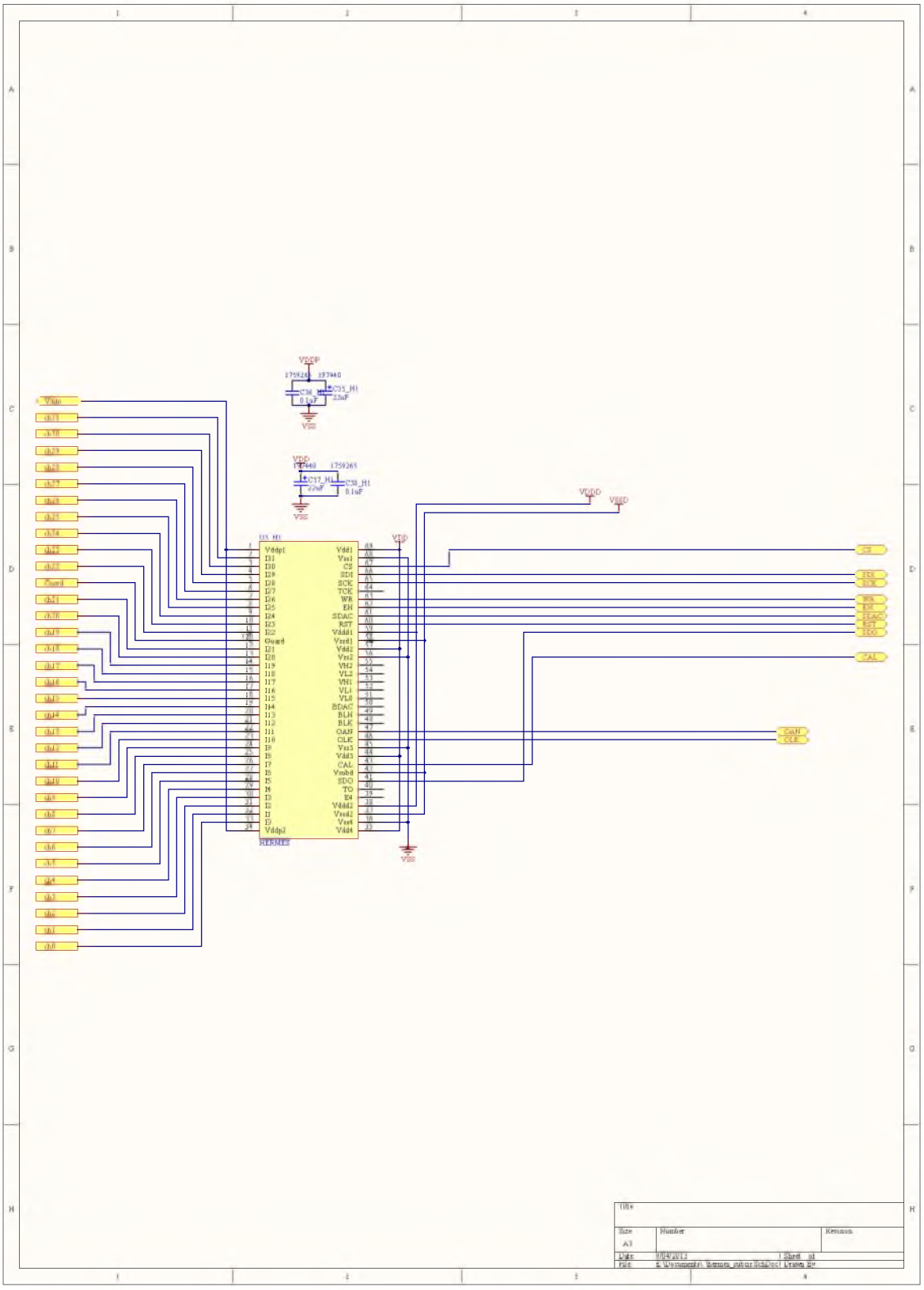

Figure C.2: Circuit schematic of the detector board HERMES ASIC connections. (2 of 3)

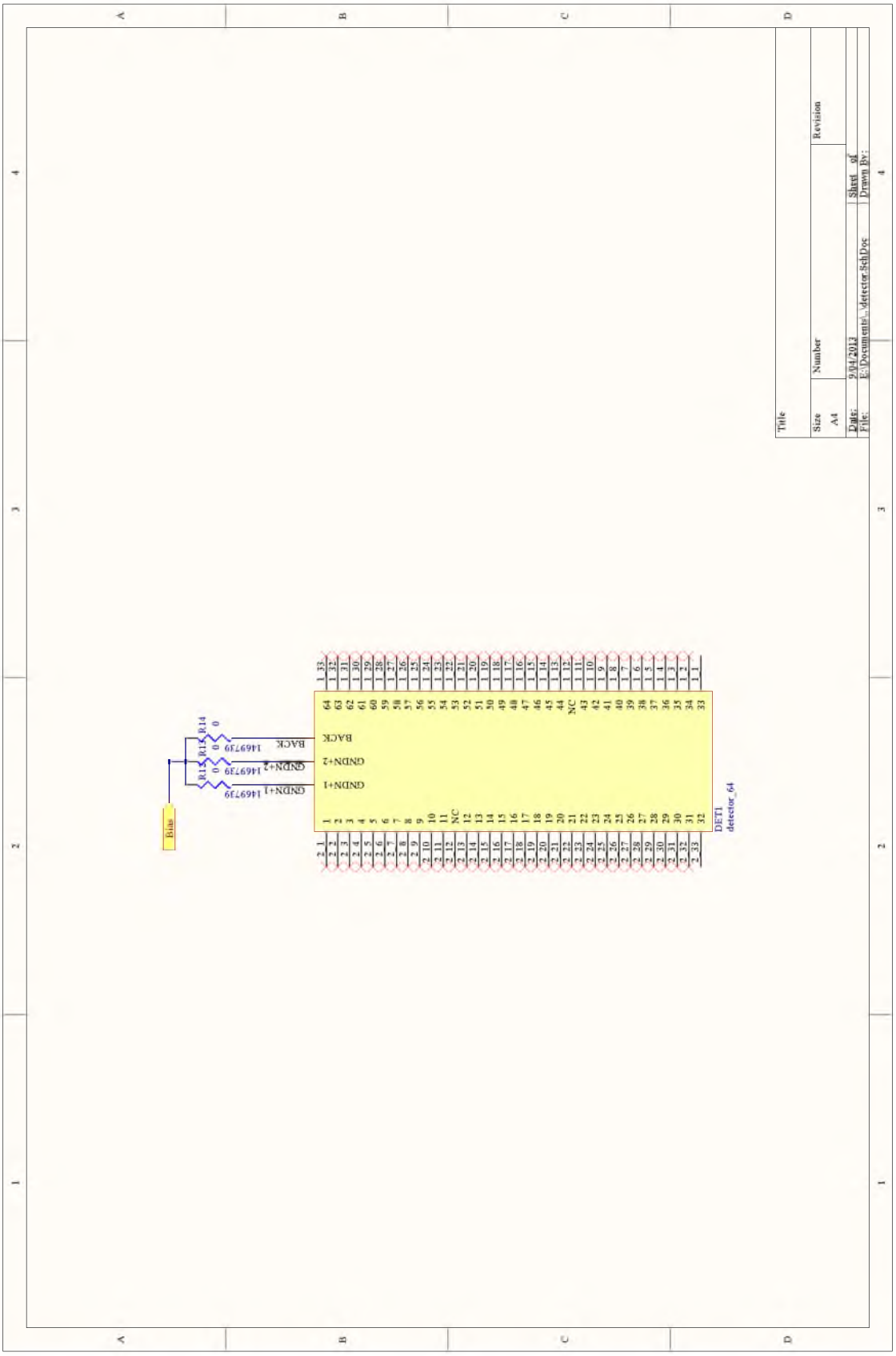

Figure C.3: Circuit schematic of the detector board showing connections to the detector. (3 of 3)

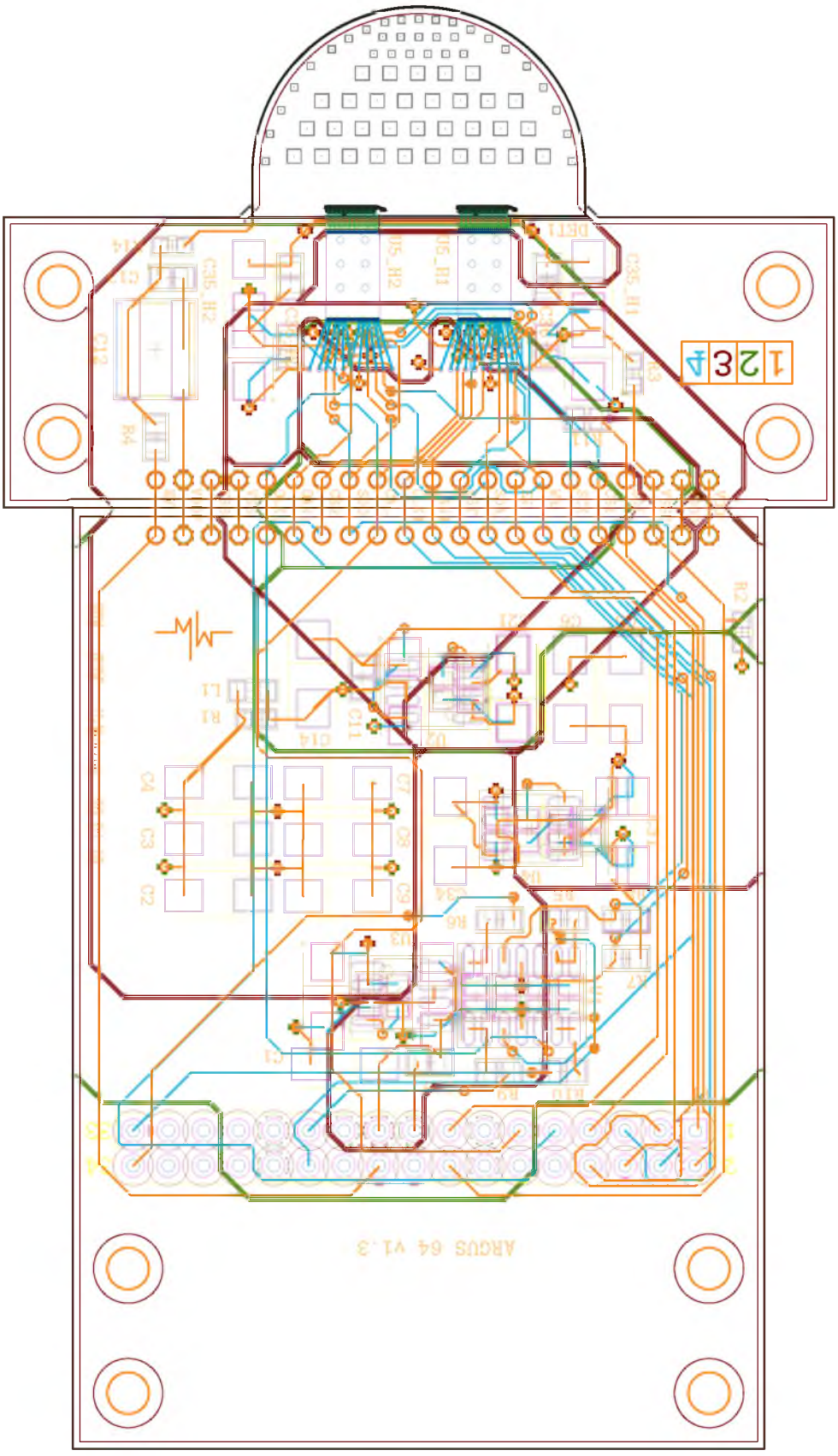

Figure C.4: Printed circuit board layout of the detector board.

Table C.1: Connection scheme for the detector board-interface board

Pin	Cable	Net
1	A	SDI
2	B	SDO
3	C	SCK
4	D	SDAC
5	E	WR
6	F	EN
7	G	RST
8	H	CS1
9	J	CS2
10	–	–
11	K	CAL
12	–	–
13	Z	VSS
14	–	–
15	L	+5VD
16	M	VSSD
17	Z	VSS
18	–	–
19	N	+5VA
20	P	DETBIAS
21	Z	VSS
22	–	–
23	R	OLK1
24	S	OAN1
25	Z	VSS
26	–	–
27	–	–
28	–	–
29	–	–
30	–	–
31	–	–
32	–	–
33	T	OLK2
34	U	OAN2

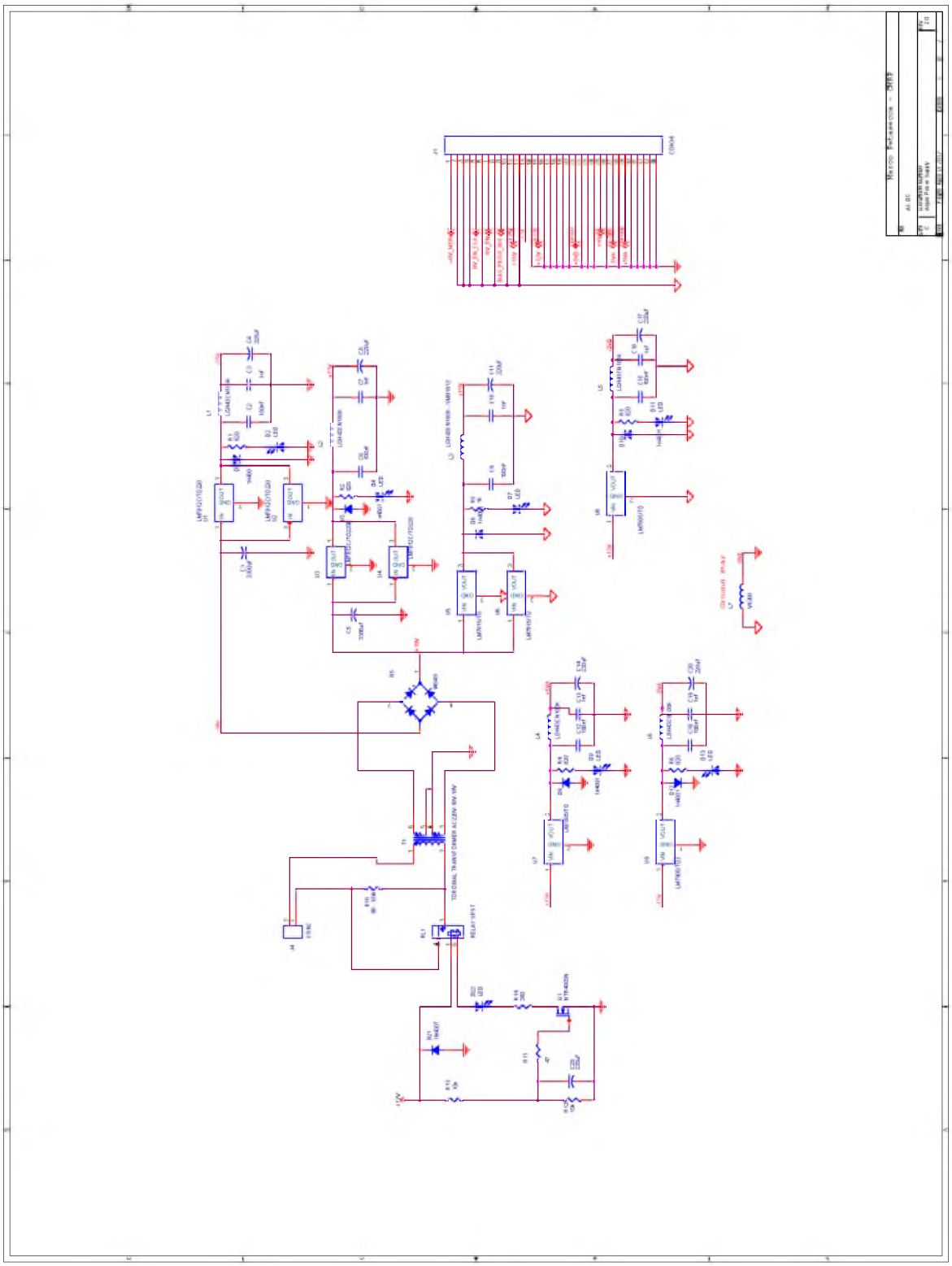

Figure C.5: Circuit schematic of the power supply board. (1 of 2)

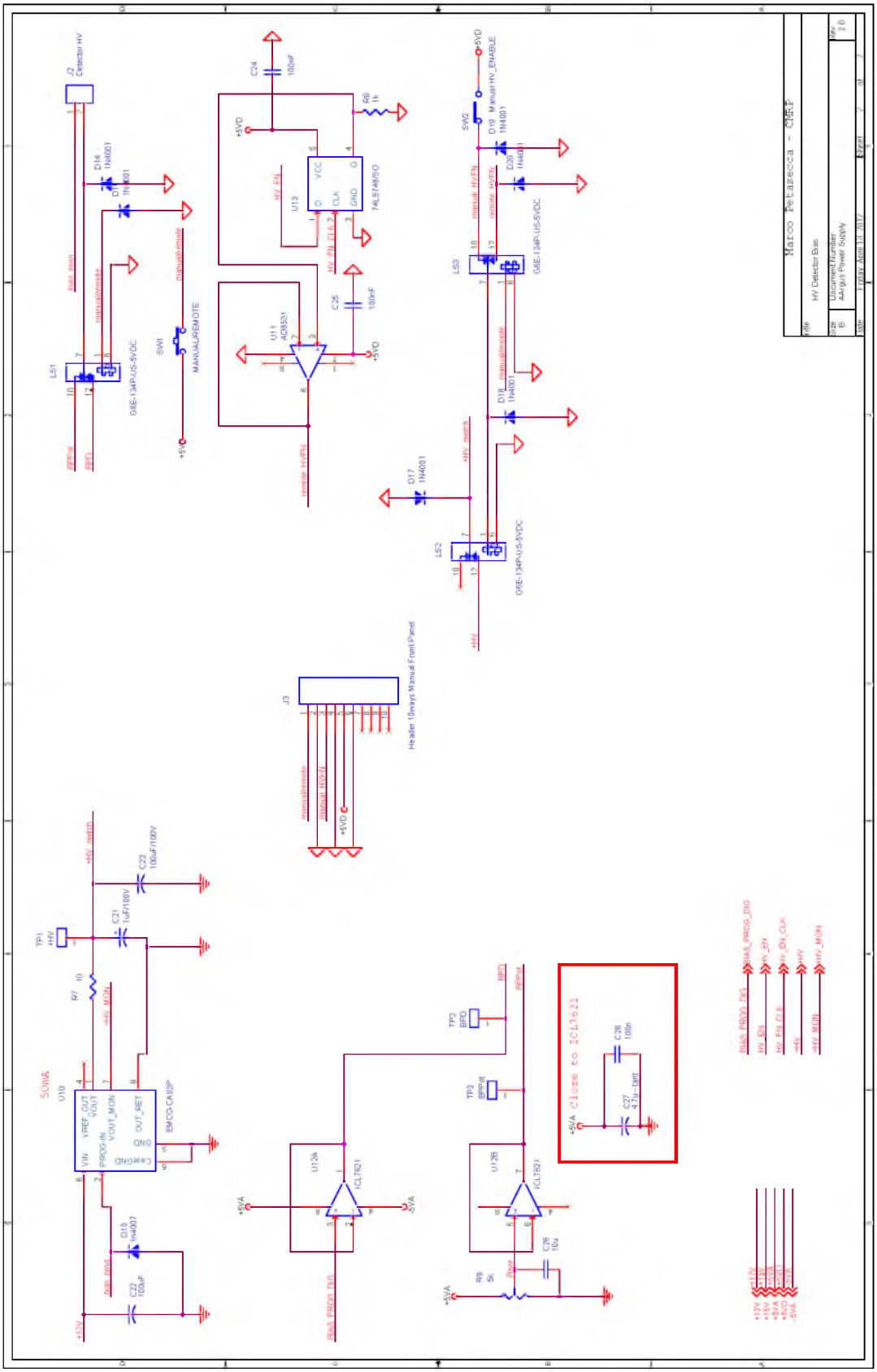

Figure C.6: Circuit schematic of the power supply board. (2 of 2)

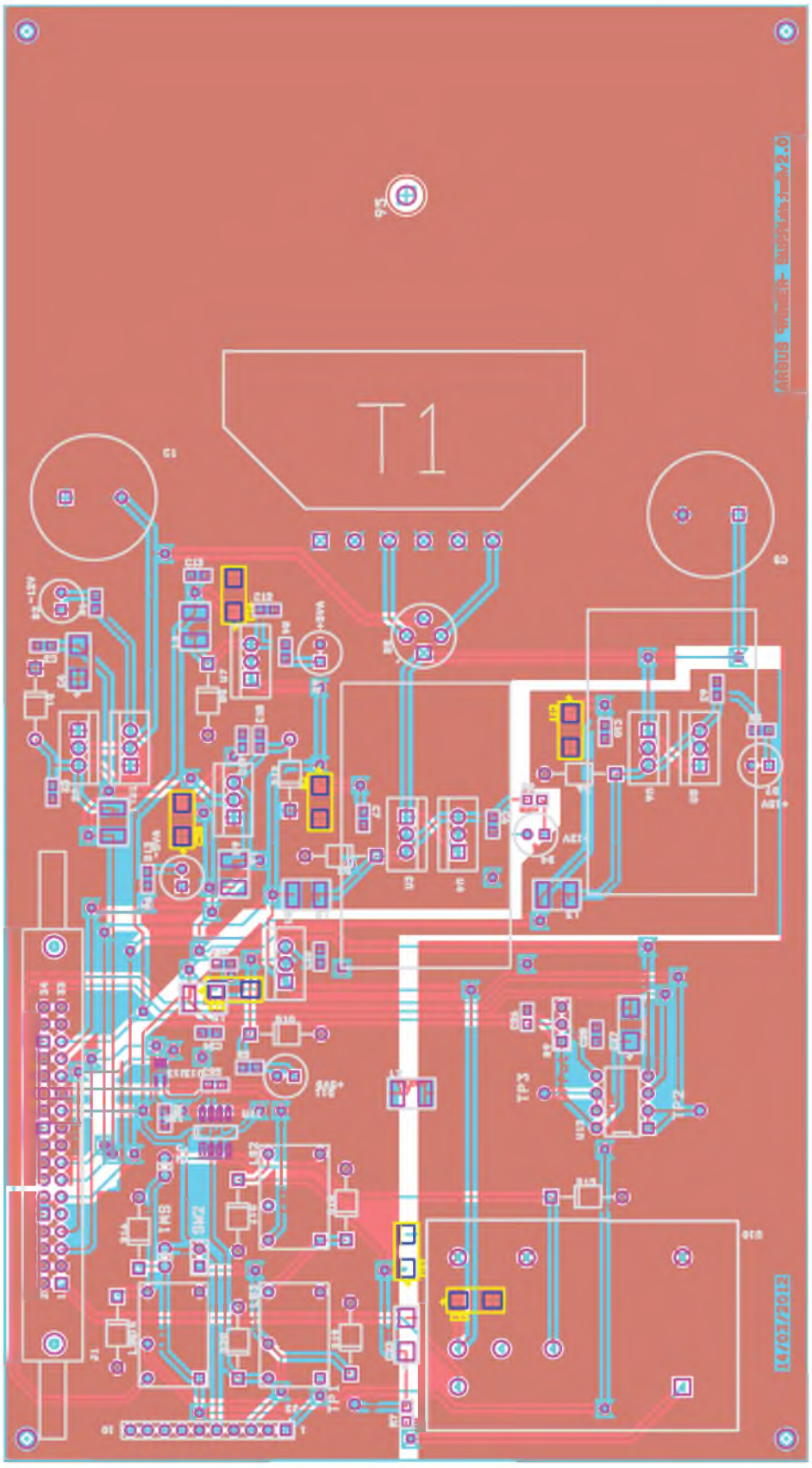

Figure C.7: Printed circuit board layout of the power supply board showing.

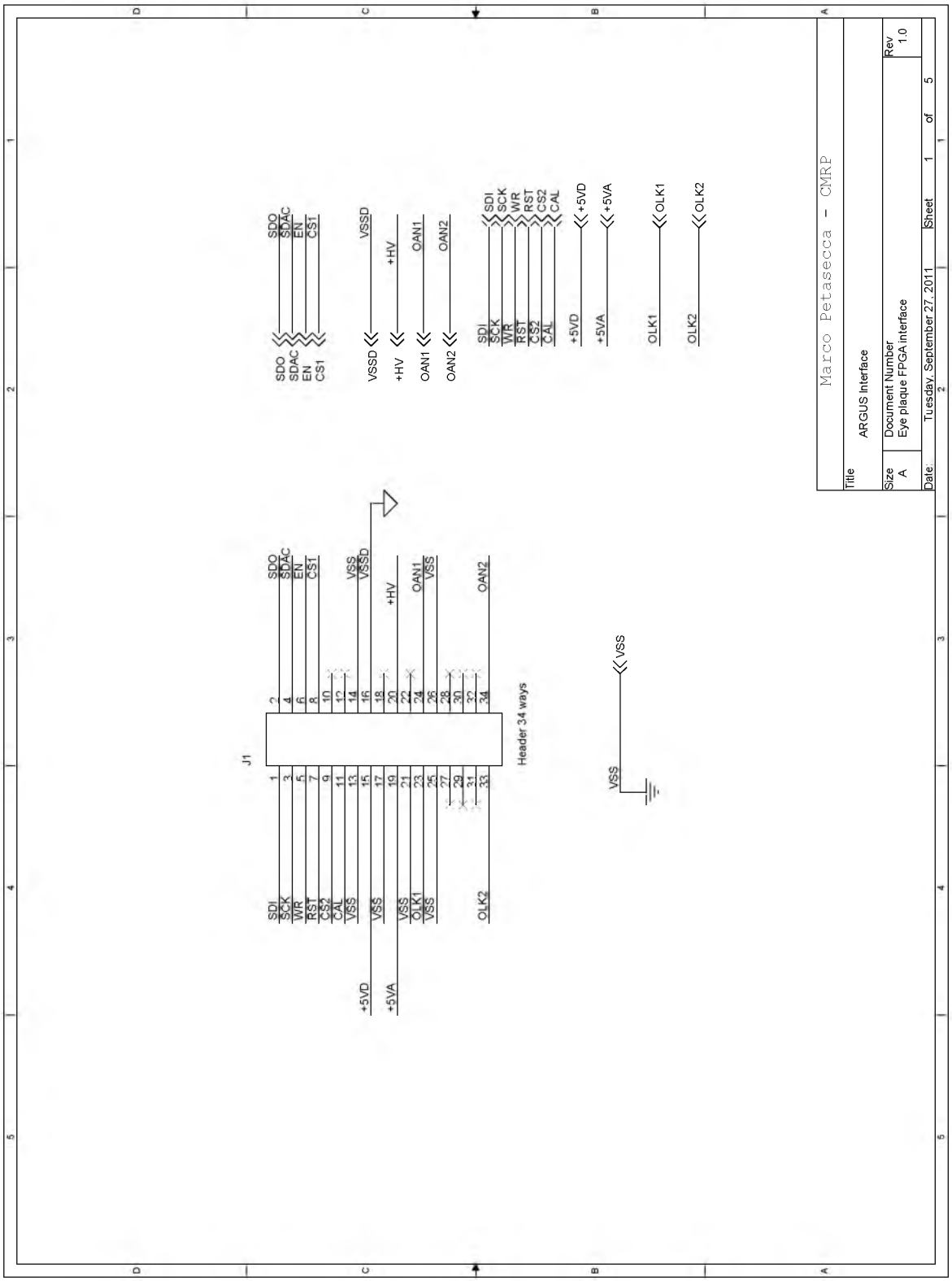

Figure C.8: Circuit schematic of the interface board. (1 of 5)

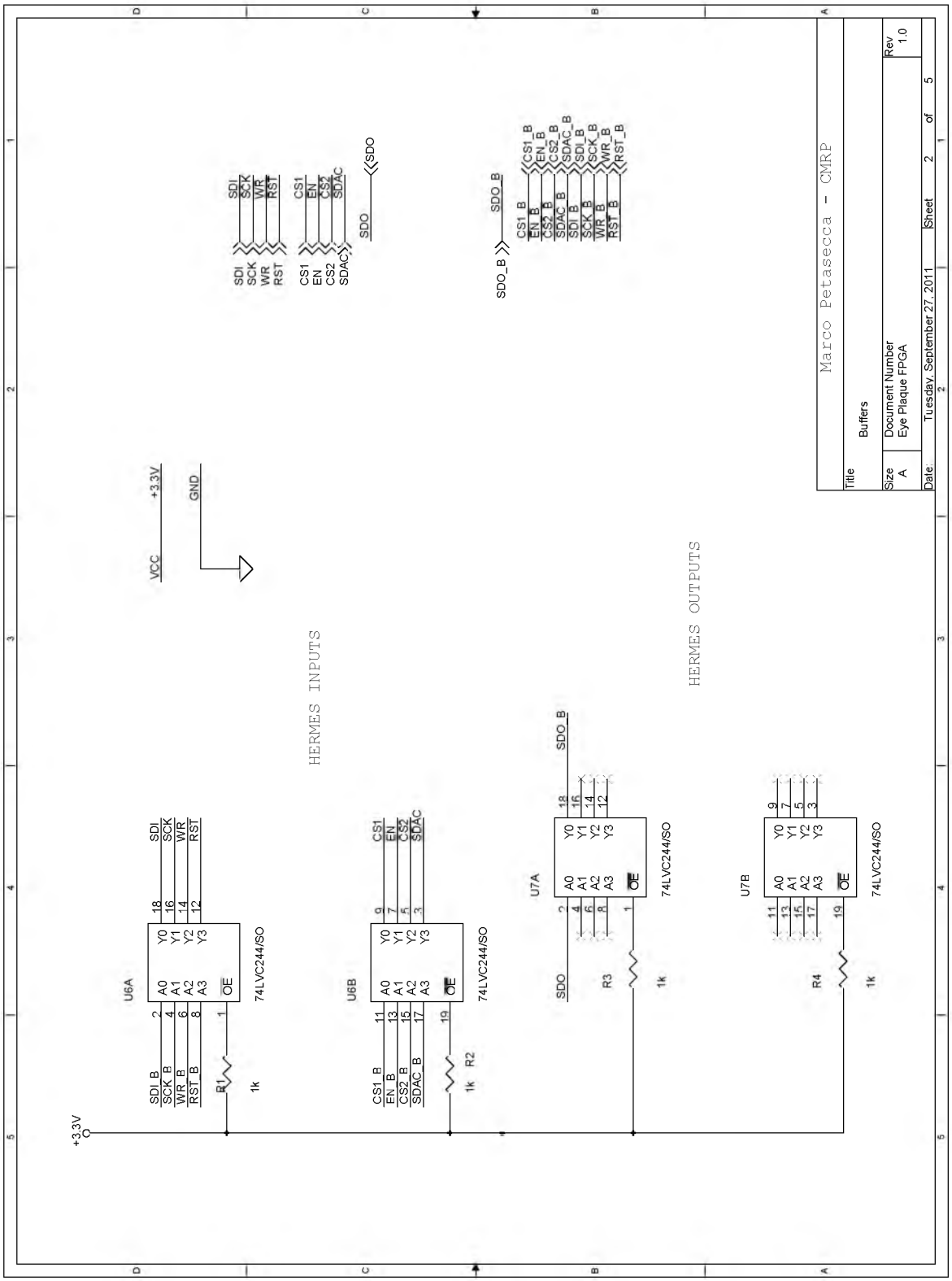

Figure C.9: Circuit schematic of the interface board. (2 of 5)

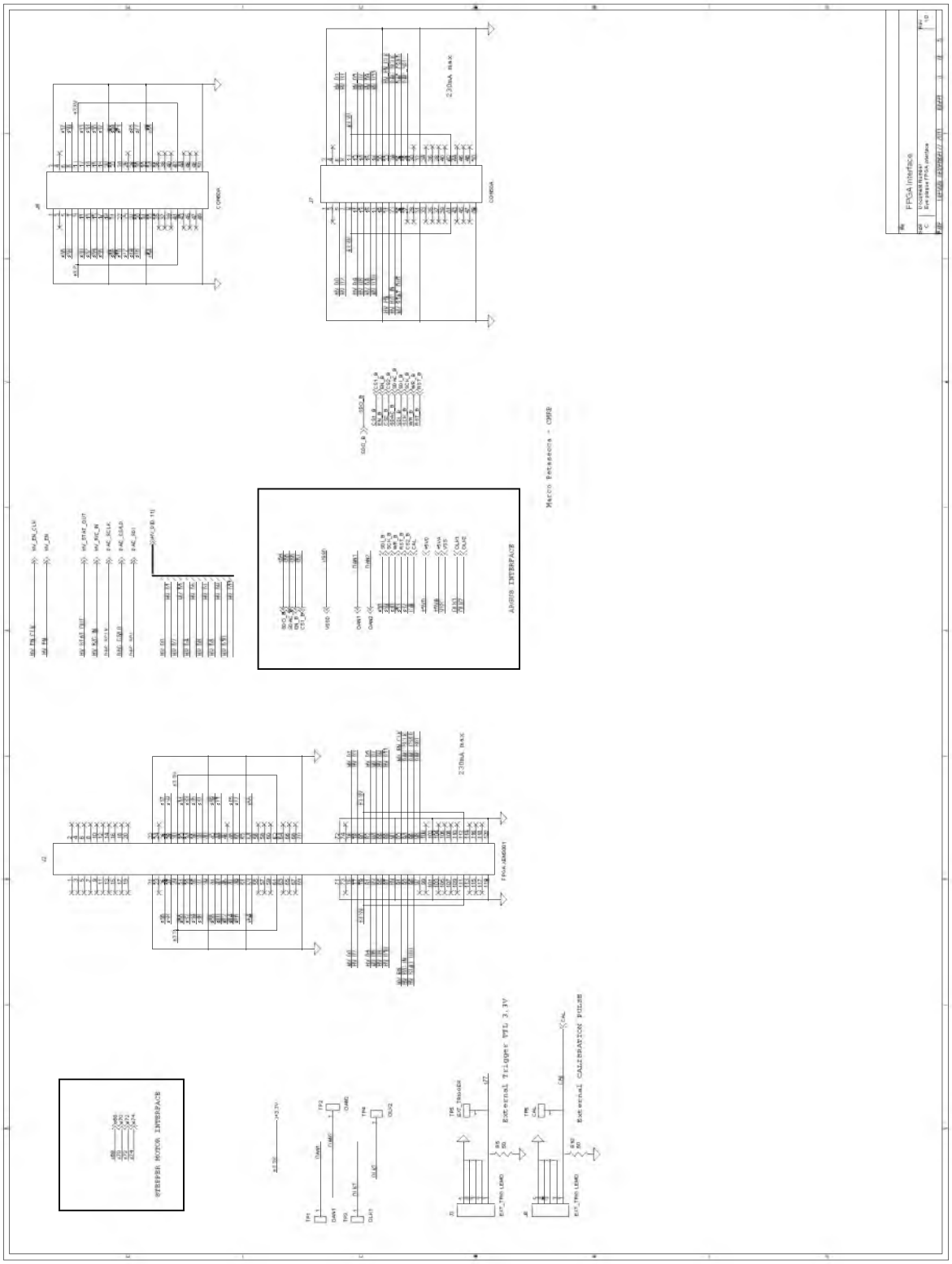

Figure C.10: Circuit schematic of the interface board. (3 of 5)

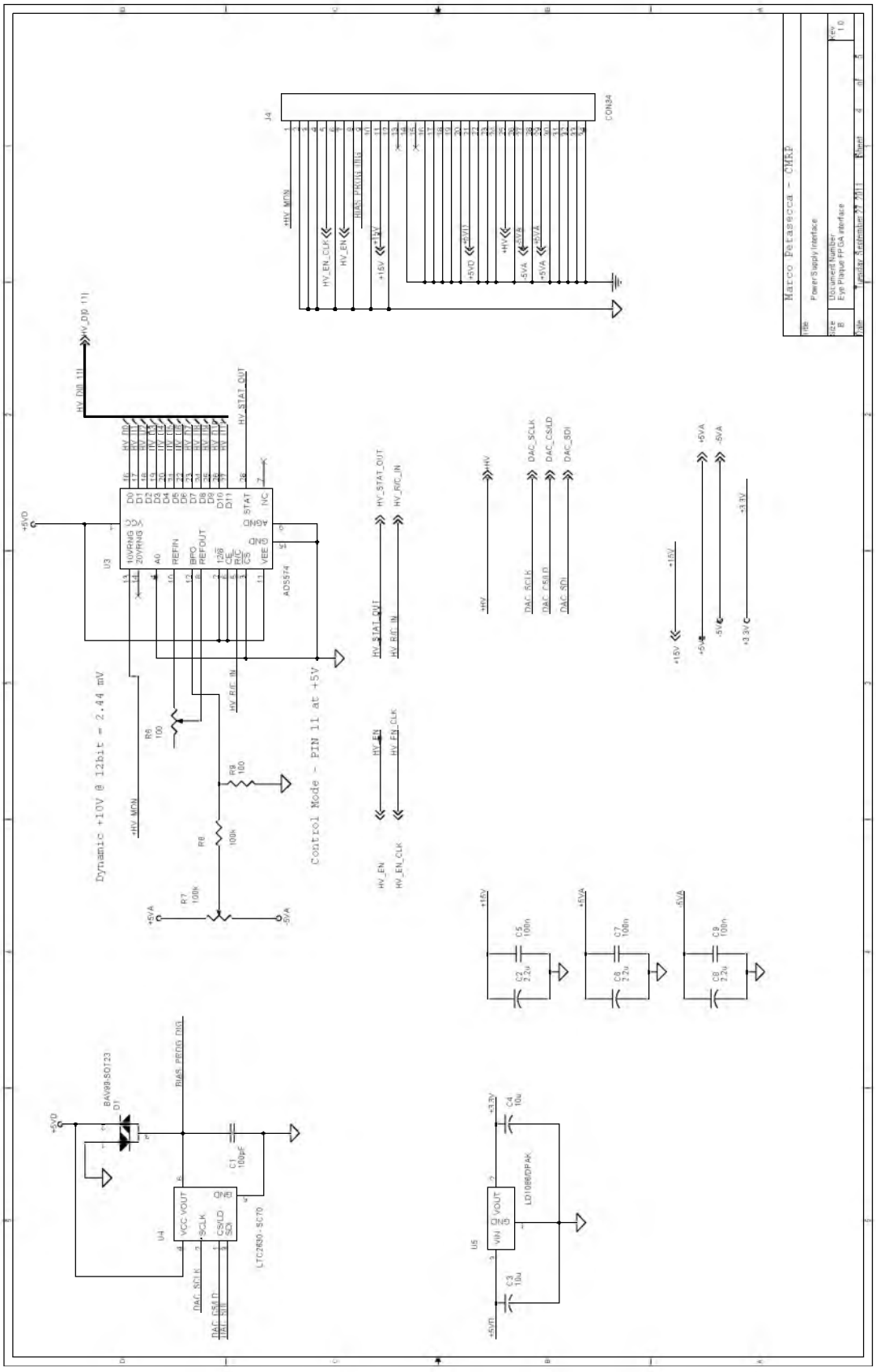

Figure C.11: Circuit schematic of the interface board. (4 of 5)

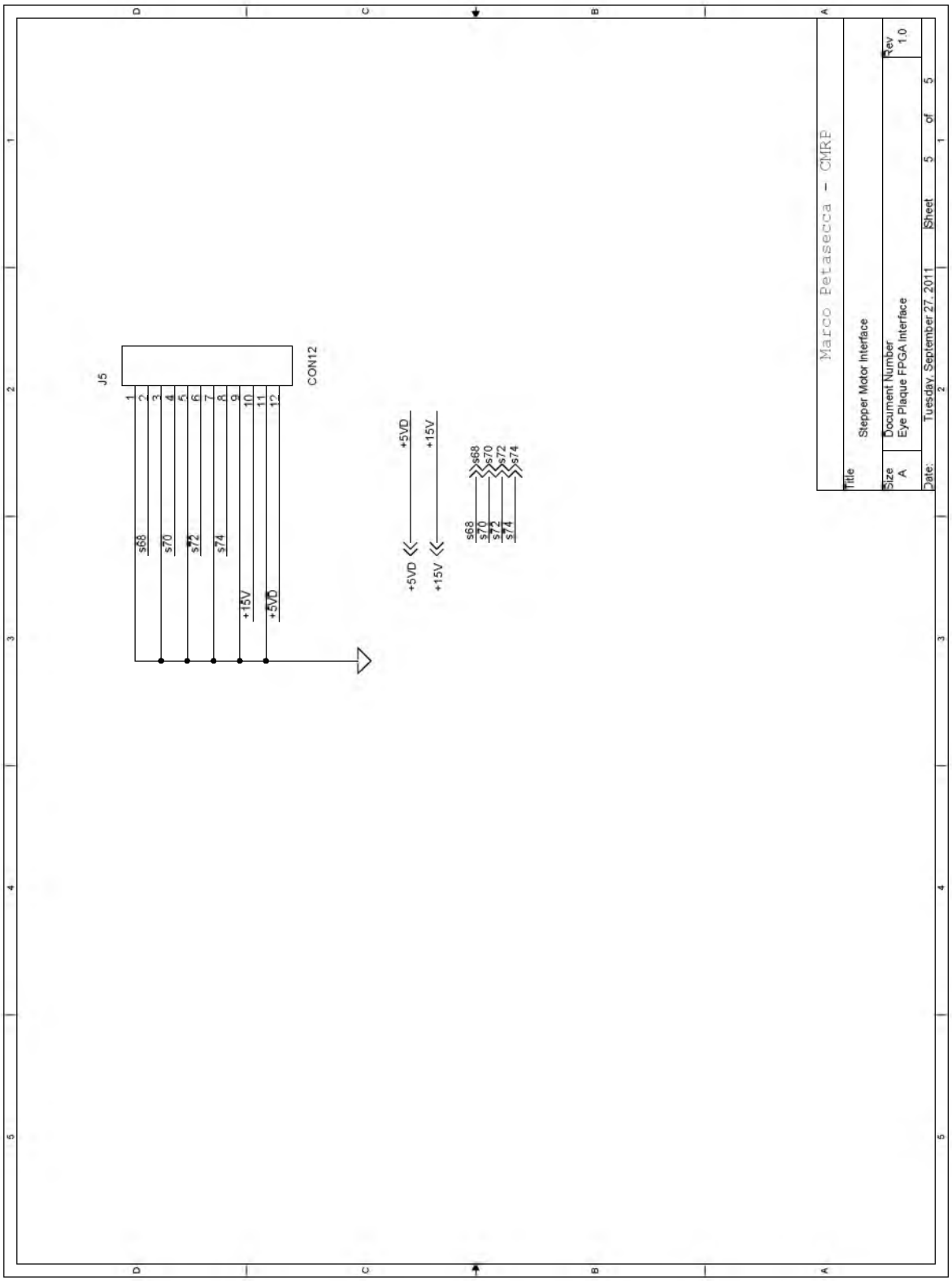

Figure C.12: Circuit schematic of the interface board. (5 of 5)

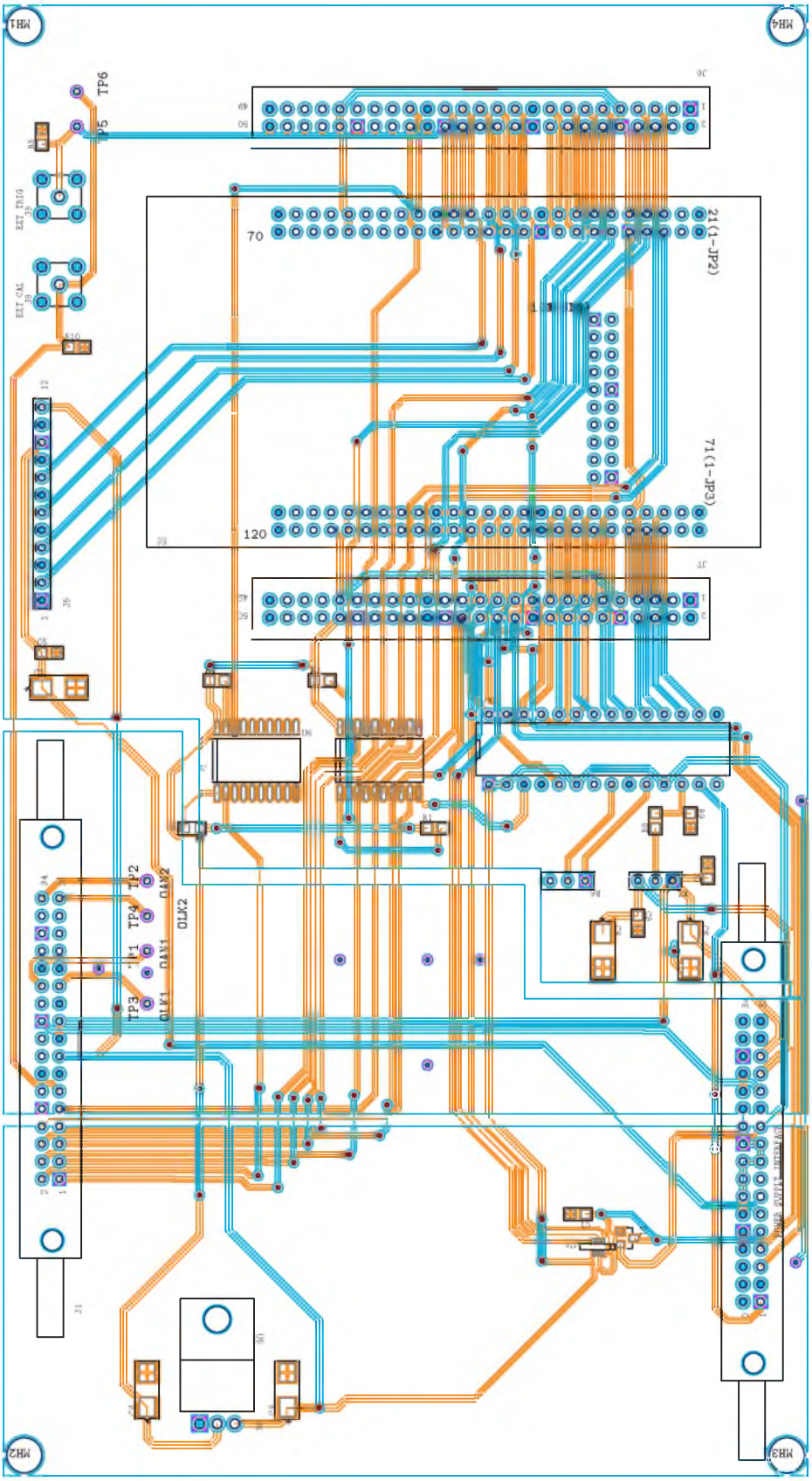

Figure C.13: Printed circuit board layout of the interface board.

Appendix D

Detector Masks

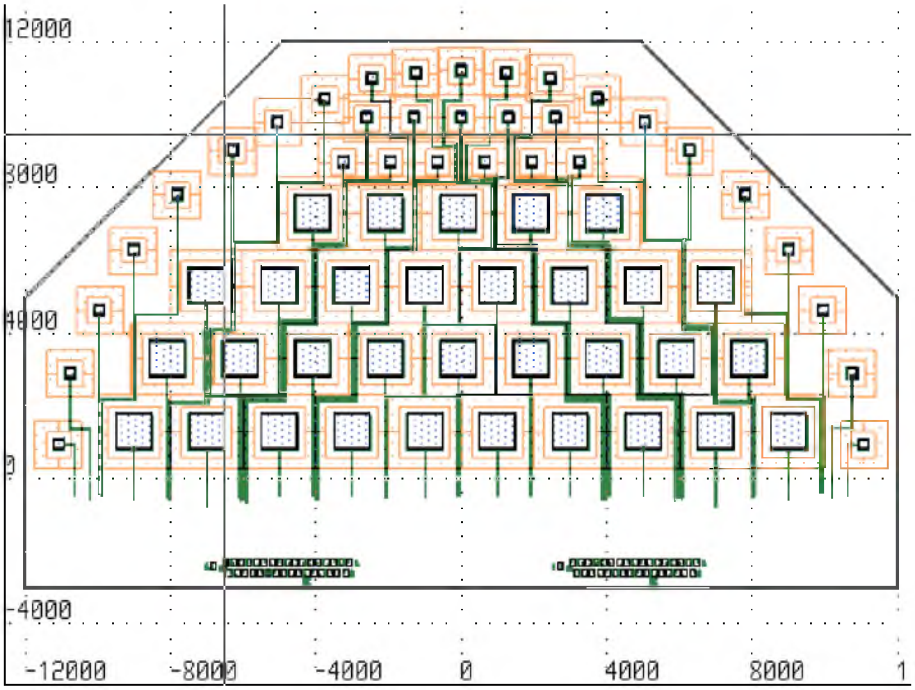

Figure D.1: Fabrication mask of the semicircular detector showing the whole wafer and the various implantation layers.

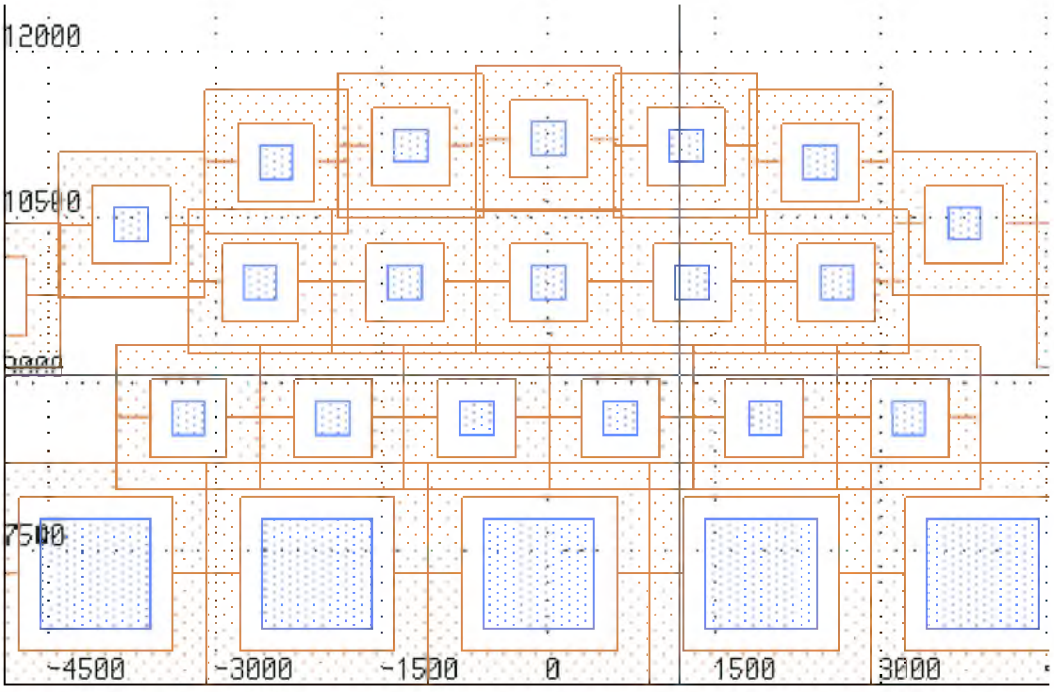

Figure D.2: Fabrication mask of the semicircular detector showing the $p+$-type (*blue*) and $n+$-type (*orange*) implantation regions at the top of the wafer.

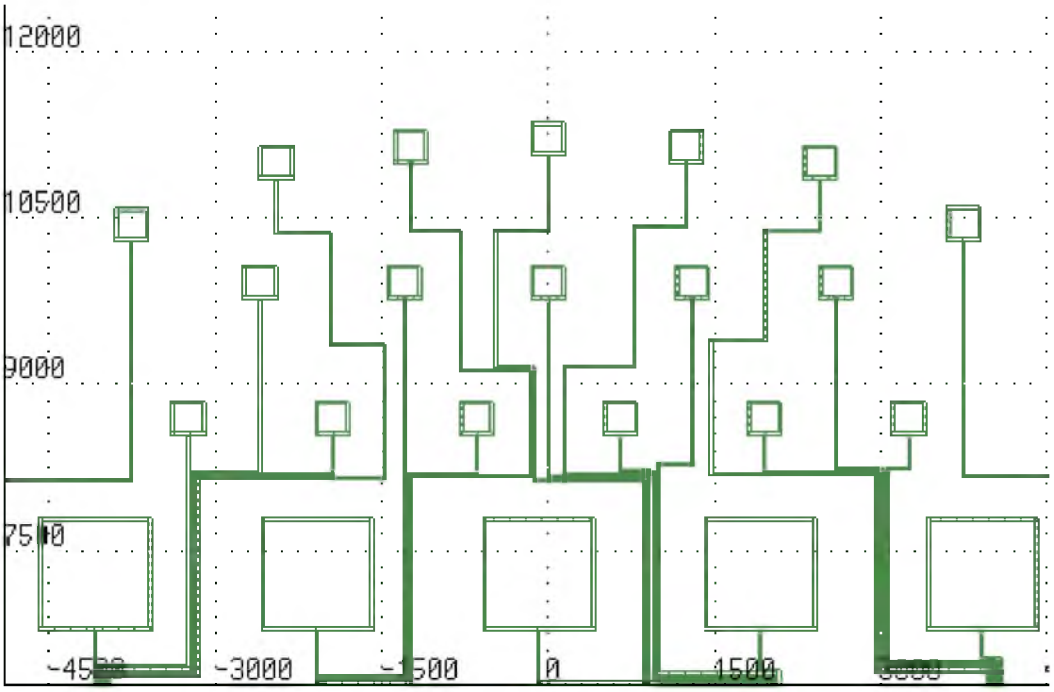

Figure D.3: Fabrication mask of the semicircular detector showing the aluminium tracks (*green*) that route current signal through to the bonding pads at the bottom of the wafer.

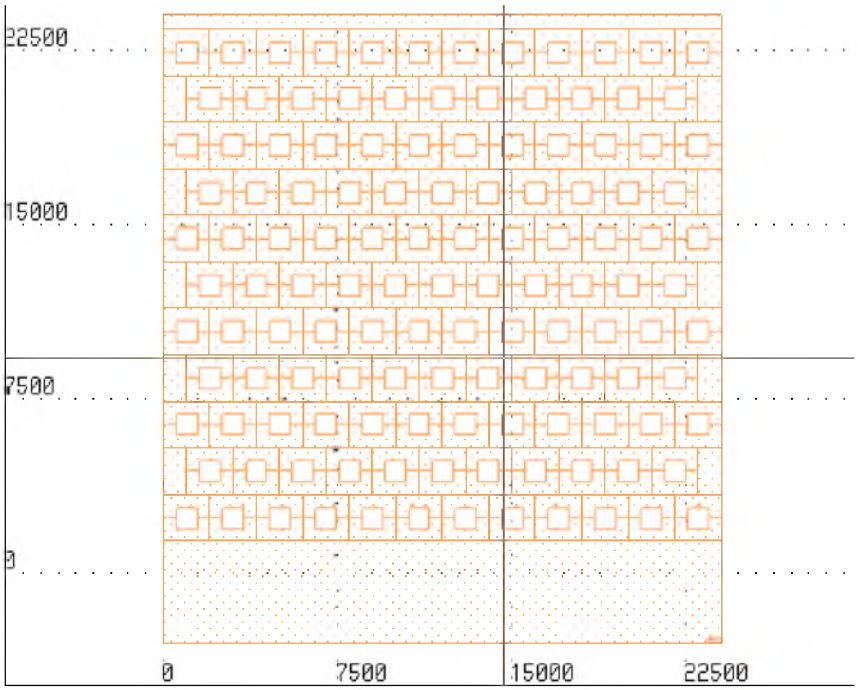

Figure D.4: Fabrication mask of the semicircular detector showing the locations of the diodes within the $n+$-type layer (*orange*).

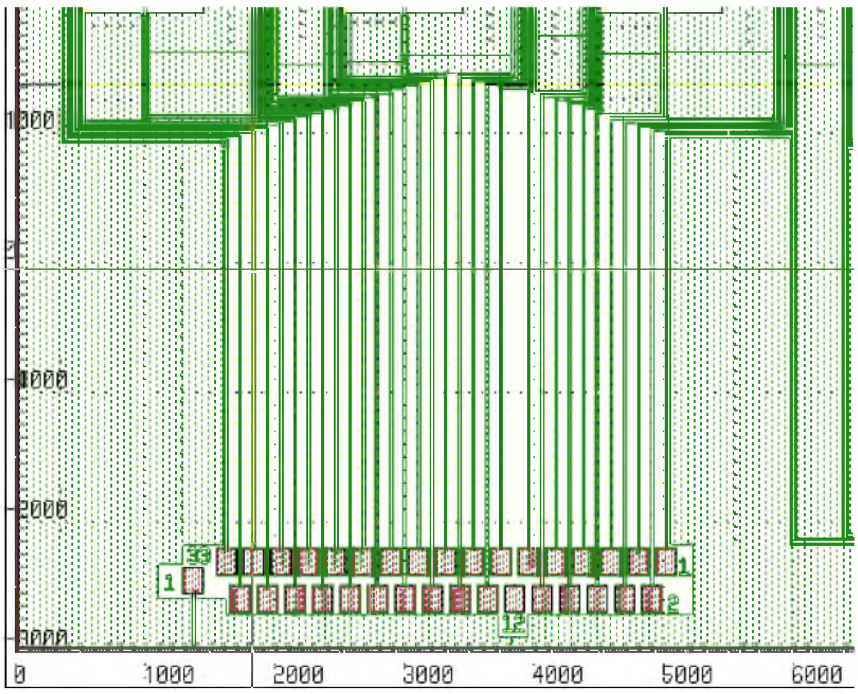

Figure D.5: Fabrication mask of the semicircular detector showing the aluminium layer and tracks (*green*) that route current signal through to the passivation layer (*red*) at the bonding pads at the bottom of the wafer.

Appendix E

Firmware Design

E.1 Schematic Firmware Modules

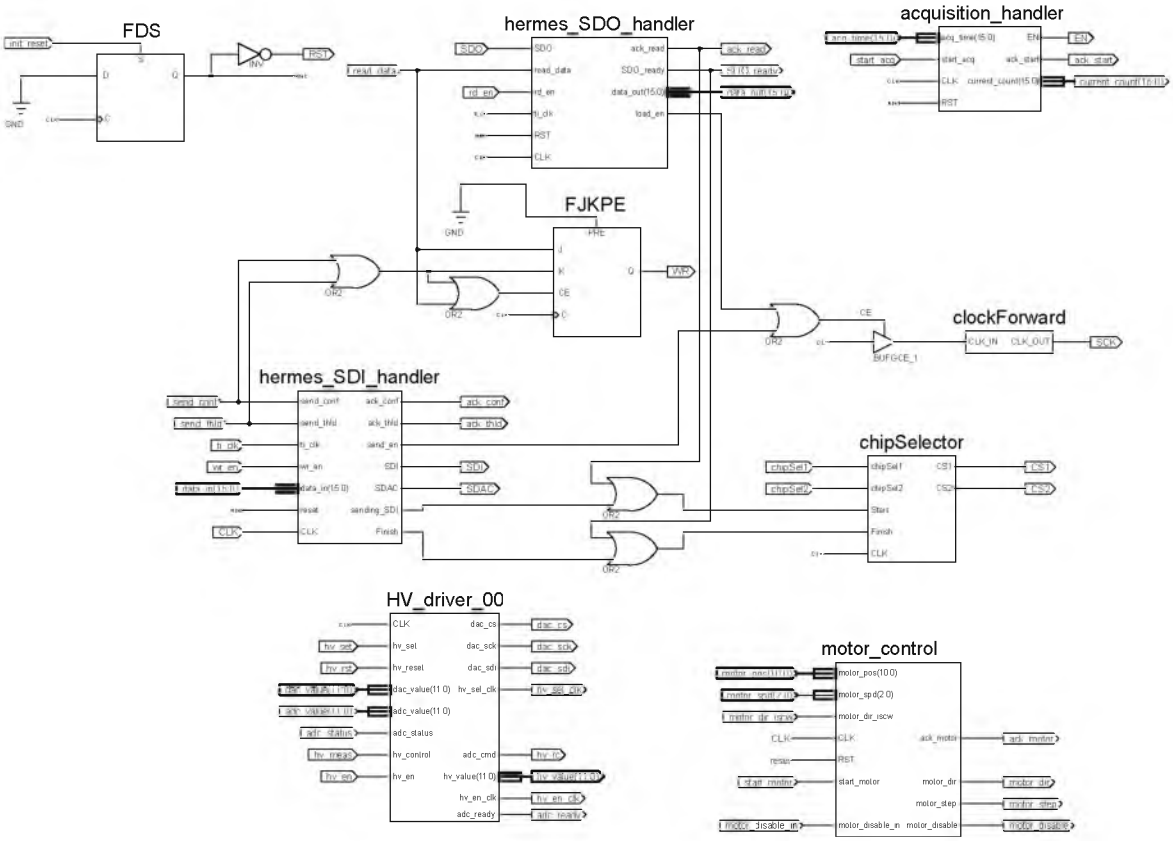

Figure E.1: FPGA firmware schematic at the main module level, showing the sub-modules and their ports.

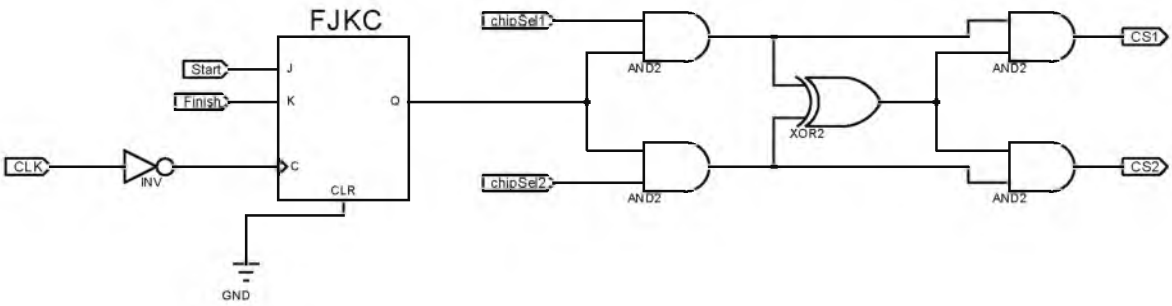

Figure E.2: FPGA firmware schematics of the chip selector, which functions to access the appropriate HERMES ASIC.

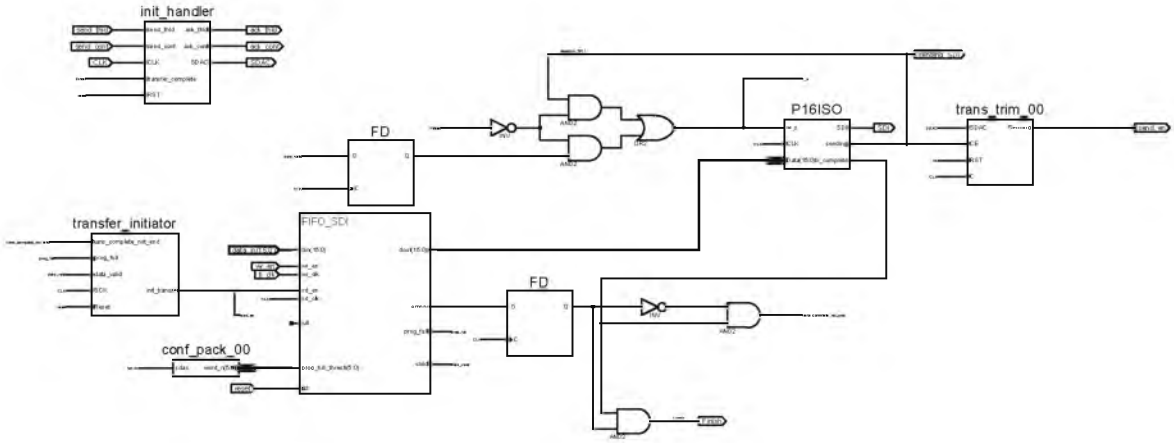

Figure E.3: FPGA firmware schematics of the SDI line which handles serial data transfers from the FPGA to the HERMES ASIC.

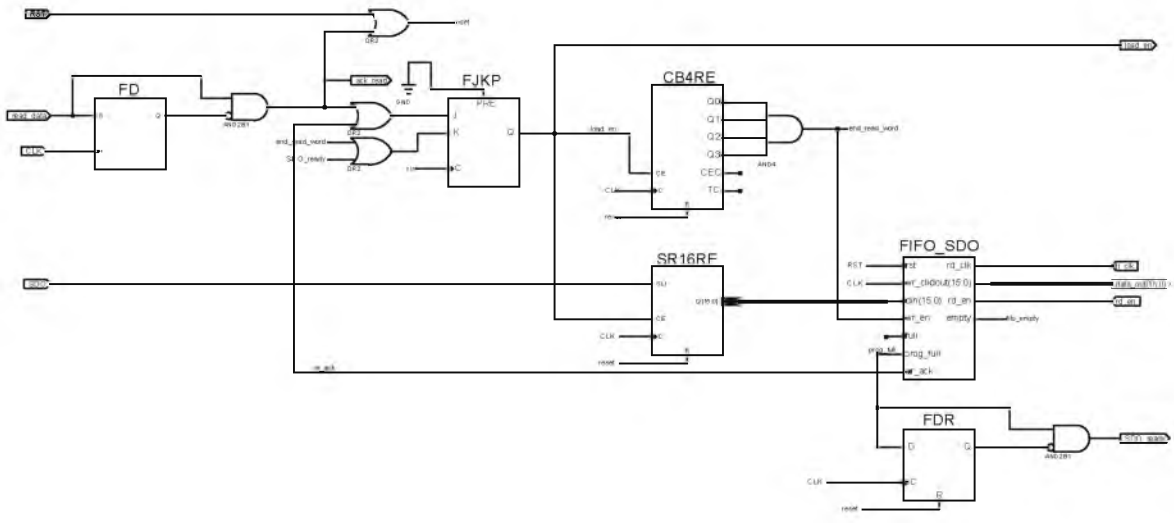

Figure E.4: FPGA firmware schematics of the SDO line which handles serial data transfers from the HERMES ASIC to the FPGA.

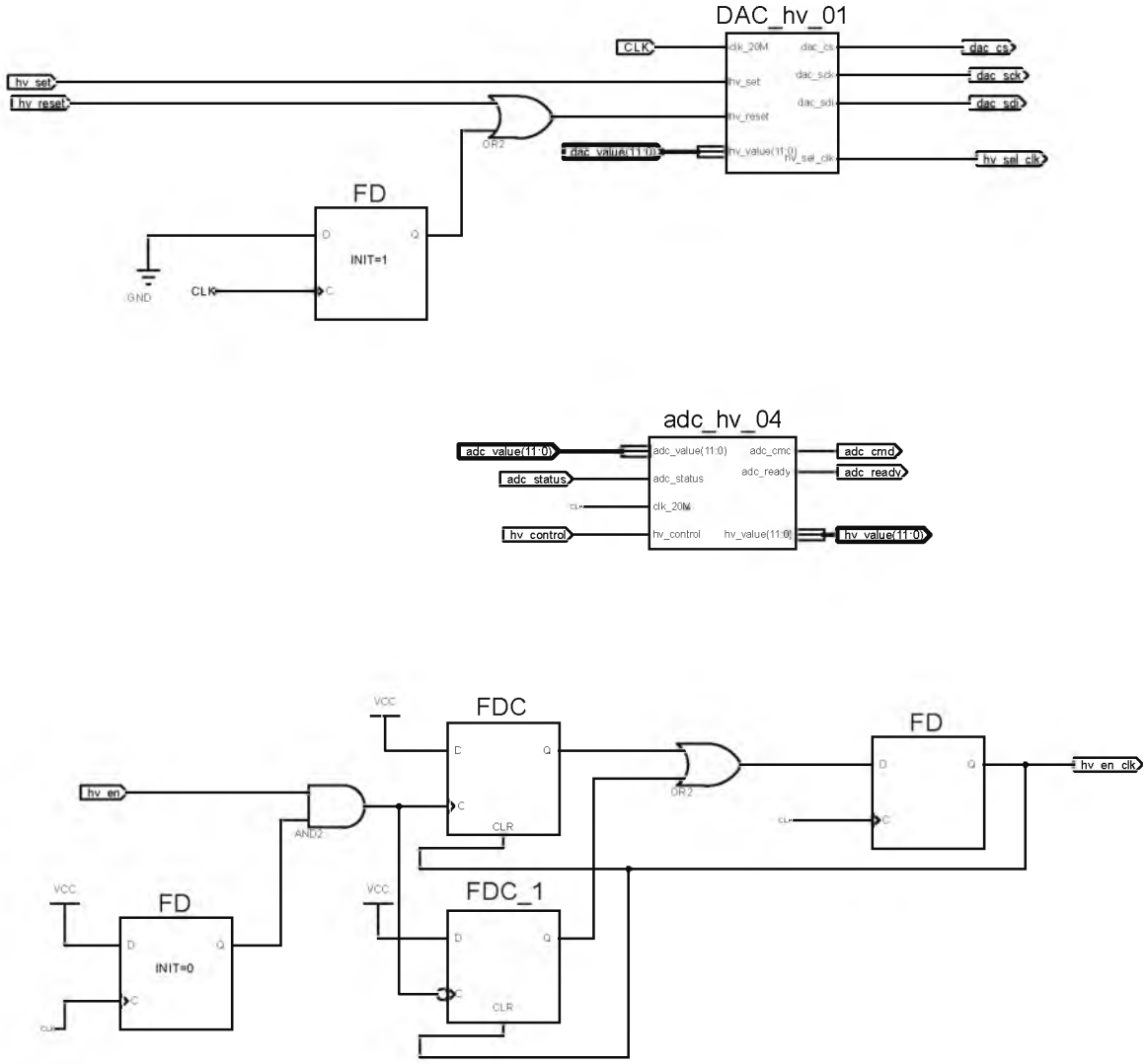

Figure E.5: FPGA firmware schematic for the high voltage system, including the ADC and DAC components.

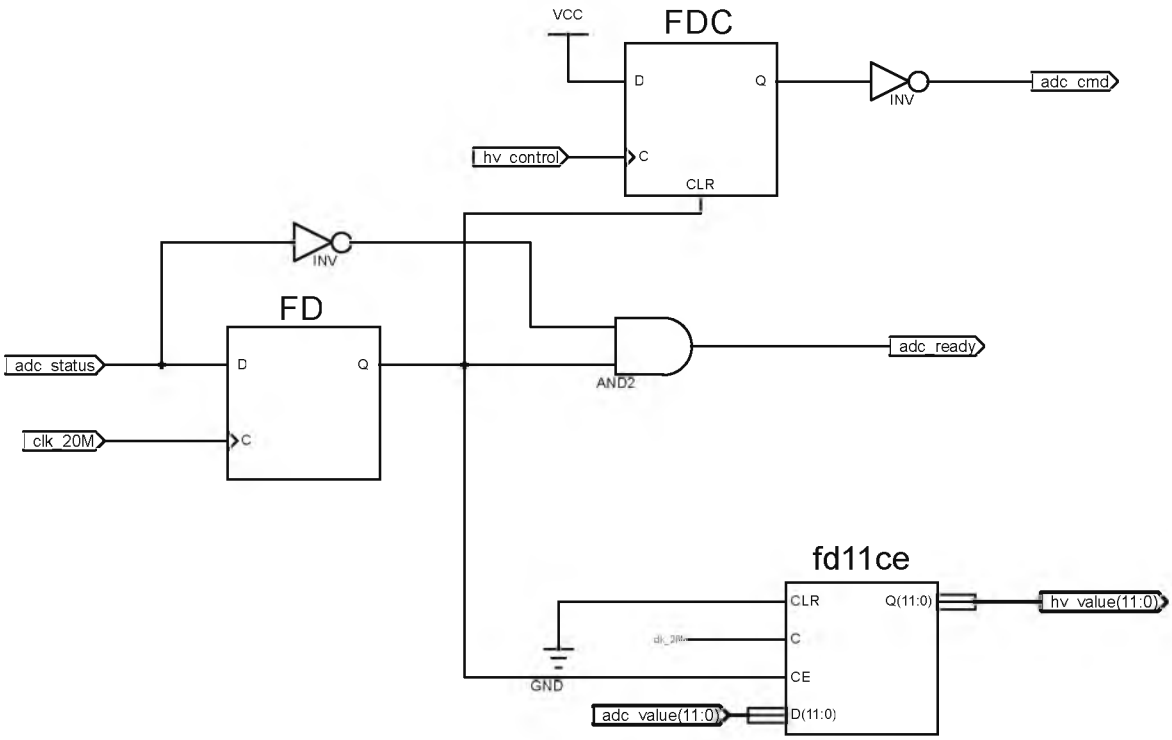

Figure E.6: FPGA firmware schematic for the ADC module of the high voltage system, responsible for measuring the voltage from the EMCO module.

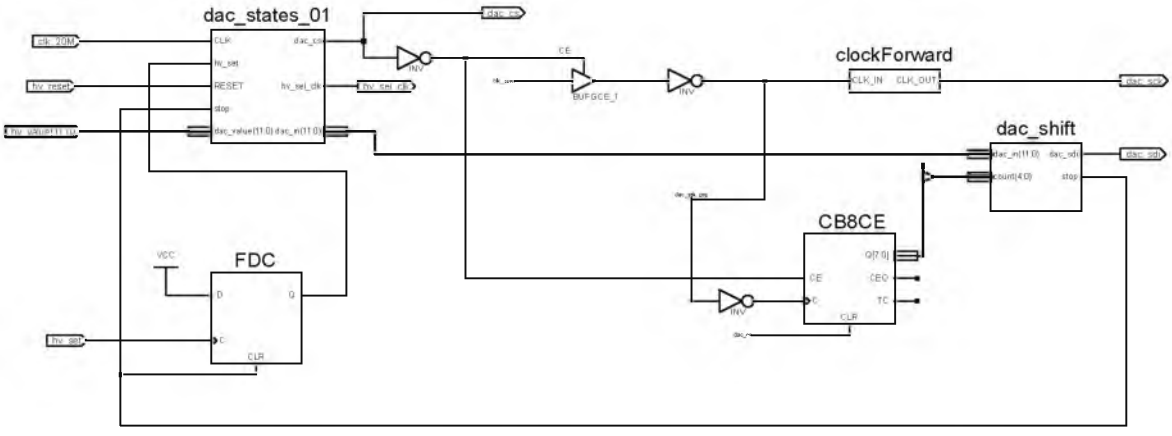

Figure E.7: FPGA firmware schematic for the DAC module of the high voltage system, responsible for setting the voltage on the EMCO module.

E.2 Verilog Firmware Modules

Listing E.1: acquisition_handler.v - A firmware module that aims coordinates the timing and signalling for acquisitions.

```
module acquisition_handler (
   input        wire    [15:0] acq_time,
        input   wire    start_acq,
   input        wire    CLK,
   input        wire    RST,
        output          reg     EN,
        output  reg     ack_start,
        output  wire    [15:0] current_count
    );


reg [15:0] quotient = 31250; // Quotient, used to slow the clock
reg [15:0] Q = 0;
reg [15:0] counter = 0;
reg start_status = 0;

assign current_count = counter[15:0];

// Count using the doubled frequency clock.
always @ (posedge CLK or posedge RST)
begin
         if(RST) begin
        Q <= 0;
                start_status <= 0;
                counter <= 0;
    end else
        begin

                if (!start_status && start_acq) begin
                        ack_start <= 1;
                        counter <= acq_time-1;
                        Q <= 0;
                        EN <= 1;
                end else begin
                        ack_start <= 0;
                end

                start_status <= start_acq; //  store the start_acq
                   for posedge detection

                if (EN) begin
                        if(Q == (quotient-1)) begin
                                // We're at the maximum value,
                                // Reset the divider counter
```

```
                                        Q <= 0;
                                        if (counter > 0) begin
                                                counter <= counter - 1;
                                        end else begin
                                                EN <= 0;
                                        end
                                end     else begin
                                        Q <= Q + 1;
                                end
                        end
                end
end

endmodule
```

Listing E.2: motor_control.v - A firmware module for controlling the stepping, direction and enable signalling to the stepper motor.

```
`timescale 1ns / 1ps
module motor_control(
    input [10:0] motor_pos,         // Motor postion [0-360 degrees
       ]->[0-2000] 0.18 deg / step
    input motor_dir_iscw,           // if true motor direction is CW
        input [2:0] motor_spd,              // motor speed    [n1 kHz-n2
           Hz]->[0-7] (this behalves more like pulse skipper)

        input   wire    start_motor,
        input           wire    motor_disable_in,
        input           wire    CLK,
        input   wire    RST,

        output  reg     ack_motor,

        output  reg     motor_step = 0,
        output  reg     motor_dir = 1,
        output  reg     motor_disable = 1
    );

//reg [15:0] quotient = 31250; // Quotient, used to slow the clock
reg [10:0] counter_step = 0;
reg [15:0] dly = 0;
reg [15:0] counter_dly = 0; // this is based on 2^(motor_spd)
reg start_status = 0;

always @ (posedge CLK or posedge RST)
begin
        if(RST)
        begin
```

```
                start_status <= 0;
                counter_step <= 0;
                dly <= 0;
                counter_dly <= 0;
                motor_disable <= 1;
                motor_dir <= 0;
end else // end reset section

      begin
      ack_motor <= start_motor;
      motor_disable <= motor_disable_in;
                if (ack_motor)
                begin
                        counter_step <= motor_pos; // motor position
                           is ditacted by the number of pulses sent
                           to the counter
                        dly <= (1<<motor_spd+6)-1; // equal to 2^(
                           motor_spd+n)-1 : NOTE: the n is used to
                           slow the motor otherwise it is too fast
                        counter_dly <= dly;
                        motor_dir <= motor_dir_iscw;
                        motor_step <= 0;
                        start_status <= 1;
                end else // end init section
                if (start_status)
                begin
                        ack_motor <= 0; // TODO : Check that this is
                           not too fast for the USB interface to
                           catch
                        if (counter_step > 0)
                        begin
                                        if (counter_dly > (dly>>1))
                                           // if first half of period
                                            - step is 1
                                                motor_step <= 1;
                                        else // second half of period
                                                motor_step <= 0;

                                        if(counter_dly > 0)
                                                counter_dly <=
                                                   counter_dly -1;

                                if (counter_dly == 0)
                                begin
                                        counter_step <= counter_step
                                           - 1;
                                        counter_dly <=  dly;
                                end // end setting pulse high
                        end else // end move counter iteration
                        begin
                                motor_step <= 0;
                                start_status <= 0;
```

```
                        end // end of steps
                    end // end stepping phase
                end // end init and stepping macro phase

end // posedge and reset phase


endmodule
```

Appendix F

Code

Listing F.1: A sample PANOPTES data file, showing the variation acquisition parameters and the channel data at the end.

```
Panopticon - Data Acquisition
Start Time          :      03:08:18.018PM 21-11-13
End Time            :      03:09:30.611PM 21-11-13

Acq. Type           :      Single Acquisition(s)
Acq. Number         :      1
Total Acq. Number   :      1
Acq. Time [s]       :      10

Positions:
Motor Increment     :      18
Motor Position      :      108

Global Settings:
Peaking Time        :      0.5 microseconds
Gain                :      0.75 mV/fC

Threshold Settings:
WL0                 :      300
WL1                 :      300
WH1                 :      1023
WL2                 :      300
WH2                 :      1023

Bias Voltage [V]    :      49.8935

Additional Details : {
```

```
N3
10 seeds - I 125 - ROPE15mm
Placed in shielded box, with black cloth and cardboard box over top
   for
light inhibition orientation of plaque  inner triangle ( the point
facing the single perpendicular seed) is  pointing toward back wall
   of
box phantom ( before spring loaded, which causes rotation )
}

Channel W0      W1      W2
0       1210    1207    1207
1       1378    1375    1378
2       1668    1668    1662
3       2052    2047    2045
4       2908    2884    2890
5       4003    3998    3988
6       5855    5842    5842
7       8738    8738    8729
8       4691    4670    4686
9       6418    6419    6419
10      4691    4677    4678
11      8081    7964    7977
12      6976    6977    6943
13      10204   10248   10223
14      16823   16879   16835
15      4663    4650    4605
16      6463    6339    6237
17      4624    4577    4598
18      9007    8123    8119
19      5123    5119    5096
20      7570    7564    7553
21      11132   11065   11068
22      17260   17224   17191
23      6062    5999    6001
24      4701    4688    4710
25      8618    8106    8167
26      5732    5613    5690
27      5585    5598    5566
28      7729    7738    7729
29      11370   11284   11305
30      5641    5601    5624
31      8465    7573    7475
32      7960    7901    7970
33      16854   16504   16550
34      5624    5585    5616
35      11116   11047   11123
36      7306    7229    7304
37      5230    5173    5199
38      8622    8376    8590
39      4286    4205    4229
40      5635    5547    5539
```

41	15712	15560	15670
42	10147	10089	10150
43	6830	6791	6819
44	4788	4768	4770
45	7517	7223	7427
46	4200	4084	4173
47	5293	5186	5203
48	4146	4101	4136
49	14535	14395	14447
50	8834	8701	8775
51	5805	5767	5810
52	5950	5719	5840
53	4175	4144	4149
54	4408	4147	4201
55	3265	3239	3272
56	7066	7012	7037
57	4868	4843	4853
58	3761	3736	3756
59	2207	2129	2162
60	1742	1712	1737
61	1471	1466	1466
62	1330	1324	1327
63	1236	1230	1234

Appendix G

Resulting Publications

Nuclear Instruments and Methods in Physics Research A 633 (2011) S276–S278

Contents lists available at ScienceDirect

Nuclear Instruments and Methods in Physics Research A

journal homepage: www.elsevier.com/locate/nima

Three-dimensional dosimetry imaging of I-125 plaque for eye cancer treatment

M. Weaver [a], J. Green [a], M. Petasecca [a], M.L.F. Lerch [a], D. Cutajar [a], D. Franklin [a], J. Jakubek [b], M.G. Carolan [a,c], M. Conway [d], S. Pospisil [b], T. Kron [e], P. Metcalfe [a], M. Zaider [f], A.B. Rosenfeld [a,*]

[a] Centre for Medical Radiation Physics—University of Wollongong, Northfileds Avenue, Wollongong 2500 NSW, Australia
[b] Institute of Experimental and Applied Physics, Czech Technical University in Prague, 12800 Prague 2, Czech Republic
[c] Illawarra Cancer Care Centre, Wollongong 2500 NSW, Australia
[d] Sydney Eye Hospital—Faculty of Medicine, The University of Sydney, Sydney 2006 NSW, Australia
[e] Peter MacCallum Cancer Centre, Melbourne Vic 8006, Australia
[f] Memorial Sloan-Kettering Cancer Centre, New York, NY 10021, USA

ARTICLE INFO

Available online 4 July 2010

Keywords:
Brachytherapy
Ocular cancer
Dosimetric imaging
Pixelated detector

ABSTRACT

Treatment of ocular cancers using eye plaque brachytherapy is now an established medical procedure. However, current QA for these eye plaques is quite rudimentary, limiting the opportunities for precise pre-tumour plaque customisation. This paper proposes and experimentally validates a new technique for imaging of eye plaque dose distributions using a high-resolution pixelated silicon detector. Results are presented demonstrating the 2D and 3D isodose surfaces produced using experimental data collected using this method.

Radiation Measurements 46 (2011) 2010–2013

Contents lists available at SciVerse ScienceDirect

Radiation Measurements

journal homepage: www.elsevier.com/locate/radmeas

Dosimetry verification in eye brachytherapy using silicon pixelated detectors

M. Weaver [a,*], M. Petasecca [a], M.L.F. Lerch [a], D. Cutajar [a], J. Jakůbek [b], S. Pospíšil [b], A.B. Rosenfeld [a,**]

[a] Centre of Medical Radiation Physics, University of Wollongong, Northfields Ave., Wollongong, NSW, Australia
[b] Institute of Experimental and Applied Physics, Czech Technical University in Prague, Prague, Czech Republic

ARTICLE INFO

Article history:
Received 30 November 2010
Received in revised form
17 September 2011
Accepted 5 October 2011

Keywords:
Eye plaque
Brachytherapy
Dosimetry
Timepix
Medipix2
Iodine-125

ABSTRACT

This study presents a high spatial resolution dosimetry system for quality assurance of I-125 eye plaques. The system is based on a silicon pixelated detector and is capable of deriving 3D dose distributions. A simple design was implemented, incorporating a movable eye plaque in a small water phantom above the silicon Medipix2 detector. It is designed for obtaining 2D dose distributions at different depths in water, for subsequent 3D dose mapping. The effect of backscattering in a medium placed behind the Medipix2 to simulate surrounding tissue has been studied in terms of dose distribution. Additionally, two modes of acquisition, event counting mode and the more complex time-over-threshold mode, were compared to the TG-43 protocol for the determination of their suitability for dosimetry.

Radiation Measurements 71 (2014) 310–314

Contents lists available at ScienceDirect

Radiation Measurements

journal homepage: www.elsevier.com/locate/radmeas

Panoptes: Calibration of a dosimetry system for eye brachytherapy

M. Weaver [a,*], M. Petasecca [a], D.L. Cutajar [a], M.L.F. Lerch [a], G. De Geronimo [b], D.A. Pinelli [b], A.J. Cullen [c], D.A. Prokopovich [d], V.L. Perevertaylo [e], A.B. Rosenfeld [a,**]

[a] Centre for Medical Radiation Physics, University of Wollongong, NSW, Australia
[b] Brookhaven National Laboratory, Upton, NY 11973, USA
[c] Illawarra Cancer Care Centre, Wollongong, NSW, Australia
[d] Australian Nuclear Science and Technology Organisation, Lucas Heights, NSW, Australia
[e] SPA-BIT, Kiev 04136, Ukraine

HIGHLIGHTS

- Volumetric detector system produced for plaque brachytherapy.
- Orthovoltage, flat-field calibration performed for detector pixels.
- Monte Carlo simulation showed mostly little angular deviation across all angles.
- Ion beam induced charge collection showed pixels uniform and fully depleted.

ARTICLE INFO

Article history:
Available online 13 April 2014

Keywords:
Eye plaque
Brachytherapy
Dosimetry
HERMES
IBICC

ABSTRACT

Intraocular cancer is a serious threat to the lives of those that suffer from it. Dosimetry for eye brachytherapy presents a significant challenge due to the inherently steep dose gradients that are needed to treat such small tumours in close proximity to sensitive normal structures. This issue is addressed by providing much needed quality assurance to eye brachytherapy, a novel volumetric dosimetry system, called Panoptes was developed. This study focuses on the preliminary characterisation and calibration of the system. Using ion beam facilities, the custom, pixelated silicon detector of Panoptes was shown to have good charge collection uniformity and a well defined sensitive volume. Flat-field calibration was conducted on the device using a 250 kVp orthovoltage beam. Finally, the detector and phantom were simulated with Monte Carlo in Geant4, to create water equivalent dose correction factors for each pixel across a range of angles.